1993-94 ANNUAL REPORT

# Reactions of Toxic Pollutants in Soil Systems

KEARNEY FOUNDATION OF SOIL SCIENCE
DIVISION OF AGRICULTURE AND NATURAL RESOURCES
UNIVERSITY OF CALIFORNIA

1993-94 ANNUAL REPORT

# Reactions of Toxic Pollutants in Soil Systems

EDITED BY DEBORAH SILVA

DR. ANDREW C. CHANG, DIRECTOR
KEARNEY FOUNDATION OF SOIL SCIENCE
DIVISION OF AGRICULTURE AND NATURAL RESOURCES
UNIVERSITY OF CALIFORNIA

# Contents



## Annual Progress Reports

## Appendix

# Kearney Foundation of Soil Science: A Brief Overview

The report that follows is the third in a series of five Annual Reports issued by the Kearney Foundation of Soil Science on the Foundation's current five-year research mission for 1991-96, **Reactions of Toxic Pollutants in Soil Systems**. Many of the Foundation's research projects are funded for two to three years; thus, several investigators are reporting intermediate research progress on projects that began in 1991-92 or 1992-93. Other reports represent first-year progress on projects whose funding cycle began in 1993-94. Each progress report indicates when the study was undertaken. Please refer to the Foundation's previous Annual Reports for this mission, as needed.

For more than 50 years, the M. Theodore Kearney Foundation of Soil Science at the University of California has established an impressive record in addressing critical research needs in the state and providing an intellectual forum for international leadership in soil science research. The Foundation has an endowment fund of more than $2 million, which supports, through a competitive grants process, fundamental and applied research by University faculty and Cooperative Extension personnel in the fields of soils, plant nutrition, and water science.

Mitigating the impacts of soil pollution is one of the major challenges facing California in the 1990s. Events that occur in soil have profound effects on surface water quality and groundwater quality, but the dynamics of the relationship between soil quality and water quality need additional study. At present, scientists lack sufficient data from field situations on the movement, transformation, and fate of soil contaminants that influence water quality. Whether soil contamination arises from seepage of solvents used to clean aircraft at military bases, from leaking petroleum storage tanks at industrial sites, from normal application of fertilizers and pesticides in farming operations, from waste disposal, or from buildup of toxic levels of metals due to trace element-laden agricultural drainage water, University of California soil scientists are the experts who must develop the knowledge base to predict the fate of toxics, provide leadership in remediation strategies, and recommend scientifically sound techniques to prevent future degradation of soil and water quality in the state.

Pesticides provide a good example of soil contaminants requiring further study. Half of the pesticides used in the United States are applied in California, which ranks fifth worldwide in terms of agricultural revenue. The state accounts for 25% of the world's annual pesticide usage. The pressing need for additional scientific research about the transport and fate of toxic chemicals as they travel down the soil profile becomes unequivocal when such consumption of xenobiotic compounds is coupled with the state's dependence on irrigation agriculture and its public health mandate to sustain groundwater quality for domestic use.

## Current Mission: Reactions of Toxic Pollutants in Soil Systems

The Foundation's 1991-96 mission, **Reactions of Toxic Pollutants in Soil Systems**, represents the first time the Foundation has focused on examination of soil pollution problems rather than production of agricultural products. Environmental problems, such as soil pollution, are characterized by an intimate intertwining of physical, chemical, and biological processes that require multidisciplinary research approaches. Many chemical sources of contamination are not miscible in water, but they can be transported, degraded, and transformed in soil. These soil processes need to be studied and managed for the protection of the state's natural resources and the public health of its citizens. The reactions, mechanisms, and interactions that occur in the soil's vadose region above the water table and in ground water under saturation conditions are not understood fully. The current five-year Kearney mission focuses only on soil pollution problems in the vadose zone as stated in the outline below:

I. Investigate soil mechanisms, processes, and interactions that control transport, degradation, transformation, and crop uptake of toxic pollutants

   Quantify and model soil processes that determine mobility and reactivity of pollutants in soil and the vadose zone, resulting in groundwater pollution.

   Investigate interactions of soil, water, rhizosphere, and pollutants

   For multi-phase and/or multi-pollutant systems, investigate physical, chemical, and biological reactions and porous media transport involved

II. Develop methodology for scaling up microscopic soil mechanisms and reactions to field-scale processes that apply to agricultural and urban soils

   Investigate spatial variation of physical, chemical, and biological reactions in soil and the vadose zone

   Improve predictive accuracy, including mathematical models' description of soil reactions

   Develop management strategies, including application of the Geographical Information System, to prevent soil and water pollution by toxic environmental pollutants.

The fundamental knowledge base, including remediation and management strategies, developed by this mission on toxics during this period will be applicable throughout the state and will serve as a basis for developing application-related programs in agricultural and urban environments. Many soil science issues, such as the fate of toxics, know few boundaries between agricultural and urban soil.

## History

The Kearney Foundation of Soil Science was established by the Regents of the University of California in 1954 to conduct research in soil science, plant nutrition and water science. Mr. M. Theodore Kearney, a prominent Fresno area farmer and founding member of the California Raisin Growers Association, died in 1906 and bequeathed his entire Fruit Vale Estate, worth close to $1.1 million, to the Regents of the University of California for agricultural research purposes. Over the years, Mr. Kearney had developed a fruitful working relationship with UC soil scientists whose advice regarding problems with drainage, salinity, and sodium had been essential to his ranch's success. Approximately 1,500 acres of Mr. Kearney's 5,000 acre Fruit Vale Estate had been planted to grapes for raisin production and the remainder was planted to alfalfa.

It was on Mr. Kearney's farm that University of California Professor W. P. Kelley conducted his classical experiments on alkali soil reclamation. UC Professor E. J. Wickson conducted field research on viticulture there. W. W. Mackie of the United States Department of Agriculture was the first to investigate land reclamation using a tile drainage system at the Kearney property in 1905. Mr. Kearney admired UC Professor E. Hilgard, widely regarded as the "father" of the California Agricultural Experiment Station. Dr. Hilgard began alkali soil studies in the San Joaquin Valley on horseback in 1877.

In 1908, the University took over management of the Kearney estate, located 10 miles west of Fresno, and operated it as a commercial farm until 1948, when the Regents authorized its sale. Income and proceeds from the sale of the farm resulted in the establishment of the Kearney Foundation of Soil Science in 1954 and the University's Kearney Agricultural Center in Parlier.

The early record shows that the in-house research staff of the Kearney Foundation was at the cutting edge of soils research. Their work had major spinoffs not only in agricultural production but also in human and animal health. For example, UC scientists funded by the Foundation studied the generation of radon gas in soils, discovered the importance of cobalt and molybdenum in nitrogen fixation, used $^{15}N$ isotopes for research, and determined selenium concentrations by X-ray fluorescence.

By the late 1960s, income from the endowment fund was insufficient to support the salaries and research programs of resident scientists, so the Foundation was reorganized to tackle new research missions every five years and to allocate research funds through a competitive grants process to existing faculty and Extension specialists, and farm advisors in the statewide Agricultural Experiment Station. The Foundation's research missions, established in five year cycles since 1970, have focused previously on nitrogen in the environment (1970-75), trace elements (1975-80), salinity (1980-85), and water penetration problems in irrigated soils (1986-91).

## Administration

The Associate Vice President for Agriculture, Division of Agriculture and Natural Resources, appoints a Director of the Kearney Foundation from one of the three Agricultural Experiment Station campuses (Berkeley, Davis, or Riverside) to oversee carrying out the designated mission. Dr. Andrew C. Chang, Professor of Agricultural Engineering and Agricultural Engineer in the Citrus Research Center - Agricultural Experiment Station at Riverside, is Director of the current mission. A Technical Committee and an Advisory Committee are appointed by the Director to help establish research priorities, administer the competitive grants process, and ensure that sufficient research progress and information dissemination occur. Current members of the Technical and Advisory Committees are listed in the Appendix.

## Information Dissemination

Since the 1980s, the Foundation has published an Annual Report of research progress. The Foundation also conducts workshops, holds seminars and technical conferences, and issues special reports to fulfill each mission's research objectives and to communicate research accomplishments.

On September 8-9, 1994, the Foundation hosted a Soil Science Conference at the University of California, Berkeley, to highlight research progress on projects funded by the Foundation during the current mission; to discuss the past, present, and future roles of soil science at the University of California; and to begin the process of selecting the next Kearney mission for the upcoming five-year cycle, 1996-2001. Speakers included principal investigators on Kearney projects, UC administrators, an industry colleague, and Kearney Foundation directors.

In June 1994, the Foundation jointly sponsored a Biosolids and Compost Workshop in conjunction with the Southern California Compost Coalition and the University of California Waste Management Work Group. The Kearney Foundation is participating in the development and publication of the first **Southern California Biosolids Resource Book**, which will be disseminated in the summer of 1995 by the Cooperative Extension Office in the Department of Soil and Environmental Sciences at Riverside.

In June 1993, the Foundation convened a Soil Pollution Workshop, which focused on identifying research and development needs in California, ranking the state's most important soil pollution problems, and recommending applied research approaches. The Foundation issued a report summarizing the workshop results.

Additional copies of Annual Reports and the Soil Pollution Workshop Report are available upon request from the Office of the Kearney Foundation Director.

# Effect of Sorption to Organic Matter on the Biodegradation of Organic Pollutants in Soil

KATE M. SCOW
*Department of Land, Air and Water Resources, Davis Campus*

## Summary

The objective of this three-year study was to determine the significance of sorption in governing rates of biodegradation of organic chemicals in soil. The emphasis was on the biodegradation of phenanthrene, phenol, *para*-nitrophenol, toluene, and trichloroethylene in soils with different organic matter contents and in soil amended with clay. For phenanthrene, no relationship was found between the sorption parameters ($K_{oc}$, $K_d$) and either the rate or percentage of phenanthrene mineralized in seven soils varying in organic matter content. The effect of clay addition to loam soil on phenanthrene biodegradation was dependent upon clay type: nontronite enhanced, halloysite substantially decreased, and montmorillonite had no impact on biodegradation. The reduction associated with halloysite was in part due to greater sorption of phenanthrene onto the clay and, supporting this hypothesis, halloysite addition had little impact on the biodegradation of a chemical subject to minimal sorption. Aging of the phenanthrene in soil had a substantial impact on the rate of biodegradation; degradation (following inoculation with bacteria) of phenanthrene incubated in sterile soil for 5 weeks was much slower than that of phenanthrene recently added to sterile soil. Inoculation of Tinker and Yolo soils with a bacterial strain able to degrade phenanthrene substantially enhanced the rate of phenanthrene biodegradation; however, a very high population density was required. Addition of surfactants or secondary carbon sources did not enhance phenanthrene biodegradation rates. Differences in the kinetics of mineralization of phenol and *para*-nitrophenol were due, in part, to phenol's ability to form irreversible bonds with soil organic matter and thus making it unavailable for degradation.

**Key Words:** biodegradation, sorption, desorption, PAH's, pollutants, soil microbiology, coupled processes.

## Project Objectives Addressed in 1993-94

1. Determine how the sorption partition coefficient, the amount and quality of sorbent, presence of additional carbon sources, soil moisture content, and initial population density influence the relationship between sorption and biodegradation rate in soil.
2. Determine the effects of clay additions on the sorption and biodegradation of phenanthrene in soil.
3. Determine the effect of aging on biodegradation of phenanthrene in soil.
4. Determine the relationship between biodegradation rate and population density of microorganisms able to degrade phenanthrene.
5. Determine if and how the amendment of soil with bacterial cultures, secondary carbon and energy sources, or surfactants enhances the biodegradation of phenanthrene and naphthalene.
6. Determine the effect of bound residue formation on the kinetics of biodegradation of organic chemicals in soil.
7. Simplify an existing model describing diffusion, sorption and biodegradation in the presence of spherical aggregates to use for screening those conditions when biodegradation may be limited by mass transfer.

## Research Plans and Procedures

(A) Measurement of biodegradation. The focus of the project was on phenanthrene, with additional studies conducted with phenol, *para*-nitrophenol (PNP), toluene and trichloroethylene (TCE). Biodegradation studies were conducted in forest soils, with organic matter content ranging from 5% to 19%, and agricultural soils, with organic matter content ranging from 1.1% to 2.5%. The forest soils (either sandy or silt loams), collected from Lake Tahoe National Forest, included Scott, Forbes, Jocal, Aiken, Sobrante, and Tinker (Table 1). The agricultural soils, collected from Yolo county, included Yolo silt loam, and Rindge soil from the Delta region. In biodegradation studies, from 10 to 50 g (dry wt) soil was incubated at 0.33 bar with phenanthrene at concentrations of 50 ng or 50 µg per ml soil solution. Soils were incubated for 2000 hours in the dark at 25 ± 2°C. Biodegradation was measured in modified biometer flasks using $^{14}C$-radiolabeled chemical to determine the amount of $^{14}CO_2$ mineralized over time. To distinguish between abiotic and biotic processes and for use in sorption and desorption experiments, soil samples were sterilized with cobalt-60 irradiation at Crocker Nuclear Lab, on the UC Davis campus.

In late 1993, our radiolabeled phenanthrene (purchased from California Bionuclear and guaranteed to be >98% pure) was found to be contaminated with a mixture of chemicals that made up approximately 50% of the total $^{14}C$ and that were more polar than the phenanthrene itself. Approximately seven compounds in addition to phenanthrene could be detected by TLC, HPLC, and GC-MS. It was not possible to identify the contaminants; however, they were suspected to be chemicals associated with the synthesis of the phenanthrene because unopened radiolabeled

chemical from the same lot showed the same pattern of contamination. The contaminated material was separated into purified phenanthrene and a mixture of the contaminants. The contaminants degraded more slowly than did the phenanthrene alone and a biodegradation rate similar to that of the original material could be attained by combining the newly purified phenanthrene with the mixture of contaminants. New radiolabeled phenanthrene was purchased from another company (Sigma), confirmed to be of 99% purity, and used in all subsequent experiments.

(B) Characterization of microbial populations. Enumeration of phenanthrene biodegraders was conducted using an overlayer plate count technique. Mineral salts medium is contained in the bottom layer and phenanthrene and the dilutions of soil are suspended in an overlayer of agar. Phenanthrene degraders can be recognized by a halo of clearing surrounding them. The same dilutions of microbial cell extract were used to determine the total soil microbial population with a viable count method using 0.1 strength TSA plates. An estimate of microbial biomass was obtained by substrate induced respiration (Anderson and Domsch, 1978)

(C) Measurement of sorption. Sorption isotherms of $^{14}C$-phenanthrene were measured in sterilized soils and clay. Four point sorption isotherms were prepared with each point measured in duplicate. So as to remain in the linear portion of the isotherm, equilibrium aqueous concentrations were kept at or less than 1/10 of phenanthrene's water solubility (Karickhoff et al., 1979). Different ratios of sterile soil or sorbent to calcium chloride solution were tested. A mixture of radiolabeled and unlabeled phenanthrene at concentrations ranging from 0.1 ng to 100 µg per ml were added to tubes containing the sorbent-solution mixture and shaken for 4 h to 1 week. The contents of the tubes were centrifuged and the supernatant measured for remaining $^{14}C$. Desorption rates were determined by placing sterile soil that had been preequilibrated with phenanthrene into clean solution and measuring the change in $^{14}C$ over time in solution. This procedure was repeated several times. Kd values were calculated by fitting a linear isotherm to these points.

(D) Other measurements. Organic carbon contents were measured using a Carlo Erba Carbon Nitrogen Gas Analyzer (model NA 1500 NC), except for Yolo soil for which organic matter was measured by the Walkley-Black Spectrophotometric Method, a technique used in the Division of Agriculture and Natural Resources (DANR) Analytical laboratories at the University of California, Davis (DANR Analytical Method 7.10--Soil Organic Carbon).

## Results

A. Relationship between sorption and biodegradation of phenanthrene in soils.

Research on the sorption and biodegradation of phenanthrene was confounded by the discovery of significant contamination in the radioisotope stock (as discussed above). This discovery was made in late 1993; thus, some

of the results reported in progress reports from 1992 and 1993 are no longer valid. Most of the results discussed below are from experiments conducted with the newly purchased, uncontaminated phenanthrene stock. In some cases, results with the contaminated material are presented (and specified as such) where the conclusions are still valid.

Experiments were conducted to determine if there is a relationship between sorption and biodegradation in different soils varying in their organic matter content. A preliminary study had suggested a relationship between biodegradation rate and the measured $K_{OC}$ for several soils. The biodegradation of a low concentration (50 ng per g) of phenanthrene was measured in six soils with organic carbon (OC) contents ranging from 3.6 to 9.5%. These soils were collected from the Sierra Nevada mountains and foothills near the Tahoe National Forrest. The seventh soil, an agricultural soil collected from the San Joaquin Valley, contained 1.1 % OC. Table 1 summarizes the soil classes, pH, and soil organic carbon content for the various soils. A low concentration of phenanthrene was selected to minimize the influence of microbial growth on phenanthrene biodegradation kinetics and high organic matter soils were selected to ensure substantial sorption of the chemical.

*1. Sorption/desorption.* The sorption of phenanthrene in soil-water suspensions was measured at four concentrations, all of which were below the calculated water solubility for phenanthrene. Fig. 1 shows the sorption isotherms for Yolo and Tinker soils. Sorption partition coefficients were calculated using the linear isotherm relationship. Measured $K_d$ values for phenanthrene in the six soils varied within a factor of 12 (Table 1). Desorption isotherms showed significant hysteresis (shown as open symbols and dotted lines in Fig. 1), indicating that sorption of some portion of the phenanthrene was irreversible. The Koc values were relatively similar, varying within a factor of two (Table 1).

*2. Biodegradation.* The biodegradation of 50 ng phenanathrene per g of soil was measured in the soils described above (Fig. 2). The soils containing the lowest (Yolo) and highest (Tinker) organic carbon contents had the highest rates of mineralization. Plots of the first derivatives of the biodegradation rates indicated that rates in both Yolo and TInker soils showed an initial period of rapid acceleration and very high rates, followed by a period of rapid deceleration (Fig. 3). Other soils accelerated more slowly and reached substantially lower maximum rates than did Yolo and Tinker before the rates began to decline. Other soils, such as Forbes, started out and continued with a low and cnstant rate of biodegradation. The initial rates of biodegradation were calculated and are summarized in Table 2. No systematic relationship was observed between sorption parameters--e.g., phenanthrene sorption partition coefficient ($K_d$) or sorption partition coefficient normalized for fraction organic carbon (Koc)--and the initial rate or final extent of biodegradation. There was also no relationship between biodegradation rate and soil OC content.

Biodegradation of phenanthrene was also measured at a higher concentration of 50 μg phenanthrene per ml in Yolo and Tinker soils (Fig. 4). The biodegradation curves showed the sigmoidal shapes characteristic of microbial growth. Again, biodegradation was more rapid in Yolo then Tinker. Unlike what was observed for the lower concentration of phenanthrene, however, the percentage of phenanthrene mineralized was lower in Yolo than Tinker.

Substrate-induced respiration (SIR) is an estimate of the total, viable microbial biomass in soil. Yolo, the soil with the highest biodegradation rate, also had the highest SIR value (Table 2). Tinker, with the second highest rate of biodegradation, had an intermediate SIR value. The soils with the two lowest SIR values, Forbes and Aiken, also had relatively low rates of degradation. However, the third highest SIR value was measured in Scott, which was ranked second from last among the soils in its biodegradation rate. Thus, there was no consistent relationship between SIR and biodegradation.

Even though the $K_{OC}$ values were relatively similar among the soils, the kinetics of biodegradation of phenanthrene in Yolo soil differed from most other soils (with the exception of Tinker) with respect to initial rate and final extent of degradation. An experiment was conducted to determine the relationship between the availability of 50 ng phenanthrene per ml over time and the rate of biodegradation in Yolo and Sobrante soil. Studies were conducted in sterile and nonsterile soils at moisture levels of 0.33 bar (unsaturated) and in slurries. Mineralization of $^{14}C$-phenanthrene (stock with contaminants) was monitored continuously, and at four points over the time-course of degradation, soil samples extracted with calcium chloride (solution phase) and methylene chloride (sorbed phase) were analyzed for $^{14}C$. The rate of biodegradation of phenanthrene by the indigenous population was significantly faster in Yolo than in Sobrante for both unsaturated and slurried soil. Biodegradation was more rapid in slurried than in unsaturated Yolo soil; however there was slightly higher degradation in the unsaturated Sobrante soil than in slurry. At the beginning of incubation, the solution phase concentration in Yolo was approximately twice as much as in Sobrante soil for both unsaturated and slurried soils. Also, approximately 4.5 and 7.4 times more chemical was available in slurry than in unsaturated Yolo and Sobrante, respectively. Over time, the solution concentration in unsaturated soil was reduced in nonsterile but remained approximately the same in sterile soil. The fraction of phenanthrene that was sorbed increased between 20 and 143 h in sterile unsaturated Yolo and Sobrante and remained at the same level at 529 h. In nonsterile Yolo and Sobrante soil, the fraction sorbed increased between 20 and 75 h, and then decreased at 143 and 529 h as biodegradation continued.

Thus, the conclusions of this study were that there was a direct relationship between biodegradation rate and availability of phenanthrene as evidenced by comparison of slurried to unsaturated Yolo soil and comparisons of Yolo to Sobrante soil. The relationship was not supported by comparison of slurried to unsaturated Sobrante soil for reasons that are unknown at this time. Another conclusion was that at least part of the fraction of phenanthrene

originally sorbed was later available for biodegradation as seen in the decline in the sorbed concentration over time in nonsterile Yolo and Sobrante soils.

Preliminary studies were conducted on the distribution of sorption and biodegradation among different soil aggregate size fractions. Mineralization of phenathrene (stock with contaminants) was twice as rapid in Yolo (1.8% OM) than Tinker (18% OM) soil. The population density of phenanthrene degraders on a whole soil basis was similar in the two soils. The sorption partition coefficient ($K_d$) was significantly higher in Tinker than Yolo soil. There was no clear difference in the distribution of potential phenanthrene degrading organisms or sorbed phenanthrene at 32 d among soil aggregates ranging in diameter from <0.5 to 2 mm in either soil. However, short-term data for Yolo indicated more phenanthene was associated with smaller than larger aggregate fractions. More phenanthrene assimilation (based on fumigation-extraction) appeared to be occurring in smaller size aggregate fractions in Yolo; whereas, there was no spatial pattern in Tinker. Thus, in Yolo soil, there was a correspondence between location of metabolism and location of phenanthrene. The % $^{14}C$ incorporated into microbial biomass was relatively low (about 3-8%), as would be expected for phenanthrene concentrations too low to support growth. These results are preliminary and are confounded by the presence of a contaminant in the radioisotope stock; thus, further research is needed on this topic.

*3. Soil moisture content .*

Numerous sorption studies are conducted in soils that are slurried rather than incubated at field moisture levels. To evaluate the effect of soil moisture on phenanthrene biodegradation, the degradation of 50 ng radiolabeled phenanthrene (stock with contaminants) per ml was measured in Yolo silt loam at soil to solution ratios of 1:0.16; 1:10, and 1:50. The initial rate of degradation of phenenthrene was substantially higher in the slurried treatments than at field moisture level, and the % degraded by 350 h was approximately 22, 20 and 9.5% for the soil to solution ratios of 1:50, 1:10, and 1:0.16, respectively.

The effect of incubating Yolo soil at moisture contents of 8, 16, 50, and 100% on the degradation of 50 ng phenanthrene (stock with contaminants) per ml was measured. Degradation was fastest at 16% moisture, and then increasingly slower at moisture contents of 50, 8 and then 100%. It is likely that the decline in rate was in part due to oxygen diffusion limitations at the higher moisture contents.

B. Effect of clay additions on biodegradation of phenanthrene in soil.

Several types of clay minerals were added to Yolo loam at levels sufficient to change Yolo's classification to a clay loam. Of the clays tested, nontronite and montmorillonite are 2:1 clays, whereas halloysite is a 1:1 clay. Specific surface areas of the minerals as determined by $N_2$-BET were 52.7, 24.6, 34.8, 7.1, and 21.9 $m^2/g$ for nontronite, montmorillonite, halloysite, kaolinite, and Yolo soil, respectively.

Addition of nontronite to Yolo soil slightly increased the rate and extent of biodegradation of phenanthrene (Fig. 5). Montmorillonite had no effect on degradation, whereas halloysite substantially decreased the rate of degradation. Measurement of sorption isotherms for phenanthrene in Yolo soil with and without clay showed that addition of nontronite did not change the isotherm or sorption partitiion coefficient much from those measured in unamended soil (Kd = 183 in soil only and 185 in nontronite-amended soil); whereas, halloysite addition increased the soil Kd by more than two-fold (to 410) (Fig. 6). Desorption was partially irreversible in both clay-amended soils, yet a greater portion of the sorbed material was not available for desorption in the halloysite-amended soil. The sequence of soil amendments influenced the degree to which halloysite affected phenanthrene biodegradation. If phenanthrene addition preceded the addition of halloysite, there was a depression in the rate of phenanthrene degradation relative to the rate in the absence of clay (Fig. 7). If clay was added before phenanthrene, or if the phenanthrene and clay were first mixed together and then added as a complex to soil, the phenanthrene biodegradation rate was severely depressed (Fig. 7). In contrast, the sequence of soil amendments when nontronite was added to soil had almost no effect on the biodegradation of phenanthrene (Fig 8). Comparison of purified, calcium-saturated halloysite with unpurified halloysite showed that unpurified material had little effect on the biodegradation of phenanthrene; whereas, the purified material repressed the rate (Fig. 9). Addition of calcium or sodium salt to soil at two concentrations had little effect on the biodegradation of phenanthrene (Fig. 10). Addition of halloysite to Yolo soil had no effect on the biodegradation of glucose, which is subject to only minimal sorption in soil; however, nontronite addition resulted in a slight stimulation of the rate of glucose degradation (Fig 11).

C. Effect of aging on biodegradation of phenanthrene in soil.

It becomes increasingly difficult to extract many chemicals the longer they have been in contact with soil. The decreased extractability, called aging, is associated with a decrease in the bioavailability and degradability of the chemicals. The phenomenon of aging has been observed for ethylene dibromide (Steinberg et al., 1987) and other volatile chemicals. We hypothesized that aged phenanthrene is degraded more slowly than freshly added phenanthrene. Samples of sterile soil were either incubated with 50 ng phenanthrene per g for five weeks (aged) or phenathrene was added at the beginning of the experiment. The soils were inoculated with a pure culture of bacteria able to degrade phenanthrene as a sole carbon and energy source (*Arthrobacter* sp.) and the mineralization of phenanthrene was measured. Soils were incubated both in soil-water suspensions or under unsaturated conditions (16% moisture). In both soil-water suspensions and unsaturated soil, there was substantially reduced degradation of the aged phenanthrene in comparison to the more rapid and extensive degradation of the recently added phenanthrene (Fig 12). There was approximately 15% more freshly added phenanthrene degraded in the soil-water suspension than in the unsaturated soil; whereas, there was no difference in the percentage of aged phenanthrene degradation between the two systems. (See also Fig. 13, described below).

D. Effect of initial population density on biodegradation of phenanthene.

A most probable number (MPN) quantification method for phenanthrene degraders using overlayer plates was adapted for this study. Preliminary studies using a pure culture of phenanthrene-degrading bacteria confirmed that the method was valid. The MPN analysis of phenanthrene degraders in soils indicated that a group of Tahoe soils (including Tinker and Sobrante collected earlier than the samples in which the biodegradation and sorption studies were conducted) had similar population densities. The densities ranged from 2-6 $x10^5$ cells per g soil and the density in Yolo soil was only slightly higher (Table 3). The differences in population density between Yolo or Tinker and Sobrante soil were not enough to explain the differences in biodegradation rate. It is possible there were changes in the population densities between the two times when the soils were collected. However, probably more important are differences in the composition of the populations responsible for phenanthrene degradation in the various soils; thus, the influence of microbial population on biodegradation kinetics cannot be ruled out altogether.

Time-course measurements of biodegradation of sorbed chemicals in soil often show an initial rapid rate followed by a slower rate of degradation (Scow et al., 1986). Model simulations (using the DSB model) of biodegradation under conditions where sorption and diffusion limit the availability of a chemical to microorganisms indicate that one explanation for this phenomenon may be that the fast rate results from degradation of readily degradable, non-sorbed material and, in the later part of the curve, the slow rate is due to degradation of material that is desorbed from the organic surface (Chung et al., 1993). Thus it was hypothesized that a higher initial population density of bacteria able to degrade the compound should result in higher initial rates and extent of degradation. Experiments were conducted under different conditions using a pure culture of *Arthrobacter* sp.

First, simulations with the DSB model were performed to test the sensitivity to the first order rate constant of the cumulative biodegradation of a chemical with a $K_d$ of 400 in the presence of spherical aggregates. Varying the rate constant over a factor of 10 had a dramatic effect on the rate of biodegradation (Fig. 14). The first order rate constant (actually a pseudo first order rate constant) is proportional to initial population density; therefore, the rate constant can be manipulated by altering the initial population density. A series of experiments was set up to test the model predictions.

The effect of inoculation was tested in nonsterile Yolo and Tinker soils to which phenanthrene had been freshly added. An initial population density of $10^7$ cells of *Arthrobacter* sp. per g of soil had no impact on the rate of biodegradation of 50 ng phenanthrene per g in either soil (Fig. 15). On the other hand, an inoculation density of $10^9$ led to a rate of degradation substantially enhanced above that in the soil with $10^7$ cells per g and the rate of biodegradation was similar in the two soils (Fig. 15).

The interaction of aging and initial population density was investigated in sterile Reiff soil (closely related to Yolo silt loam). Soil was aged for 10 weeks with phenanthrene and then incubated under unsaturated conditions with one of three initial population densities. At the same time, soil that had been freshly amended with the same concentration of phenanthrene also received one of the three population densities. In the freshly amended soil, inoculation with $5x10^5$ cells per g led to degradation of less than 10% of the added phenanthrene; whereas, inoculation with 1 or $4x10^8$ cells per g led to rapid and similar rates of degradation, which resulted in the mineralization of between 50 and 60% of the added phenanthrene (Fig. 13). In soil aged with phenanthrene, on the other hand, inoculation with $5x10^5$ cells per g of sterile soil did not result in any mineralization of phenanthrene. Inoculation with 1 or $4x10^8$ cells per g resulted in greater degradation than at the lower inoculum density; however, the initial rate and final percentage mineralized (approximately 20% for both densities) were significantly lower than in freshly amended soil.

Another means by which to increase the population size of phenanthrene-degrading organisms is to pre-expose the soil to phenanthrene. The assumption is that by the time a second allotment of phenanthrene is added, the population has grown to a higher density than in unexposed soil. The microbial population in Yolo soil was initially exposed to either 50 ng or 50 µg of phenanthrene per g of soil, and then the biodegradation of a second addition (50 ng per g) of phenanthrene was measured. Soil that had been initially exposed to phenanthrene showed higher rates of phenanthrene degradation than unexposed soil and the degree of stimulation was proportional to exposure concentration (Fig 16). The stimulation could have been due to either growth of an initially small population able to degrade phenanthrene or due to enzyme induction during the initial exposure.

Experiments were conducted using different initial population densities of *Arthrobacter* sp. able to degrade phenanthrene. The organisms were inoculated at three different population densities into mineral salts medium or sterile soil slurry containing 50 ng of phenanthrene (stock with contaminants) per ml. The % of phenanthrene degraded was significantly greater in mineral salts medium than in soil slurry. The fraction of phenanthrene degraded in mineral salts medium by 60 h was 21, 10, and 1% at initial population densities of $10^9$, $10^7$, and $10^5$ cells per ml, respectively. The fraction degraded in soil slurry by 60 h was 4.5, 2, and 1.5% at initial population densities of $10^9$, $10^7$, and $10^5$ cells per ml, respectively.

The *Arthrobacter* strain was also reintroduced into sterile and nonsterile Yolo soil containing 1 µg naphthalene per g soil. Inoculation caused a significant enhancement in both the initial and second phase rate of degradation. By 1580 h, approximately 52% of the naphthalene had been mineralized to $CO_2$; whereas, 38% had degraded in uninoculated soil. In the sterile soil, by 1580 h the organism degraded 32% of the added napthalene after a 50 h lag period.

E. Enhancement of PAH biodegradation in soil.

In addition to the inoculation studies described above, other approaches were tested to enhance the biodegradation of phenanthrene and naphthalene in soil. For some experiments, simulations using the DSB model of cumulative biodegradation over time were performed to develop hypotheses for which manipulations would increase biodegradation rates.

Another means by which some pollutants' biodegradation rate constants can be increased is by adding a secondary substrate or cometabolite in addition to the pollutant. Three different carbon sources were tested for their ability to inhibit or accelerate the degradation of 50 ng of phenanthrene (stock with contaminants) per ml in Yolo soil. The compounds tested were 50 μg per g of salicylic acid (SA), a metabolite and inducer of naphthalene and certain phenanthrene metabolic pathways; 50 μg per g of phthalic acid, a metabolite of another phenanthrene metabolic pathway; and 500 μg per g of glucose, not expected to have any specific interaction with phenanthrene. None of the compounds had an effect on the biodegradation of 50 ng per g of phenanthrene (Fig. 17). Studies with radiolabeled SA showed that degradation of SA in Yolo soil was completed in less than 30 hours; whereas, phenanthrene degradation was far slower and on the order of weeks rather than hours.

Another means to enhance the biodegradation of a sorbed chemical is to lower its sorption partition coefficient. Directly altering the soil's or the chemical's characteristics, which could change the Kd, may not be possible or feasible; however, addition of a surfactant can alter sorption by lowering the surface tension of the sorbate through its interaction with the surface active surfactant. Figure 18 shows the sensitivity of biodegradation to alterations in the $K_d$. Experiments were conducted using three surfactants reported to enhance, at least under some conditions, the biodegradation of sorbed chemicals. Of the surfactants tested, Tween 20 and Tween 80 had little impact on the biodegradation of 50 ng phenanthrene per g of unsaturated soil; whereas, polyethyleneglycol (PEG) slightly inhibited phenanthrene degradation in unsaturated soil (Fig. 19). In soil suspensions, none of the surfactants affected phenanthrene biodegradation (Fig. 20).

A study was also conducted to determine the possibility of enhancement of the rate of degradation of naphthalene in soil. Addition of 0.5 ml of a 10% solution of the detergent, Tween 80, at the beginning of an experiment resulted in a slight stimulation of naphthalene mineralization (by 2%) within the first 16 h of incubation. Addition of Tween 80 after 100 h of incubation with napthalene had no effect on subsequent degradation.

F. Sorption and biodegradation of phenanthrene in Yolo soil amended with artificial sorbent.

Exeriments were conducted in soils amended with artificial sorbents to test the effects of manipulating sorption on biodegradation. Naphthalene at a concentration of 500 ng per g soil exhibited a rapid rate of mineralization within the first 20 h of incubation. Over the period of 20 to 80 h, the rate slowly

declined and stabilized at a slow and constant rate. The shape of the curves were similar in unamended soil as well as in soil to which had been added 1.0 or 2.0 g SM-7 beads per 50 g soil. However, the greater the amount of beads added, the slower the initial rate of degradation and the lower the percent mineralized within 200 h. The percentage of radioisotope-labeled naphthalene mineralized was approximately 27, 22.5, and 20% for soil that had been amended with 0, 1.0 or 2.0 g beads, respectively.

Sorption isotherms were measured for phenanthrene on sterilized Yolo silt loam, activated carbon, and SM-7 chromatography beads. The chemical was incubated with the sorbents for different durations to determine the time at which an equilibrium concentration distribution was reached. Isotherms were linear over the concentrations tested for soil and sorbents. The $K_{OC}$'s for phenanthrene on synthetic sorbents were one and a half to two orders of magnitude higher than for soil, with values of approximately 2-6 x $10^6$ for both activated carbon and beads. Sorption was, for the most part, irreversible for both artificial sorbents.

A preliminary experiment measuring the biodegradation of 10 µg phenanthrene (stock with contaminants) per g Yolo silt loam, with and without the addition of 1 g activated carbon per 50 g soil, showed a strong effect of activated carbon on the rate of biodegradation. In the absence of activated carbon, the rate of mineralization of phenanthrene accelerated within the first 200 h of incubation, and then decelerated over the next 1300 h. At 1600 h, 27% of the phenanthrene was mineralized. In the presence of activated carbon, there was a lag period of approximately 180 h, and then the phenanthrene was mineralized at a slow, linear rate. By 1600 h only 10% had been mineralized in the presence of activated carbon.

A second experiment was designed to test the effect of phenanthrene concentration and activated carbon concentration on the kinetics of mineralization of phenanthrene. Fifty g of Yolo silt loam was amended with 0, 0.2, and 1.0 g of activated carbon and then mixed with either 50 (no-growth) or 2000 (presumably growth conditions) ng of phenanthrene per g of soil. At a concentration of 50 ng per g, phenanthrene (stock with contaminants) degradation in unamended soil began immediately and the rate declined over time. By 1400 h, approximately 43% (21.5 ng per g) of the chemical had been mineralized. At the higher concentration, phenanthrene degradation in unamended soil showed an initial period of acceleration in the rate and then the rate declined. By 1400 h, 30% (600 ng per g) of the chemical had been mineralized. Activated carbon substantially lowered the rate of mineralization of phenanthrene. By 1400 h, less than 10% of either concentration of phenanthrene was mineralized in the presence of activated carbon.

Mineralization of 50 ng of phenanthrene (stock with contaminants) per g soil was measured in 10 g Yolo silt loam amended with 0, 100 or 500 mg SM-7 chromatography beads. In one set of treatments, pre-equilibrated chemical-sorbent complexes were added to soil; in another set, phenanthrene was added to soil containing SM-7 beads. There was a direct relationship between

amount of sorbent and the rate of mineralization in the treatments where the chemical was added to soil containing beads. There was no mineralization of the phenanthrene that had been pre-sorbed to 500 mg of beads; however, there was a slow, linear rate of degradation of the same mass of chemical pre-sorbed to 100 mg of beads.

G. Sorption, bound residue formation, and biodegradation of phenol and PNP in soil.

Bound residues are defined as chemical species that are not extracted by methods that significantly change the chemical nature of these residues (Calderbank, 1989). The formation of bound residues between organic chemicals and soil organic matter can confound studies of sorption because sorption partition coefficients do not reflect the potential for bound residue formation. Because the process of bound residue formation is usually irreversible, rather than reversible, as sorption is alleged to be, bound residues should influence biodegradation kinetics differently from sorption.

A study was conducted to determine why phenol and PNP, which are structurally similar chemicals, differ with respect to their kinetic patterns in soil. Both chemicals are highly soluble and the log octanol water partition coefficients are similar, with values of 1.46 and 1.91 for phenol and PNP, respectively. The pKs for phenol and PNP are 10.02 and 7.15, respectively. Even with this difference, however, the same trends in biodegradation kinetic patterns were observed in eight soils ranging in pH from 4 to 8. A major difference between PNP and phenol, however, is that phenol has a strong propensity to be oxidized by extracellular enzymes called phenoloxidases, the products of which become covalently linked to soil organic matter and form bound residues (Claus and Filip, 1990). PNP, on the other hand, does not appear to form bound residues.

Studies of the biodegradation of low concentrations of the two chemicals in eight soils showed that the two-compartment model (Scow et al., 1986) fits significantly better than does the first order model for phenol; whereas, there is no significant difference in the fits of the two models for the PNP data. In looking at the biodegradation of PNP and phenol in Yolo silt loam, the most obvious difference between the two chemicals is that about 8-12% more PNP than phenol is always mineralized to $CO_2$. A less obvious difference is the shape of the curves: phenol abruptly levels off asymptotically; whereas, the decrease in rate of PNP is more gradual.

Sorption and desorption isotherms were measured in Yolo soil. Although the slope of the sorption isotherm was almost the same for the two chemicals, PNP sorption was largely reversible; phenol sorption was not reversible.

An experiment was conducted to determine the availability of remaining phenol and PNP in Yolo soil at the point at which 26% of both chemicals had been mineralized. Three treatments were investigated, including nonsterile soil in which biodegradation had occurred; soil sterilized by gamma-irradiation,

which eliminates cellular activity but not that of extracellular enzymes (Lensi et al., 1991); and soil sterilized by sodium azide in which case extracellular enzymes are also inactivated. The soils were extracted with calcium chloride and acetonitrile. Less than 10% of the phenol could be extracted in nonsterile soil and in soil that was sterilized by gamma-irradiation; whereas, over 95% of the phenol could be extracted in the sodium azide-treated soil. More than 95% of the PNP could be extracted from the soils sterilized by gamma-irradiation and sodium azide and approximately 65% from the nonsterile soil. This suggested that formation of bound residues may account for the lower availability of phenol in gamma-irradiated and nonsterile soil, and may also affect availability of phenol to microbial populations.

Assuming phenol forms irreversible, bound residues with soil, it was hypothesized that there should be less degradation of phenol that had time, before the onset of biodegradation, to form these residues with soil than there would be of PNP treated in the same way. Therefore, biodegradation was measured of phenol and PNP that had been presorbed to sterile soil and then mixed with nonsterile soil or inoculated with a mixed culture of organisms. Phenol was degraded to less than 15% in 200 h, as compared to approximately 30% in the same period when it had been freshly added to soil. PNP, on the other hand, was degraded by approximately 32% when it was presorbed to soil, as compared to 45% when freshly added.

H. Sorption and biodegradation of toluene and trichloroethylene (TCE) in soils.

Biodegradation of TCE by indigenous microbial populations is dependent on the presence of toluene in three soils with different organic matter contents. There was no relationship between the initial distribution of the chemicals among the solution, sorbed and gaseous phases in the different soils and their rates of biodegradation. Mass transfer experiments showed that the rate of desorption of these chemicals was rapid compared to the rate of biodegradation. The sorption partition coefficients for toluene and TCE were 88 and 114, respectively. The presence of toluene at 20 µg per ml of soil solution lowered the sorption of TCE ; however, TCE at 1 µg per ml had no effect on toluene sorption. These results are summarized in Fan and Scow (1993).

I. Organic matter characterization.

Preliminary studies were conducted on whole soils and organic matter extracted from several soils (in collaboration with Rick Higashi and Teresa Fan, Dept. of LAWR, UC Davis). Figure 21 shows pyGC-FID tracings of three soils--Tinker, Yolo organic (managed without pesticides and receiving organic forms of fertilizer) and Yolo conventional (received pesticides and mineral fertilizers). In each case, a few mg of freeze-dried sample was pyrolyzed under He at 1 °C/msec to 800 °C, and the evolved products resolved on 0.18 mm x 40 m DB-1 capillary column with $H_2$ carrier gas. The ordinate is GC detector response per mg of sample, and the relative scales are (A)= 1:7, (B)=1:1, (C)=1:1, (D)=1:10. In all chromatograms, many of the peaks from 2-12 min arise from polysaccharidic structures (e.g. cellulose) with a few of lignin origin, while most of those from 10-17 min represent structures of aromatic and phenolic

composition (e.g. of lignin and protein origin), and 14-40 min can arise from aliphatic (e.g. fatty acids, cuticle derivatives) and other structures. The Tinker (A) soil had a much greater number of peaks in the later regions than did organic (B) and conventional (C) Yolo soil. The organic and conventional Yolo soils were relatively similar in composition except that only the conventional soil had numerous peaks in the 14-40 min region. Panel D shows the spectrum for humics extracted from the conventional Yolo and which is similar to the spectrum for the entire soil (C). This result indicates the important contribution of the humic fraction to a soil's organic matter characterization.

Characterization of the Ca-bound humic fractions (Ca-humates) of the organic and conventional Yolo soils by $^{13}C$ NMR indicated that the Ca-humate from the conventional soil was more enriched in aromatic and phenolic structures than that of the organic matter-amended soil (Fig. 22).

The results presented here are preliminary and require confirmation and additional experiments. Clearly, considerable work is needed on the effect of soil organic matter on microbial processes and bioavailability in order to develop new hypotheses and refine existing ones.

J. Kinetics model development.

To help interpret the effects of sorption/desorption and diffusion on the metabolism of organic chemicals, a mathematical model (DSB model) was developed to describe biodegradation in substrate-limited systems (Scow and Hutson, 1992). The model assumes diffusion is described by Fick's second law, sorption by a linear isotherm, and biodegradation by any of various rate equations that can be derived from the Monod equation, including first-order kinetics. Other assumptions are that only the solution phase of the chemical is used; microorganisms are excluded from inside the aggregates; sorption is instantaneous once the chemical diffuses to the sorption site; and there is no surface diffusion. The assumption that the sorbed phase cannot be used by microorganisms is debatable and requires additional research. However, on an aggregate scale, most aerobic organisms and activity appear to be associated with the outer layers, and populations in inner regions are limited by diffusion of substrate, nutrients and oxygen.

The model was adapted to include nonlinear conditions for adsorption and a mass transfer term across the surface of the aggregate. Also, a dimensionless group (analogous to a Thiele modulus), consisting of the diffusivity, the biodegradation rate constant, aggregate radius, and adsorption capacity, was derived as a criterion for evaluating when intraparticle diffusion resistance can be ignored. The criterion was applied to data from the literature describing sorption and biodegradation of two chemicals in soil slurries and confirmed the experimental results. This simplification will facilitate use of the model as a screening tool without having to perform data-intensive and lengthy model simulations. These results are summarized in Chung et al. (1993).

Sensitivity analyses were performed using the DSB model to determine the dependence of a chemical's biodegradation kinetics on soil physical and

chemical properties (Chung et al., 1993). In soil, the rate of biodegradation is a function of a chemical's diffusion coefficient, sorption partition coefficient, the distance it must diffuse from the site of sorption to microbial populations that can degrade it, and its biodegradation rate constant. Different kinetics expressions describe biodegradation over time, depending on whether the reaction is controlled by mass transfer (diffusion and sorption) or the biological rate, and whether the chemical starts out as sorbed (inside the aggregate) or not sorbed (in the outside solution) (Fig. 23). The $\phi$ depicted on the graphs is a dimensionless term consisting of the diffusivity ($D_e$), the biodegradation rate constant (k), aggregate radius (R), adsorption capacity (K), and porosity (e) and is expressed as:

$$\phi = \sqrt{\frac{R\{\varepsilon + K(1+\varepsilon)\}k}{D_e}}$$

Thus, an increase in $\phi$ can result from an increase in the sorption partition coefficient or aggregate radius; or from a decrease in the diffusion coefficient. If biodegradation is rapid relative to the mass transfer rate ($\eta$ = 0.1), there is little impact of sorption on the rate of degradation of a chemical starting out in the solution phase; however, sorption is more important if the chemical is already sorbed. For chemicals starting out in solution and with slower degradation rates relative to the mass transfer rate ($\eta$ = 1.0), initially there is a brief and rapid rate of biodegradation of the chemical available in solution. Once most of the solution concentration has been depleted by biodegradation or diffusion into the aggregate, there is a much slower rate of biodegradation controlled by mass transfer of the chemical back out of the aggregate. When the chemical starts out sorbed, an increase in the sorption partition coefficient changes the kinetics of biodegradation from first order to zero order within the simulated time period. Considering that many organic pollutants sorb strongly and numerous soils have some degree of aggregation and organic matter, taking into account the physical and chemical processes affecting a chemical's concentration may improve mathematical models of the kinetics of biodegradation in soil.

## Discussion

Sorbed chemicals present one of the most challenging environmental problems in the bioremediation of contaminated soils and sediments. Rates of biodegradation of sorbed chemicals are lower than in aqueous systems and laboratory cultures, in part because sorption reduces the availability of the chemical to soil microorganisms. Understanding of the biodegradation of sorbed chemicals is confounded by the fact that the term "sorption" is often used to describe different interactions between pollutants and the soil matrix. These interactions include different mechanisms of adsorption, diffusion, bound residue formation and "aging" of residues. Multiple processes may affect the same chemical and, in soil, it is difficult to isolate one process from another. It is crucial to the future success of bioremediation that research is

conducted on the physical and chemical aspects of pollutant-soil interactions and their impact on biodegradation.

In this study, we started with the simple premise that mass transfer processes control biodegradation rates and we purposefully placed less emphasis on the biological influences on biodegradation rates (e.g. physiology of microorganisms). Thus, we hypothesized that a low concentration of phenanthrene (presumably in the first-order region according to Monod kinetics) would degrade at a rate proportional to the concentration available to microorganisms able to metabolize the chemical. The available concentration (assumed to be what is in solution) would be proportional to the sorption partition coefficient. What we found, however, was no relationship between the sorption partition coefficient and biodegradation rate or extent. In fact, among the soils tested, the two with the highest (Tinker) and lowest (Yolo) sorption partition coefficients had the highest rates of biodegradation. Both of these soils also showed very rapid initial rates of biodegradation. The remaining soils, which had relatively similar sorption partition coefficients, varied considerably in their rates of phenanthrene biodegradation. Microbial population could not be ruled out as an important variable affecting the rate.

Clay is generally assumed to be unimportant in the sorption of nonpolar, nonionized organic chemicals in most surface soils. However, addition of different clays to Yolo loam altered the biodegradation of phenanthrene and the effect was dependent on clay type. Nontronite slightly stimulated, montmorillonite had little effect, and halloysite decreased the rate of degradation. Whether or not clay additions increased the sorption partition coefficient for phenanthrene appeared to be, at least partly, responsible for the observed effects. The sorption and desorption isotherms for nontronite-amended soil were virtually indistinguishable from those for unamended soil. Addition of halloysite, on the other hand, significantly increased the $K_d$ for phenanthrene relative to its value in unamended soil, and sorbed chemical was less easily desorbed in halloysite-amended than in unamended soil. Halloysite addition had little impact, however, on glucose which is only minimally sorbed to soil. The fact that the effect of halloysite was eliminated if unpurified clay was used was unexpected. Addition of calcium (or low levels of sodium) directly to soil had little effect on phenanthrene biodegradation. Additional studies are needed to determine whether phenanthrene can be trapped within the clay lattice of halloysite, but not montmorillonite, and whether smaller amounts of added clay also influence biodegradation rates.

Aging clearly reduces rates of phenanthrene biodegradation. This was suprising because the phenomenon of aging has generally been observed for chemicals with substituents that can form bound residues with soil organic matter or for small, volatile chemicals such as TCE and ethylene dibromide. There is nothing about the phenanthrene molecule expected to render the molecule subject to aging except, perhaps, that phenanthrene is a planar molecule and may insert inself into the lattice of swelling clays. However, addition of the 2:1 clay, montmorillonite, to soil did not reduce phenanthene bioavailability, even though halloysite addition did so. One of the impacts of

aging on biodegradation is, through its impact on both the rate and extent of degradation, that predictions of biodegradation kinetics are confounded. Thus the kinetics of aging may need to be considered in pollutant transport models. It has been argued that aged chemicals are no longer a threat to the environment. Before making this assumption, this hypothesis needs to be tested by conducting plant and animal toxicity bioassays with soil containing aged chemicals.

Several pieces of evidence in this study supported the importance of microbial population characteristics in determining the rate of phenanthrene degradation. For instance, population density had the most dramatic effect on the biodegradation of phenanthrene in soil of the several methods tested to enhance biodegradaton. There was a clear relationship between population density and biodegradation rate, both in solution culture, soil slurries, sterile and nonsterile unsaturated soil. Forbes, a soil which had a very low biodegradation rate, showed a substantial rate of biodegradation when inoculated with *Arthrobacter* sp. at a density of $10^8$ cells per g. Both Yolo and Tinker soils showed enhanced biodegradation rates when inoculated with bacteria; however, the population density required to enhance the already existing high rate of degradation was very high. For example, $10^7$ (a relatively high density itself) had no effect, whereas $10^9$ had a very pronounced effect. Whether high populations are required to overcome mass transfer constraints on phenanthrene in the soils we studied needs to be tested. Using the dimensionless groups derived from the DSB model would help in estimating how high a biodegradation rate, and hence population density, is required to overcome sorption limitations.

Two other methods tested, both of which are frequently discussed as approaches to enhance rates of sorbed chemicals, were the addition of secondary substrates or surfactants. Neither approach had a positive effect on the biodegradation of phenanthrene. Salicylic acid is an inducer for naphthalene (and possibly phenanthrene) degradation and has been shown to enhance rates of naphthalene degradation in soil. We found no such effect for phenanthrene degradation in the presence of salicylic nor with phthalic acid, the latter which occurs in another phenanthrene degradation pathway. The lack of response to salicylic acid may be because the phenanthrene pathway in our soil does not go through salicylic acid or, more likely, because there was signficant competition for the substance by faster growing organisms that do not degrade phenanthrene. This is evidenced by the rapid rate of salicylic acid degradation relative to the rate of phenanthrene degradation.

In the literature, the use of surfactants has mixed results, depending on the surfactant used, the soil type, and the chemical being enhanced. Sometimes addition of a surfactant to a soil slurry results in some stimulation of the biodegradation of a sorbed chemical, but just as frequently no effect or even a reduction in rate is observed. One would expect a surfactant to be even less successful in a static, unsaturated soil because of the possibility that the surfactant would associate with soil surfaces or with itself and not be available. A surfactant might enhance degradation of a sorbed chemical if the surfactant is

serving as a secondary substrate. In both slurried and unsaturated soils, issues of the toxicity of the surfactant, metabolic inhibition (e.g. diauxy), and surfactant-pollutant complexes forming a new unavailable phase must also be considered.

The kinetics of mineralization of an organic chemical in soil is strongly influenced by the nature of the chemical's interaction with organic matter. Biodegradation of chemicals, such as PNP, that undergo simple, reversible sorption to organic matter can be described by first order kinetics. More complex interactions, such as the formation of bound residues, may account for the lower availability of phenol in gamma-irradiated and nonsterile soil. These interactions appear to affect the availability of phenol to microbial populations. Therefore, it is important to ascertain the mechanism of a chemical's interaction with soil surfaces before assuming that mathematical expressions typically used to describe biodegradation kinetics are appropriate. Simple approaches, such as compartment models, may improve our ability to describe the behavior of chemicals that do not exhibit equilibrium sorption behavior.

New methods are needed to study the biodegradation of sorbed pollutants in soil because existing approaches, such as use of soil slurries, may significantly alter soil properties (e.g. available carbon, access to sorption sites), decrease the time needed for sorption to reach equilibrium, and are not representative of field conditions. Especially needed are non-invasive techniques that preserve the physical distribution of microorganisms and pollutants in soil and do not destroy soil structure. One of the greatest limitations in this and similar studies is the lack of availability of techniques for quantification of microbial populations degrading specific pollutants. Application of new methods still in development with regard to their use in soil, such as molecular probe technologies or antibody techniques, are needed to address these questions. Especially needed are techniques with very low detection limits and methods that can be visualized on the pore-scale.

Many important research questions remain to be explored which consider the interaction between the coupled processes of sorption, diffusion, and biodegradation. What are the different mechanisms involved in the variety of pollutant-soil interactions that exist and do they differ in their impact on bioavailability? What is the spatial distribution of sorbed pollutants and microbial populations in the soil matrix at the pore scale? What specific properties of microorganisms (e.g. surfactant production, ability to attach, ability to use the sorbed phase directly) may enhance the degradation of sorbed pollutants? To enhance *in situ* biodegradation rates, what economically-feasible physical treatments of soil at field moisture levels increase bioavailability without adversely affecting microbial populations? If inoculation is used, are the densities required too high to be feasible or can the approach be made more cost-effective by promoting growth of smaller inocula after addition to soil?

## References


Anderson, J.P.E. and K.H. Domsch. 1978. A physiological method for the quantitative measurement of microbial biomass in soils. Soil Biol. Biochem. 10:215-221.

Calderbank, A. 1989. The occurrence and significance of bound pesticide residues in soil. Rev. Environ. Contam. Toxicol. 108:71-104.

Chung, G.-Y., B.J. McCoy, and K.M. Scow. 1993. Criteria to assess when biodegradation is kinetically limited by intraparticle diffusion and sorption. Biotechnol. and Bioeng. 41:625-632.

Claus, H., and Z. Filip. 1990. Enzymatic oxidation of some substituted phenols and aromatic amines, and the behavior of some phenoloxidases in the presence of soil related adsorbents. Water Sci. Technol. 22:69-77.

Fan, S., and K.M. Scow. 1993. Biodegradation of trichloroethylene and toluene by indigenous microbial populations in soil. Appl. Environ. Microbiol. 59:1911-1918.

Karickhoff, S.W., D.S. Brown, T.A. Scott. 1979. Sorption of hydrophobic pollutants on natural sediments Water Res. 13:241-248.

Lensi, R., C. Lescure, C. Steinberg, J.-M. Savoie and G. Faurie. 1991. Dynamics of residual enzyme activity, denitrification potential, and physico-chemical properties in a gamma-sterilized soil. Soil Biol. Biochem. 23:367-373.

Scow, K. M., and J. Hutson. 1992. Effect of diffusion and sorption on the kinetics of biodegradation: theoretical considerations. Soil Sci. Soc. Amer. J. 56:128-134.

Scow, K. M., S. Simkins, and M. Alexander. 1986. Kinetics of mineralization of organic compounds at low concentrations in soil. Appl. Environ. Microbiol. 51:1028-1035.

Steinberg, S. M., J. J. Pignatello, and B. L. Sawhney. 1987. Persistence of 1,2-dibromoethane in soils: entrapment in intraparticle micropores. Environ. Sci. Technol. 21:1201-1208.

Table 1. Soil properties and phenanthrene sorption partition coefficients

| Soil | Class | pH | Organic C (%) | Kd | Koc |
|---|---|---|---|---|---|
| Tinker | Sandy loam | 4.8 | 9.5 | 2230 | 23548 |
| Aiken | Sandy loam | 5.6 | 5.4 | 927 | 17230 |
| Forbes | Loam | 5.6 | 4.0 | 869 | 21944 |
| Jocal | Sandy loam | 4.9 | 4.8 | 794 | 16611 |
| Scott | Loam | 5.3 | 3.6 | 780 | 21667 |
| Sobrante | Loam | 5.5 | 6.4 | 945 | 14743 |
| Yolo | Loam | 6.8 | 1.1 | 183 | 16636 |

Table 2. Initial biodegradation rates and substrate-induced respiration in soils

| Soil | Initial rate* (%/hr) | Initial rate* (ng/day) | Substrate-induced respiration (µg CO2/g/hr) |
|---|---|---|---|
| Tinker | 0.0777 | 18.4 | 13.9 |
| Aiken | 0.0068 | 1.61 | 4.4 |
| Forbes | 0.0033 | 0.78 | 6.4 |
| Jocal | 0.0222 | 5.26 | 13.2 |
| Scott | 0.0105 | 2.49 | 15.5 |
| Sobrante | 0.0203 | 4.81 | 21.1 |
| Yolo | 0.1140 | 29.5 | 25.0** |

*Linear fit to data points from the first 150 h.
** Measured at a different time than other samples. Number is average of numerous measurements.

Table 3. Microbial population densities of heterotrophs and phenanthrene degraders in California soils (CFU[1]/g)

| Soil | Viable heterotrophs[2] | Phenanthrene degraders[3] |
|---|---|---|
| Tinker | $3.4 \pm 0.4 \times 10^6$ | $6.1 \pm 0.4 \times 10^5$ |
| Windy | $1.5 \pm 0.25 \times 10^6$ | $3.7 \pm 0.7 \times 10^5$ |
| Josephine | $2.2 \pm 0.15 \times 10^7$ | $5.7 \pm 0.1 \times 10^5$ |
| Crozier | $7.5 \pm 0.7 \times 10^6$ | $3.9 \pm 0.6 \times 10^5$ |
| Sobrante | $6.2 \pm 0.5 \times 10^6$ | $2.5 \pm 0.2 \times 10^5$ |
| Yolo | $5.3 \pm 0.5 \times 10^7$ | $7.5 \pm 0.15 \times 10^5$ |

1 CFU is colony forming units.
2. 1/10 strength tripticase soy agar plates.
3. Clear zones on overlayer plates with phenanthrene.

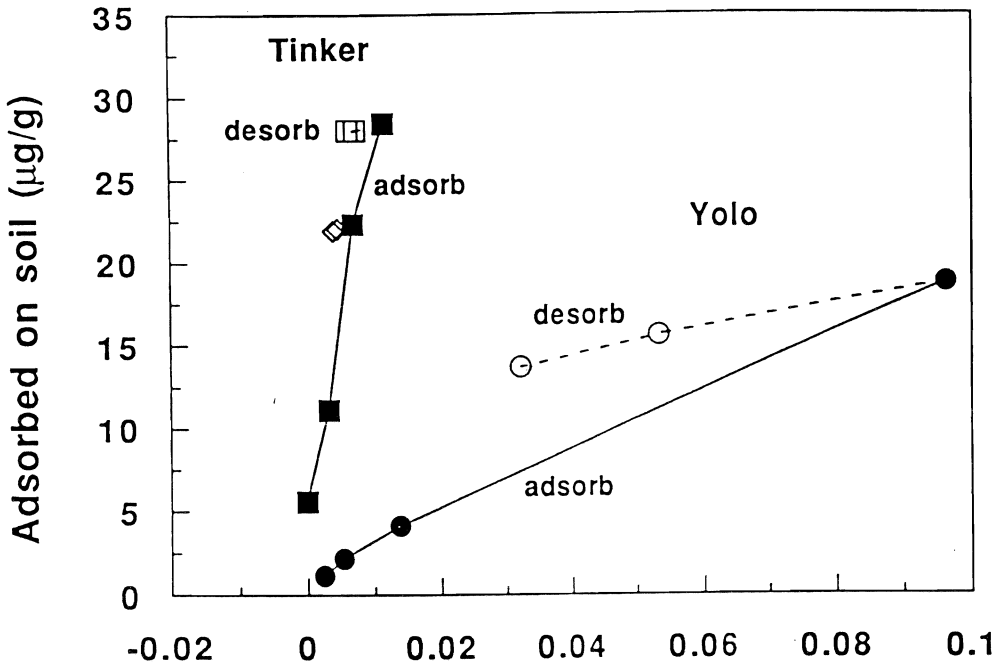


Figure 1. Phenanthrene sorption and desorption isotherms for Yolo and Tinker soils.

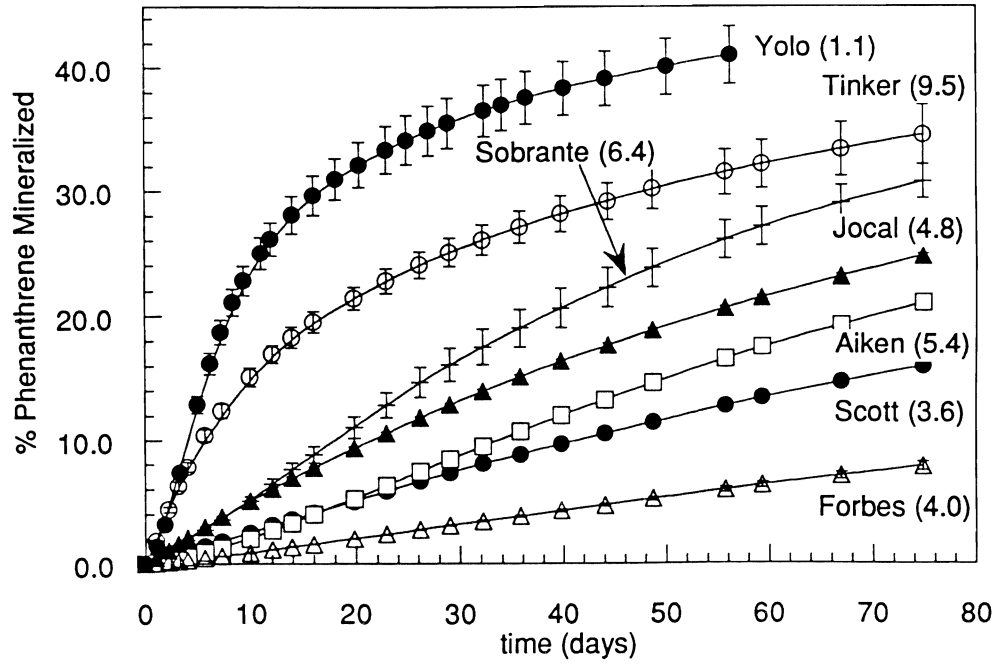


Figure 2. Phenanthrene biodegradation in various soils (% organic carbon).

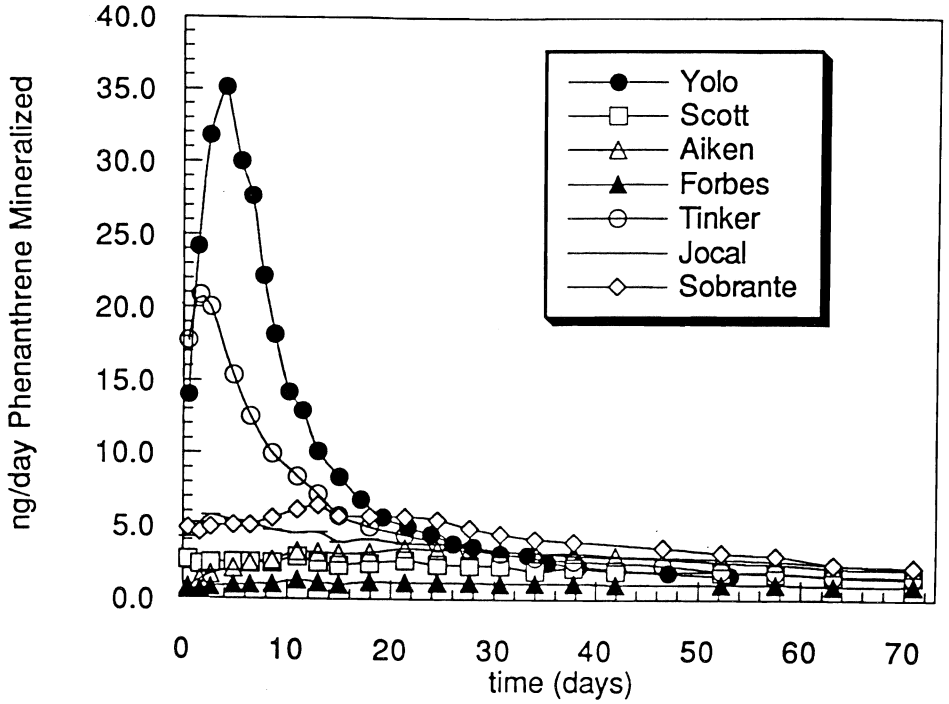


Figure 3. Phenanthrene mineralization rates in various soils.

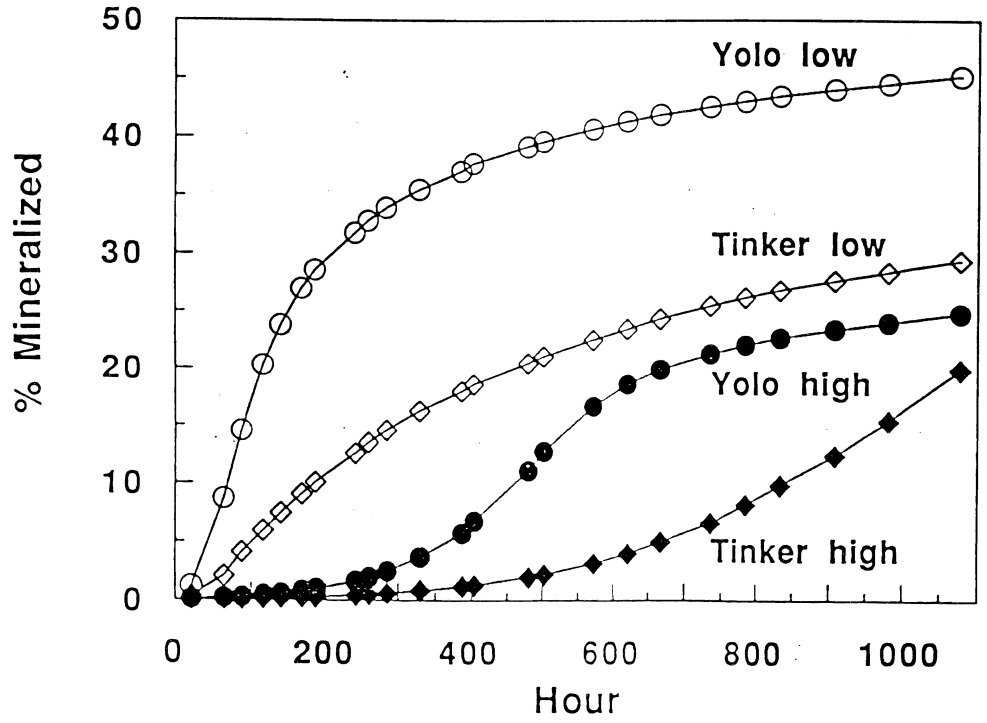


Figure 4. Effect of phenanthrene concentration on biodegradation kinetics in Yolo and Tinker soils.

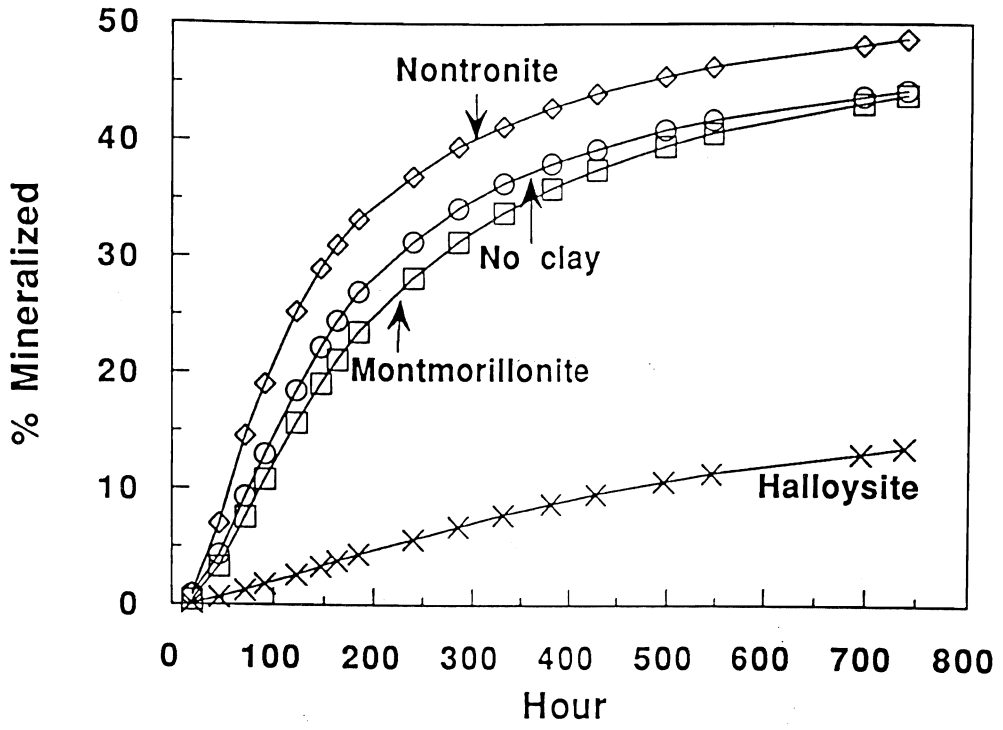


Figure 5. Effect of clay addition on phenanthrene biodegradation in Yolo soil.

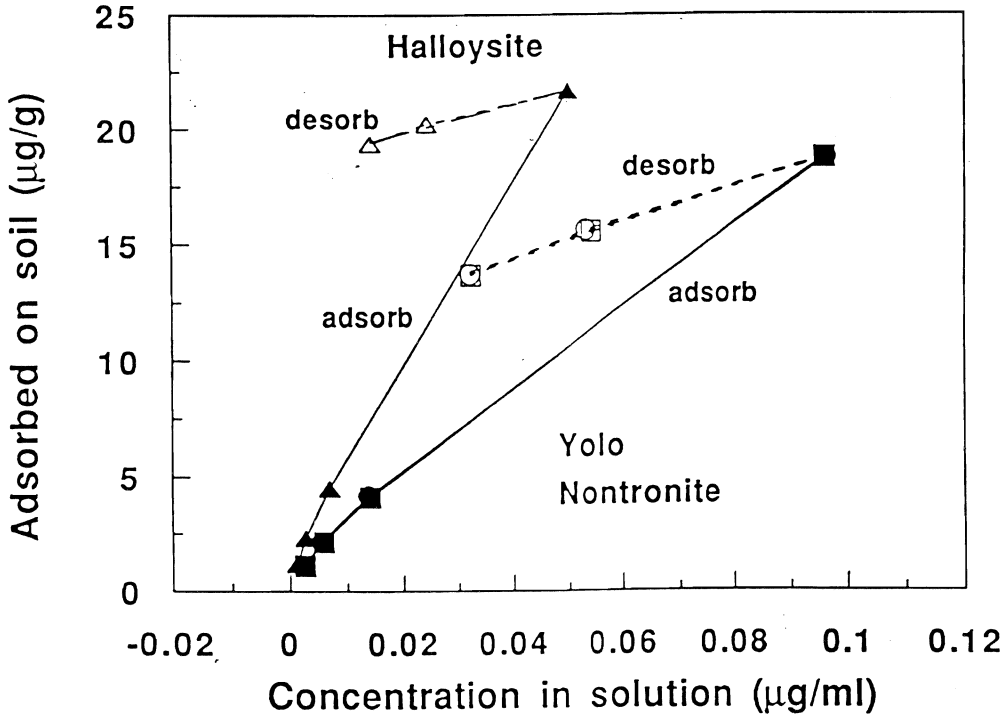


Figure 6. Phenanthrene sorption and desorption isotherms for clay-amended Yolo soil.

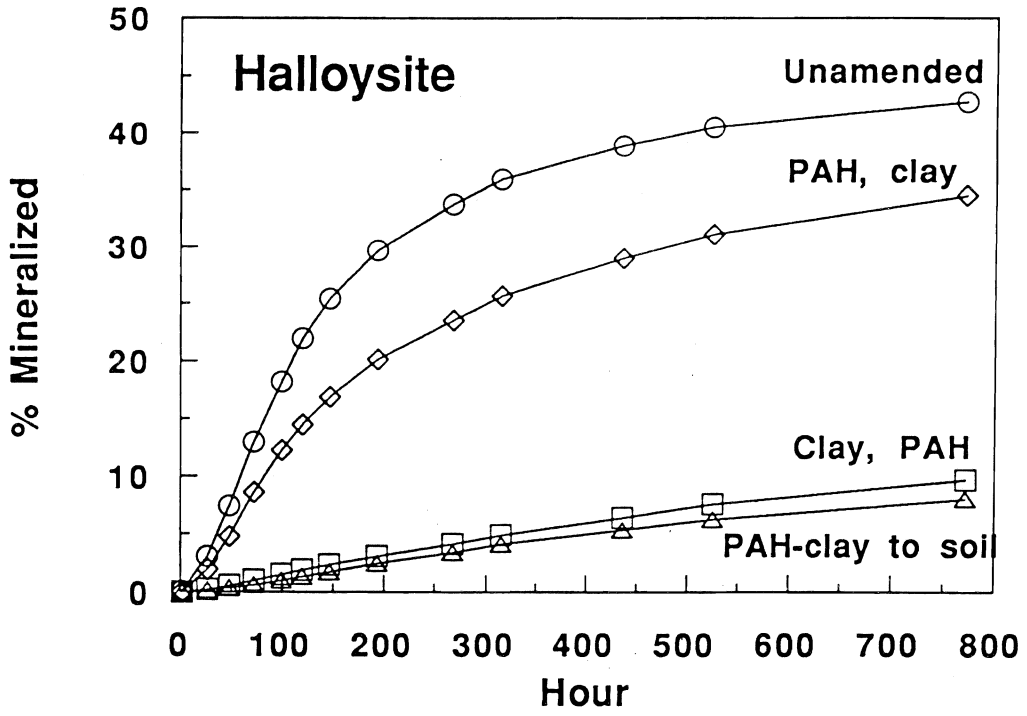


Figure 7. Phenanthrene biodegradation in halloysite-amended Yolo soil.

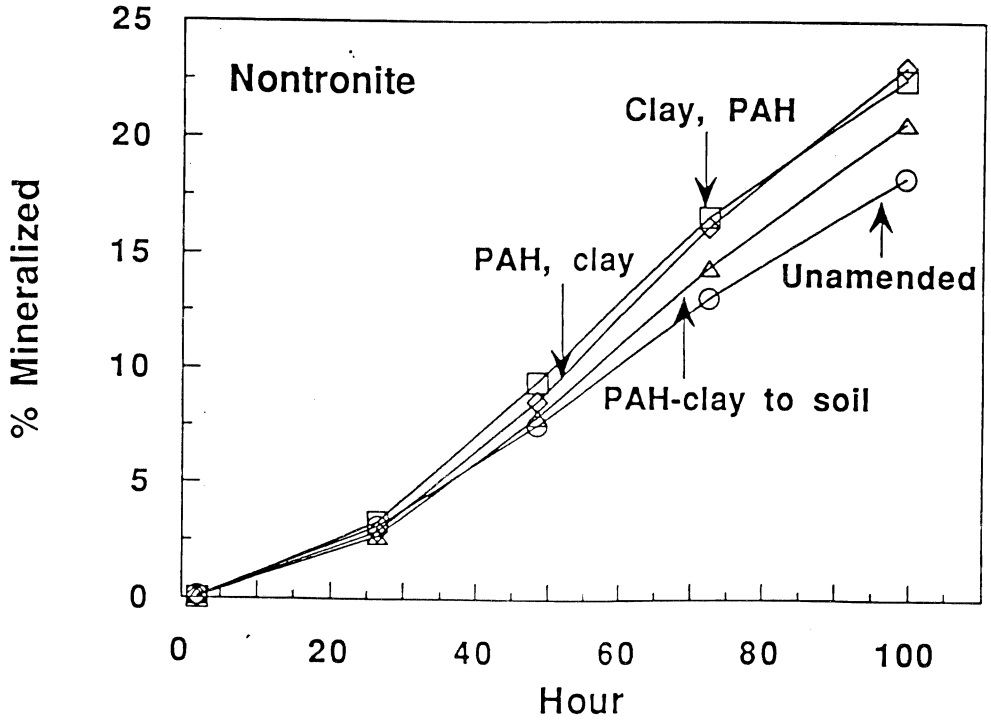


Figure 8. Phenanthrene biodegradation in nontronite-amended Yolo soil.

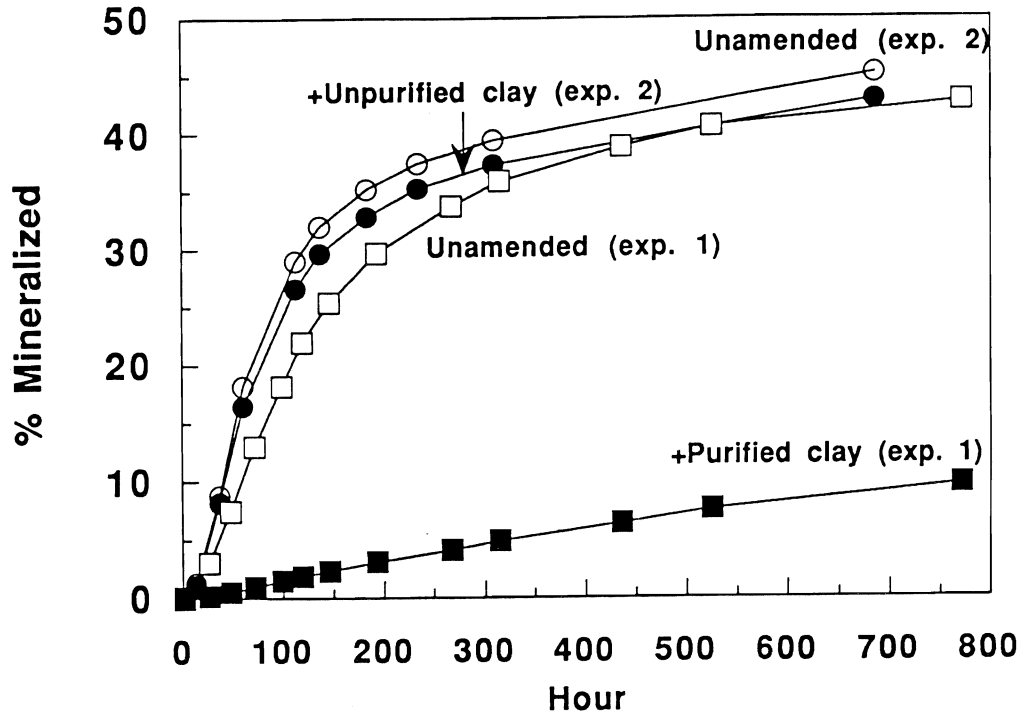


Figure 9. Phenanthrene biodegradation in Yolo soil amended with purified or unpurified halloysite.

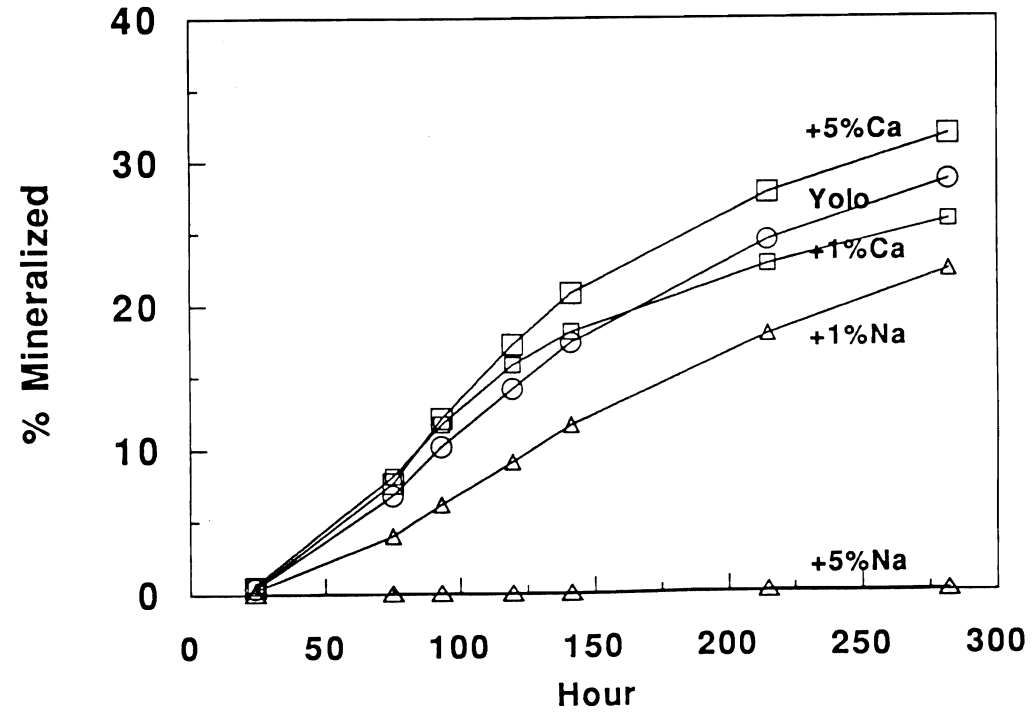


Figure 10. Phenanthrene biodegradation in Yolo soil amended with sodium or calcium.

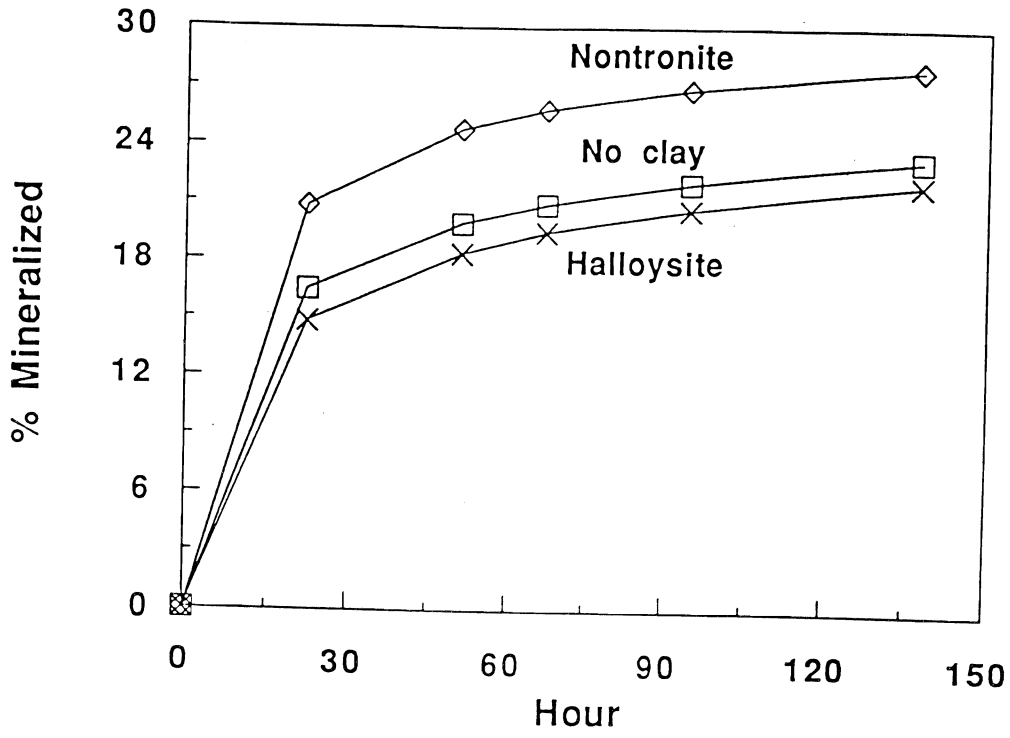


Figure 11. Effect of clay addition on glucose biodegradation in Yolo soil.

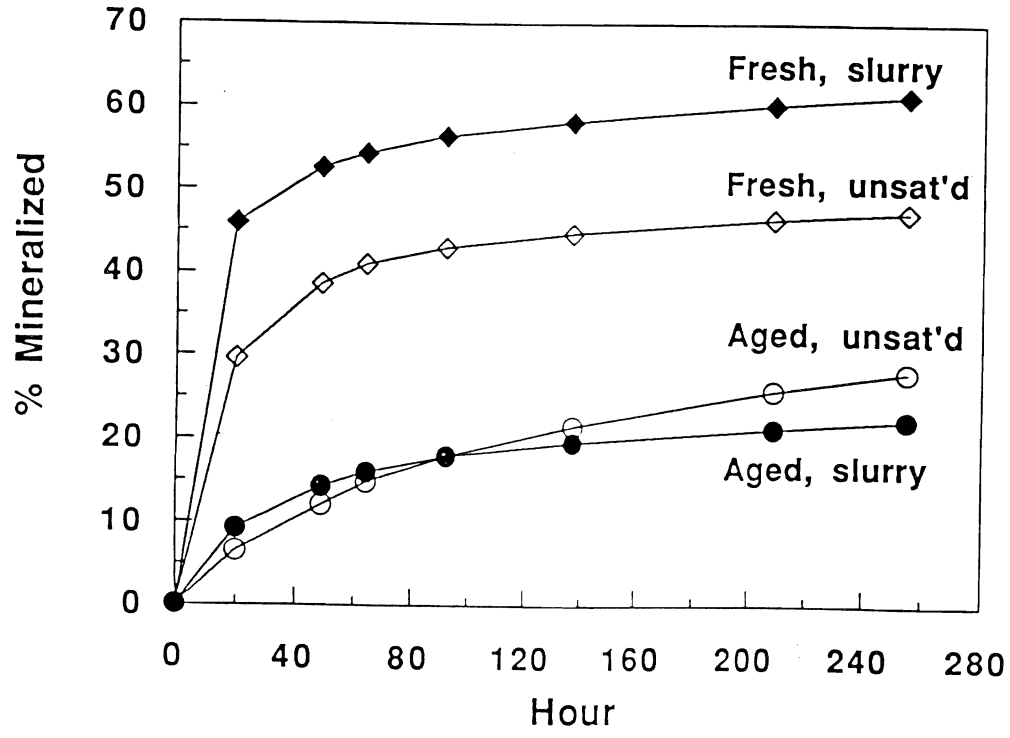


Figure 12. Effect of aging on phenanthrene biodegradation in Yolo soil.

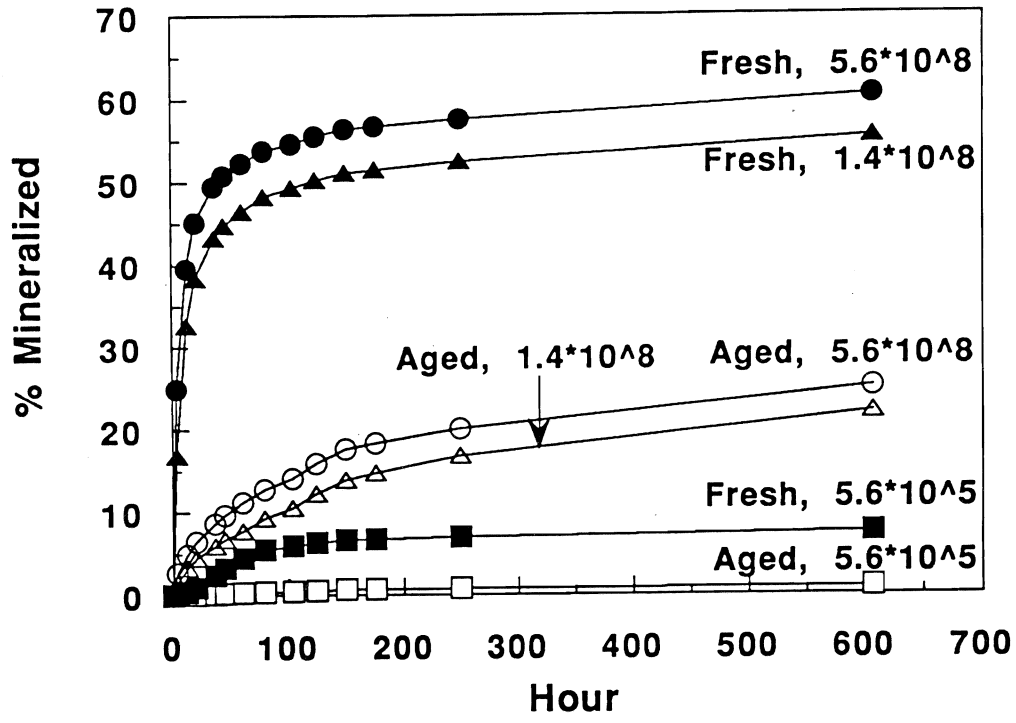


Figure 13. Effect of aging and inoculum size on phenanthrene biodegradation in Reiff soil.

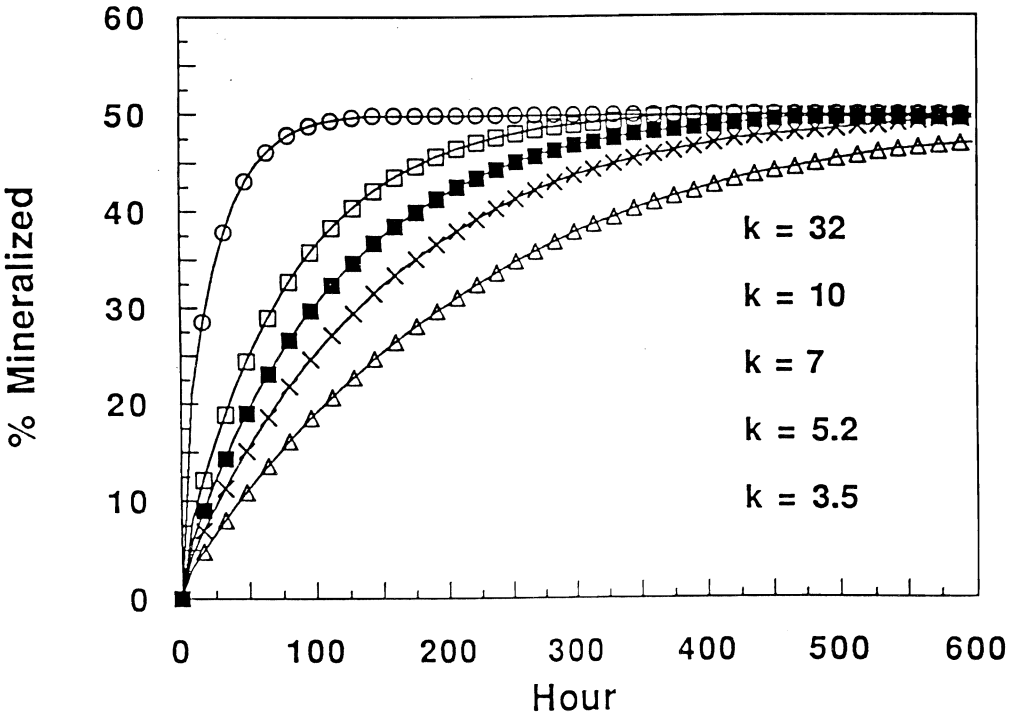


Figure 14. Sensitivity analysis using DSB model: Effect of biodegradation rate constant (k:hour$^{-1}$).

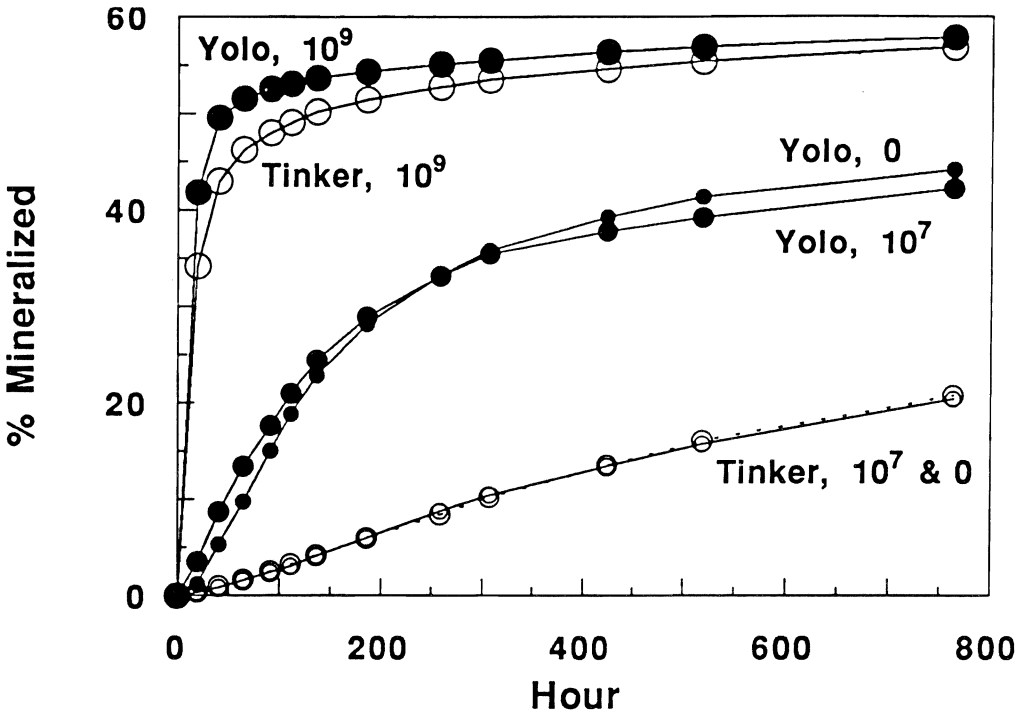


Figure 15. Effect of additional inoculum on phenanthrene biodegradation in Yolo and Tinker soils.

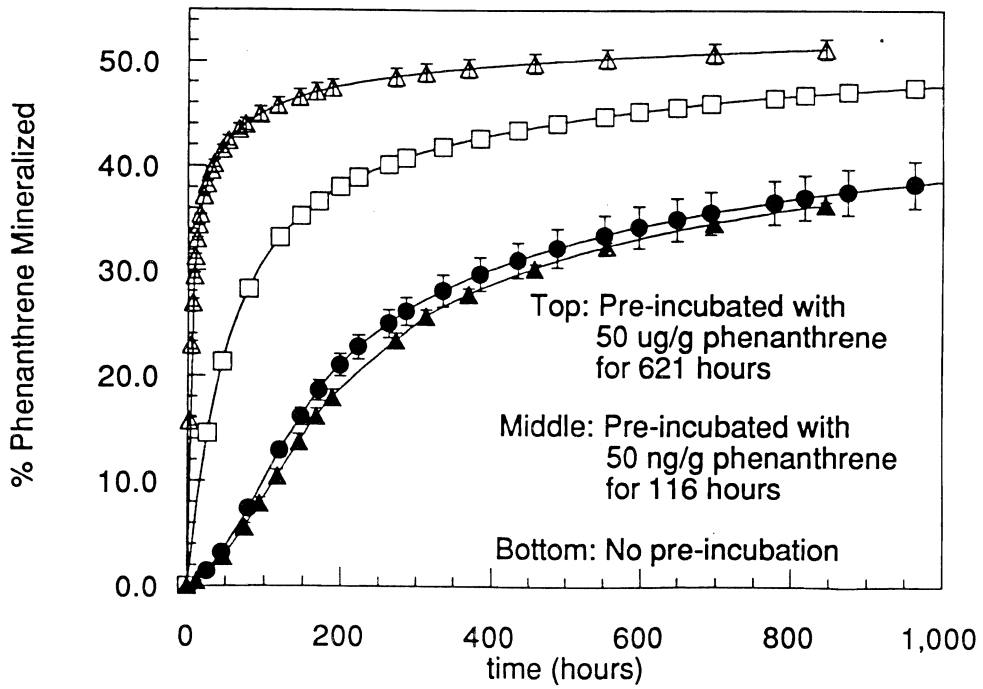


Figure 16. Effect of pre-exposure to phenanthrene on phenanthrene biodegradation in Yolo soil.

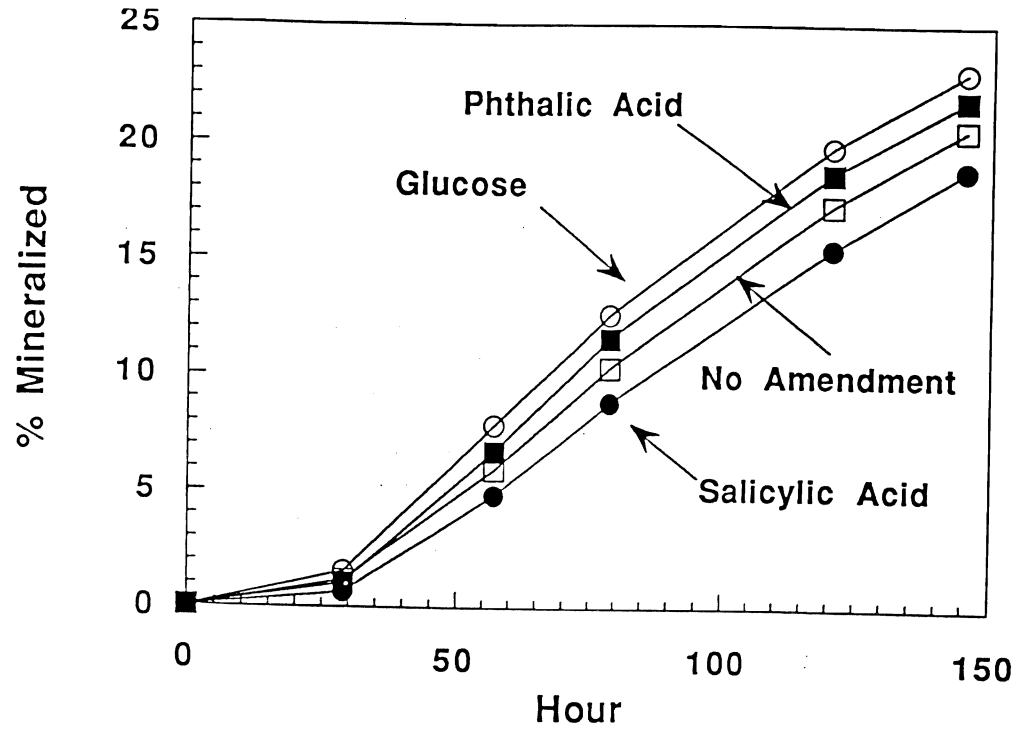


Figure 17. Effect of organic amendments on phenanthrene biodegradation in Yolo soil.

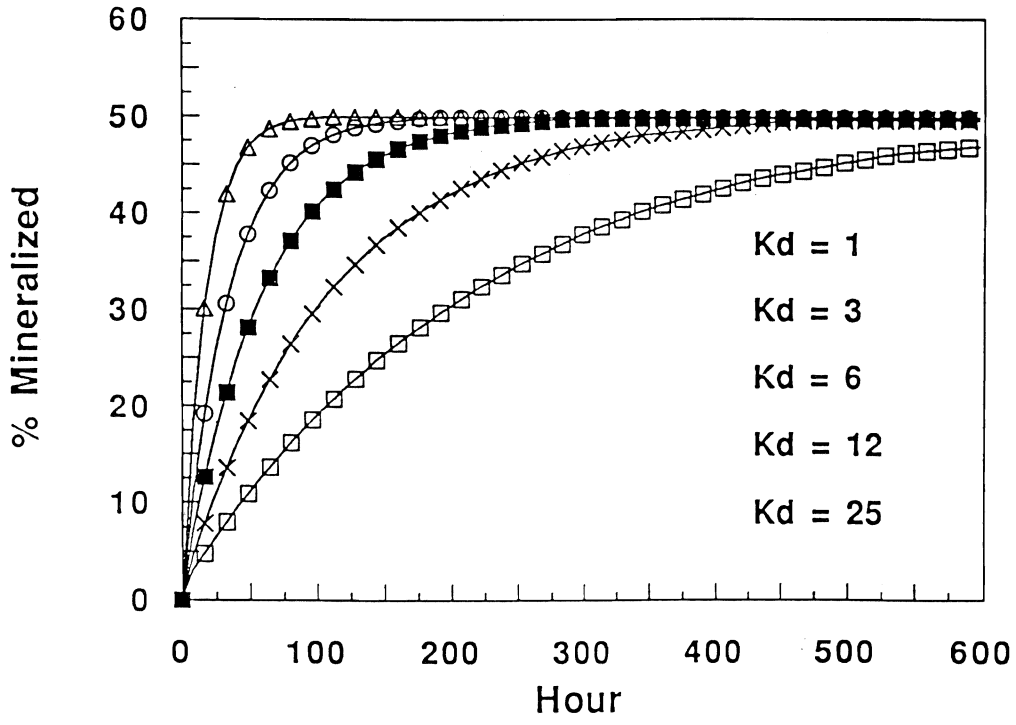


Figure 18. Sensitivity analysis using DSB model: Effect of soil sorption partition coefficient.

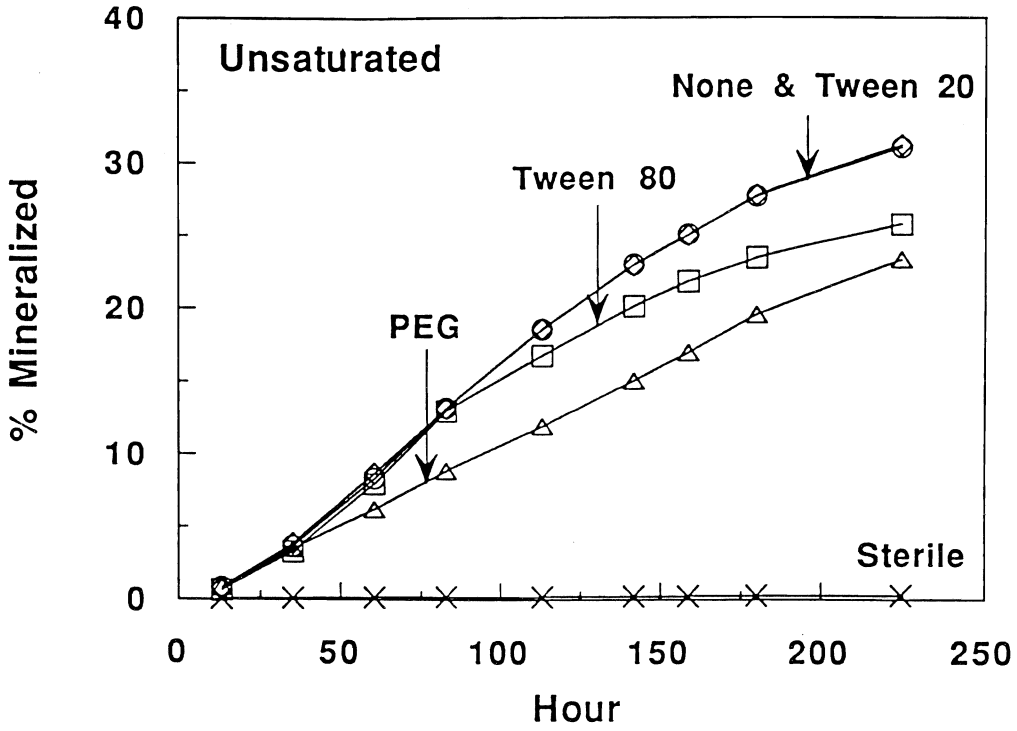


Figure 19. Effect of surfactants on phenanthrene biodegradation in unsaturated Yolo soil (16% moisture content).

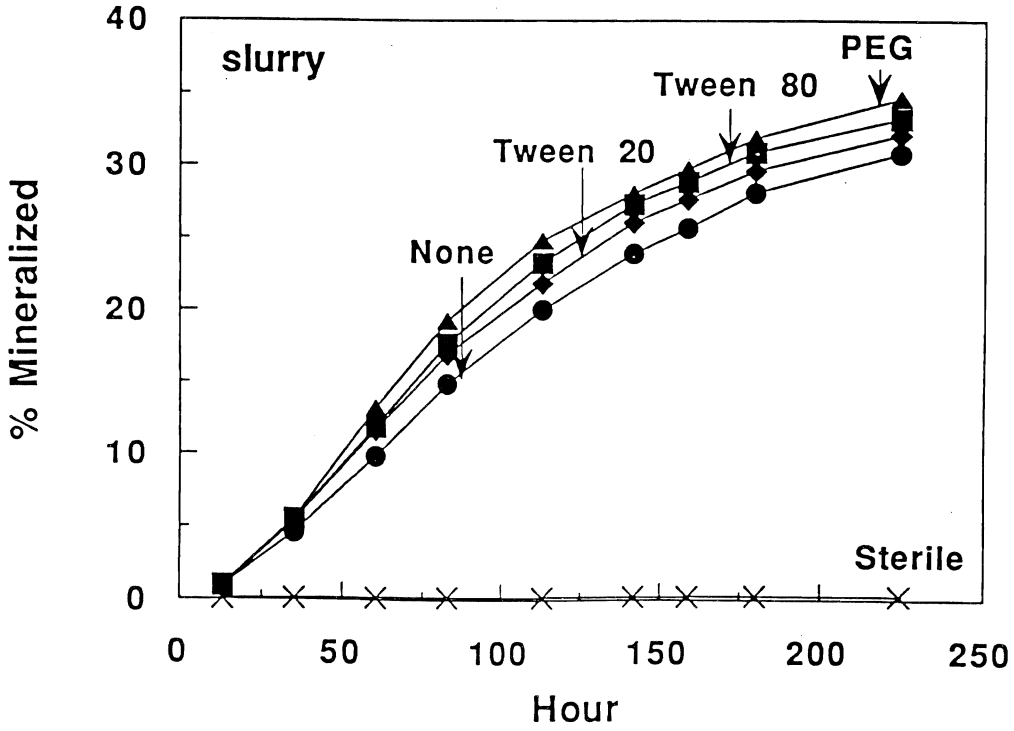


Figure 20. Effect of surfactants on phenanthrene biodegradation in Yolo soil slurries.

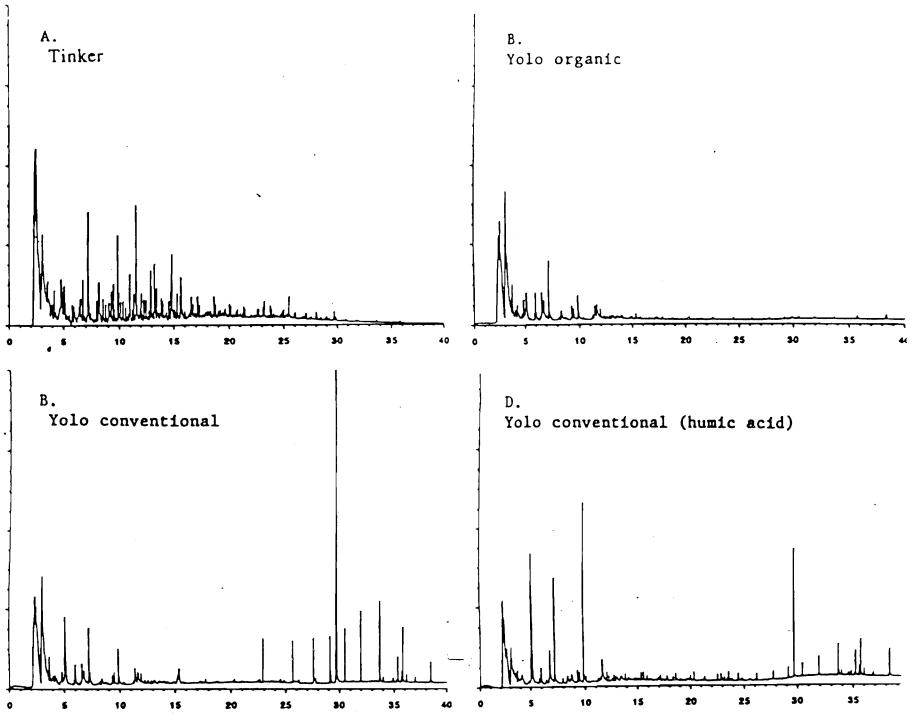


Figure 21. Pyrolysis GC-FID chromatograms of soils and humic acid extract.

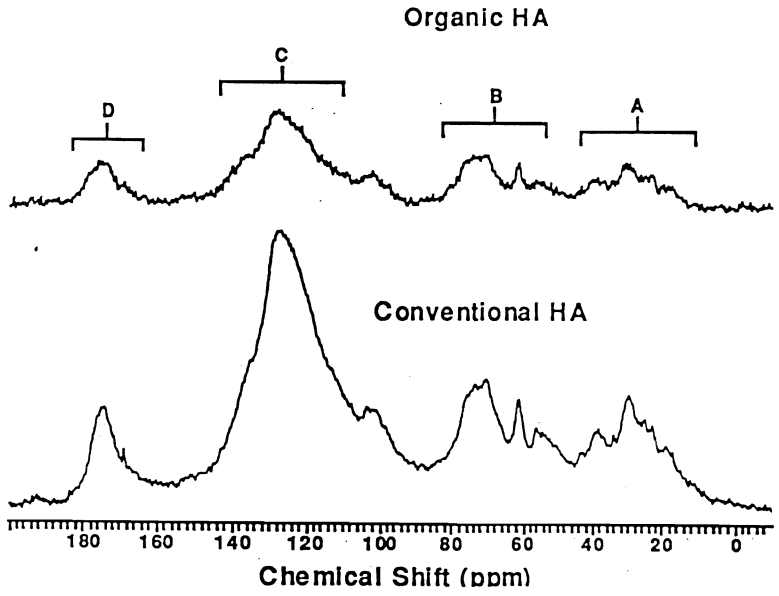


Figure 22. $13^{C}$ NMR spectra of humates from Yolo soil. A. B. C. and D. delineate carbon signals arising from unsubstituted, aliphatic, substituted, aromatic/phenolic, and carbonyl/carboxylic carbons, respectively.

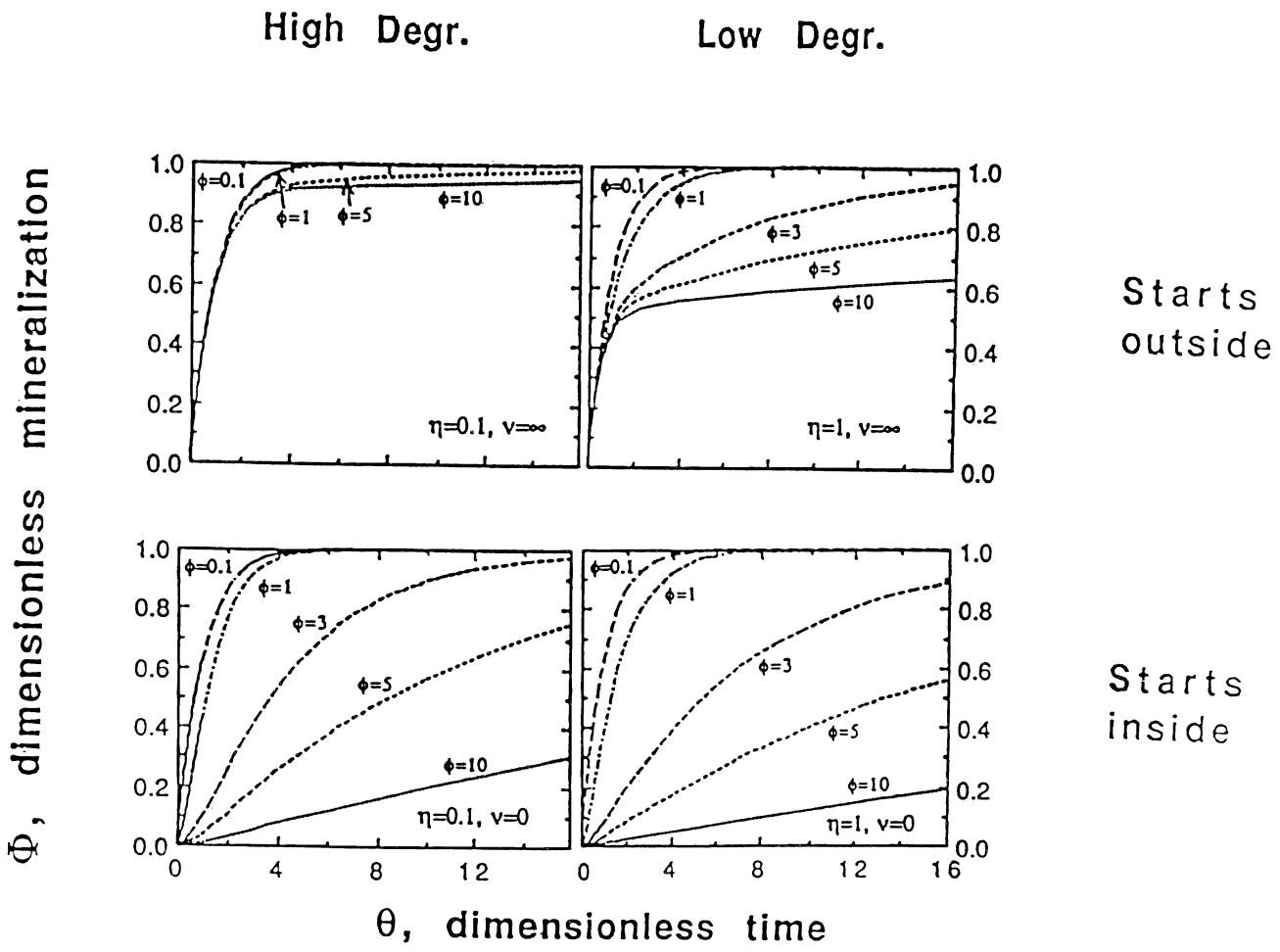


Figure 23. Mass transfer effects on biodegradation kinetics (from Chung et al., 1993).

# Rhizosphere Effects on Degradation of Pesticides in Soil

DAVID E. CROWLEY, PAUL HABY, CATHY IRWIN, STEVE RIES,
SAM ALVEY and MARIA BRENNEROVA
*Department of Soil and Environmental Sciences, Riverside Campus*

## Summary

Biodegradation of several xenobiotics has been shown to occur at elevated rates in the plant rhizosphere, but has not been examined mechanistically. This research investigated three soil contaminants: chlorobenzoates (CB); the highly chlorinated insecticide, chlordane; and the herbicide, atrazine. The results showed that the rhizosphere enhanced the mineralization of 3-CB, but had no effect on mineralization of chlordane or atrazine. With 3-CB, elevated numbers of degraders and cometabolizers were present in the rhizosphere, and there was selective enrichment for cometabolizers. In separate experiments, rapid degradation of highly recalcitrant 2,5-dichlorobenzoate (2,5-DCB) was achieved after introduction of a catabolic plasmid into a rhizosphere pseudomonad. This plasmid was subsequently transferred in situ to other soil bacteria. Primary benefits of the rhizosphere appear to involve enhanced cometabolic activity, increased plasmid and catabolic gene transfer between microorganisms, and generally elevated microbial population numbers which may or may not contain bacteria capable of degrading a specific xenobiotic.

Our ongoing studies, which have been funded by the Kearney Foundation since 1992, are based on the fact that biodegradation of chlorinated hydrocarbon pesticides can be achieved in soil providing there are sufficient nutrients and microbial populations capable of metabolizing the target compound. Knowledge obtained from these studies should provide basic information on rhizosphere processes that affect pesticide persistence in soil and may aid in development of bioremediation technologies for contaminated soils.

**Key Words:** biodegradation, microbial ecology, pesticide, root, rhizosphere

## Project Objectives Addressed in 1993-94

1. Determine the effects of root exudates and the plant rhizosphere on rates of disappearance of CB from soil mediated by a consortia of microorganisms obtained from plant rhizosphere soil.

2. Evaluate the survival and biodegradation activity of the genetically engineered chlorobenzoate degrader organism, *Pseudomonas fluorescens RLD 111*, using the bioluminescence reporter gene system for tracking this bacterium in rhizosphere and nonrhizosphere soil.

3. Investigate the importance of physical and chemical vs. biological processes involved in the disappearance of chlordane under defined redox conditions and in the rhizosphere of a turfgrass.

4. Characterize root-microbial effects on degradation of the herbicide, atrazine, and particularly on the differential formation of recalcitrant atrazine metabolites that are produced in soil microcosms with and without plants.

## Research Plan and Procedures

The use of plant-microbial systems for bioremediation is a rapidly developing technology that may be particularly beneficial for in situ treatment of low-level contaminated soils (Shimp et al., 1993). Since the late 1970s, sporadic reports have appeared in the literature, demonstrating that plants may enhance the degradation of several different compounds, including organophosphates (Hsu and Bartha, 1979), parathion (Reddy and Sethunathan, 1983) polyaromatic hydrocarbons (Aprill and Sims, 1990), and organic solvents such as trichloroethylene (Anderson and Walton, 1990). However, to date these studies have been mostly descriptive and have yet to provide much insight into the specific mechanisms by which plants influence the microbial communities that are responsible for xenobiotic degradation. Successful application of plant-microbial systems against a wide range of contaminants that occur in the field will require that we have a better understanding of how soil microbial communities are influenced by the presence of plant roots, and the benefits and limitations of using plants to increase the activity of specific, introduced xenobiotic biodegraders.

During their normal growth, plants release relatively large quantities of carbon into the rhizosphere as amino acids, organic acids, sugars, and numerous other structurally diverse materials. As all of these compounds are eventually degraded by soil microorganisms, we hypothesize that the rhizosphere may selectively enrich for microorganisms that fortuitously cometabolize xenobiotics structurally analogous to naturally occurring compounds. In general, microbial population numbers are approximately 100-fold greater in the rhizosphere than in the bulk soil. If there is selective enrichment, cometabolizers should be present at a level that is greater than the general increase in population numbers that occurs simply as a result of

increased carbon availability. We also propose that the rhizosphere may enhance indirectly the evolution of new catabolic pathways for degradation of xenobiotics based on the increased rates of gene mutation, genetic recombination, and transfer of catabolic genes on plasmids that are mobile within the microbial community.

In exploring these hypotheses, we have selected several different xenobiotic compounds which normally accumulate in surface soils and thus are particularly good candidates for bioremediation using plant-microbial systems. Chlorobenzoates were selected as model compounds with well known catabolic pathways. They are common metabolites of many pesticides and polychlorinated biphenyls (PCBs). Two other compounds of interest are the insecticide, chlordane, and the herbicide, atrazine, both of which are common groundwater contaminants. Chlordane is a potential carcinogen that has been banned for use in the United States for the past decade, but is presently one of the most important groundwater contaminants affecting the water quality of urban areas. Presently, the entire 600 mile length of the Ohio River along the Kentucky border has a fish consumption advisory due to chlordane contamination, most of which has been caused by surface soil runoff from residential areas treated for termites. Similarly, the herbicide, atrazine, and other related triazines reside primarily in surface soils in agricultural areas and are now the second most common groundwater contaminants in drinking water wells located in rural areas of the United States.

Chlorobenzoate biodegradation. During the first year of our research, we reported experiments which demonstrated that 3-chlorobenzoate (3-CB) disappeared much more rapidly in soil planted with ryegrass than in bulk soil, but conclusions regarding the role of the rhizosphere microbial community were confounded by plant uptake of the target compound. To overcome this problem, a series of experiments was conducted in year two using shaking flasks containing cultures enriched for rhizosphere and nonrhizosphere soil microorganisms to examine the effects of root exudates and other carbon sources on degradation rates. This research demonstrated that chlorobenzoates may be degraded both by cometabolism in the presence of any readily degradable carbon source, such as glucose, and that over time there may be selection for bacteria which can directly mineralize CB as a carbon source for growth. During the third year of this project, reported here, we investigated the population dynamics of these cometabolizer and direct degrader organisms in rhizosphere and nonrhizosphere soil after long term exposure to CBs.

To determine changes in the population numbers of 3-CB cometabolizer and mineralizer populations, we have used the most probable number (MPN) method in which soils are diluted using a dilution series. Population numbers of the 3-CB cometabolizers are measured in liquid media containing 100 ppm 3-CB plus 500 ppm glucose. The CB mineralizers that utilize 3-CB directly as a carbon source are measured using minimal media plus 3-CB with no additional carbon source. During the course of these experiments, erratic variation in the MPN determinations for 3-CB mineralizers suggested that there may be genetic

recombination events occurring within the soil microbial population that result in a random appearance of 3-CB catabolic activity in long-term cultures exposed to the substrate. This hypothesis was subsequently confirmed in an experiment designed to measure the stochastic appearance of degradation activity in replicated soil microbial cultures.

A second direction of our research on CBs involved the introduction of catabolic genes for 2,5-dichlorobenzoate (2,5 DCB) degradation into our bioluminescent strain of root-colonizing *Pseudomonas fluorescens* 2-79RL, which was developed during the first two years of this project. Recently, further modification of this strain was accomplished by transferring a plasmid containing these genes from a very slow-growing strain of *P. putida* P111 originally isolated from sewage sludge in the laboratory of Dr. Dennis D. Focht, Professor of Soil Microbiology, Department of Soil and Environmental Sciences, University of California, Riverside. Degradation activity of the new strain designated, *P. fluorescens* 2-79 RLD, was studied in rhizosphere and nonrhizosphere soil contaminated with 50 ppm 2,5 DCB. Degradation of 2,5 DCB was compared initially in a nonsterile garden soil without plants and in soil planted with beans (*Phaseolus vulgaris*). Subsequent experiments focused on grasses, which have a more fibrous root system than dicotyledonous plants. These included barley (*Hordeum vulgare*), grown under field moist conditions, and rice (*Oriza sativa*), grown under both dryland (aerobic) and submerged (anaerobic) conditions.

Since degradation of 2,5 DCB involves an oxygenase enzyme for ring cleavage, it was hypothesized that in submerged soils, degradation would be enhanced in the presence of rice plants which contain aerenchyma vessels in their stem tissue that transport oxygen to the roots. In addition to quantifying the disappearance of 2,5 DCB in relation to bioluminescence, we also examined the possible transfer of the plasmid to other soil microorganisms over the time course of the experiment by plating the soils on selective agar media containing 2,5 DCB as a carbon source, after which distinct bacterial colonies were isolated and identified using the Biolog nutritional fingerprinting identification system.

Chlordane biodegradation. Research on chlordane focused on the disappearance of this compound in the rhizosphere of bermudagrass and the effect of soil redox on reductive dechlorination of chlordane. The soil selected for this research was a chlordane-contaminated history soil that was obtained from a local yard used by a pest control operator as a disposal site to clean his equipment. In the experimental setup, soil was placed in nylon mesh cylinders submerged into media containing different carbon and nitrogen supplements. Studies on redox effects were conducted using gas-air mixtures delivered through a manifold to replicate Erlenmeyer flasks in which dissolved oxygen and redox were monitored over time in relation to the appearance of chloride and disappearance of chlordane in soil extracts. Ohter experiments were also conducted with bermudagrass in soils subjected to different water and aeration regimes. In these experiments, the soil incubated in tubes with and without

plants was subjected to constant immersion, a diurnal wet-dry cycling period, or constant field moist conditions provided by wick irrigation.

Atrazine biodegradation. Recently, it has been reported that atrazine mineralization can be achieved under conditions in which it is utilized as a nitrogen source, and a few atrazine degrading microorganisms have been isolated (Mandelbaum et al., 1993). One of our new goals is to determine the influence of plants on survival and activity of an atrazine degrader after its introduction into soils and to determine whether degradation is actually accomplished by a single strain, or a microbial consortium. Experiments examining the influence of the rhizosphere on degradation of atrazine used [$^{14}$C]-atrazine containing the radiolabel in either the ring or alkyl side chain position. Mineralization of atrazine in soil microcosms was quantified in the presence and absence of corn plants by collection of [$^{14}$C]-$CO_2$ in sodium hydroxide traps that were sampled and replaced at weekly intervals for 6 weeks. At the end of the experiment, the soils were extracted and analyzed for atrazine metabolites using HPLC. The first plant experiments were conducted with a soil that had no prior exposure to atrazine. The results showed significant rhizosphere effects on transformation of atrazine to more polar metabolites, but there was essentially no mineralization of the recalcitrant triazine ring. Subsequent experiments with organic matter amendments were conducted using a similar experimental apparatus, but with a history soil from the UCR Agricultural Experiment Station that had a 15 year continuous exposure to atrazine. In future experiments, degrader organisms selected from this study will be inoculated into planted and nonplanted nonhistory soils to determine the effect of the rhizosphere on survival and activity of these strains.

## Results

Rhizosphere effects on the population and activity of 3-chlorobenzoate degraders. Prior research demonstrated that different monochlorobenzoates may be degraded either by direct utilization as a carbon source for growth or may be degraded through a cometabolic process requiring a nonspecific alternate carbon source. The pattern of 3-CB disappearance observed in rhizosphere soil planted with ryegrass suggested that initial degradation involved a cometabolic process in which disappearance of 3-CB is dependent on utilization of an alternative, readily degradable carbon source contained in the root exudate or provided as glucose. There was also a random component that usually involved a lag phase prior to the appearance of specific degraders or consortia which could utilize 3-CB directly, resulting in a very rapid disappearance of the compound. These results suggested several hypotheses:

1. The presence of plant roots exerts a selective pressure on the microbial community such that organisms that have the ability to degrade 3-CB proliferate more than in nonrhizosphere soil.

2. The faster degradation of 3-CB involves increased cometabolism due to the abundance of carbon sources available to microorganisms in the rhizosphere.

3. The faster degradation is simply due to the general microbial population increase found in the rhizosphere (commonly 10 to 100 times that of nonrhizosphere soil).

Results of the long-term experiment examining microbial community dynamics showed that after 6 months of repeated exposure to 100 ppm 3-CB, degradation rates were similar in both rhizosphere and nonrhizosphere soils when samples of these soils were transferred to suspension culture systems (Fig. 1). Both soil types had the capacity for degradation of 500 ppm 3-CB in less than 4 days with little variation among the replicates. Nevertheless, as observed in our prior research with soils that had not been exposed previously to 3-CB, the onset of degradation and the time for complete disappearance in all replicates occurred much faster in the rhizosphere soil than in the nonrhizosphere soil, suggesting that the rhizosphere enhanced the population of 3-CB degraders either by selective enrichment or by generally increasing the soil microbial population.

To test the possibility that there was selective enrichment of degrading populations in the rhizosphere, estimates were made of the relative size of the populations capable of degrading 3-CB. Normally, counts of xenobiotic degrader populations are made using agar plates containing the substrate of interest as the sole carbon source. We have found that this method does not give an accurate representation of the microbial population capable of degrading 3-CB and usually yields more colonies capable of degrading agar than those capable of degrading 3-CB. This may be because in natural systems, 3-CB is degraded by non-plateable organisms or by a microbial consortium. Therefore, to obtain a more representative estimate of degrading populations, degradation of 3-CB in liquid media was measured in successive dilutions using the MPN technique. As shown in Fig. 2, the results demonstrated that there are about 40 times more microbes capable of using 3-CB as a sole source of carbon in the rhizosphere soil than in the non-rhizosphere soil. As this is within the 10 - 100 fold general increase in population in the rhizosphere, these results tend to support the third hypothesis for the 3-CB degraders. However, with respect to cometabolizers, when glucose was present in the suspension culture media, the relative numbers of microbes capable of degrading 100 ppm 3-CB was 250-fold greater in rhizosphere soil than in nonrhizosphere soil. These results strongly suggest there is selective enrichment for cometabolizers of 3-CB in the rhizosphere, but that there is no selection for organisms capable of utilizing 3-CB as a sole carbon source.

Other experiments examined the possibility that acclimation of the microbial community to yield a 3-CB degrader may involve a stochastic genetic recombination event. This experiment employed two sets of 12 replicate soil samples incubated as suspension cultures with and without supplemental glucose under uniform conditions on an orbital shaker. Samples were removed

from each culture daily for a period of three weeks or until the 3-CB substrate had disappeared. The results showed that even though each culture came from the same sieved and uniformly mixed soil, the appearance of a degrader population that could directly utilize 3-CB as a carbon source was completely random, with some containers yielding a degrader population in 7 days; whereas, others took up to 2 months before 3-CB degradation occurred (Fig. 3). In solutions amended with glucose, cometabolic disappearance of the substrate began uniformly until the degrader population appeared and rapidly degraded the 3-CB. Inclusion of glucose in the medium slightly shortened the mean time required for appearance of the 3-CB degrader population by approximately one week. These data are strongly suggestive of a genetic event required for appearance of the degrader. For example, this could involve transfer of a plasmid from a slow-growing oligotrophic bacterium to a more competitive organism or gene rearrangement that results in activation of a 3-CB catabolic pathway.

Introduction of a 2,5-Dichlorobenzoate Catabolic Pathway into a Bioluminescent Strain of Root Colonizing *Pseudomonas.* A major difficulty in studies on rhizosphere ecology is tracking the survival and activity of specific bacteria that are introduced into soils. To this end, we previously developed a bioluminescence marker which can be used to monitor individual bacterial strains that are active in degradation of xenobiotics. In brief, we first constructed a chromosomally-based marker system by coupling a strong ribosomal promoter from *E. coli* to the lux cassette containing the luciferase (bioluminescence) genes from *Vibrio fischerii.* These genes were then placed into the transposon Tn7, which, in the presence of a helper plasmid, allowed us to introduce the marker into the chromosome of the target organism. The helper plasmid was then cured from the newly transformed strain so that the lux marker was no longer mobile. The marked bacterium thereafter produces light during active growth which can be used to localize and quantify the bacterium. During the course of this project, several attempts were made to introduce the bioluminescence marker into known degrader strains. However, many of these strains, such as *Pseudomonas putida* P111, are slow growing and have been isolated from environments other than the rhizosphere. After several failed attempts to obtain a bioluminescent degrader with good competitive fitness, we shifted our strategy to incorporate a plasmid from *P. putida P111* carrying the genes for 2,5-DCB degradation into our bioluminescent strain of *Pseudomonas fluorescens* 2-79, which is an aggressive, rhizosphere-colonizing soil bacterium.

Results of these experiments showed that after *P. fluorescens* (Pf 2-79) was transformed with the plasmid, the organism had the ability to rapidly catabolize 2,5-DCB added to soil at 10 ppm. When the bacterium was introduced at a high population number of approximately $10^8$ cells per gram of soil, there was little benefit having a plant in the system (Fig. 4a). Slightly higher rates of disappearance were observed in the presence of plants, but this result could possibly be accounted for through plant uptake. The major benefits of the plant, however, were to increase the long-term survival of the bacterium after most of the substrate was gone (Fig. 4b) or to amplify the population if it was

inoculated into the soil at a low level. This was demonstrated in subsequent experiments with barley and rice, in which greater rates of disappearance occurred in planted systems when the bacterial inoculum was added at a density of $10^6$ cells per gram soil and addition of 2,5-DCB was delayed until one week after inoculation. After 10 days of exposure to the 2,5-DCB, all of the xenobiotic substrate disappeared in the planted systems; whereas, in the absence of plants, only 40% of the 2,5-DCB had been catabolized.

The first indication that transfer of the 2,5-DCB catabolic plasmid to other microorganisms was occurring in our system was suggested from an experiment with barley which was conducted under greenhouse conditions where ambient temperatures exceeded 40°C. Under these conditions, the *Pf* 2-79 died off to low numbers that were undetectable using bioluminescence or plate counts on 2,5-DCB selective media. However, at least four new bacterial species were isolated on the 2,5-DCB media which were tentatively identified using the Biolog Microbial ID system. These strains were not present in noninoculated soil. Thus, we speculate that in this particular experiment the plasmid carried by *Pf* 2-79 was transferred to these new strains either by conjugation or transformation, which enabled these bacteria to catabolize 2,5-DCB in the plant rhizosphere. We are currently attempting to reisolate the plasmid from these strains to confirm our hypothesis. Previous research has shown that there is increased plasmid mobility in the rhizosphere due to the increased microbial population numbers that occur in this zone. Nevertheless, the data from our experiments suggest that we should be concerned as much with plasmid ecology in the rhizosphere as with monitoring the activity of specific strains which degrade a particular xenobiotic. Similar scenarios can be devised to explain our results with 3-CB degradation. The stochastic event that results in appearance of a degrader may be due to plasmid transfer from a slow growing oligotrophic bacterium to a rapid growing organism that suddenly takes advantage of its ability to utilize the new xenobiotic substrate for growth.

The Effect of the Bermudagrass Rhizosphere and Soil Redox on Disappearance of Chlordane. In contrast to our expectations that alteration of the rhizosphere or soil redox conditions could be used for bioremediation of chlordane, results of our experiments showed that for certain highly recalcitrant compounds, bioremediation may have limited, if any, potential application. In the redox experiments with controlled gas mixtures and nutrient additions, the primary factor affecting reductive dechlorination of a technical formulation of chlordane (which contains 150 compounds) was high microbial activity maintained under high carbon conditions in the absence of nitrate. Appearance of chloride, however, was not correlated with disappearance of the cis-chlordane isomer peak used as a specific indicator of chlordane degradation. In experiments with plants, the rhizosphere had no significant effect on the rate of disappearance of chlordane irrespective of irrigation/redox treatment (Fig. 5).

Mineralization and Transformation of Atrazine in Rhizosphere and Organic Matter-Amended Soils. Initial studies ascertaining the importance of the plant rhizosphere in atrazine degradation examined nonsterile and sterile soils, with and without corn plants, to separate out the effects of plants and their root-

associated microbes on atrazine transformation and degradation rates. Using a soil that had not been exposed previously to atrazine, nonsterile soils showed no difference in $^{14}CO_2$ liberation from ring-labeled or chain-labeled atrazine. Mineralization of the side chain was approximately 5 times more rapid than destruction of the ring. Eleven percent of the chain-labeled atrazine was N-dealkylated while only 2.4% of the ring-labeled atrazine was degraded during the 5 week period. However, hydroxyatrazine formation in the planted system was significantly higher than in nonplanted treatments (57% vs. 18%, respectively) under nonsterile conditions (Fig. 6a). These results showed that although $^{14}CO_2$ evolution was unaffected by the presence of plants, the formation of hydroxyatrazine by root-associated microflora is greatly enhanced. After the plants were harvested, the presence of the root-microbial populations continued to have an effect on atrazine metabolite formation in comparison to nonplanted soils. During a 3-week postharvest incubation, both atrazine and hydroxyatrazine levels continued to drop, while the fraction of other metabolites (hydroxydeethylatrazine, hydroxydeisopropylatrazine, and hydroxydiamino atrazine) increased from 5% to 31% of the total remaining material, whereas there were negligible changes in the nonplanted treatments (Fig. 6b).

One possible reason for the negligible difference in mineralization rates in planted and nonplanted soils may have been that there was no active degrader population in that soil. Consequently, we have since conducted research on an atrazine history soil that has been exposed regularly to atrazine for the past 15 years. Our initial experiments focused on the effects of organic matter amendments and provided results that are in striking contrast to our first experiments with the nonhistory soil. When spiked with 25 ppm atrazine, 54% of the atrazine was mineralized after 10 weeks in the history soil. This already rapid rate of degradation was further enhanced in soils amended with 5% rice hulls, starch, or compost (77%, 76%, and 72% mineralization, respectively). However, atrazine mineralization was inhibited to less than 10% in soil amended with citrate or with Sudan hay. Beneficial treatments of starch were also negated in the presence of supplemental nitrogen (Fig. 7). These results strongly suggest that atrazine is utilized as a nitrogen source, but also show that these rates may be influenced by poorly understood population dynamics related to the composition and structural complexity of specific organic amendments.

In the next year, we will continue to focus on atrazine degradation in the rhizosphere. Recently we have isolated a bacterium from the organic matter-amended soils which is able to grow on carbon supplemented agar media using atrazine as a sole nitrogen source. Once this organism has been fully characterized, we will attempt to transform this bacterium with our bioluminescent marker to follow its survival and activity after introduction into the rhizosphere of plants in a nonhistory soil.

## Discussion

Plant-enhanced bioremediation is a promising new technology for decontamination of soils that are potential nonpoint sources of xenobiotics that cause water pollution. For the past 40 years, huge quantities of agricultural chemicals and pesticides have been applied over most of the farming regions and urban areas of the United States. Many of these contaminants are still located in surface soils that are normally under some sort of vegetation that may influence their biodegradation or transport into the subsurface. Other opportunties exist in the use of plants in constructed wetland systems for water treatment. However, the successful application of plants in bioremediation will require a better understanding of how plant roots influence the chemical and physical environment of the soil, as well as microbial communities that are involved in xenobiotic degradation.

First, It should be recognized that bioremediation using plant-microbial systems may be effective only for certain types of compounds as revealed in our experiments on different chlorobenzoates, chlordane, and atrazine. Despite the fact that we have identified specific catabolic pathways, the actual degradation of these compounds may involve other pathways not yet known or involve communities of microorganisms or consortia that interact in carrying out different steps of xenobiotic transformations. In the rhizosphere, we predict that cometabolism may be one of the most important ways in which plants enhance biodegradation. Other indirect, but no less important, effects may include increases in the rates of genetic rearrangement or plasmid transfer between microorganisms and amplification of catabolic genes within the soil microbial community. In this respect, it is important to consider not only the fate and activity of specific degrader populations but also how the rhizosphere affects selection and mobility of catabolic genes within the microbial gene pool. When an organism is isolated that degrades a certain compound on agar media, it remains necessary to demonstrate that the same organism is responsible for this activity in soil. This is particularly important when enrichment culture techniques are used to isolate these bacteria, since strains with new catabolic activity may eventually evolve as an artifact of the selection process.

Yet another important factor identified in this research was the potential influence of the rhizosphere on nitrogen availability to the degrader populations. For example, nitrogen may enhance degradation of a mono-chlorobenzoate, but impede dechlorination of chlordane or mineralization of atrazine (see Kearney Foundation of Soil Science Annual Report, 1991-92, p. 19). In the rhizosphere, there are likely to be nitrogen depleted microsites as the plant takes up this element from the soil solution. On the other hand, the use of large quantities of nitrogen in agriculture and high concentrations of residual nitrate left over in the soil at the end of the growing season may be partly responsible for accumulation of compounds such as atrazine which are utilized as a nitrogen source. Previously, most research on degradation of xenobiotics has emphasized the catabolism of these compounds as a carbon source. Microbial utilization of compounds, such as atrazine as a nitrogen source, is a new concept which will require consideration of a different set of optimization factors when vegetation is managed for bioremediation purposes in the field.

## References


Aprill W. and R. C. Sims. 1990. Evaluation of the use of prairie grasses for stimulating polycyclic aromatic hydrocarbon treatment in soil. Chemosphere. 20: 253-265.

Hsu T.S. and R. Bartha. 1979. Accelerated mineralization of two organophosphate insecticides in the rhizosphere. App. and Env. Microbiol. 37:36-41.

Mandelbaum, R. T., L. P. Wackett, and D. L. Allan. 1993. Mineralization of the s-triazine ring of atrazine by stable bacterial mixed cultures. App. and Env. Microbiol. 59:1695-1701.

Reddy B. B. and N Sethunathan. 1983. Mineralization of parathion in the rice rhizosphere. App and Env. Microbiol. 1983. 45: 826-829.

Shimp, J. F., J. C. Tracy, L. C. Davis, E. Lee, W. Huang, L. E. Erickson, and J. L. Schnoor. !993. Beneficial effects of plants in the remediation of soil and groundwater contaminated with organic materials. Crit. Reviews in Env. Sci. and Technol. 23:41-77.

Walton, B. T. and T. A. Anderson. 1990. Microbial degradation of trichloroethylene in the rhizosphere: potential application to biological remediation of waste sites. App. and Env. Microbiol. 56: 1012-1016.

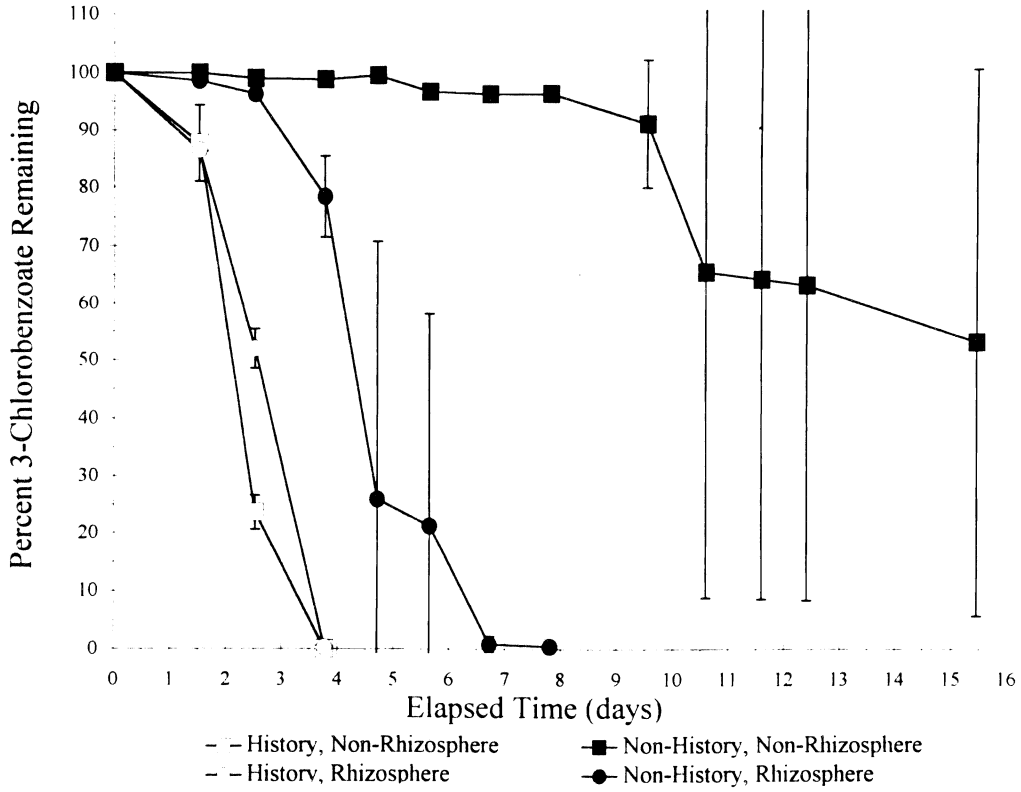


Figure 1. Degradation of 100 ppm 3-chlorobenzoate (3-CB) in soil suspensions from planted and nonplanted soils having a 6-month exposure period or no exposure to the substrate. Results show there was rapid degradation of 3-CB after a 6-month exposure in both rhizosphere and nonrhizosphere soil suspensions, but, in a nonhistory soil, disappearance of the substrate was much more rapid in rhizosphere soil than in soil from the nonplanted system. Vertical bars indicate standard errors of the mean for 4 replicate samples at each point.

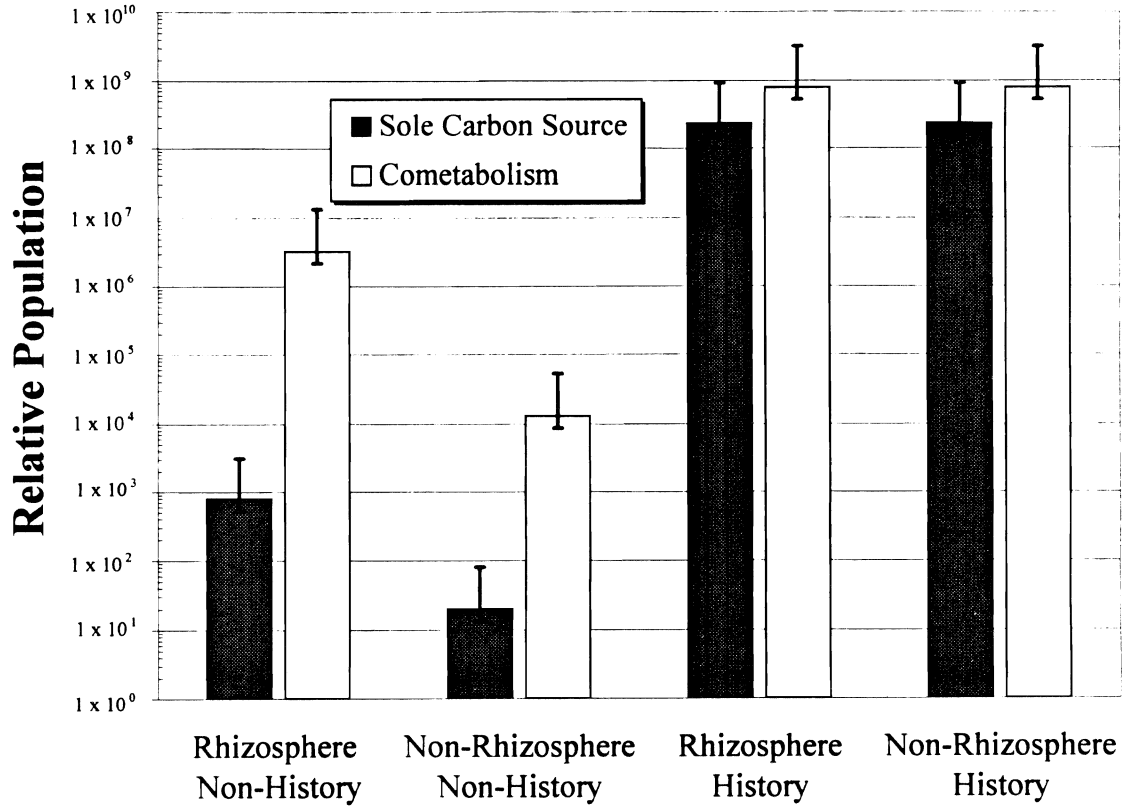


Figure 2. Microbial population numbers of 3-chlorobenzoate (3-CB) degraders and cometabolizers in planted and nonplanted soils having a 6-month exposure period or no exposure to 100 ppm 3-Cb. Population numbers were determined by the most probable number method using a log 10 dilution series with mediacontaining 500 ppm 3-CB for degraders and 100 ppm 3-CB plus 500 ppm glucose for 3-CB cometabolizers. Results show population numbers for both groups of microorganisms were similar in history soils; whereas, in the rhizosphere, 3-CB degraders were elevated by approximately 40-fold and 3-CB cometabolizers were increased by 250-fold. Vertical bars indicate standard errors of the mean for 4 replicate samples at each point.

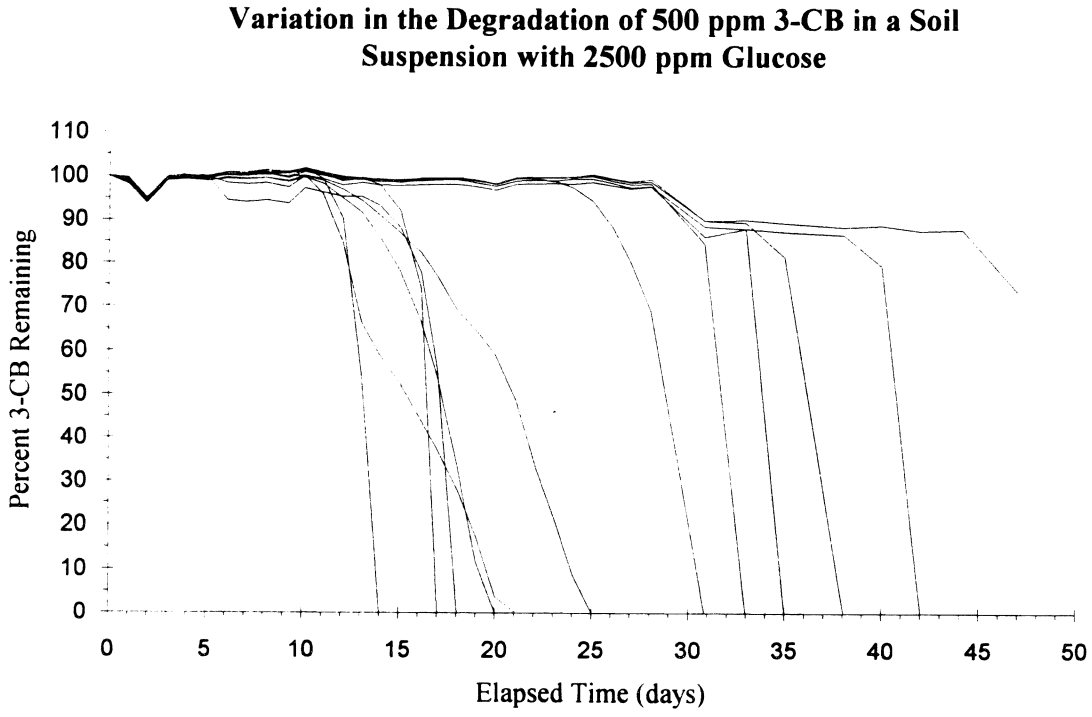


Figure 3. Appearance of 3-chlorobenzoate (3-CB) degraders in soil suspensions over a two-month interval for 12 replicate suspension cultures incubated under uniform aerobic conditions on a rotary shaker. Results show that the appearance of degradation activity is a stochastic event, which is suggestive of a genetic recombination event that leads to the eventual appearance and amplification of genes for 3-CB catabolism.

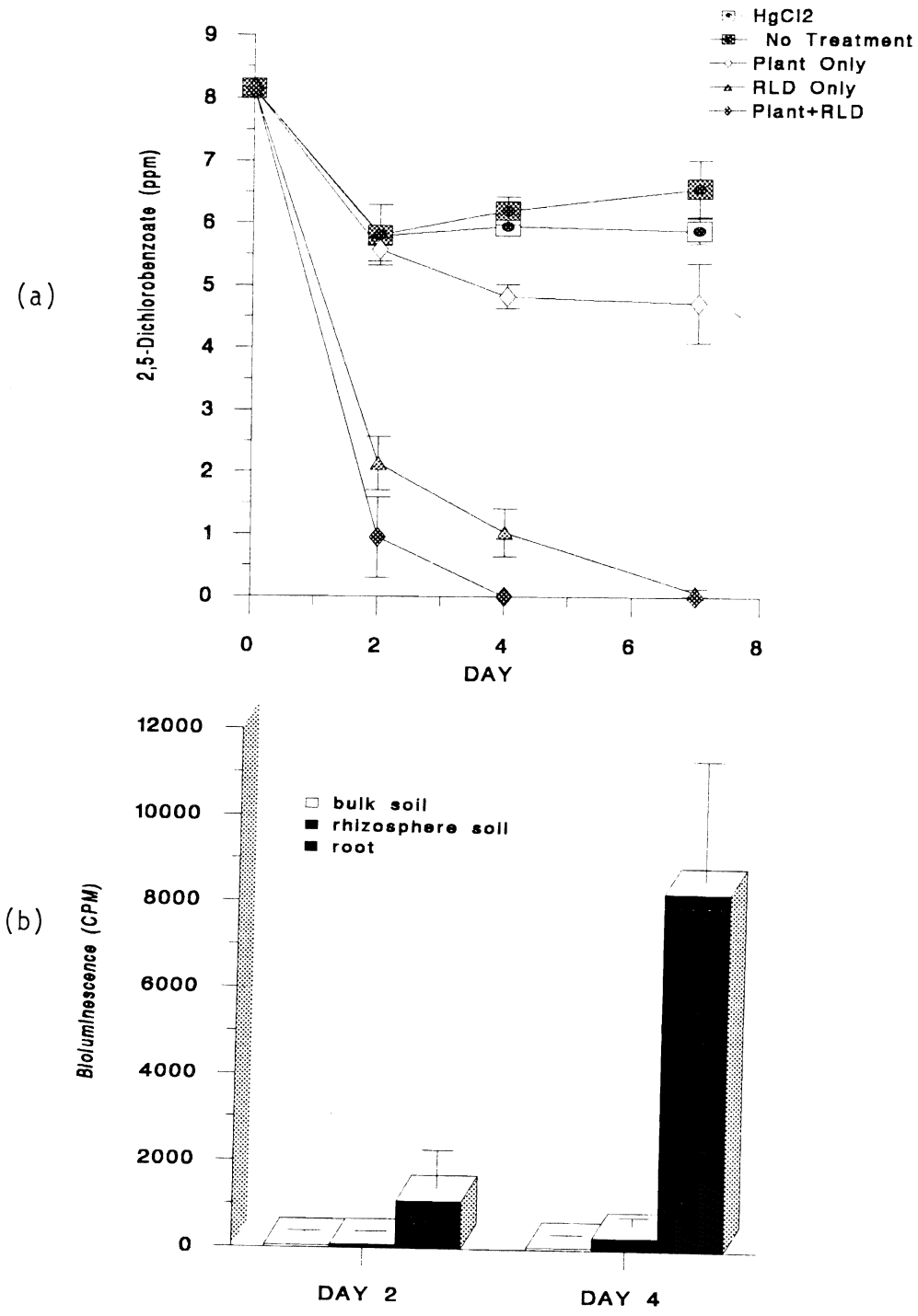


Figure 4. (a) Disappearance of 10 ppm of highly recalcitrant 2,5-dichlorobenzoate (2,5-DCB) over time in nonplanted soils or in soils planted with bean in the presence and absence of *Pseudomonas fluorescens* 2-79 (Pf 2-79) RLD containing a catabolic plasmid for degradation of 2,5-DCB. (b) Activity of Pf 2-79 RLD in bulk soil, rhizosphere soil, or on the root surface of bean as determined by expression of a bioluminescence marker inserted into the chromosome

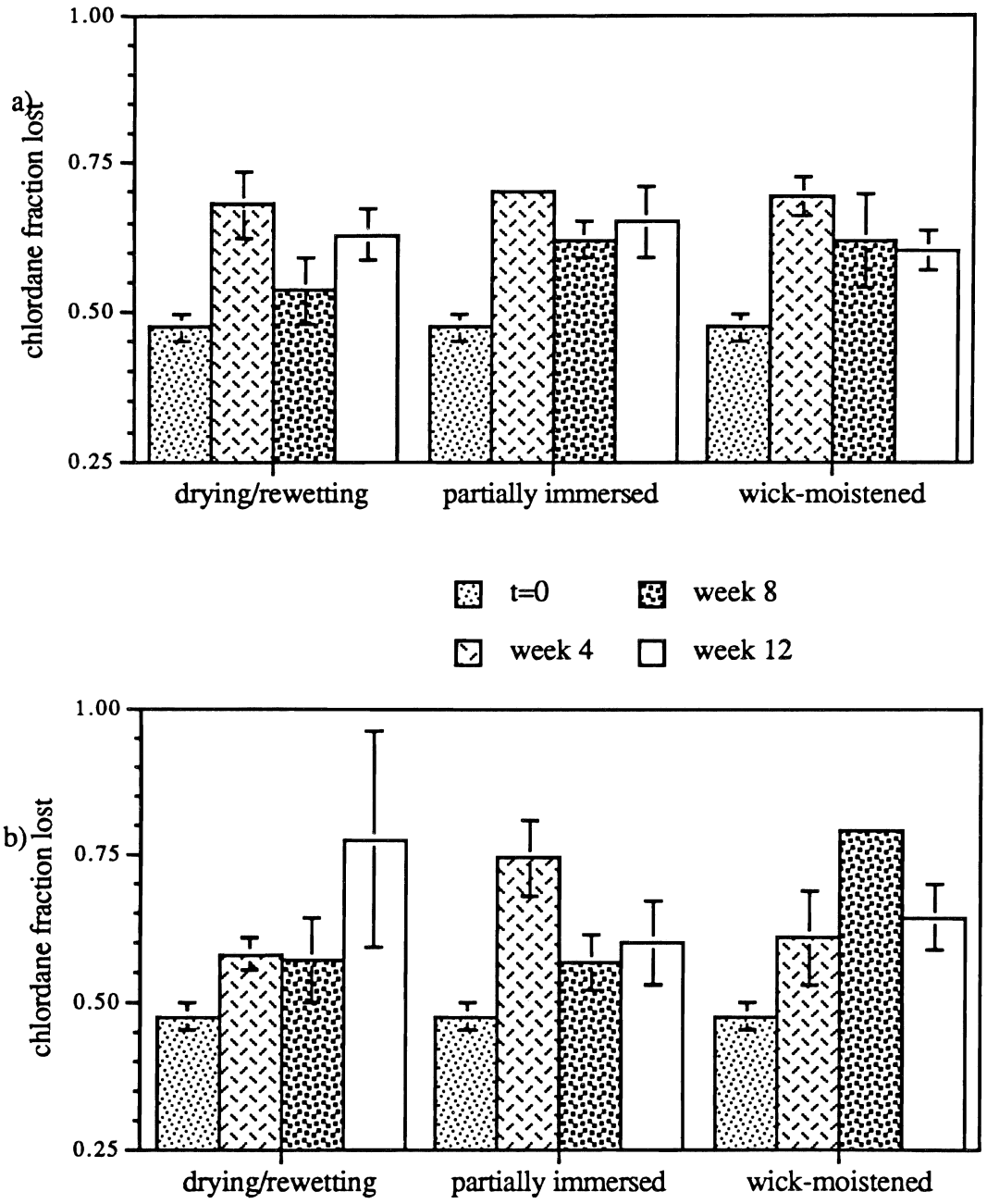


Figure 5. Chlordane loss at 4 week intervals under three different water regimes for a) rhizosphere and b) nonrhizosphere soils. Results show much of the chlordane is nonextractable immediately after application. After incubation, simiilar decreases in quantities of extractable chlordane occur in both rhizosphere and nonrhizosphere soil, irrespective of irrigation/redox regime. Vertical bars indicate standard errors of the mean.

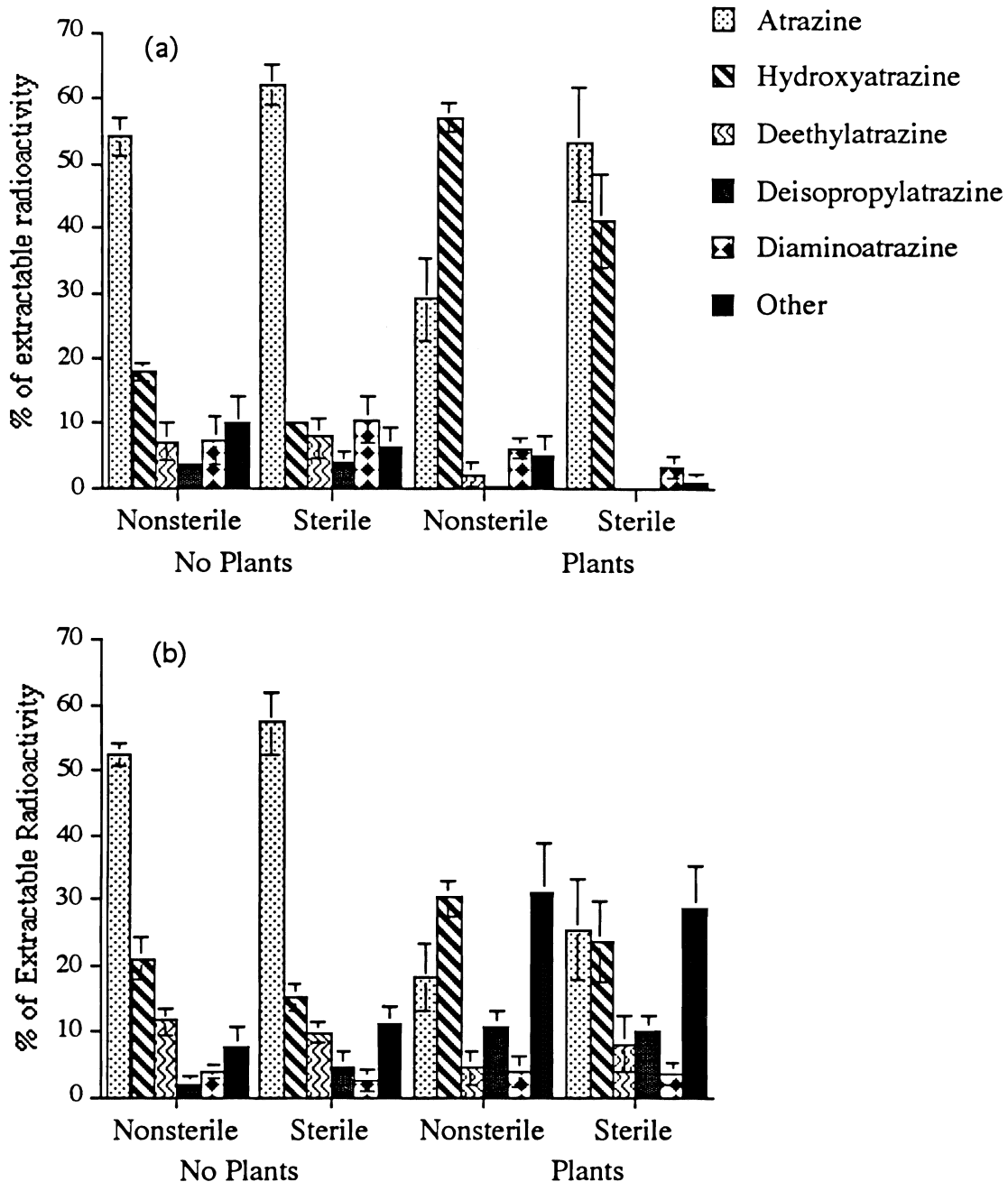


Figure 6. (a) Formation of hydroxyatrazine and other atrazine metabolites under nonsterile and sterile conditions in the presence or absence of corn plants grown in soil microcosms. (b) Atrazine metabolite accumulation in the same microcosms after another 6-week incubation in the absence of corn plants. Results show disappearance of hydroxyatrazine that had been produced in the planted microcosms, with concurrent appearance of other metabolites.

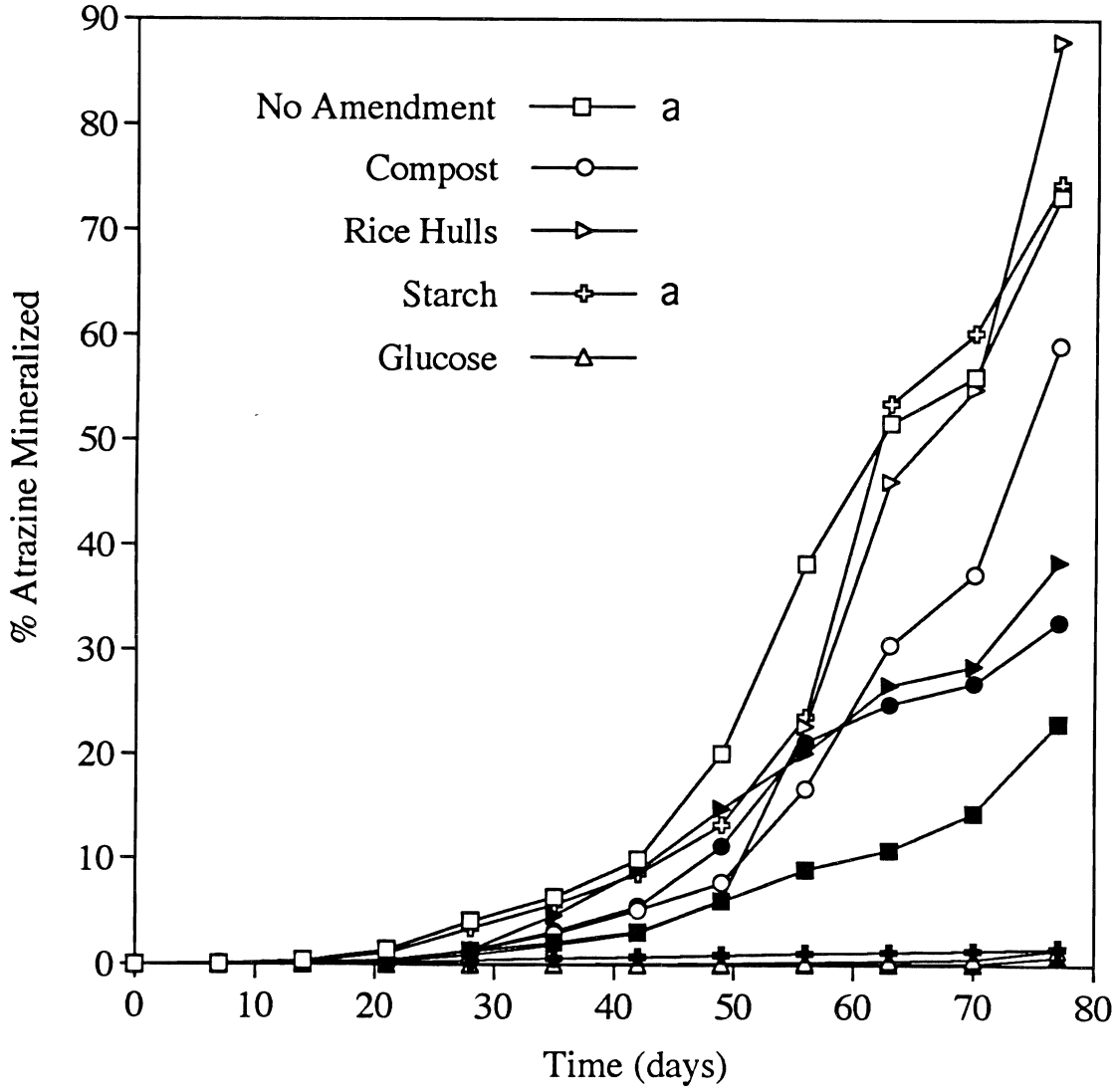


Figure 7. Influence of nitrogen and organic matter amendments on mineralization of $^{14}C$-ring labeled atrazine in soil microcosms containing a soil with a 15-year continuous exposure to atrazine. Results show relatively rapid mineralization of atrazine in all soils, except those amended with supplemental nitrogen, suggesting the utilization of atrazine as a nitrogen source for microbial growth under high carbon conditions.

# The Effects of a Chlorinated, Volatile Hydrocarbon (1,1,1-TCA) on the Diversity and Function of the Microbial Community in Surface and Subsurface Soil

K. A. DUNKIN AND M. K. FIRESTONE
*Department of Environmental Science, Policy and Management, Berkeley Campus*

## Summary

The objective of this two-year study is to assess effects of 1,1,1-trichloroethane (1,1,1-TCA) on microbial communities in surface and subsurface soils. Emphasis is on describing the effect of the microbial community structure and function. Volatile chlorinated hydrocarbons may affect the microbial communities of unsaturated surface and subsurface soils by changing the diversity of the microbial community and eliminating or reducing useful functions. Additionally, the potential for contaminant degradation may be affected. The subsurface soil studied was tuffaceous volcanic material from 85 to 87 feet deep from Los Alamos National Laboratory that contained 10 µl/l volatile hydrocarbons at the time of sampling. The contaminated subsurface soil had low numbers of viable counts and had activity measurements below detection limits. The surface soil (0 -10 cm) from an uncontaminated site had colony forming units of approximately 1,000,000 per gram dry soil and measurable rates of activity. The condition of the microbial community in the subsurface site may indicate that the potential for bioremediation by the indigenous organisms is substantially limited.

**Key Words:** soil microbiology, 1,1,1-trichloroethane, microbial ecology, microbial activities, subsurface soil, Los Alamos National Laboratory, microbial community structure, microbial community function.

## Project Objectives Addressed in 1993-94

1. Evaluate effects on soil microbial communities from exposure to controlled dosages of 1,1,1-trichloroethane (1,1,1-TCA).
2. Investigate effects on the microbial community of volatile, gas-phase contamination of subsurface and surface soils in field sites.

## Research Plan and Procedures

Laboratory studies of dose-response. The overall objective of this on-going study is to evaluate effects on microbial community structure and function of gas-phase volatile contaminants in unsaturated soil. One phase of this study addresses changes in the microbial community under a range of concentrations of the contaminant in a controlled laboratory environment. To meet this goal, a gas-phase delivery system has been developed and is currently undergoing testing. The system involves a gas chromatograph, multi-channel sampling valve and computer-automated delivery of the gas phase contaminant. The soil samples will be exposed to a range of contaminant concentrations and the structure and function of the microbial community evaluated through the use of methods described below.

Community function. In order to investigate the effect of gaseous hydrocarbon contamination on the microbial community, we optimized a number of procedures for measurements of community function and population sizes. We identified candidate media for assessment of colony forming units (CFU). These include 0.1 strength trypticase soy agar, 1% PTYG agar, 21C agar without added carbon, and Kings B agar (Balkwill, 1989; Gerhard, 1994). Also, our experiments showed that acridine orange staining gave the best results for direct microscopic determination of cell numbers when compared to DAPI or FITC staining. Methods to determine activity levels of total respiration, dehydrogenase activity and nitrification were adopted. Respiration was measured with a soil respirometer in a 90 hour assay with 6 hour sampling intervals. Dehydrogenase activity was assessed colorimetrically as the amount of iodonitrotetrazolium violet (INT) reduced to INT-formazan in a 24 hour incubation. Nitrification potential activity was measured as the amount of nitrate and nitrite produced when soils were slurried with 1 *mM* $NH_4^+$ as $(NH_4)_2SO_4$. Radioactively labeled sodium acetate and glutamic acid have been identified as substrates to evaluate the effect on degradative function. An extraction technique utilizing density gradient centrifugation has been adopted to extract cells for use in community structure assessments (Bakken and Lindahl, 1994).

Community Structure. Methods assessing community structure are being developed and include reverse sample genome probing, phylogenetic staining and Biolog plating. Reverse sample genome probing involves detecting changes in whole community DNA by comparison with known standards (Voordouw et al., 1991). Biolog is a commercially available 96-well plate with 95 different carbon sources. Growth of bacteria is determined by a color reaction in the well. The resulting pattern of positive wells indicates the community capacity for different substrates and is an index of community

structure. In phylogenetic staining, cells from soil are exposed to fluorescently-labeled strands of synthetic DNA. The cells that retain the DNA are those that contain complementary ribosomal-RNA and become fluorescent ("stained"). The technique is somewhat analogous to the more common use of fluorescently-labeled antibodies against cell surface antigens, but without the prerequisite for organism cultivation prior to raising antibodies (Olsen et al. 1986). Phylogenetic staining has been used to enumerate the magnetotactic bacteria in freshwater sediment (Spring et al., 1992) and to enumerate introduced *Pseudomonas aeruginosa* in soil (Hahn et al., 1992). It is used in this study to evaluate the effects on *Pseudomonas* spp. and ammonia-oxidizing bacteria.

Subsurface soils from a gas-phase, chlorinated hydrocarbon contaminated area and surface soil from an adjacent uncontaminated site at Los Alamos National Laboratory have been evaluated using methods to describe community function.

## Results

During the first year of this two-year study, the initial goal was to establish and evaluate methods for the assessment of the soil microbial community structure and function. Many of these methods are now established and are being utilized for evaluations of soils exposed to contaminants in the field. Controlled laboratory systems for laboratory-scale experiments are under development. Further development of community structure assays are underway.

Laboratory studies of effects from exposure to controlled dosages of 1,1,1-TCA. For laboratory experiments, a system was developed in which soils could be exposed to a volatile contaminant in a controlled manner while allowing the soil to remain in as close to in-situ condition as possible. Initial studies with closed batch systems demonstrated problems with oxygen limitations. A system to expose a soil community to 1,1,1-TCA has been designed that allows for containment of the volatile compound at a set concentration while controlling relative humidity, temperature and other gas concentrations. The system employs a 36-port sampling valve and the contaminant is supplied as a gas to gas-tight containers containing soil. The samples are then incubated for a predetermined time. A gas chromatograph is used to monitor the $CO_2$ levels in the headspace of the sample containers. A second gas chromatograph is used to confirm the concentration of the contaminant. The system automation has been completed and tested. In the final stage of development, several designs for the contaminant supply tank are under consideration. Measurements of physical adsorption to the soil and the Henry's coefficient are being determined for 1,1,1-TCA in order to verify the concentration of 1,1,1-TCA in soil solution.

Field soils from Los Alamos. Soil samples from 85, 86, and 87 feet were sampled aseptically by drilling in a contaminant gas plume at the Los Alamos National Laboratory. Surface soils (0-10 cm) were also sampled in a nearby

location. The contaminated soil contained 10 to 12 µl/l gas-phase organic carbon at the drill head. Gas chromatographic analysis at Berkeley of the headspace of sample cores 48 hours after sampling confirmed contamination by 1,1,1-TCA and by several other unidentified volatile compounds. Moisture content, water potential, pH and bulk density were determined and showed the subsurface soil to be an unsaturated, neutral, slightly welded volcanic tuff and the surface soil to be slightly acidic and moist at the time of sampling (Table 1). The surface soil has been classified as a clayey, mixed, mesic, Aridic Haplustalf of the Hackroy series developed in volcanic ash (Nyhan et al., 1978).

Assessments of community activity and population sizes were made in the soils. The Hackroy soil had moderately low levels of soil respiration of 1.92 $\mu g\ g^{-1}\ hr^{-1}$. The rate of nitrification in a 24 hour slurry was 0.053 $\mu g\ N\ g^{-1}\ hr^{-1}$ and dehydrogenase activity was 2.97 $\mu g$ INT-formazan $g^{-1}\ hr^{-1}$ (Table 2). Viable counts for the surface soil ranged from $5.0 \times 10^6\ g^{-1}$ to $4.2 \times 10^7\ g^{-1}$ (Table 3). Viable counts and activity levels measured in the subsurface soil were below the detection limit (Tables 2 and 3).

## Discussion

A preliminary sampling of the subsurface soil at Los Alamos National Laboratory demonstrated the presence of cells at 50, 100 and 150 ft depths (Hersman and Sinclair, 1988). From this earlier study, cell numbers were determined to be approximately 100,000 per gram and viable counts were measured at 10 to 100 CFUs per gram. Twelve gram-positive bacteria were isolated. No determination of potential contamination was made in the early study.

In the present sampling (contaminated site), the subsurface soil contained CFUs in very low numbers. Between 2 to 14 CFU were found on 40% of the plates; however, the counts were always below 20 CFU even on dilutions of 1 gram of soil in 100 ml of solution and furthermore, CFU did not decrease with dilution. Three months after the initial plating, 60% of the plates had no detectable growth, indicating that those plates with growth were not likely due to procedural problems resulting in contamination.

Three attempts were made to establish the numbers of cells in the subsurface samples via microscopy. We attempted to enumerate cells both in the soil directly and after harvest of cells in a density gradient. In the first two attempts by staining with acridine orange directly in the soil, cell numbers were marginally above the detection limit. We counted from 160,000 to 600,000 cells per gram soil where the detection limit was 100,000 cells per gram. With these low cell numbers, contributions from contaminating cells (determined on control samples without soil) were very important since blank values were in the range of 100,000 cells per sample. In the third attempt, blank values were reduced to approximately 30,000 cells per sample by a rigorous washing routine utilizing 0.1 µm filtered water containing 1% sodium azide. In this experiment, cell

numbers were determined to be between 100,000 to 160,000 per gram soil. This value corresponds well with estimates from the preliminary experiment and with parallel samples taken from the same bore hole and analyzed at New Mexico Institute for Technology (T. Kieft, personal communication).

Attempts to harvest cells from the subsurface soil resulted in yields that were less than 1% of the cells estimated to be in the soil. This result indicated that the soil failed to release cells into solution when treated with normal disruption methods of shaking, sonication, and detergents. There is some indication that cells in dry soils are particularly difficult to dislodge from the mineral surface (L. Bakken, personal communication). The difficulty in removing cells from this soil may also have adversely affected our attempts to measure CFU since dilutions are normally made from suspended material with much of the larger fraction already settled. Possibly, with reduced numbers of cells released into solution, numbers of CFU may have been underestimated. Also, because of the low numbers of cells released, no attempt was made to determine community structure with Biolog plates.

Measurements of activity were below the detection limit for rates of respiration, nitrification potentials and dehydrogenase enzyme activity in the subsurface soil (Table 2). In order to test for the possibility of very low levels of activity, three samples received 100 µl of 72 nmolar 2-$^{14}$C-acetate (18 MBq/l). After one month of incubation for both samples and combusted-control samples, the amount of $CO_2$ formed was less than 0.1% of the added substrate (data not shown), which indicates that the current condition of the cells found in the soil are either dead or in some state of non-activity.

The surface soil from the Los Alamos National Laboratory was volcanic in origin and had measurable bacterial cell numbers and activity. The magnitude of both cell numbers and activity is low when compared to measurements made in non-volcanic soils from less arid sites; however, these values are much higher than those found in the subsurface samples. The sampled subsurface soil consisted of slightly welded tuff with little evidence of weathering. It contained measurable levels of volatile hydrocarbons including 1,1,1-TCA. The samples had very little water and very few cells were located by microscopy. Biological activities measured with the methods we employed were undetectable. Importantly, the levels of activity as well as the community size indicate that the potential for biodegradation of the contaminant by the indigenous community is limited and possibly untenable. Once we receive and analyze the uncontaminated control subsurface sample, we will be able to discern the importance of the volatile hydrocarbons in determining these effects on community function.

## References

Bakken, L.R, and V. Lindahl. 1994. Recovery of bacterial cells from soil. In: Van Elsas and Trevors, Eds. Extraction of genetic materials from the environment. J. Wiley. (in press)

Balkwill, D.L. 1989. Numbers, diversity, and morphological characteristics of aerobic chemoheterotrophs in deep subsurface sediments from a site in South Carolina. Geomicrobiology J. 7:33-52.

Gerhard, P. editor-in-chief, R.G.E. Murray, W.A. Wood, N.R. Krieg. 1994. Methods for General and Molecular Bacteriology. American Society for Microbiology, Washington, D.C.

Hahn, D., R.I. Amann, W. Ludwig, A.D.L. Akkermans, and K-H. Schleifer. 1992. Detection of micro-organisms in soil after *in situ* hybridization with rRNA-targeted, fluorescently labelled oligonucleotides. J. Gen. Microbiol. 138:879-887.

Hersman, L. and J. Sinclair. 1988. Preliminary analysis of the vadose zone, Parjarito plateau, New Mexico. Abstracts of the American Society for Microbiology Annual Meeting. American Society for Microbiology, Washington, D.C.

Nyhan, J.W., L.W. Hacker, T.E. Calhoun, and D.L. Young. 1978. Soil Survey of Los Alamos County, New Mexico. LA-6779-MS. Los Alamos National Laboratory, New Mexico. U.S. DOE. Informal Report.

Olsen, G.J., D.J. Lane, S.J. Giovannoni, and N.R. Pace. 1986. Microbial ecology and evolution: a ribosomal approach. Ann. Rev. Microbiol. 40:337-365.

Spring, S., R. I. Amann, W. Ludwig, K-H. Schleifer, N. Petersen. 1992. Phylogenetic diversity and identification of nonculturable magnetotactic bacteria. System. Appl. Microbiol. 15:116-122.

Voordouw, G., J.K. Voordouw, R.R. Karkhoff-Schweizer, P.M. Fedorak and D.W.S. Westlake. 1991. Reverse sample genome probing, a new technique for identification of bacteria in environmental samples by DNA hybridization, and its application to the identification of sulfate-reducing bacteria in oil field samples. Appl. Enviro. Microb. 57 (11): 3070-3078.

Table 1. Physical characteristics of Los Alamos surface and subsurface soils.

| | pH | $H_2O$ (kg $kg^{-1}$) | Water Potential (J $kg^{-1}$) | Bulk Density (g $cm^{-3}$) |
|---|---|---|---|---|
| Surface | | | | |
| 0-10 cm | 6.7 | 0.103 | -0.13 | nd† |
| Subsurface | | | | |
| 85-85.5 ft. | 7.6 | 0.025 | -1.30 | 1.23 |
| 86-86.5 ft. | 7.7 | 0.034 | -0.98 | 1.22 |
| 87-87.5 ft. | 7.6 | 0.035 | -0.92 | 1.23 |

†Not determined

Table 2. Activity measurements in Los Alamos surface and subsurface soils.

| | Nitrification Potential μg $g^{-1}$ $hr^{-1}$ | Respiration μg $CO_2$-C $g^{-1}$ $hr^{-1}$ | Dehydrogenase Activity μg INT $g^{-1}$ $hr^{-1}$ |
|---|---|---|---|
| Surface | | | |
| 0-10 | 0.053 | 1.92 | 2.97 |
| Subsurface | | | |
| 85-85.5 ft. | <0.020 | <1.00 | <0.10 |
| 86-86.5 ft. | <0.020 | <1.00 | <0.10 |
| 87-87.5 ft. | <0.020 | <1.00 | <0.10 |

Table 3. Aerobic heterotrophic bacteria colony forming units per gram soil from Los Alamos surface and subsurface soil.

| | 1/10 strength Trypticase soy | 1/2 strength 21C (no carbon added) | King's B | 1% PTYG | Heat shocked 1/10 strength Trypticase soy |
|---|---|---|---|---|---|
| Surface | | | | | |
| 0-10 cm | $1.6 \times 10^7$ | $5.0 \times 10^7$ | $5.5 \times 10^6$ | $4.2 \times 10^7$ | $6.3 \times 10^6$ |
| Subsurface | | | | | |
| 85-85.5 ft. | $<2.0 \times 10^2$ | $<2.0 \times 10^2$ | nd† | $<2.0 \times 10^2$ | $<2.0 \times 10^2$ |
| 86.86.5 ft. | $<2.0 \times 10^2$ | $<2.0 \times 10^2$ | nd | $<2.0 \times 10^2$ | $<2.0 \times 10^2$ |
| 87-87.5 ft. | $<2.0 \times 10^2$ | $<2.0 \times 10^2$ | nd | $<2.0 \times 10^2$ | $<2.0 \times 10^2$ |

†not determined

# Site Reactivity Probes

C. E. CASTRO
*Department of Nematology, Riverside Campus*

## Summary

Establishing the reactivity of a given site or soil for chemical or biochemical conversion is a valuable requisite for predicting the fate and rate with which xenobiotics may be transformed in the soil-water sphere. Reactivity can guide the choice of environmentally tolerable pesticides that may be employed at a given location. This project, which is in its second year, is measuring directly a site's capacity for transformation by exposing it to a defined substance that is capable of undergoing the fundamental processes of oxidation, reduction, and substitution. The underlying strategy is to incubate soil with a defined substrate and let the chemistry that occurs define the site. Both the nature and rates of transformation can be assessed. We are accomplishing this assessment with carbon-labeled $^{13}C$ substrates and $^{13}C$ nuclear magnetic resonance spectroscopy analysis ($^{13}C$ NMR).

In the first year of the project, we chose chloroacetic acid, 1,2-$^{13}C$(CA) as the first site reactivity probe (SRP) to investigate. A protocol was developed to assess a given soil's capacity for transformation. The CA probe's response to hydrolytic substitution, oxidation, and reduction was demonstrated.

In the second year of the project, a serious limitation in the CA probe's use with soil has been found and overcome. Binding of the probe to soluble organic matter can broaden the NMR resonances and greatly diminish the analytical capacity of the probe, but this limitation was overcome by the simple addition of acid following centrifugation. A dramatic example of the probe's initial inability to respond to a basic soil containing zinc metal for reduction is showing. But following acidification, the probe responded quite clearly to both hydrolysis and reduction simultaneously in this soil. Comparative rate data for the response of CA and chloroacetonitrile to a series of soil organisms indicate the latter may be a more responsive probe than CA. Particularly striking differences were observed with a soil methylotroph. CA is essentially inert; whereas, chloroacetonitrile is rapidly metabolized. A variety of attempted model syntheses of the chloronitrile from the acetonitrile failed. A new route through CA itself is under investigation.

**Key Words:** transformation capacity, oxidation, reduction, substitution, soil, soluble organic matter, $^{13}C$ NMR

## Project Objectives Addressed in 1993-94

1. Distribute the CA probe to the Western Regional W-82 Committee for testing.

2. Scan for additional SRPs and refine usage of the CA probe synthesized and purified during the first year of this study.

3. Develop experimental procedures for synthesizing new probes.

## Research Plan and Procedures

Work during the first year established that chloroacetic acid-1,2-$^{13}C$ (CA) can be used as a "site reactivity probe" (SRP) for soil. A simple protocol was established that entails incubation of CA with soil slurries followed by centrifugation and direct $^{13}C$-NMR analysis of the centrifugate. In this way products of oxidation (glyoxylic acid, $HCO_3^-$), reduction (acetic acid), and hydrolysis (glycolic acid) are easily determined. Their distribution and quantity read the site's capacity for transformation (Castro, 1994). The methods for syntheizing and purifying CA and the protocol for incubating CA with soil slurries with subsequent $^{13}C$-NMR analysis are described in detail on page 44 of the 1992-93 Annual Report of the Kearney Foundation of Soil Science.

## Results

### I. Distribution of CA to the Western Regional W-82 Committee

A greater quantity of the CA probe was synthesized for the purpose of distributing it to the Western Regional W-82 Committee. Following a discussion of the probe and its use, sealed ampules of a 1 M solution of CA in dimethyformamide were distributed to the committee in September 1993, along with instructions for its use. While no results from the committee are yet available, Dr. Helling (USDA-Beltsville) is employing the probe to determine whether soils change their reactivity upon storage.

### II. Soil Organic Matter - A Complicating Factor in Analysis

In efforts to obtain a better spectra attendant upon reduction in soil, a basic soil (pH 8 in the initial slurry) was adjusted to pH 5.0 and incubated with Zn° for three days. Following centrifugation/filtration, the clear solution (now pH 6.7) exhibited the NMR spectrum in Fig. 1. This spectrum is poorly resolved. DMF resonances predominate and the methyl group of acetic acid is suppressed. It is discernible, but only as a broadened multiplet. The carboxyl resonances are not seen. However, addition of one drop of concentrated $H_2SO_4$ to the same NMR tube resulted in the clean and well-resolved spectrum shown in Fig. 2. Resonances for acetic acid (21, 178 d) and glycolic acid (60, 177 d) are clear. Thus, the artificially forced reduction did occur, but the hydrolytic capability of the soil was also manifest. In this case, the probe has responded to both reduction

and hydrolysis by the soil/Zn° mixture. Again, it is the $CH_3$ and $CH_2OH$ resonance that are diagnostic. The results above showed that in the event poorly resolved spectra are obtained, they can be greatly improved by the addition of acid to the final filtrate used for NMR analysis. The broadening observed in this experiment was not observed in other incubations.

## III. Reactivity of Microbes to CA and Chloroacetonitrile

Initial results (Castro, 1994) indicated chloroacetonitrile may be transformed by a wider array of soil microbes than CA is. Thus, it may be a more sensitive SRP. Table I lists the conversions of CA and chloroacetonitrile by two *Pseudomonads*, a methylotroph, and an anaerobe known to be reactive in dehalogenation processes (Castro and Belser, 1990; Castro et al., 1992; Bartnicki and Castro, 1994; Krone and Thauer, 1992). In addition, the chloronitrile and chloroacetamide are both dehalogenated by the soil denitrifier *Pseudomonas aeruginosa*.

The actual rate of conversion of $ClCH_2CN$ by the soil methylotroph *Methylosinus trichosporium* OB-3b is much quicker than indicated in Table 1. The rate of $Cl^-$ release is shown in Fig. 3. The half life of ClCH2CN is ~7.5 min under these conditions. Although reaction is slow, the chloronitrile is dehalogenated by the anaerobe.

## IV. Attempted Syntheses of Chloroacetonitrile-1,2-$^{13}$C

As model preparations for this substance, we have attempted to chlorinate acetonitrile by the $SO_2Cl_2/PCl_5$ system that worked so well with acetic acid. This failed. In addition, chlorination with t-butyl hypochlorite, N-chlorosucciminde, and chlorine under photolytic conditions did not result in significant yields of the desirable product. None of the reactions are useful as small scale preparations of the $^{13}C$ labelled compound. However, we are now pursuing a route from CA itself. The overall process is (Eq. 1).

$$CH_3CO_2H \rightarrow ClCH_2CO_2H \rightarrow ClCH_2CO_2Me \rightarrow ClCH_2CONH_2 \rightarrow ClCH_2CN \quad (1)$$

A related sequence through the acid chloride (rather than the ester) is under investigation. Both sequences work, but we need to establish which gives the best overall yield of pure substance. Via this process, CA itself, as well as the corresponding amide and nitrile, should be available in good yield.

## Discussion

While no information has yet been forthcoming from the W-82 Committee, the results of Dr. Hellings' tests of soil stability (or lack of it) upon storage should be available soon. The idea of using the CA probe in this way is novel.

The results with the basic soil/zinc reduction experiment are most encouraging. They demonstrate the probe's simultaneous response to both

hydrolysis and reduction. That is, the probe reads the sample despite initial experimental difficulties. The broadening and poor resolution initially observed in the reduction experiment deserve some additional comment. The initial centrifugate/filtrate was clear and homogeneous. The greatly enhanced spectrum observed following the addition of acid suggests the products (in this case, both acetic and glycolic acid) were bonded to soluble substances extracted from the slurry. These may have been a composite of soluble organic matter and $Zn^{+2}$. The broadening was not the result of this ion alone, because experiments in the absence of soil did not show it. We infer soluble matter from soils may interfere with these analyses by complexing and occluding the corresponding acid anions. In any case, acidification of the solution releases the products. Thus, with those soils from which poorly resolved spectra are obtained, acidification of the sample following centrifugation/filtration may be a requisite.

The enhanced reactivity of the nitrile to a soil methylotroph, a denitrifier and an anaerobe suggest it will be a more sensitive SRP than CA . Also, the new synthetic route will yield the corresponding amide (chloroacetamide). The amide itself is a potential SRP and may be a metabolite of chloroacetonitrile. Both will be examined in the coming year.

## References


C. E. Castro. 1994. 1992-93 Kearney Foundation of Soil Science Annual Report.

Castro, C. E. and N. O. Belser. 1990. Biodehalogenation: Oxidative and reductive metabolism of 1,1,2-trichloroethane by *Pseudomonas putida*-biogeneration of vinyl chloride. *Environ. Toxicol. Chem.* 9:707-714.

Castro, C. E., R. S. Wade, D. M. Riebeth, E. W. Bartnicki and N. O. Belser. 1992. Biodehalogenation. Rapid metabolism of vinyl chloride by a soil *Pseudomonas* sp. direct hydrolysis of a vinyl C-Cl bond. *Environ. Toxicol.Chem.* 11:757-764.

Bartnicki, E. W. and C. E. Castro. 1994. Biodehalogenation: Rapid oxidative metabolism of mono- and polyhalomethanes by *Methylosinus* trichosporium OB-3b. *Environ. Toxicol. Chem.* 13:241-245.

Krone, U.E. and R. K. Thauer. 1992. Dehalogenation of trichlorofluoromethane (CFC-11) by *Methanosarcina barkeri*. *FEMS Microbiol. Lett.* 90:201-204.

Table I. Percent conversion of CA and chloroacetonitrile by resting cells in 24 hrs.

| Organism[a] | CA[b] | $ClCH_2CN$[b] |
|---|---|---|
| OB-3b | 0 | 100% |
| Pa | 0 | 50 |
| PpG-786 | 40 | 40 |
| Ps | 40 | 30 |
| Msb | 0 | 10 |

[a]OB-3b=*Methylosinus trichosporium*-OB-3b, PpG-786=*Pseudomonas putida*, Ps=*Pseudomonas* sp, Msb=*Methanosarcina barkeri*, Pa=*Pseudomonas aeruginosa*; [b]initial concentration=$10^{-3}$M.

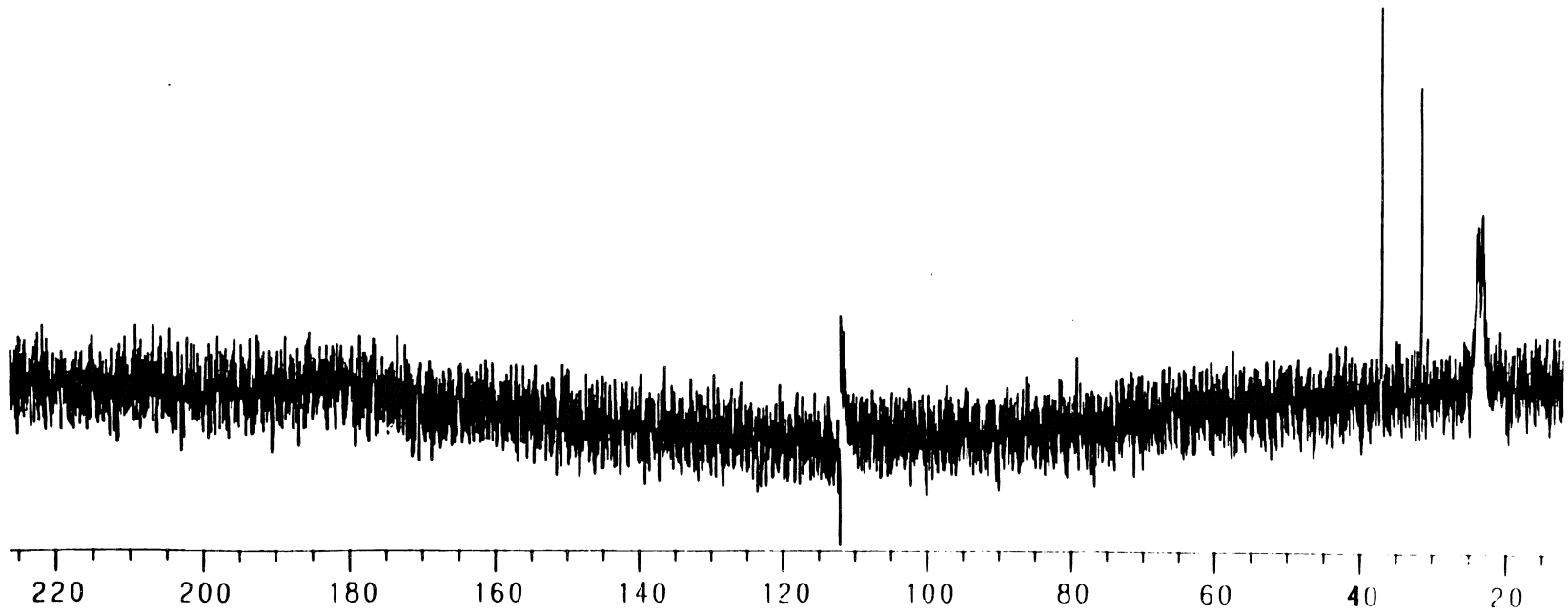


Figure 1. $^{13}C$-NMR spectrum following reduction of CA with Zn° in a "basic" soil.

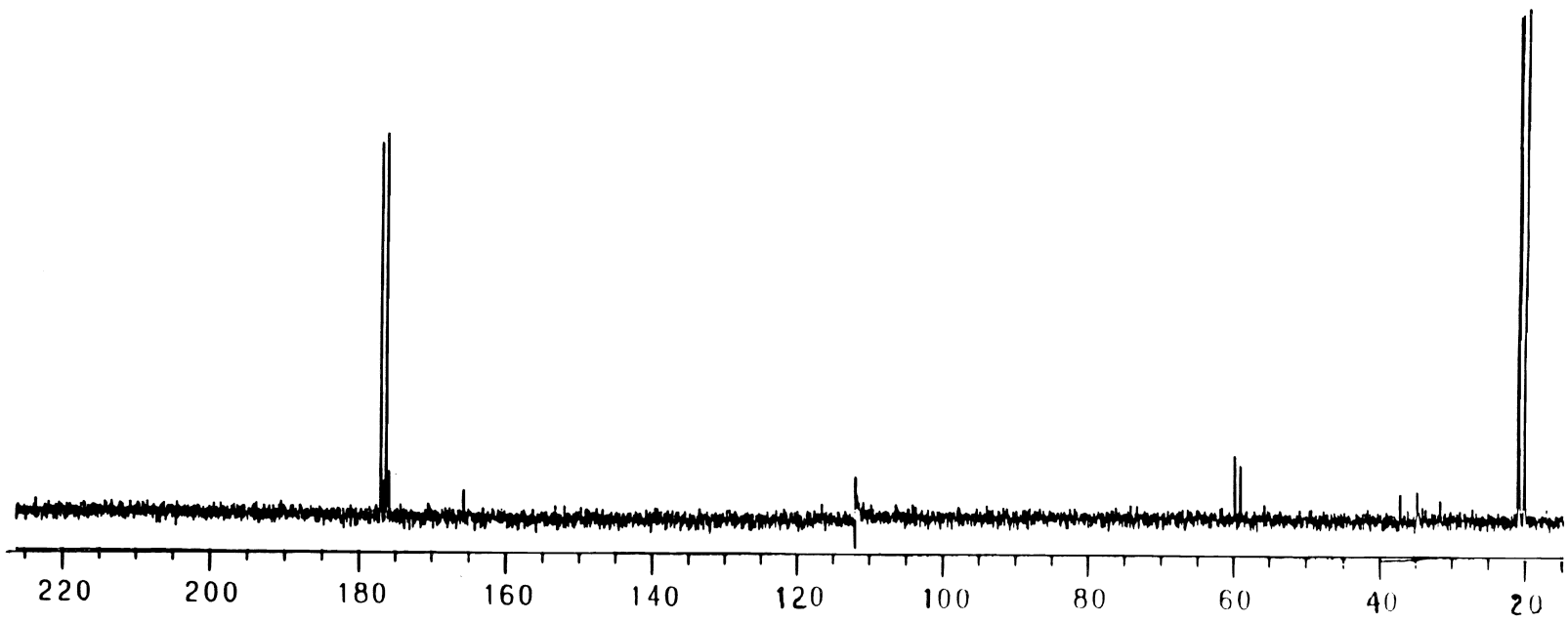


Figure 2. The $^{13}C$-NMR spectrum of the products of the Zn° reduction experiment (Fig. 3) after acidification (to pH 1).

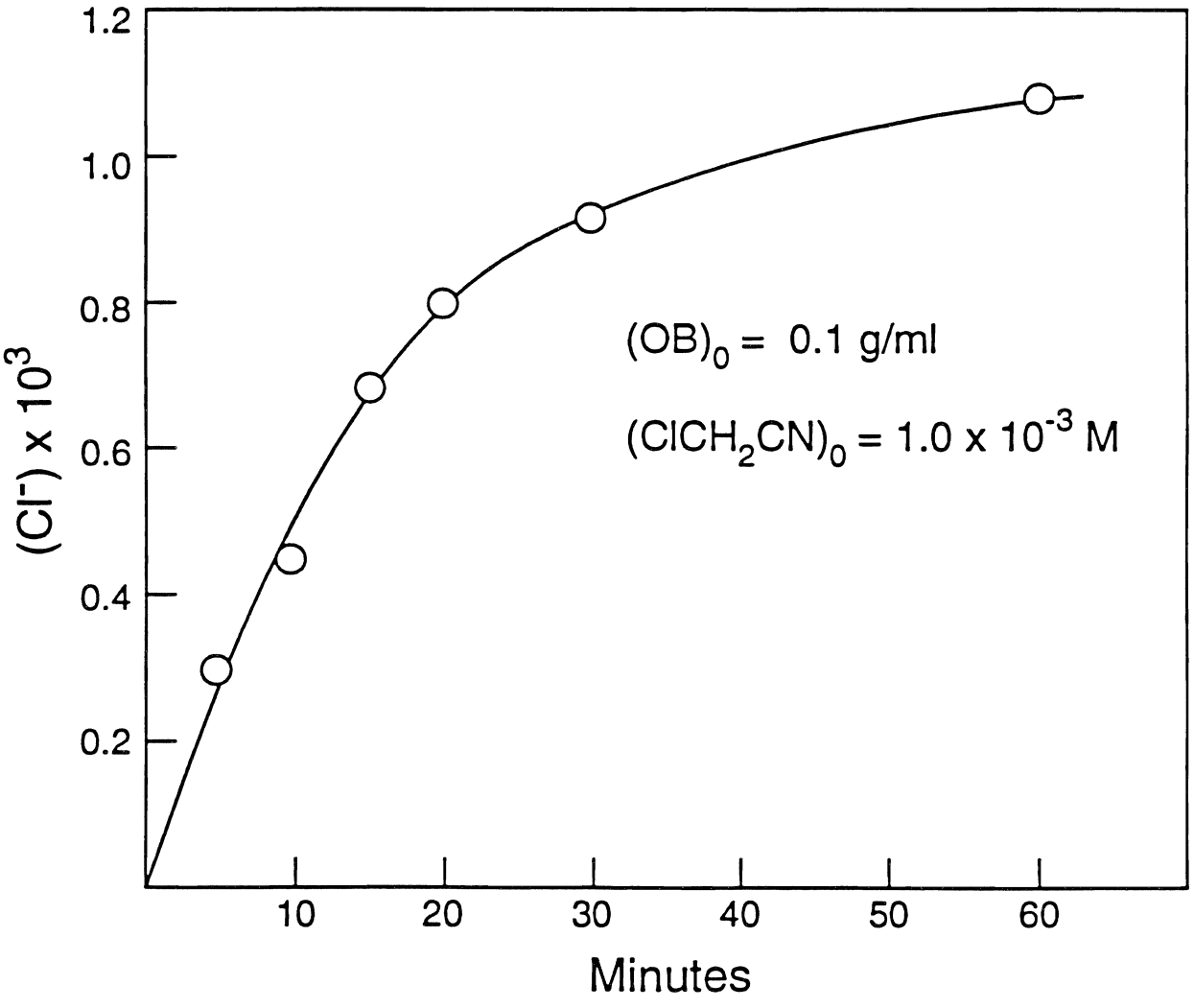


Figure 3. Dehalogenation of chloroacetonitrile by resting cells of *Methylosinus trichosporium* OB-3b.

# Development and Assessment of a Stable Isotope Tracer Method for Determining the Lability of Cadmium Pools in Metal-Contaminated Soils

DAVID R. PARKER AND PAULA J. BOSSERMAN
*Department of Soil and Environmental Sciences, Riverside Campus*

## Summary

The objective of this project is to develop and critically evaluate a stable isotope tracer method for studying the lability of cadmium (Cd) in soils using newly available inductively-coupled plasma mass spectrometry (ICP-MS) technology. Second-year progress includes final optimization of the ICP-MS instrumental parameters for the measurement of isotopic $^{111}Cd$:$^{110}Cd$ ratios. Instrumental mass discrimination has been assessed, and protocols for correcting for this effect have been developed. Four high-Cd soils have been sampled and characterized, and an evaluation/optimization of a sequential fractionation procedure to operationally define soil Cd pools is nearly complete. The chemical matrices of the fractionation procedure do not interfere with accurate measurement of isotopic ratios. One short-term incubation study has been conducted using a sewage sludge-amended soil, and the results suggest that the method yields data of high accuracy and precision. In the third year, we will utilize the stable isotope tracer method to monitor changes in the isotopic abundance of the operationally defined Cd pools over extended incubation periods (e.g., 150 d) and to derive estimates of the inherent lability of each pool. The results should provide new insights into the reactivity of the various metal pools in contaminated soils and should be particularly useful in situations where cleanup or abatement is required.

**Key Words:** isotopic exchange, inductively-coupled mass spectrometry, sequential fractionation

## Project Objectives Addressed in 1993-94

1. To critically evaluate the feasibility and to optimize the experimental design for using stable isotopic tracers to study Cd lability in contaminated soils. Key factors include optimization of the inductively-coupled plasma mass spectrometer (ICP-MS) for measurement of isotopic ratios, accuracy and precision of these ratios, and selection of the most appropriate tracer isotope.
2. To conduct detailed chemical and mineralogical characterizations of the soils to be studied, to identify the significant Cd pools present in each, and to develop workable routine chemical fractionation procedures for each soil.

## Research Plan and Procedures

All isotopic ratio measurements were made using the VG PlasmaQuad 2 ICP-MS housed in our department. We have found that the following parameters optimized measured isotopic ratios (MIRs) with Cd: peak jump scan mode, pulse counting detection, a peak dwell of 10.2 msec, and a scan time of 0.18 sec/sweep. All MIRs are based on 10 replicate acquisitions of 30 sec each, such that each determination requires 10 min total (including rinses). Standard ICP-MS protocols are used for measuring natural Cd levels in soils.

To assess the importance of mass discrimination (or bias), we purchased enriched samples of $^{110}Cd$ (95.9% abundance), $^{111}Cd$ (96.3%), and $^{112}Cd$ (97.3%), and prepared individual stock solutions of each. Using atomic absorption spectrophotometry, these stocks were then rigorously analyzed for total Cd (16 replicate determinations), and means and SDs were computed for each. From these stocks, several series of isotope ratio (IR) standard solutions were prepared ($\approx 9 \times 10^{-7}$ mol $L^{-1}$ total Cd for all). By accounting for the slight uncertainties in $Cd_T$ of the stock solutions and in the volumetric glassware ("Class A" throughout), we were able to prepare standards with known degrees of uncertainty in IR; all were within ±0.3 to 0.5% of the nominal value.

Bulk soil samples were collected from four field sites, thoroughly mixed, passed through a 2-mm screen, and stored at 4°C without additional drying (i.e., at field moisture content). Basic soil characterization and Cd analyses using standard methods have been completed for these soils, and results are presented herein.

We have adopted a tentative protocol for sequential extraction of the major Cd pools present in each soil (see Table 1). Selection of these extractants was largely based on the recent review and evaluation of Shuman (1991), along with a goal of maximizing the specificity of each extraction.

One short-term incubation study using the MV-1 soil has been completed. A number of replicate centrifuge tubes were set up, each containing 2.0 g of soil (ODW basis). A solution containing $^{111}Cd$ equivalent to 0.53% of the total soil Cd content was added to each tube, the gravimetric water content

adjusted to 0.42 g $g^{-1}$, and the soils incubated at 25°C for 5 d, with daily readjustment of water content. After 2, 24, 48, 96 and 144 h, duplicate tubes were extracted with 0.1 *M* $Sr(NO_3)_2$ and the MIRs ($^{111}Cd/^{110}Cd$) determined using ICP-MS.

## Results and Discussion

Finalization of SIT protocols.

In order to maximize accuracy and precision in measured isotopic ratios (MIRs), we have optimized a number of instrumental and chemical parameters (Janghorbani and Ting, 1989; Russ, 1989). First, we identified candidate Cd isotopes for use as the tracer (i.e., the "spike") and as the reference isotope: $^{110}Cd$ (12.4% natural abundance), $^{111}Cd$ (12.8% NA), and $^{112}Cd$ (24.1% NA). Based on a number of criteria (including absence of isobaric interferences from $^{112}Sn$) and experimental results, we have selected $^{111}Cd$ as the tracer isotope, and $^{110}Cd$ as the reference. We have also conducted a number of sensitivity analyses of the effects of isotopic abundances (tracer vs. reference, sample vs. spike), spike size relative to the soil Cd content, and obtainable precision in MIRs in order to optimize the experimental design for soil incubation experiments (see below). The overall precision in the MIRs is best expressed as the percentage relative standard deviation (%RSD) of the 10 replicate acquisitions, a fundamental "figure of merit" commonly used in isotope research (Janghorbani and Ting, 1989). We now routinely obtain %RSDs of $\leq$1% for $^{111}Cd/^{110}Cd$ MIRs, although the precision decreases somewhat at very low Cd concentrations (i.e., <0.3 μmol $L^{-1}$).

A rigorous suite of tests has been conducted to evaluate the problem of mass discrimination (or bias) arising from differences in response of the interface, quadrupole, and/or detector of the ICP-MS as a function of atomic mass (Russ, 1989). Results from a typical run using known $^{111}Cd/^{110}Cd$ standards are depicted in Fig. 1, and illustrate the extremely high accuracy and precision in MIRs obtained. Early runs suggested consistent, linear relationships wherein the heavier isotope is detected preferentially by the instrument. However, subsequent tests using an expanded range in $^{111}Cd/^{110}Cd$ revealed that the calibration plots were often described best by a nonlinear function (see Fig. 1). Moreover, the slight mass discrimination observed can favor either the lighter or the heavier isotope, depending on the actual daily run; results obtained on a given day are, however, quite consistent. Consequently, we now include IR standards in each run of our experimental samples to permit correction for mass discrimination and to yield maximum accuracy in the MIRs.

We also evaluated the effects of various solution matrices (corresponding to our selective extraction procedures outlined in Table 1) on the accuracy and precision of MIRs and on mass discrimination. The results, summarized in Table 2, indicated that the matrices used for dissolution of organic, oxide, and

residual forms of Cd had no significant, adverse effects on MIRs. Due to its high electrolyte content and instrumental space-charge effects, the $Sr(NO_3)_2$ solution used for the exchangeable Cd fraction causes some problems in accuracy and precision of both MIRs (Table 2) and natural Cd determinations (not shown). The results are acceptable, however, especially since the exchangeable Cd pool is generally small in our study soils (see below). Thus, we have concluded that matrix-matched IR standards are not required for accurate determinations of $^{111}Cd/^{110}Cd$ ratios during our sequential fractionation procedure.

Collection and characterization of soils.

We obtained a soil sample from long-term field-plots at the UCR Moreno Valley Field Station that had received very heavy applications of Cd-rich sewage sludge for 15 consecutive years (sample MV-1). A second sample was collected from a naturally high-Cd soil (Millsholm series) formed in Cd-rich shale in the Santa Monica Mountains (Lund et al., 1981). The Penn mine soil is from a site immediately adjacent to a holding pond for acidic mine drainage from a derelict Pb-Zn mine located in Calaveras County. The fourth soil is from a site in close proximity to a zinc smelter in Palmerton, PA that is heavily contaminated with airborne sources of trace metals. We have also adopted the use of two Certified Reference Material soils recently made available by the National Institute of Standards and Testing (NIST). These are being employed to check for quantitative recovery of Cd using our "total" analysis method and during fractionation.

The four soils obtained thus far represent significant diversity in Cd source characteristics and soil properties (Table 3). Organic carbon ranges from <1% to >7%, and soil pH ranges from extremely acidic (Penn mine) to neutral. Free carbonates range from 0 to 0.6% in the four soils (Table 3). Cadmium extractable with 0.1 *M* $Sr(NO_3)_2$ is <4% of the total in the MV-1, Millsholm, and Palmerton soils, but is about 10% of total Cd in the Penn mine soil. Additional analyses to be completed by the end of this year include particle size distribution, clay mineralogy, and operationally defined amorphous and crystalline Fe(Al) and Mn oxides by selective dissolution methods.

During the past year, scrutiny of the results from several whole-soil analyses conducted using the Milward and Kluckner (1989) microwave digestion procedure revealed unacceptably high variability in the "total" Cd values obtained (data not shown). Although these authors cautioned that their method did not recover the most refractory forms of most metals (and the results are thus operationally defined), greater stability in the values obtained were needed for the method to be useful. We solved this problem by adopting a protocol wherein each sample was digested twice in succession, and higher, more stable recoveries of soil Cd were obtained. Persistently low Cd recoveries (81%) with the NIST 2710 reference soil led to the discovery that this soil contains an unusually high level of indium (In) which we normally employ as an

internal standard for ICP-MS determinations of Cd. We are presently switching to rhodium (Rh) as the internal standard in an attempt to improve recoveries with this soil.

Last year, we adopted a tentative protocol for sequential extraction of the major Cd pools present in each soil (Table 1). Further investigations and refinements to this procedure were made during the past year and include the following:

1. Use of 0.1 *M* NaCl as a "wash" between each successive step in the procedure. Our original use of distilled $H_2O$ led to problems with sample dispersion and low Cd recoveries.

2. Routine inclusion of the "carbonate" step after careful analysis revealed that all soils (except the Penn Mine) contained at least traces of free carbonates. The "carbonate" Cd fraction seems to be significant or dominant in all soils except the very acidic Penn Mine soil (Table 4).

3. Variability in the operationally defined organic Cd fraction led us to investigate this step more completely, and we discovered that the reagent must be prepared immediately (i.e., within 10 min) prior to addition to a given soil sample. The number of repetitive treatments with NaOCl required for optimal removal of soil organic C was also evaluated, and five treatments were adopted as the optimal method for fractionating organically-bound Cd in these soils.

Using the resulting modified procedure, indigenous Cd fractions were extracted from the four soils (plus the two NIST reference soils), and the results are summarized in Table 4. With the four experimental soils, the sum of the Cd recovered in the sequentially extracted fractions was 99.6 to 105.9 of that measured in an independent, whole-soil digestion made using the "residual" fraction procedure, indicating excellent mass balance of Cd in this soil using the proposed sequential fractionation scheme. Recovery was also excellent for the NIST 2711 reference soil, and the low recovery with the NIST 2710 soil may be overcome when we switch to Rh as the internal standard.

Additional checks on the specificity and precision of the fractionation procedure are underway. Using the MV-1 soil, we conducted a complete elemental analysis (Cd, Fe, Al, Ca, Mg, Mn, K, Ti, Cr, Ni) of each extracted fraction to look for "markers" that might indicate poor specificity (e.g., high Fe in the "organic" fraction). The results, summarized in last year's report, were quite encouraging, and similar studies using the other soils are ongoing.

Soil incubations with stable isotope tracers.

One short-term incubation using the MV-1 was completed last year. After just 2 h of incubation, the measured $^{111}Cd/^{110}Cd$ ratios had declined dramatically (data not shown), suggesting rapid isotopic equilibration with a

large fraction of the nonextractable native soil Cd. Following this rapid initial decrease, a much slower rate of decline (approximately exponential) continued and, after 5 d of incubation, the $Sr(NO_3)_2$-extractable Cd pool was still quite far from isotopic equilibrium with the entire native Cd pool. These results suggested that the MV-1 soil contains at least two nonexchangeable Cd pools of quite differing lability. Similar short-term incubations with the remaining three soils will be completed in the coming year.

## Anticipated Results During Year III

Final assessments and refinements of the sequential fractionation procedure will include continued analyses for "marker" elements to help assess specificity.

Short-term incubations similar to the one described for the MV-1 soil will be conducted using all soil samples collected. These experiments will permit further evaluation of the short-term rates of isotopic equilibrium between the soluble/exchangeable Cd fraction and the less labile soil pools.

Long-term incubations will be set up using larger soil samples, and water content will be readjusted every 2 to 3 d such that moisture fluctuations that occur under field conditions are simulated. Subsamples of each soil will be taken on days 5, 15, 30, 60, 90, and 150 and subjected to the appropriate sequential fractionation procedure. Isotopic ratios ($^{111}Cd/^{110}Cd$) will be measured in each fraction, and compared to the indigenous (i.e., natural) ratio. These results will permit evaluation of the kinetics of isotopic redistribution and, thus, the indigenous lability of Cd in each pool.

Because empirical tests of plant uptake of metals, their mobility in soils, and lability during clean-up/remediation efforts are inherently time-consuming and inefficient, greater predictive capabilities are needed. A fundamental understanding of kinetic processes governing the removal of metals from the soil system will provide critical knowledge needed for the development of better conceptual and predictive models. Our stable isotope tracer method, coupled with a detailed analysis of soil chemical and mineralogical properties, will offer new insights into the reactivity of various Cd "pools" in contaminated soils. The results should be particularly useful in the context of highly contaminated soils or sediments for which cleanup or abatement is deemed necessary.

## References

Gibson, M. J., and J. G. Farmer. 1986. Multi-step sequential chemical extraction of heavy metals from urban soils. Environ. Pollut., Ser. B 11:117-135.

Janghorbani, M., and B. T. G. Ting. 1989. Stable isotope trace applications of ICP-MS. p. 115-140. *In* A. R. Date and A. L. Gray (ed.) Applications of inductively coupled mass spectrometry. Blackie & Son, London.

Lund, L. J., E. E. Betty, A. L. Page, and R. A. Elliott. 1981. Occurrence of naturally high cadmium levels in soils and its accumulation by vegetation. J. Environ. Qual. 10:551-556.

Milward, C. G., and P. D. Kluckner. 1989. Microwave digestion technique for the extraction of minerals from evironmental marine samples for analysis by inductively coupled plasma emission spectrometry and atomic absorption spectrometry. J. Anal. Atomic Spectrocs. 4:709-713.

Russ, G. P. 1989. Isotope ratio measurements using ICP-MS. p. 90-114. *In* A. R. Date and A. L. Gray (ed.) Applications of inductively coupled plasma mass spectrometry. Blackie & Son, London.

Shuman, L. M. 1983. Sodium hypochlorite methods for extracting microelements associated with soil organic matter Soil Sci. Soc. Am. J. 47:656-660.

Shuman, L. M. 1985. Fractionation method for soil microelements. Soil Sci. 140:11-22.

Shuman, L. M. 1991. Chemical forms of micronutrients in soils. p. 113-144. *In* J. J. Mortvedt (ed.) Micronutrients in agriculture. 2nd ed. Soil Sci. Soc. Am. Book Ser. 4. SSSA, Madison, WI.

Table 1. Proposed method for sequential, selective extraction of operationally defined soil Cd fractions.

| Extractant | Duration | Temp. | Fraction | Reference |
|---|---|---|---|---|
| | h | °C | | |
| 0.1 M $Sr(NO_3)_2$ | 2 | 25 | "soluble + exchangeable" | -- |
| pH 5.0, 1 M NaOAc | 5 | 25 | "carbonate" | Gibson & Farmer, 1986 |
| pH 8.5, 5% NaOCl | 0.5 | 95 | "organic"† | Shuman, 1983 |
| 0.4 M ammonium oxalate + 0.1 M ascorbic acid, pH 3.0 | 0.5 | 95 | "Fe/Mn-oxiddes"† | Shuman, 1985 |
| 3:1 $HNO_3$:HCl | 0.3 | na‡ | "residual" | Milward & Kluckner, 1989 |

†To be repeated as needed to obtain complete dissolution.

‡Digestion at high temperature and pressure (≈ 150 psi) in a microwave oven. Each sample is digested twice in succession.

Table 2. Summary of assessment of mass discrimination and precision in MIRs using two sets of known $^{111}Cd/^{110}Cd$ standards made up in chemical matrices to match those employed in fractionation of soil Cd. Values represent the regression of the MIRs against the known IRs, four standards per set.

| | | Matrix† | | | |
|---|---|---|---|---|---|
| Parameter | $Cd_T$, mol $L^{-1}$ | $Sr(NO_3)_2$ | NaOCl | Oxalate | $HNO_3$:HCl |
| regression slope | $9 \times 10^{-7}$ | 1.014 | 0.967 | 0.965 | 0.966 |
| regression $r^2$ | | 0.9998 | 0.9999 | 0.9999 | 0.9999 |
| mean % RSD | | 1.47 | 0.24 | 0.34 | 0.34 |
| regression slope | $9 \times 10^{-8}$ | 1.008 | 1.021 | 1.013 | 1.021 |
| regression $r^2$ | | 0.9999+ | 0.9999+ | 0.9999+ | 0.9999+ |
| mean % RSD | | 1.21 | 1.47 | 0.88 | 1.14 |

†Matrices are those used to extract the exchangeable, organic, oxide, and residual fractions, respectively (see Table 3). Concentrations of the reagents in these standards were adjusted to reflect the dilution that occurs during the actual fractionation procedure.

Table 3. Characteristics of four Cd-enriched soils collected and selected for further study, and two Certified Reference Material soils from the National Institute of Standards and Testing (NIST).

| Soil | pH | Organic C | $CaCO_3$ | Total Cd† | Exch. Cd‡ |
|---|---|---|---|---|---|
| | | % | % | μg $g^{-1}$ | μg $g^{-1}$ |
| MV-1 | 6.0 | 7.7 | 0.2 | 34.0 | 0.8 |
| Millsholm | 7.3 | 1.9 | 0.6 | 26.1 | 0.1 |
| Penn mine | 3.5 | 0.7 | 0.0 | 21.8 | 2.0 |
| Palmerton | 7.0 | 3.7 | 0.1 | 30.5 | 1.1 |
| NIST 2710 | 5.8 | 3.0 | 0.3 | 17.7 | 9.3 |
| NIST 2711 | 8.7 | 1.2 | 4.4 | 37.8 | 0.3 |

†Operationally defined "total" Cd using Milward and Kluckner's (1989)microwave digestion procedure; the samples are digested twice in succession. Certified values for the NIST 2710 and 2711 soils are 21.8 and 41.7 μg $g^{-1}$, respectively, with corresponding recoveries of 81% and 91%.
‡Exchangeable Cd determined by extraction with 0.1 *M* $Sr(NO_3)_2$.

Table 4. Representative results from sequential extraction of operationally defined soil Cd fractions (μg $g^{-1}$).

| | Fraction | | | | | | |
|---|---|---|---|---|---|---|---|
| Soil | Exchangeable | Carbonate | Organic | Oxide | Residual | Sum | % Recovery † |
| MV-1 | 0.76 | 10.4 | 18.3 | 2.5 | 2.0 | 33.9 | 99.6 |
| Millsholm | 0.12 | 8.6 | 9.4 | 5.9 | 2.4 | 26.4 | 101.1 |
| Penn mine | 2.05 | 0.3 | 18.8 | 0.9 | 0.9 | 23.0 | 105.9 |
| Palmerton | 1.11 | 13.2 | 12.2 | 2.0 | 1.8 | 30.2 | 99.1 |
| NIST 2710 | 9.4 | 3.4 | 5.0 | 0.45 | 0.7 | 15.4 | 86.9 |
| NIST 2711 | 0.32 | 33.2 | 6.7 | 1.2 | 1.6 | 42.9 | 102.9 |

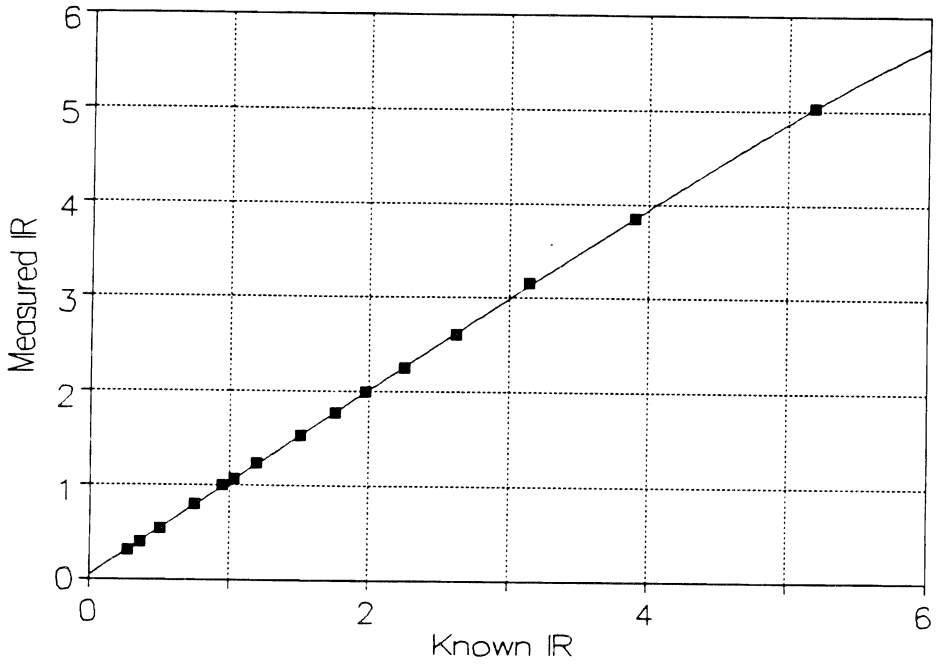


Figure 1. Typical calibration plot for measured $^{111}Cd/^{110}Cd$ ratio by ICP-MS versus the known isotope ratio in a series of prepared standard solutions (all are ca. 0.9 μmol $L^{-1}$ in total Cd). Best-fit regression equation for this calibration is $y = 0.457 + 0.983x - 0.000668e^{x}$, with a degree-of-freedom-adjusted $r^2$ of 0.99989.

# Chemical Factors Affecting Colloid-Mediated Transport of Organic Pollutants in Soils

GARRISON SPOSITO
*Department of Environmental Science, Policy and Management*
*Berkeley Campus*

## Summary

Dynamic and static light scattering methods were applied to dilute suspensions of 90-nm Na-illite particles in varying concentrations of NaCl solution at pH 8. The effective hydrodynamic radius of the Na-illite floccules increased exponentially with time at low ionic strength (< 40 mol $m^{-3}$) and as a power law in time at higher ionic strength, indicating a gradual transition from reaction control to transport control in the flocculation mechanism. Measurements of the Stability Ratio (rate of transport-controlled flocculation to reaction-controlled flocculation) indicated a critical coagulation concentration of 100 mol $m^{-3}$, in agreement with the trend in the growth kinetics. Static light scattering measurements were analyzed to infer a cluster fractal dimension of $2.1 \pm 0.1$ for the illite floccules, also supporting a reaction-control mechanism.

**Key Words:** colloid stability, flocculation, fractal dimension, groundwater quality, light scattering

## Project Objectives Addressed in 1993-94

1. To perform light-scattering experiments on flocculating suspensions of illitic colloids under varying conditions of electrolyte concentration, and to evaluate the light-scattering data in terms of transport- or reaction-control kinetics and fractal concepts.

## Research Plan and Procedures

Clay stock suspension. Illite Imt-1 (Silver Hill illite) obtained from the Source Clays Repository of the Clay Mineral Society was prepared in stock suspension using the procedure of Sposito and Levesque (1985), but with the samples being washed with a mixed solution of NaCl and KCl instead of $NaClO_4$ and $KClO_4$. To recover the smallest size fraction, the last washing operation was done at a 2 mol $m^{-3}$ concentration of NaCl. The suspension was then centrifuged on a Sorvall SS-3 automatic centrifuge for 60 min at 10,000 rpm. The stock suspension was stored in a refrigerator to reduce microbial activity.

About 10 g of illite stock suspension were placed in a tared 10 ml porcelain crucible. The suspension was then oven-dried for 12 h. The dried solid mass was corrected for the presence of NaCl. The final illite concentration was 0.114 g clay per kg suspension (114 ppm).

The particle size distribution in the clay stock suspension (Fig. 1), measured by light scattering, was unimodal, with a z-average mean diameter (effective hydrodynamic diameter, see below) of 90 nm.

Light scattering experiments. Measurements were performed on a Malvern PCS 100 light-scattering goniometer. The incident light source was a 35 mW He-Ne laser operating at 632.8 nm wavelength with vertical polarization. The temperature was held constant at 25 °C. Flocculation was initiated by mixing $10^{-5}$ $m^3$ of stock suspension rapidly with 3 ¥ $10^{-5}$ $m^3$ of NaCl solution adjusted to pH 8.0 with $NaHCO_3$. The concentration of Na in the solution was calculated by weighing the mass of $NaHCO_3$ added to reach pH 8, yielding 3.45 ¥ $10^{-4}$ mol per kg solution. Solid NaCl was added to bring the final mixture of 40 ml to a desired Na concentration. Once mixed, the preparation was poured into a cylindrical Burchard cell (20 ml capacity) used for the light scattering measurement. From mixing to measurement, less than 10 s pass. The duration of data acquisition was 30 s, but automatic data analysis increases the total measurement time to about 60 s.

The variation of the total scattering intensity with scattering vector **q** was measured between scattering angles of 30° and 132° (0.0068 $nm^{-1} < q < 0.024$ $nm^{-1}$). The time required for data acquisition was 5 s and a measurement was made every 3° to give a total of about 180 s for each intensity [I(q)] curve. Measurements were made continuously during the flocculation process in order to follow the evolution of the apparent fractal dimension of the clay floccules.

Particle size measurement. In photon correlation spectroscopy, the time-fluctuations of light scattered by particles in suspension in a scattering volume are autocorrelated at a given angle. The measured autocorrelation function, $G^{(2)}(\tau)$ is (Berne and Pecora, 1976; Grabowski and Morrison, 1983):

$$G^{(2)}(\tau) = A\left(1 + \beta\left|g^{(1)}(\tau)\right|^{(2)}\right) \quad (1)$$

where $g^{(1)}(\tau)$ is the normalized first-order autocorrelation function at the delay time $\tau$; A is the baseline constant; and $\beta$ is an equipment-related "instrument constant" (Grabowski and Morrison, 1983). If the suspension comprises monodisperse, dilute, and optically isotropic particles, $g^{(1)}(\tau)$ is (Berne and Pecora, 1976; Ostrowsky, 1988):

$$g^{(1)}(\tau) = \exp(-\Gamma\tau) = \exp(-D_T q^2 \tau) \quad (2)$$

where $D_T$ is the particle translational diffusion coefficient; $\Gamma$ is the decay constant; $q = \frac{4\pi n}{\lambda} \sin(\theta/2)$ is the magnitude of the scattering vector; n is the refractive index of the medium; $\theta$ is the scattering angle; and $\lambda$ is the wavelength of the incident light in vacuum. In a polydisperse medium, $g^{(1)}(\tau)$ takes the form (see, e.g., Ostrowsky, 1988):

$$g^{(1)}(\tau) = \int G(\Gamma)\exp(-\Gamma\tau)d\Gamma \quad (3)$$

with $G(\Gamma)$ being the distribution function of decay constants.

The data analysis method used is cumulant analysis, with ln g(1)($\tau$) fitted to a power series in $\tau$ (Ostrowsky, 1988):

$$\ln g^{(1)}(\tau) = -<\Gamma>\tau + \frac{1}{2!}\mu_2\tau^2 - \frac{1}{3!}\mu_3\tau^3 + \ldots \quad (4)$$

The first cumulant in the expansion eq. (4) is the average decay constant, $<\Gamma>$. It is determined by the logarithmic slope at the zero-time limit of the autocorrelation function. A mean hydrodynamic radius $R_h$ (z-average mean particle size) of the scattering particles can be obtained using the Stokes-Einstein relationship:

$$<D_T> = \frac{k_B T}{6\pi\eta <R_h>} \quad (5)$$

where $\eta$ is the viscosity of the medium, $k_B$ is the Boltzmann constant, and T is

absolute temperature. In our experiments, the influence of rotational particle diffusion has to be taken into account because the radius of gyration of the floccules, $R_g$, will be of the order of or greater than the inverse of the scattering vector (Lin et al., 1990). Thus, an *effective* diffusion coefficient is measured, including the effects of rotational diffusion:

$$< D_{eff} > \equiv \frac{k_B T}{6\pi\eta < R >} \tag{6}$$

where R is an average size parameter (average radius of the floccules, including rotational effects). Rotational diffusion also contributes to the decay of the autocorrelation function [see eq. (2)]; thus, a higher apparent value than $D_T$ will be obtained, yielding a smaller value of the size parameter. Internal particle modes, which can also contribute to the decay of an autocorrelation function, can be neglected.

Floccule structure measurement. Different methods for measuring cluster fractal dimensions are known (Vicsek, 1992), but the most practical for our purposes is measurement by static light scattering. In a cluster fractal, the particle pair density-density correlation function, $\rho_2(r)$, has a power-law form (Dale et al., 1984):

$$\rho_2(r) \propto r(d - d_f) \tag{7}$$

where r is a radial separation lying between the primary particle size and the cluster size; $d_f$ is the fractal dimension; and d is the Euclidean dimension (d = 3 in our case). In a static light scattering experiment, changing the scattering vector q by changing the scattering angle will yield information about the structure factor S(q), the Fourier transform of $\rho_2(r)$. An equivalent power law is then obtained (Teixeira, 1985):

$$S(q) \sim q^{-df} \tag{8}$$

This structure factor power law is valid over the range:

$$R_g^{-1} << q << R_{h,1}^{-1} \tag{9}$$

where $R_{h,1}$ is the hydrodynamic radius of a primary particle. In this domain the form factor of the primary particles is equal to 1; the scattered intensity is proportional to S(q) (Teixeira, 1985); and a plot of log I(q) versus log q will give the fractal dimension $d_f$. As pointed out by Teixeira (1985), outside the limits of the condition in eq. (9), important errors can occur in a fractal dimension measurement.

Stability Ratio measurement. We have followed the method of Novich and Ring (1984), wherein the early stage of flocculation is considered, with the

average hydrodynamic radius dependent only on the number of doublets or primary particles present in suspension. The formation of doublets under transport-controlled flocculation is described by the second-order rate law (Smoluchowski, 1917):

$$-\frac{dN}{dt} = kN_o^2 \qquad (10)$$

where k is a rate constant for diffusion-limited flocculation and $N_o$ is the initial primary particle concentration ($2 \times 10^{13}$ per kg suspension). At 298K, k is (Smoluchowski, 1917):

$$k = \frac{8k_BT}{3\eta} = 1.233 \times 10^{-17} m^3 s^{-1} \qquad (11)$$

If an electrostatic barrier to doublet formation exists, flocculation will be retarded by a factor 1/W, where W is the Stability Ratio, equal to $\frac{k}{k_R}$, and $k_R$ is a "barrier-limited" flocculation rate constant, given by (Novich and Ring, 1984):

$$k_R = \left[R_{h,1}\left(\sqrt{2}-1\right)N_o\right]^{-1}\frac{dR_h}{dt} = 2.68 \times 10^{-9}\frac{dR_h}{dt} \qquad (12)$$

where $R_{h,1}$ is the hydrodynamic radius of a primary particle (45 nm).

## Results

Figure 2 shows a log-log plot of the Stability Ratio against NaCl concentration for Na-saturated Silver Hill illite at pH 8.0. All experiments were performed at a clay concentration of 5 mg per kg suspension. The critical coagulation concentration (ccc) is defined by (see, e.g., Sposito, 1994):

$$\lim_{c \uparrow ccc} \ln W = 0 \qquad (13)$$

Extrapolation of the linear portion of the graph in Fig. 2 yields ccc ≈ 104 mol $m^{-3}$, whereas identification of the ccc at the change in slope of the graph yields 80 mol $m^{-3}$ instead.

The values obtained are similar to the value reported by Goldberg and Forster (1990) for the same illite: 130 mol $m^{-3}$ at pH 8.0. The difference can be attributed to differences in the clay washing procedure and the time-dependent ccc determination. (In their experiments, the ccc was defined operationally as the concentration which corresponds to 20% of the clay remaining in suspension after 3 h.) Hesterberg and Page (1990) found ccc values ranging from 30 to 45 mol $m^{-3}$, corresponding to settling times ranging from 36 to 2.2 h,

respectively. They used the same washing procedures as in our experiments, but the size, solid particle concentration, and pH equilibration were different.

Figure 3 shows the evolution in time of the effective diameter of the floccules at pH 8 in 20 mol $m^{-3}$ NaCl. The important feature in Fig. 3 is the initially slow growth of the floccules, followed by an exponential increase in floccule size. This behavior can be explained by making qualitative use of the DLVO theory of interparticle interactions (Sposito, 1989). [The acronym DLVO refers to the last names of the scientists Dergaguin, Landau, Verwey, and Overbeek associated with the model for forces between surfaces, such as repulsion, attraction, shrinking, swelling, etc.] At low concentration of electrolyte, a potential barrier exists, and successful flocculation is possible only after a number of collisions between clusters. When a certain size of the floccules is reached, the "sticking probability" increases because of the increased number of contact possibilities between two incoming floccules. The growth rate then increases dramatically.

At higher electrolyte concentrations, we should expect a higher initial growth rate, as shown in Fig. 4. The shapes of the curves at 30 and 35 mol $m^{-3}$ are identical, but with sudden changes in growth rate at longer times. Additional experiments will show if this phenomenon is reproducible. At 40 mol $m^{-3}$, the general shape of the curve changes, with an initial exponential growth followed by a power-law shape. The large scatter in the data at longer times is from the transition to a settling regime and the fact that the number density of the floccules in the scattering volume is low.

In Fig. 5 the initial floccule growth (first hour) is represented. At 40 to 45 mol $m^{-3}$ NaCl, the transition from exponential (reaction control) to power-law (transport control) kinetics occurs. This transition can be explained by a "critical" value of the "sticking probability" being reached. A power-law growth curve is then obtained. This interpretation of power-law and exponential growth curves comes from the literature on colloidal aggregation kinetics (Sposito, 1994) and is based on data for suspensions of monodisperse spherical colloids.

Figure 6 shows a log-log plot of I(q) against q for Na-illite at pH 8 in 40 mol $m^{-3}$ NaCl. If we assume that the slope of the whole curve at later times is representative of the fractal dimension, and that the condition in eq. 9 is met, then we obtain $d_f \approx 2$, typical of floccules comprising spherical, monodisperse colloids in the reaction-controlled regime (Aubert and Cannell, 1986). Computer simulation (Meakin, 1983; Kolb et al., 1983) leads to $d_f$ values of 1.8 under transport-control conditions and 2.1 under reaction-control conditions. The particle dynamics in these simulations correspond to the flocculation of particles having an equal "sticking probability" in all directions. These two $d_f$ values have been confirmed in experimental systems of spherical, monodisperse particles (Aubert and Cannell, 1986).

A flocculation mechanism cannot be proposed yet, but if our value of the ccc is correct (around 100 mol $m^{-3}$), all of our static scattering profiles would be

in the reaction-control regime (NaCl concentration less than 60 mol $m^{-3}$). We find an average $d_f$ value over the whole scattering profiles of 2.1 ± 0.1 (90% confidence interval), in agreement with the theoretical value for reaction-controlled flocculation. On the other hand, anisotropic sticking effects arising from both particle shape and the interparticle interaction potential have been found to lower the value of the fractal dimension (Zxelos et al., 1985). If this were the case, our values would be too high, and a more complex flocculation mechanism would have to be considered. Another possibility is floccule restructuring after each collisional event, which has the effect of raising the fractal dimension (Meakin, 1988).

## Discussion

Our results thus far suggest that the experimental methodologies and theoretical framework developed for studying the flocculation of monodisperse spherical colloidal suspensions can also be applied to the clay mineral illite. The interpretation of the observed growth kinetics and static light scattering data can be based on concepts and parameters for model colloidal systems, but anisotropies in the shapes of clay particles and in the distribution of their surface charge should be considered. In most natural colloidal systems, a variety of processes can occur, and there is no one-to-one relationship between a fractal dimension and the flocculation mechanism that yields it. As Meakin (1988) states, "In some cases fractal dimensionalities have been measured which do not agree with those associated with any of the simple models.... In other cases the apparent agreement may be fortuitous since there is no reason to believe that aggregation is occurring under conditions which can be well represented by a simple model."

## References


Aubert, C. and D.S. Cannell. 1986. Restructuring of colloidal silica aggregates. Phys. Rev. Lett. 56:738-741.

Axelos, M. D., D. Tchouchbar, J. Y. Botters, and F. Fiessinger. 1985. Small-angle S-ray scattering of two aluminum hydroxide aggregates, $Al(OH)_x$, with x=2.5 and 3.0: Structure and Power-Law Correlation of Cluster Fractals. J. Phys. (Paris) 46: 587.

Berne, B.J. and R. Pecora. 1976. Dynamic light scattering. Wiley, New York.

Dale, W., E. Schaefer, P. Wiltzius, and D.S. Cannell. 1984. Fractal geometry of colloidal aggregates. Phys. Rev. Lett. 52:2371.

Goldberg, S. and H.S. Forster. 1990. Flocculation of reference clays and arid-zone soil clays. Soil Sci. Soc. Am. J. 54:714-718.

Grabowski, E.F. and I.D. Morrison. 1983. Particle size distributions from analysis of quasi-elastic light scattering data. *In* B.E. Dahneke (ed.) Measurements of suspended particles by quasi-elastic light scattering. Wiley, New York.

Hesterberg, D. and A.L. Page. 1990. Critical coagulation of sodium and potassium illite as affected by pH. Soil Sci. Soc. Am. J. 54:735-739.

Kolb, M., M. Botet, and R Jullien. 1983. Scaling of kinetically growing clusters. Phys. Rev. Lett. 41:1123-1126.

Lin, M.Y., H.M. Lindsay, D.A. Weitz, R. Klein, R.C. Ball, and P. Meakin. 1990. Universal diffusion-limited colloid aggregation. J. Phys. Condens. Matter 2:3093-3113.

Meakin, P. 1983. Formation of fractal clusters and networks by irreversible diffusion-limited aggregation. Phys. Rev. Lett. 51:1119-1122.

Meakin, P. 1988. Fractal aggregates. Advan. Colloid Interface Sci. 28:249-331.

Novich, B.E. and T.A. Ring. 1984. Colloid stability of clays using photon correlation spectroscopy. Clays Clay Minerals 32:400-406.

Ostrowsky, N. 1988. Particle characterization by photon correlation spectroscopy. *In* P.J. Lloyd (ed.) Particle size analysis 1988. Wiley, New York.

Smoluchowski, M.V. 1917. Versuch einer mathematischen Theorie der Koagulationskinetik kolloider Losungen. Zeitschrift physik. Chemie 92:129.

Sposito, G. 1989. The chemistry of soils. Oxford Univ. Press, New York.

Sposito, G. 1994. Chemical equilibria and kinetics in soils. Oxford Univ. Press, New York.

Sposito, G. and C.S. Levesque. 1985. Sodium-calcium-magnesium exchange on Silver Hill illite. Soil Sci. Soc. Am. J. 49:1153-1159.

Teixeira, J. 1985. Experimental methods for studying fractal aggregates. *In* E. Stanley and N. Ostrowsky (ed.) On growth and form. Reider, Dordrecht.

Vicsek, T. 1992. Fractal growth phenomena (2nd ed.). World Scientific, Singapore.

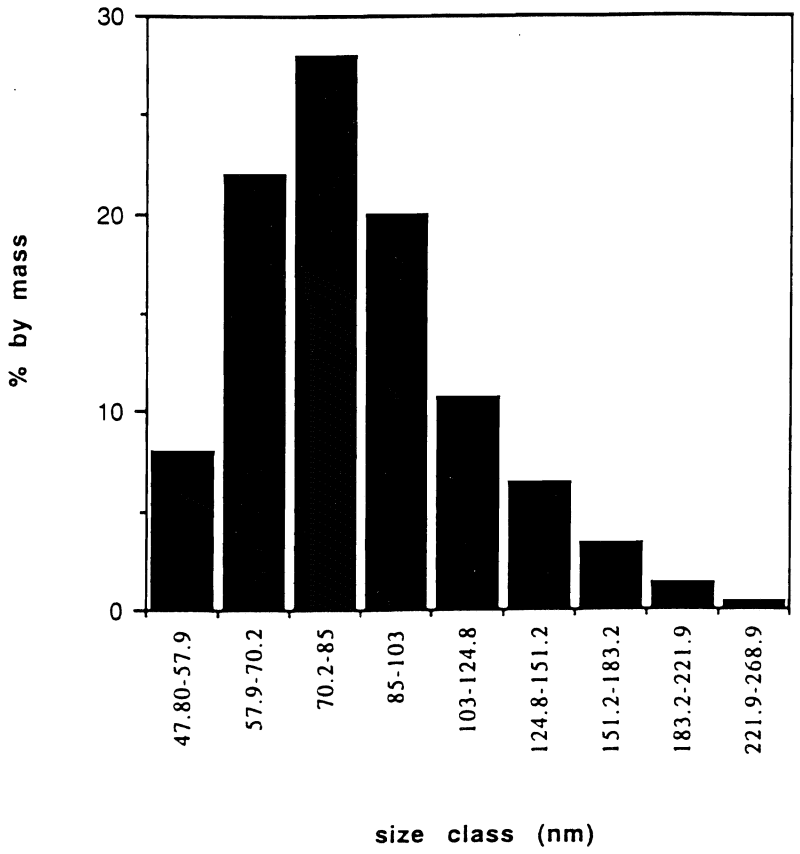


Figure 1. Particle-size distribution in the clay stock suspension.

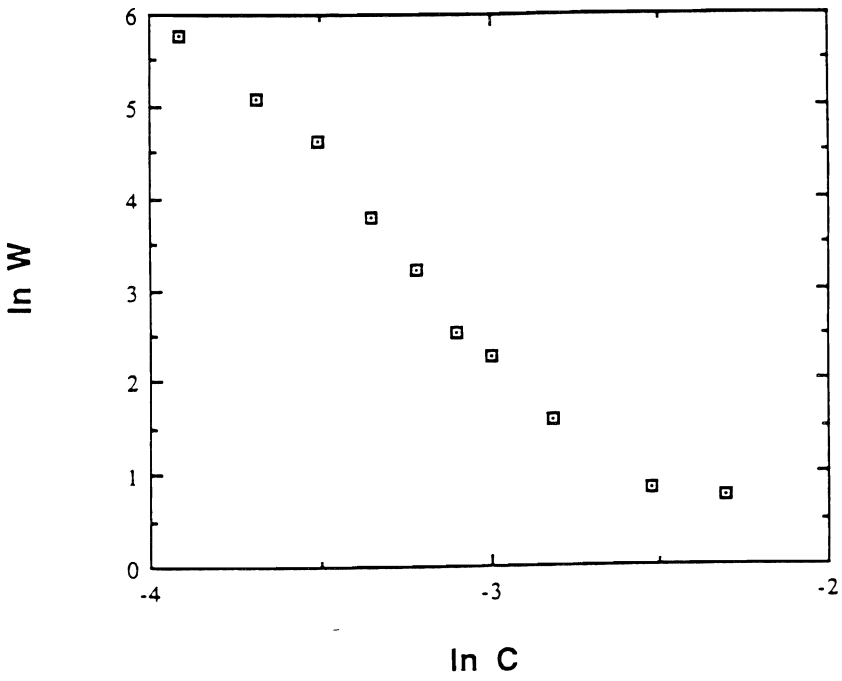


Figure 2. Plot of the Stability Ratio (W) against NaCl concentration (c) for Na-

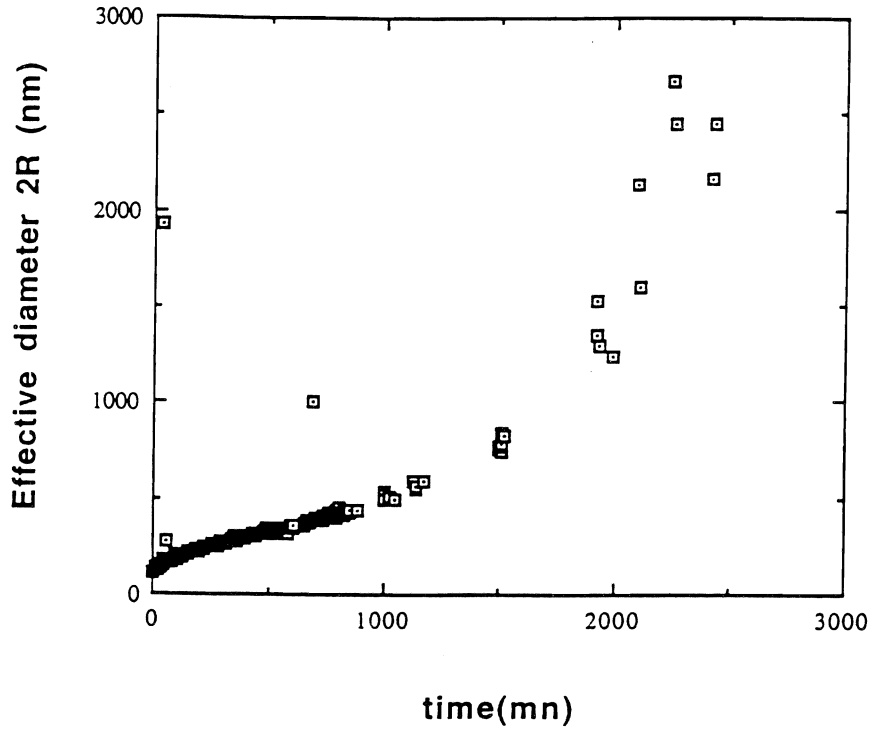


Figure 3. Time evolution of the average effective floccule diameter for Na-illite particles in 20 mol $m^{-3}$ NaCl solution at pH 8.

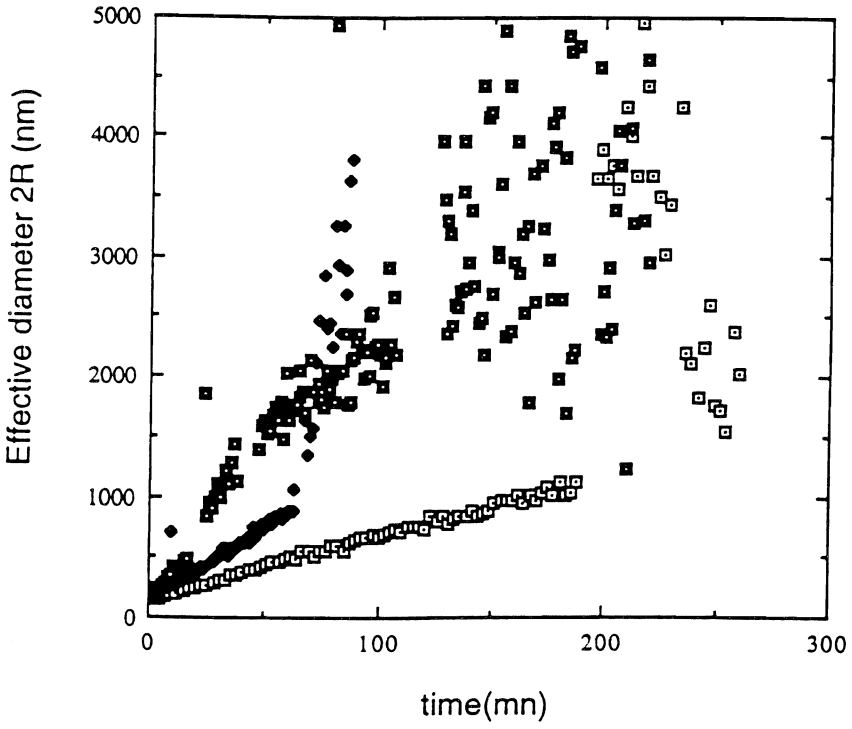


Figure 4. Time evolution of the average effective floccule diameter for Na-illite particles in 30 (⊡), 35 (♦), or 40 (◘) mol $m^{-3}$ NaCl solution at pH 8.

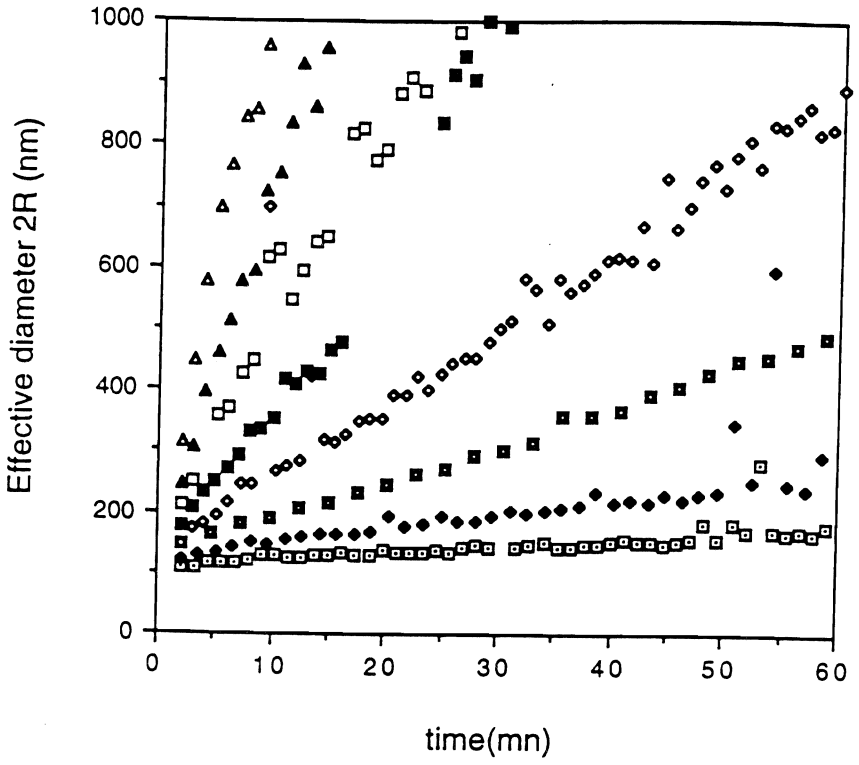


Figure 5. Initial growth kinetics of Na-illite floccules in 20 (⊡), 25 (♦), 30 (◘), 35 (◊), 40 (■), 45 (□), 50 (▲), or 60 (Δ) mol $m^{-3}$ NaCl solution at pH 8.

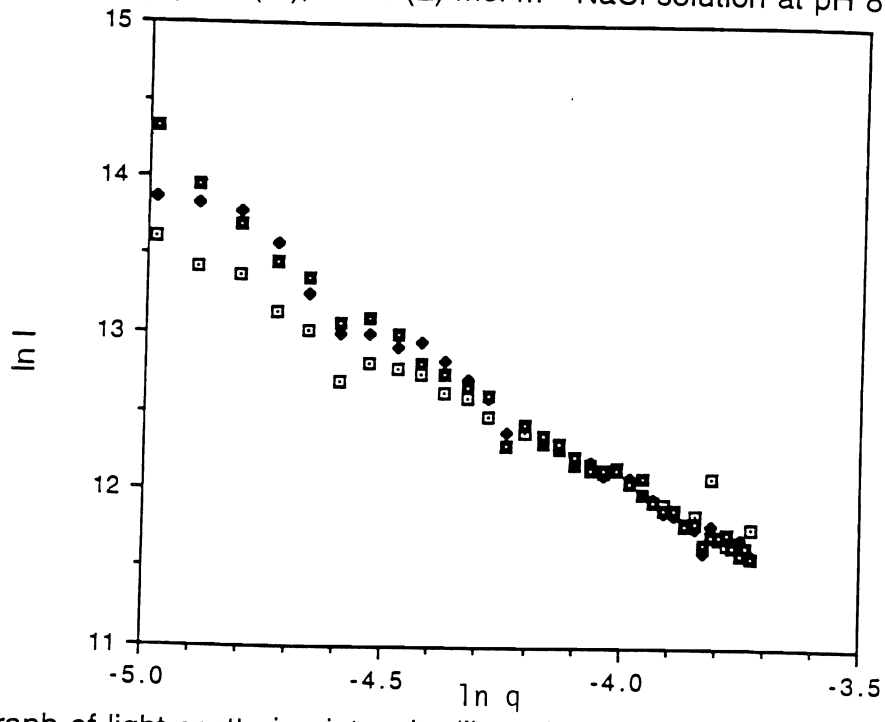


Figure 6. Graph of light-scattering intensity (I) against light-scattering vector (q) for Na-illite particles during consecutive flocculation periods of 0-3 min (⊡), 3-6 min (♦), or 6-9 min (◘) in 40 mol $m^{-3}$ NaCl solution at pH 8. A linear log-log plot is achieved after 5 min.

# Kinetics and Mechanisms of Degradation of Herbicides in California Forest Soils

JOHN G. MCCOLL
*Department of Environmental Science, Policy, and Management*
*Berkeley Campus*

## Summary

The increased use of herbicides in forested areas and the lack of research on the sorptive properties of oxide minerals typical of weathered soils with low organic matter (OM) are a prescription for future groundwater contamination. Researchers have often claimed that sesquioxides in weathered soils are strong adsorbents of organic pollutants because of their high surface area and variable surface charge. In this study we examine the sorptive and catalytic properties of two oxides on the persistence and availability of three herbicides. Sorption, degradation, and iron-herbicide stability constants were measured to determine the fate and persistence of the herbicides atrazine, picloram, and triclopyr on redox-active oxides birnessite and ferrihydrite, and treated red, weathered, metavolcanic forest soils (whole, minus OM, and minus OM and sesquioxides). Herbicide adsorption onto the oxide minerals varied with herbicide type and oxide. Birnessite adsorption of all three herbicides was low over the pH range studied (4-7) with adsorption maxima occurring at low pH. Ferrihydrite adsorbed high concentrations of picloram and triclopyr, but very little atrazine. All mineral adsorption was found to be completely reversible. Soils treated for OM and sesquioxide removal adsorbed the herbicides with varying efficiency. Picloram and triclopyr adsorbed well on soils even after OM removal, but adsorption decreased drastically with sesquioxide removal. Atrazine adsorption did not follow a discernible trend for all of the three soils, but for the two low-OM soils it adsorbed strongly even after OM removal. Little to no degradation was observed over the pH range of 3-7. Modeling picloram and triclopyr adsorption onto ferrihydrite showed that outer-sphere adsorption best fits the changes observed in adsorption with increasing ionic strength. Therefore, charge-transfer reactions that would be expected to lead to degradation are unlikely to occur, because inner-sphere coordination with the surface does not occur. The adsorption mechanism studies agree with observed degradation and adsorption kinetics data for ferrihydrite adsorption. We conclude that these herbicides are persistent in soils with low OM and microbial activity, and can potentially threaten groundwater because oxide adsorption was completely reversible.

**Key Words:** herbicides, metal oxides, adsorption, modeling, fluorescence.

## Project Objectives Addressed in 1993- 94

1. Determine mechanism of adsorption and desorption.
2. Determine abiotic mechanisms of degradation.
3. Determine kinetics of the reactions and the rate-limiting step of degradation.

## Research Plan and Procedures

### Herbicides

The herbicides atrazine (2-chloro-4-ethylamino-6-isoropylamino-s-triazine), picloram (3,5,6 trichloro-4-amino-picolinic acid), and triclopyr (3,5,6-trichloro-2-oxy-acetic acid pyridine) were chosen for this study because of their widespread use in vegetation control and their variety of chemical properties (Table 1). The herbicides vary in stability in soils and have markedly different octanol-water partitioning coefficients. Chemical structure controls the stability and reactivity of each compound, as well as its ability to adsorb onto mineral and organic colloids.

### Minerals

The minerals used in this study are presented in Table 2. Their synthesis and preparation have been reported previously in the 1992-93 Kearney Foundation of Soil Science Annual Report.

### Soils

Soils used in this study were described in the 1992-93 KearneyFoundation of Soil Science Annual Report. Table 3 contains the physical properties of the soils measured for the purposes of this study. The three soils used were all subsurface horizons of the Whitmore (11 and 50 cm horizons), and New York (N25 cm horizon) sites. Each soil was treated for organic matter (OM) removal by hydrogen peroxide (termed minus OM) and sesquioxide removal by dithionite-citrate-bicarbonate (termed minus Fe).

### Herbicide Solutions

Technical grade purity samples of the atrazine, picloram, and triclopyr were used. Carbon-14-labeled herbicides were provided by Ciba-Geigy (atrazine, Greensboro, NC) and Dow-Elanco (picloram and triclopyr, Midland, MI). Stock solutions of each carbon-14-labeled herbicide were prepared and diluted to the following concentrations: atrazine (20.00, 10.00, 5.00, 2.50, and 1.25 mg $kg^{-1}$); picloram and triclopyr (40, 20, 10, 5, and 2.5 mg $kg^{-1}$). All solutions were made to have either varying pH (4 to 7) and constant ionic strength (0.01M LiCl), or constant pH (5) and varying ionic strength (0.01 to 1.0 M LiCl).

## Analytical Techniques

Adsorption was quantified using a Beckmann liquid scintillation counter (Brunswick, N.J.) and calibrated with Bureau of Standards Carbon-14 standards. One ml of herbicide supernatant solution was removed after centrifugation at 8,000 rpm and added to 10 ml of scintillation cocktail (Biosafe, RPI, Mount Prospect, IL).

High pressure liquid chromatography (HPLC) (Hewlett-Packard model 1040A, San Jose, CA) was used to quantify herbicide degradation and herbicides. A C-18 column (Chromspher Pesticides, Chrompack, The Netherlands) with a mobile phase of 10-40% acetonitrile and 90-60% 0.008 N $H_2SO_4$, and a flow rate of 1.0 ml/minute was used. Herbicide concentrations were analyzed using an UV-vis. light diode-array detector set at 210 and 254 nm.

## Herbicide Adsorption

Adsorption was measured under three sets of conditions: (1) constant ionic strength (0.01M LiCl) and temperature (20°C) and varying pH (4, 5, 6, and 7, pH adjusted under $N_2$ using 1.0 N LiOH and HCl) with an oxide/soil load of 100 g $L^{-1}$; (2) constant pH and temperature (pH 5 and T = 20°C), and varying ionic strength (0.01, 0.1, and 1.0 N LiCl for picloram and triclopyr sorption onto ferrihydrite only) with an oxide load of 12.0 g $L^{-1}$; and (3) constant pH and ionic strength (pH = 5.0, and I = 0.01 N LiCl), and varying temperature (10°C, 20°C, and 30°C) using picloram and triclopyr and ferrihydrite with an oxide load of 12.0 g $L^{-1}$. Desorption was measured by removing half the equilibrium supernatant volume and replacing the aliquot with an equal volume of clean buffer solution (pH 5, ionic strength 0.01 M LiCl, and 12.0 g $L^{-1}$ oxide loading). Samples were centrifuged and equilibrium concentrations were analyzed by liquid scintillation. All solutions were prepared using Milli-Q filtered water and were run in triplicate.

Oxide and soil adsorption of atrazine were fitted to a Freundlich isotherm and the sorption constant $K_f$ and the slope (1/n) were calculated. Atrazine adsorption plots were made using a log-log transform of the Freundlich equation: $x/m = K_f C_{eq}^{1/n}$; where x/m is the adsorbed concentration in mmol $kg^{-1}$, and $C_{eq}$ is the equilibrium concentration of the supernatant in mmol $m^{-3}$. Picloram and triclopyr adsorption onto oxides were linear and slope values of the linear regressions were reported. Soil adsorption was fitted to a Freundlich isotherm.

Adsorption kinetics of picloram and triclopyr sorption onto ferrihydrite were measured using batch techniques and reactions were buffered at pH 5 with an acetate buffer and maintained at 20°C. Oxide loading was maintained at 12.0 g $L^{-1}$ with constant stirring.

## Oxide Catalyzed Degradation

Degradation experiments consisted of incubation periods of seven days. Buffered herbicide solutions (0.01 N ionic strength with pH 3 and 5) were added to oxides in similar proportions used in the adsorption experiments and replicated in triplicate. Concentrations were monitored by HPLC (The procedure was described in the 1992-93 Kearney Annual Report). Degradation concentrations were corrected for adsorption onto the oxides.

## Metal-Ligand Binding

The fluorescence of the herbicides was measured in the presence of Fe (III), Mn (II), and Al (III) ions over an increasing pH (2.1 - 5.4). Stability constants were measured at metal-ligand ratios that minimize collisional quenching (~1.0 X $10^{-4}$ M) using a fluorescence spectrometer (Perkin-Elmer model MPF-66, Norwalk, CT). Excitation wavelengths (and emission range) were 392 (420-600), 398 (410-600), 350 (360-500), and 281 nm (310-500 with 290 nm filter), for atrazine, picloram, salicylic acid, and triclopyr, respectively. Fluorescence quenching of herbicide and reference (salicylic acid) solutions were measured under two sets of conditions: (1) over a range of pH (2.0-3.5) in the presence and absence of dissolved metal cations at high concentrations (0.01 M); and (2) at constant pH (2.7 and 4.0) where metal ion concentrations were varied from 0.25 x $10^{-4}$ M to 5.0 x $10^{-4}$ M. Herbicide concentrations were 17.0, 20.0, 20.0, and 25.7 mg $kg^{-1}$ for atrazine, picloram, salicylic acid, and triclopyr, respectively. The stability constant for triclopyr was determined from plots of fluorescence intensity (plotted as % quenched) versus metal concentration ($C_M$) by fitting a non-linear regression of the data with Eq. (1) (Ryan and Weber, 1982).

$$I = ((I_{ML} - 100)/(2KC_L))[(KC_L + KC_M + 1) - \sqrt{(KC_L + KC_M + 1)^2 - 4K^2C_LC_M}] + 100 \quad (1)$$

where I is the intensity, $I_{ML}$ is the intensity minimum, $C_L$ and $C_M$ are the ligand and metal concentrations, and K is the stability constant. The method was verified by calculating the percent salicylic acid bound to iron using accepted stability constants and comparing the result to the measured values.

## Modeling Adsorption onto Ferrihydrite

Mechanisms of adsorption were modeled using the HYDRAQL computer program following the TLM (Papelis et. al, 1988). [Editor's note. The TLM acronym refers to the Triple Layer Model of adsorption. Adsorption is understood to occur at three different types of sites which correspond to three different levels of adsorption (inner sphere adsorption, outer sphere adsorption, or the formation of diffuse ions]. HYDRAQL models adsorption of inorganic and organic ligands onto metal oxides based on physical properties of adsorbate, adsorbent, and solution composition. Stability constants derived from fluorescence measurements were compared to the model fitting value for $K^{int}$ of triclopyr. Changes in adsorption were modeled at varying ionic strength, assuming two different possible mechanisms of adsorption. Equations (2) and (3) outline the

adsorption reactions modeled by HYDRAQL for outer-sphere and inner-sphere adsorption respectively (Fig. 1).

$$SOH_2^+ + Pic^- \Leftrightarrow SOH_2^+ - Pic^- \quad (2)$$

$$SOH + Pic^- + H^+ \Leftrightarrow S - Pic + H_2O \quad (3)$$

The log $K^{int}$ values are reported for these two reactions with picloram and triclopyr. Parameters used in the simulations are taken from simulations of amorphous oxide adsorption of metals run by Papelis et al. (1990). The surface area measurement used is taken from Davis and Leckie (1978) and is 600 $m^2\ g^{-1}$ because BET measurements of amorphous oxide surface areas often underestimate the true specific surface area (Yates and Healy, 1975). This value is much higher than the measurement reported herein, but is the best estimate of the available surface area given that $N_2$ does not measure the internal surface area. A site density of 3.3 sites $nm^{-2}$ and log $K^{int}$ values for ferrihydrite of 5.10 and -10.70 for protonation and deprotonation were used (Papelis et al., 1990). The lower hydroxyl site density was used because the adsorbate cannot interact with a greater number of surface hydroxyls, and higher densities result in overestimation of adsorption because the model does not account for the molecular size of the adsorbate (Papelis et. al., 1990). Use of a lower surface and higher hydroxyl site density would also have the same result, but the surface sites calculated from these parameters have been tested and are therefore better estimates of the reactive sites.

## Results

### Mineral Adsorption

Atrazine. Atrazine adsorbed weakly onto both oxides over the pH range 4-7 (Fig. 2). Adsorption onto birnessite increased with decreasing pH, whereas on ferrihydrite the adsorption had a small maxima at pH 6. The maxima in slope values at pH 6 coincided with a minima in the $K_f$ value for ferrihydrite adsorption of atrazine. In both cases oxide adsorption appeared inconsequential for contaminant binding even in oxide-rich soils. Slope values from plots of atrazine adsorption onto birnessite were approximately unity or lower (Table 4). Slopes for birnessite adsorption of atrazine steadily increased with pH while $K_f$ (intercept) values decreased. The highest $K_f$ value ($1.30 \times 10^{-2}$) for birnessite adsorption coincided with the lowest slope value (0.46) and the adsorption maxima. Ferrihydrite adsorption slopes (1/n) for atrazine are also approximately unity, except at pH 6 where the adsorption maxima is observed. The maxima in the slope also coincides with the lowest $K_f$ value (Table 4).

Picloram and Triclopyr. Picloram and triclopyr adsorption onto both oxides increased with decreasing pH (Fig. 2). A comparison of birnessite and ferrihydrite demonstrated that ferrihydrite adsorbed more picloram and triclopyr

than birnessite. Slope values for the herbicides decreased with increasing pH (Table 4). Slope values were unusually high for picloram and triclopyr adsorption onto ferrihydrite and imply that there is some sort of mechanism increasing adsorption with increased solution concentration. $R^2$ values for lines fit to ferrihydrite adsorption data were near 1.00, verifying that the unusual slopes are not a result of poor fit. Adsorption trends for picloram and triclopyr onto birnessite were significantly different than those for ferrihydrite. Atrazine and picloram adsorbed following a similar trend with pH, while triclopyr showed very little affinity for the surface or sensitivity to changes in pH.

Picloram and triclopyr adsorption onto ferrihydrite decreased significantly with increasing ionic strength. As ionic strength increased from 0.01 to 1.0 M, adsorption decreased for both compounds from 30% sorbed to approximately 8% sorbed (Table 5). Oxide loading (100 versus 12 g $L^{-1}$) did not significantly affect adsorption slopes. The resultant percent of herbicide adsorbed increased with increasing oxide loading. All adsorption was also completely reversible. Slopes were comparable for adsorption and desorption plots, and hysteresis was minimal.

Temperature had little effect on ferrihydrite adsorption of both picloram and ticlopyr. Adsorption increased slightly with decreasing temperature, although the trend was very weak in both cases, with insignificant differences in adsorption (Fig. 3). Slopes did increase slightly more for triclopyr than picloram, but the differences were not great enough to be distinguishable from potential measurement errors.

Picloram and triclopyr adsorption kinetics were extremely fast, approximating the rate observed for ion swarm adsorption. Fig. 4 contains a plot of surface concentrations of triclopyr versus time. The half-life of the adsorption reaction was less than 15 seconds, which is faster than can be measured by batch kinetics techniques, and thus the rate of adsorption cannot be accurately measured using these techniques (Sparks, 1988). Because the rate of adsorption is in the range of ion swarm adsorption kinetics, there is little reason to use more sophisticated techniques to attempt to get more thermodynamic and mechanistic data on this process.

**Adsorption onto Soils**

For a comprehensive discussion of herbicide adsorption onto soils (treated and untreated) the reader is referred to the 1992-93 Kearney Annual Report.

Atrazine. Atrazine adsorption increased with the OM content of the untreated soils (Fig. 5). Adsorption of atrazine decreased after the removal of OM only in the case of N25 (Fig. 5C), the soil with the highest OM concentration. For soils W50 and W11, the soils with the lowest and intermediate OM concentrations, respectively, atrazine sorption was either greater (W50, Fig. 5B) after OM removal. The untreated N25 soil sorbed the highest concentration of atrazine, and the N25 minus Fe treatment sorbed the lowest concentration of all the soils.

Picloram and Triclopyr. Only the data for picloram are presented because triclopyr adsorption agrees closely with it. In every soil, the minus Fe-treated soil sorbed the lowest concentration of picloram and triclopyr (Fig. 5). In the soil with the lowest OM, sorption increased after the minus OM treatment. In all other soils, sorption remained the same (W11) or decreased slightly (N25).

**Oxide-Catalyzed Degradation**

No degradation was observed during the 7-day reaction period. Neither oxide catalyzed hydrolysis reactions nor charge-transfer reactions. The lack of degradation is not surprising given the weakness of metal-ligand binding shown by the effects of ionic strength on adsorption. Redox reactions between ligand and metal oxide surfaces do not occur because the ligand is unable to out compete hydroxyl groups for metal coordination sites. The lack of hydrolysis reactions catalyzed by the surface is surprising given the low PZNPC of birnessite and therefore the high surface concentration of hydronium ions. Coordination of ligands with the metal surface cannot facilitate hydrolysis or charge-transfer reactions because ligand binding is weak with either birnessite or ferrihydrite.

**Metal-Ligand Binding**

The high concentration solution of aqueous Fe (III) quenches the fluorescence of all three compounds by collisional and coordinated metal quenching from pH 2.0 to approximately 2.8. None of the other metals influenced the fluorescence. Quenching of atrazine, picloram, and triclopyr above pH 2.8 is not observed in the presence of Fe (III) gels (Fig. 6), whereas salicylic acid remains quenched over the same pH range (2.8 to 5.4). At low Fe (III) concentrations, the triclopyr-iron stability constant was calculated (at 0.01 M ionic strength and pH 2.7 and 4.0) by fitting equation (1) to a plot of the fluorescence intensity versus the ratio of metal cation to ligand concentration using a nonlinear regression model (Fig. 7) and yielded values of $3.30 \times 10^4$ and $9.57 \times 10^3$ for pH 2.7 and 4.0 respectively (Saar and Weber, 1980).

Measures of atrazine and picloram stability constants failed due to the low intensity of fluorescence and insensitivity of the observed fluorescence peak to varying metal cation concentrations. The analogous fluorescence peak for triclopyr showed the same weak intensity but a higher sensitivity to metal-cation concentrations.

**Adsorption Modeling**

HYDRAQL modeling of picloram and triclopyr adsorption resulted in log $K^{int}$ values of: 4.7 and 6.8 for triclopyr outer-sphere and inner-sphere adsorption; and 5.4 and 6.7 for picloram outer-sphere and inner-sphere adsorption. The log $K^{int}$ value was varied until the model values gave the best fit for the adsorption edge of the compound. Fit of the model to picloram adsorption edge was excellent. The model was not able to match the slope of the triclopyr adsorption edge. HYDRAQL predictions overestimated picloram adsorption from pH 5.5 to

6.5 and underestimated very slightly at pH 7 and 5. HYDRAQL significantly underestimated triclopyr adsorption at pH 6 to 7 (greatest variation at pH 7, 6 versus 20%) and slightly overestimated adsorption at pH 4.5 to 5 (90 versus 100%).

Simulations run with varying ionic strength produced two sets of predictions based on the different adsorption mechanisms: inner-sphere and outer-sphere adsorption. Picloram and triclopyr adsorption onto ferrihydrite were affected by ionic strength assuming either mechanism of adsorption. The outer-sphere complexes were more susceptible to changes in ionic strength because adsorption in these cases occurs outside the sphere of hydration and the adsorbate is screened from the surface charge by the ion swarm (Sposito, 1984). Table 5 contains the observed values for percent decrease in adsorption for both herbicides as ionic strength increases from 0.01 to 1.0 M (corrections were made for an ionic strength greater than 0.5 M). The effect of ionic strength is more pronounced with the outer-sphere complex, and more herbicide is adsorbed. Model predictions for the effects of ionic strength agree well with measured values.

## Discussion

### Mineral Adsorption

Oxide mineral adsorption of weakly acidic/basic ligands occurrs between the PZNPC of the oxide (equal to the point of zero charge, PZC, if no permanent charge or contaminating ligands are complexed) and the $pK_a$ of the ligand (Schindler, 1990). Weber (1970) hypothesized that the adsorption maxima of organic ligands onto soil colloids occurs at or near the $pK_a$ of the ligand. The hypothesis is that at some pH the repulsive and attractive forces, either electrostatic or van der Waals or hydrogen bonding, maximize adsorption based on the degree of dissociation of the surface and the ligand. Adsorption of the four ligands in this study can be understood in this manner.

Atrazine Adsorption. Many researchers have attributed the mechanism of adsorption for atrazine to hydrogen bonding resulting from protonation of one of the substituted amine nitrogens, and have named the pH at which this very weak base protonates its $pK_a$ (Russel et al., 1968). The lone pair electrons on nitrogen can be shared to facilitate weak hydrogen bonding. Using NMR, Welhouse and Bleam (1993) demonstrated that hydrogen bonding is a significant binding mechanism for atrazine. We observed a change in atrazine adsorption with pH, such that adsorption increased onto a mineral with a negative charge (birnessite) with decreasing pH and decreased onto a mineral with a positive charge (ferrihydrite) with decreasing pH. Given that the $pK_a$ of atrazine is 1.68 (Plust et al., 1981), it is not surprising to find that its adsorption occurs at pH ranges where repulsive forces are minimized, and hydrogen bonding is enhanced. Given that atrazine is not positively charged at pH 5 to 2.5, it is surprising that adsorption onto ferrihydrite decreased, because hydrogen bonding would be expected to be more likely at lower pH where the surface has a high concentration of protons.

The adsorption concentrations of atrazine onto birnessite and ferrihydrite surfaces compare favorably to data compiled by other researchers using a variety of oxides (for example, Weber, 1970; Terce and Calvet, 1978; Borggaard and Streibig, 1988). Terce and Calvet (1978) showed that Al oxides are significant mineral adsorbents of atrazine, but significantly less efficient than Al hydroxy-montmorillonite. Borggaard and Streibig (1988) observed that Fe oxides extracted from soils are the most significant adsorbents of atrazine, but assumed that mineral adsorption is negligible. From the few data sets on oxide adsorption of atrazine, atrazine appears to adsorb weakly to oxides although Al hydroxy-montmorillonite and other smectites have a higher adsorptive capacity for atrazine (Laird et al., 1992). However, atrazine adsorption onto birnessite (BET surface area of 39.5 $m^2\ g^{-1}$ and adsorption of 78.5 $\mu mol\ kg^{-1}$), at pH 4.0, falls in the middle of the range observed by Laird et al. (1992) for a variety of smectites (BET surface areas ranging from ~10 to 190 $m^2\ kg^{-1}$). Ferrihydrite adsorption of atrazine (20.2 $\mu mol\ kg^{-1}$) falls in the lower quarter of the range for smectites. Given the prevalence of ferrihydrite coatings in many weathered forest and tropical soils, it may be a significant adsorbent of atrazine in organic matter-poor soils. Problems arise from the fact that atrazine binding to most mineral surfaces studied is completely reversible, and binding to ferrihydrite is extremely low at low pH. Therefore, mineral adsorption only weakly retards the movement of the herbicide in soils and sediments, depending on the moisture regime of the soil (Laird et al., 1992; Clay and Koskinen, 1990; Borggaard and Streibig, 1988).

Picloram and Triclopyr Adsorption. The adsorption of picloram and triclopyr follow similar trends because of their similarity in structure. Both acids dissociate in the same pH range as a result of their structural similarities, although triclopyr appears to have a $pK_a$ value that is approximately 3.0, whereas picloram has a value somewhere between 3.5 and 4.1 (Hamaker et al., 1968). Adsorption of both herbicides is controlled by hydrogen bonding and coulombic forces. Both herbicides adsorbed more easily onto ferrihydrite than birnessite in the 4 to 7 pH range. This might be attributed to the greater surface area of ferrihydrite, but is more likely a result of the difference in charge states of the two oxides and herbicides. Ferrihydrite has a predominantly positive charge in contrast with the strong negative charge on birnessite over the pH range studied (Table 1). Both herbicides are predominantly anionic over this pH range given their $pK_a$ values. They are therefore repelled by the birnessite surface above pH 4, and attracted to the ferrihydrite surface, because it has a predominantly positive surface charge between pH 4 and 7. But, because adsorption onto ferrihydrite reaches a maxima near the $pK_a$ of the herbicides, where the concentration of the anionic species is decreasing rapidly, adsorption appears to be controlled by hydrogen bonding rather than electrostatic forces.

Birnessite demonstrates the difference between picloram and triclopyr in that adsorption changes differently with pH for the two species. Picloram adsorption increases with decreasing pH much the same way atrazine adsorption increases. Triclopyr adsorption does change significantly. The presence of the positive charge on the amine group, and the decrease in the negative charge on the carboxylic group account for the difference in adsorption.

Torrents (1992) and Hamaker et al., (1968) have demonstrated that crystalline and poorly crystalline Al and Fe oxides adsorb high concentrations of picloram, and that oxide adsorption of picloram is strongly influenced by pH and ionic strength. Torrents (1992) found that crystalline Fe oxide adsorption of picloram is lower than that of poorly crystalline oxides, such as goethite and the partially amorphous oxide used in her study (surface areas of the two Fe oxides used by Torrents (1992) were 0.501 and 212.0 $m^2\ g^{-1}$). Despite having lower surface area, the Al oxide ($Al_2O_3$, 92.8 $m^2\ g^{-1}$) used by Torrents (1992) adsorbed higher concentrations of picloram than the Fe oxides studied. The differences in picloram adsorption onto different oxides demonstrate that surface area alone cannot account for greater adsorption. Even hydroxyl site densities on different oxides cannot account for the disparities in adsorption (Torrents, 1992). The extent of adsorption is most likely a result of the combination of surface area, $pK_a$ and PZNPC (coulombic forces due to oxide surface charge), hydroxyl site density, and steric hindrance in the organic ligand, making impossible simple determinations of what factor is dominant under varying conditions.

Desorption of picloram and triclopyr at constant pH (5.0) resulted in near complete release of the additional herbicide adsorbed. Very little hysteresis was observed for either of the herbicides, indicating that even at a pH where adsorption is high (4 to 5), the mechanism of adsorption is predominantly weak and reversible. Slope values for the desorption and adsorption isotherms were very similar and differences were insignificant. Hamaker et al., (1968) also observed complete removal of picloram from oxide-rich soils by altering the pH. McGrath and McColl (1993) also found that picloram and triclopyr desorb easily from soils rich in oxides and poor in organic matter, and that low concentrations of organic matter have little influence on the sorption of the two herbicides. These results imply that adsorption does not lead to long-term sequestration of the herbicides. Adsorption by oxides, although high at acid soil pH (4 to 5), only retards the mobility of picloram and triclopyr. Thus mobility depends on the hydraulic conductivity of the soil and the climatic moisture regime of the area.

The weak increase in adsorption with decreasing temperature implies that an exothermic process controls adsorption. Given the slight differences involved, it is difficult to determine if the observations are real or a consequence of measurement errors. Biggar and Cheung (1973) found that picloram adsorption was exothermic when they measured it onto two smectite-dominated soils. The differences they observed were much stronger and clearly pointed to an exothermic process. The adsorption models they proposed do not fit the weak change in energetics found for ferrihydrite.

## Soil Sorption of Herbicides

The purpose of this work was to determine the importance of sesquioxides on the adsorption of atrazine, picloram, and triclopyr. Huang et al. (1984) found that sesquioxides were the most important adsorbent fraction of atrazine in red weathered soils after organic matter. Borggaard and Streibig (1988) reported

that extracted iron oxides adsorbed very little atrazine, and used these observations to contradict the results in the Huang et al. (1984) study. The results of sorption onto the three different soils and the three different treatment types demonstrate clearly that the technique of sequentially extracting soil fractions and studying the properties of the residual is a particularly unsatisfactory technique. Many undesired chemical transformations occur druing chemical destruction of OM and DCB removal of oxides which convolute the results of sorption studies. Sequential additions of pure soil fractions into a mixture of pure oxides, clays, and organic matter are also unsatisfactory because the resulting mixture does not have the properties of a naturally formed soil of identical composition. Mineral and OM fractions are all separate particles that have not coprecipitated or coated each other as is commonly observed in oxide-rich soils. Therefore, neither technique is able to examine the role of the parts in sorption and explain the properties of the whole.

Based on the present results, picloram and tricloyr adsorption can be correlated with sesquioxide fractions in soils that have low OM concentrations. In every case, picloram and triclopyr adsorption decreased drastically after DCB-treatment. For a comprehensive discussion of the adsorption results with picloram and triclopyr see the 1992-93 Kearney Annual Report.

The results of atrazine adsorption onto minus OM soils is greater than that onto the minus Fe soils in two cases (W50 and W11, but not N25). The results therefore do not conclusively determine the role of sesquioxides in whole soils. Certainly pure mineral adsorption implies that the sesquioxide fraction is as important as many other mineral fractions when OM concentrations are low, but the increase in adsorption after OM removal has been observed frequently with a variety of different pesticides (Curtis et al., 1986). Two views of this process have been proposed: (1) humic material blocks sorption sites and is removed by oxidation, freeing mineral surfaces for adsorption; (2) oxidation preferentially destroys soluble organics which decrease the sorption intensity because the DOC binds the organic thus keeping it in solution. With our observations for atrazine, picloram, and triclopyr adsorption, both theories can apply for different cases. The best explanation of the effect OM removal has on adsorption is probably a combination of the two theories, depending on the amount of OM present in the soil. At low OM concentrations, surface coverage is probably the dominant factor, and at high OM concentrations soluble organics are probably important.

## Oxide-Catalyzed Degradation

Lack of direct degradation of the herbicides by oxide catalysis is indicative of the weak outer-sphere adsorption that occurs with both minerals. Oxide catalysis at the mineral surface requires increased surface concentrations to be effective. Only ferrihydrite adsorption of picloram and triclopyr and birnessite adsorption of aniline were significant enough that the surfaces could have acted as catalysts. HPLC analysis of aniline adsorption showed evidence of degradation (or polymerization) but more detailed analysis would be required to

quantify and determine the exact degredation products. HPLC analysis of picloram and triclopyr reactions showed no evidence of degradation.

The lack of hydrolysis reactions with triclopyr is surprising because Torrents and Stone (1994) have observed the hydrolysis of several different types of esters. The fact that triclopyr is an oxyacetic acid tricloropiridinol accounts for the difference in reactivity. Hydrolysis of an ester is much more energetically favored than hydrolysis of an ether group, even if it is adjacent to a carboxylic acid group. Mineral catalysis of hydrolysis may be possible at high pH, where $OH^-$ concentrations are much greater and nucleophilic substitution is enhanced. Reactions at high pH (above pH 8) are not pertinent to the soil systems being modeled and therefore were not studied.

Lack of atrazine hydrolysis is also surprising given that other acid minerals, such as smectites, have been shown to catalyze the formation of hydroxy atrazine (Russel et al., 1968). Birnessite, because it has a PZC of 1.7 to 1.5, is an excellent mineral for acid hydrolysis of atrazine. Adsorption of atrazine by birnessite is comparable to most smectites; therefore, surface concentration should not be the limiting factor in degradation. One problem may be that birnessite specifically adsorbs $K^+$ which may interefere with herbicide-surface interactions, or surface protonation. $K^+$ interference with degradation is unlikely, given that no hydrolysis is observed. It is more likely that acid hydrolysis is a slow reaction that is not sufficiently catalyzed by either birnessite or ferrihydrite because of other unforeseen factors which prevent activation of atrazine through protonation on the minerals' surfaces (Welhouse and Bleam, 1993).

The occurrence of solid-state degradation of 2,4-dichlorophenoxy acetic acid by birnessite to $CO_2$ demonstrates that oxidation reactions which result in complete, direct degradation of contaminants is possible (Cheney, Casey, and Sposito, in progress). The lack of degradation in aqueous systems for the same reaction implies that hydrating water prevents charge transfer reactions that are necessary to drive the reaction. The same reactions may be possible with other herbicides with similar structures, such as picloram and triclopyr, even though they are not formed from phenol.

**Metal-Ligand Binding**

The quenching effects of paramagnetic metal ions on the fluorescence of atrazine, picloram, and triclopyr were compared to the effect of metal ions on salicylic acid fluorescence at low and high metal concentrations and varying pH. Salicylic acid forms a strong complex with Fe (III), keeping Fe (III) in solution above pH 3.25, a pH at which Fe (III) forms complexes with hydroxyl groups, aggregating into stable gels. When Fe (III) concentrations are high (0.01 M) collisional quenching occurs, reducing the fluorescence of the herbicide. At pH 2.8 to 3.2, Fe (III) hydroxy gels begin to form, removing free Fe (III) ions from solution and reducing collisional quenching. If the organic ligand complexes the Fe (III) in solution and prevents Fe (III) hydroxide precipitation with rising pH, then the fluorescence of the complexed ligand remains quenched, thereby acting as an indicator of ligand strength. Because only salicylic acid was able to

complex Fe (III) under these conditions, all three herbicides can be considered weaker ligands than salicylic acid and the hydroxide ion. These results suggest that salicylic acid is more able to form an inner-sphere complex with Fe oxides than atrazine, picloram, and triclopyr at ambient soil pH.

Below pH 3, high metal ion concentrations allow for collisional quenching, indicating that quenching is not a result of coordination for compounds such as atrazine and picloram, which are not quenched by metal cation concentrations below $1.0 \times 10^{-4}$ M. Fluorescence from solutions of triclopyr with varying low Fe (III) concentration (~$1.0 \times 10^{-4}$ M) were partially quenched at pH 2.7 and 4.0 (Fig.7). Using the intensity versus metal cation concentration, we determined the metal-ligand stability constant for triclopyr complexes with Fe (III). A comparison of critical stability constants obtained for salicylic acid and picolinic acid (the parent structure of picloram and triclopyr) coordination with dissolved Fe (III) demonstrates that complexation is more stable for salicylic acid than picloram and triclopyr. The salicylic acid stability constant is only half an order of magnitude larger than that of triclopyr (log K = 4.52 and 4.97 for complexes of triclopyr and salicylic acid with Fe(III) respectively). Using first stability constants from the literature for salicylic acid at pH 2.0, salicylic acid data were plotted against the predicted points and the empirical and calculated data were in good agreement.

Changes in the triclopyr stability constant with pH demonstrate the difference in affinity between the protonated and unprotonated form of triclopyr to the free Fe (III) and the hydroxyl coordinated Fe (III). As pH approaches 4.0, the relative concentration of unprotonated triclopyr species increases to approximately 50% or greater, while Fe (III) goes from the free hydrated species (only water in coordination sites) to the hydroxyl coordinated species $Fe(OH)^{2+}$. Binding of triclopyr to Fe appears to be significantly affected by changes in pH as a result of changes in the coordination of Fe, as shown by the decrease in the stability constant determined using fluorescence (Fig. 7).

## Adsorption Modeling

A comparison of the HYDRAQL predictions with the experimental results revealed that the best model fit was with an outer-sphere complex assumption (Table 5). Torrents (1992) observed a decrease in picloram adsorption onto $Al_2O_3$ (from 30 to 8%) with increasing ionic strength, which the HYDRAQL model predicted for the outer-sphere complex. Torrents (1992) also observed that adsorption is strongly influenced by the type of metal in the oxide adsorbent and not the surface area or hydroxyl site densities. Therefore, despite the fact that adsorption is considered outer-sphere (because of the effect of ionic strength on sorption), metal cations in the oxides strongly influence the extent of sorption observed. As discussed earlier, many factors influence organic ligand adsorption (for example $pK_a$, PZNPC or oxide, stereochemistry of the compound); therefore the effect of the metal cation influencing the extent of adsorption is difficult to isolate and study.

Measurements of triclopyr fluorescence quenching at low Fe(III) concentrations resulted in log $K^{int}$ values (4.52 to 3.95) that are within an order of magnitude for the fitting constant of model predicted outer-sphere adsorption (4.7), and greater than an order of magnitude for inner-sphere adsorption (6.8). Similarities in the values are expected given that metal-ligand stability constants are measures of the attractive forces between metals and ligands, which are the same attractive forces responsible for adsorption, although surface reactions have steric hindrance and structural rigidity that can inhibit binding. Difficulties arise in comparing model-predicted, stability constant values with measured values because models depend on many parameters and assumptions that may not be verifiable or true in the system under study. Most studies fit HYDRAQL simulations to adsorption of metal cations onto oxides - - measurements which obviously have no correlation to metal-ligand stability constants (Papelis et al., 1990). Therefore, the accuracy of the log $K^{int}$ values predicted by the HYDRAQL model (assuming inner-or outer-sphere adsorption) and fluorescence quenching (resulting from dissolved metal-ligand inner-sphere binding) need to be verified using a series of additional fluorescent ligands and paramagnetic metals/oxides.

## Conclusions

(1) Ferrihydrite is an extremely important sorbent of carboxylic acid herbicides such as picloram and triclopyr, but a poor sorbent of weak bases, such as atrazine. Moderately strong bases, such as aniline, adsorb well onto ferrihydrite, despite the positive surface charge at ambient soil pH. Birnessite is not a significant adsorbent of atrazine, picloram, or triclopyr, but is comparable to smectites in the adsorption of atrazine. The observation by Huang et al., (1984), that sesquioxides are important in the adsorption of atrazine, was not observed with pure Fe or Mn oxides over the 4 to 7 pH range but was true for both aromatic carboxylic acids.

(2) The adsorbates formed outer-sphere complexes with the oxide surfaces. Phenomena indicative of this outer-sphere adsorption were the following: the effect of ionic strength; the effect of pH on fluorescence quenching; the ease of desorption at constant pH; the rapid kinetics of atrazine, picloram, and triclopyr adsorption which are typical of ion swarm kinetics; and the lack of charge-transfer reactions. Given the mechanism of adsorption, the lack of degradation due to charge-transfer reactions was predictable.

(3) pH appears to have a strong effect on triclopyr stability constants with aqueous Fe (III). Hydroxyl groups appear to out-compete triclopyr for coordination sites on Fe (III) and diminish the apparent Fe charge felt by triclopyr molecules, thus preventing coordination.

(4) Soil adsorption of picloram and triclopyr can be correlated with oxide adsorption, but increases in atrazine adsorption after soil treatment appear to be due to artifacts of treatment or due to decreased interference from OM.

(5) Using fluorescence quenching to measure ligand-metal stability constants is a technique for predicting adsorption constants for modeling that has great potential.

(6) Birnessite and ferrihydrite have very little effect on the stability of the herbicides atrazine, picloram, and triclopyr. Further studies with solid-state reactions may prove to result in greater degradation.

(7) We conclude that Fe, Al, and Mn oxides only weakly adsorb atrazine and would only be important in soils with extremely low concentrations of organic matter. Highly weathered forest and tropical soils are likely to be susceptible to rapid movement of atrazine through profiles due to the reversibility and low affinity of atrazine for oxide mineral surfaces. Lack of abiotic degradation on oxides suggests that atrazine has a long half-life in weathered soils low in organic matter.

Picloram and triclopyr adsorb readily onto Al and Fe oxide minerals, but poorly onto acid minerals such as birnessite, at ambient pH (4 to 7). Their high $K_f$ values on Al and Fe oxides indicate that picloram and triclopyr adsorption may be retarded in highly weathered forest and tropical soils. The reversibility of adsorption and lack of abiotic degradation could result in long half-lives and significant mobility despite high adsorption of picloram and triclopyr.

## References


Biggar, J. W. and M. W. Cheung. 1973. Adsorption of picloram (4-amino-3,5,6-trichloropicolinic acid) on Panoche, Ephrata, and Palouse soils: A thermodynamic approach to the adsorption mechanism. Soil Sci. Soc. Amer. Proc. 37:863-868.

Borggaard, O. K. and J. C. Streibig. 1988. Atrazine adsorption by some soil samples in relation to their constituents. Acta Agric. Scand. 38:293-301.

Clay, S. A. and W. C. Koskinen. 1990. Characterization of alachlor and atrazine desorption from soils. Weed Sci. 38:74-80.

Curtis, G. P., M. Reinhard and P. V. Roberts. 1986. Sorption of hydrophobic organic compounds by sediments. p. 191-216. *In* J. A. D. a. K. F. Hayes. (ed.). Geochemical processes at mineral surfaces. Amer. Chem. Soc. Symp. Ser., NY.

Davis, J. A. and J. O. Leckie. 1978. Surface ionization and complexation at the oxide/water interface. II. Surface properties of amorphous iron oxyhydroxide and adsorption of metal ions. J. Colloid Inter. Sci. 67:90-98.

Hamaker, J. W., C. A. Goring and C. R. Youngson. 1968. Sorption and leaching of 4-amino-3,5,6-trichloropicolinic acid in soils. p. 23-37. *In* Organic pesticides in the environment. Amer. Chem. Soc., Washington D.C.

Huang, P. M., R. Grover and R. B. McKercher. 1984. Components and particle size fractions involved in atrazine adsorption by soils. Soil Sci. 138:20-24.

Laird, D. A., E. Barriuo, R. H. Dowdy and W. C. Koskinen. 1992. Adsorption of atrazine on Smectites. J. Soil Sci. Soc. Amer. 56:62-67.

McGrath, A. E. and J. G. McColl. 1993. Sorption thermodynamics of polar contaminants by ferrihydrite and forest soils. *In* (ed.), Agronomy Society of America. p. 47.

Papelis, C., K. F. Hayes and J. O. Leckie. 1988. HYDRAQL: A program for the computation of chemical equilibrium composition of aqueous batch systems including surface-complexation modeling of ion adsorption at the oxide/solution interface. Stanford University. p. 180.

Papelis, C. M. and J. O. Leckie. 1990. Modeling heavy metal adsorption onto ferric oxides. Technical Report. Stanford University. p. 235.

Plust, S. J., J. R. Loehe, F. J. Feher, J. H. Benedict and H. F. Herbrandson. 1981. Kinetics and mechanism of hydrolysis of chloro-1,3,5-triazines. Atrazine. J. Org. Chem. 46:3661-3665.

Russel, J. D., M. Cruz and J. L. White. 1968. Mode of chemical degradation of s-triazines by montmorillonite. Sci. 160:1340-1342.

Ryan, D. K. and J. H. Weber. 1982. Fluorescence quenching titration for determination of complexing capacities and stability constants of fulvic acid. Anal. Chem. 54:986-990.

Saar, R. A. and J. H. Weber. 1980. Comparison of spectrofluorometry and ion-selective electrode potentiometric for determination of complexes between fulvic acid and heavy-metal ions. Anal. Chem. 52:2095-2100.

Schindler, P. W. 1990. Coadsorption of metal ions and organic ligands: Formation of ternary surface complexes. p. *In* M. Hochella and A. F. White (ed.). Mineral-Water Interface Geochemistry. Mineralogical Society of America, NY.

Sparks, D. L. 1988. Kinetics of soil chemical processes. Academic Press, New York. p. 238.

Sposito, G. 1984. The surface chemistry of soils. Oxford University Press, NY. p. 245.

Terce, M. and R. Calvet. 1978. Adsorption of several herbicides by montmorillonite, kaolinite, and illite clays. Chemosphere 4:365-370.

Torrents, A. 1992. Hydrolysis of organic esters at the mineral/water interface. Ph.D. Johns Hopkins University. p. 310.

Torrents, A. and A. T. Stone. 1994. Oxide surface catalyzed hydrolysis of carboxylate esters and phosphorothioate esters. Soil Sci. Soc. Am. J. 58:738-745.

Weber, J. B. 1970. Adsorption of s-triazines by montmorillonite as a function of pH and molecular structure. Soil Sci. Soc. Amer. Proc. 34:401-404.

Welhouse and Bleam. 1993. Hydrogen bonding of atrazine measured by NMR. Environ. Sci. Tech.. 27:243-250.

Yates, D. E. 1975. The structure of the oxide/aqueous electrolyte interface. Ph.D. Thesis. University of Melbourne, Australia.

Table 1. Herbicide physical properties

| Property | Atrazine | Picloram | Triclopyr |
|---|---|---|---|
| Solubility $H_2O$ (g $m^{-3}$) | 33 | 430 | 430 |
| Vapor Pressure (Pascal) $10^{-8}$ | 4.0 | 8.1 | 16.7 |
| M.P. (°C) | 173-175 | N/A§ | 117 |
| $pK_a$† | 1.68 | 4.1 | 3.5 |
| $K_{ow}$ | 212-216 | 2.0 | N/A |

From: Herbicide Handbook Committee, Herbicide Handbook of the Weed Science Society of America (1989)
† - Data from Dow-Elanco and Ciba-Geigy.
§- Data not available.

Table 2. Mineral physical properties

| Metal Oxide | PZNPC -log[$H^+$] | BET Surface Area $m^2\ kg^{-1}$ |
|---|---|---|
| Birnessite | 2.2 | $3.96 \times 10^4$ |
| Ferrihydrite | 8.4 | $2.63 \times 10^5$ |

Table 3: Chemical Properties of Soils

| Soil Treatment | Organic Matter % | DCB[1] Extr. Fe (mmol $kg^{-1}$) | DCB Extr. Mn (mmol $kg^{-1}$) | Oxalate Extr. Fe (mmol $kg^{-1}$) | pH (-log[$H^+$]) |
|---|---|---|---|---|---|
| New York Flats 25cm | 3.63 | | | 29.2 | 5.6 |
| minus OM | 1.24 | 1100.0 | 3.6 | 23.3 | 5.2 |
| minus Fe | 0.69 | 0.0 | 0.0 | 0.0 | 5.9 |
| Whitmore 11cm | 0.76 | | | 53.5 | 5.3 |
| minus OM | 0.38 | 1189.0 | 3.6 | 40.9 | 5.6 |
| minus Fe | 0.11 | 0.0 | 0.0 | 0.0 | 5.8 |
| Whitmore 50cm | 0.38 | | | 35.8 | 5.4 |
| minus OM | 0.12 | 970.0 | 2.5 | 35.46 | 5.6 |
| minus Fe | 0.12 | 0.0 | 0.0 | 0.0 | 5.9 |

[1]DCB = dithionitrite-citrate-bicarbonate buffer

Table 4. Constants for herbicide adsorption onto birnessite and ferrihydrite

| Oxide | pH | Atrazine $K_f$ $mmol^{1-1/n}\ m^{3/n}\ kg^{-1}$ | 1/n | Picloram Slope $m^3\ kg^{-1}$ | Triclopyr Slope $m^3\ kg^{-1}$ |
|---|---|---|---|---|---|
| Birnessite | 4 | $1.30 \times 10^{-2}$ | 0.46 | 0.0015 | 0.0013 |
| | 5 | $8.89 \times 10^{-4}$ | 0.92 | 0.0010 | 0.0008 |
| | 6 | $3.51 \times 10^{-4}$ | 1.08 | 0.00025 | 0.0005 |
| | 7 | N/A† | N/A | N/A | N/A |
| Ferrihydrite | 4 | N/A | N/A | 0.436 | 1.178 |
| | 5 | $3.59 \times 10^{-4}$ | 0.99 | 0.385 | 0.309 |
| | 6 | $1.19 \times 10^{-4}$ | 1.08 | 0.023 | 0.063 |
| | 7 | $8.26 \times 10^{-4}$ | 0.84 | 0.008 | 0.015 |

†- Data not available.

Table 5. Effect of ionic strength to adsorption onto ferrihydrite at pH 5

| Ionic Strength (M) | Picloram Empirical | Picloram Model Inner-sphere | Picloram Model Outer-sphere | Triclopyr Empirical | Triclopyr Model Inner-sphere | Triclopyr Model Outer-sphere |
|---|---|---|---|---|---|---|
| | <---------- | ---------- | (% sorbed) | ---------- | ---------- | ----------> |
| 1.0 | 8.1 | 65.8† | 9.0† | 7.2 | 65.0† | 27.8† |
| 0.10 | 15.5 | 71.9 | 25.6 | 15.6 | 68.3 | 60.1 |
| 0.010 | 33.7 | 73.2 | 44.0 | 30.7 | 90.0 | 77.5 |

† - Ionic strength and activity coefficients corrected for high concentration.

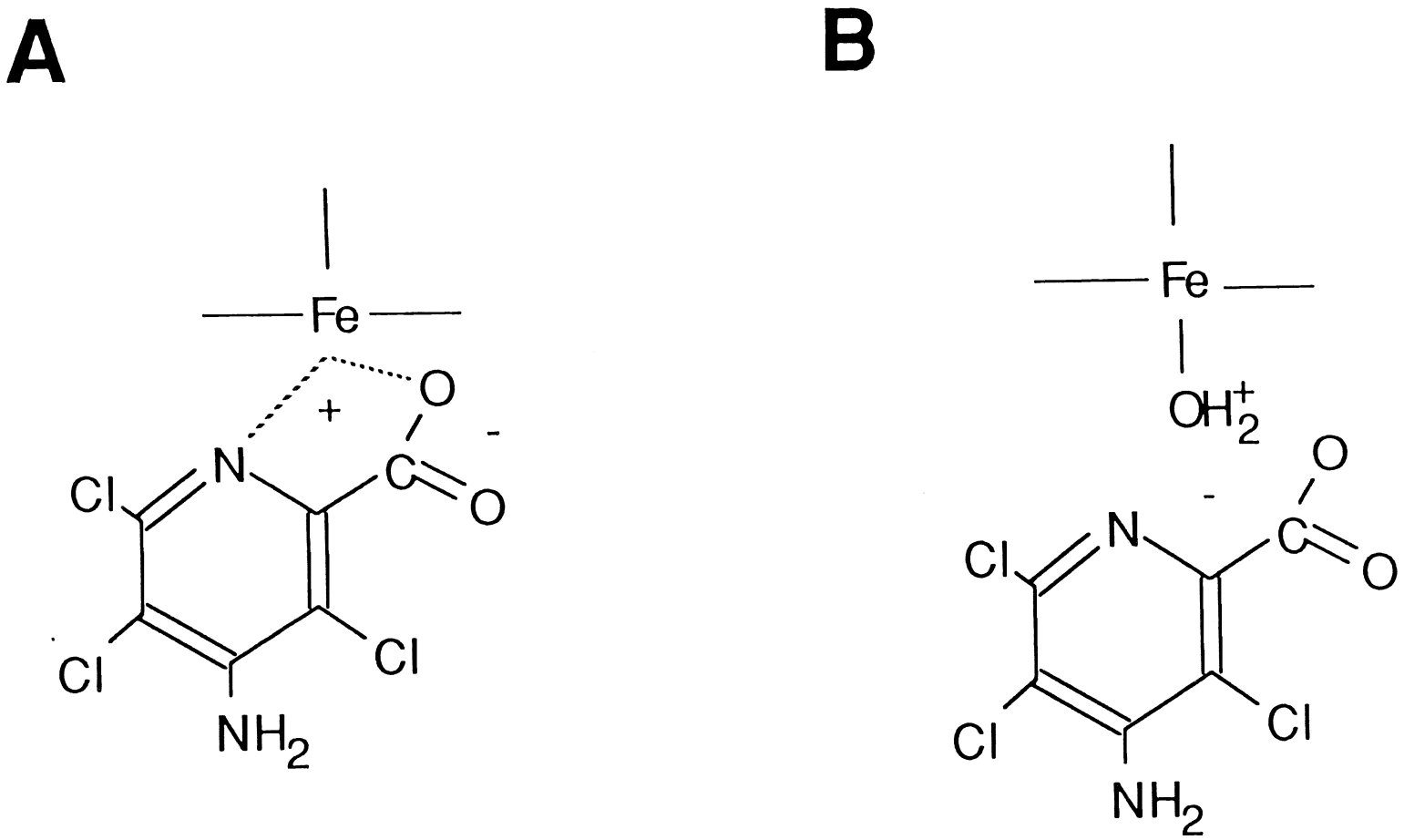


Figure 1. Mechanisms of adsorption for picloram and triclopyr onto ferrihydrite. A. inner-sphere complexation; B. outer-sphere complexation.

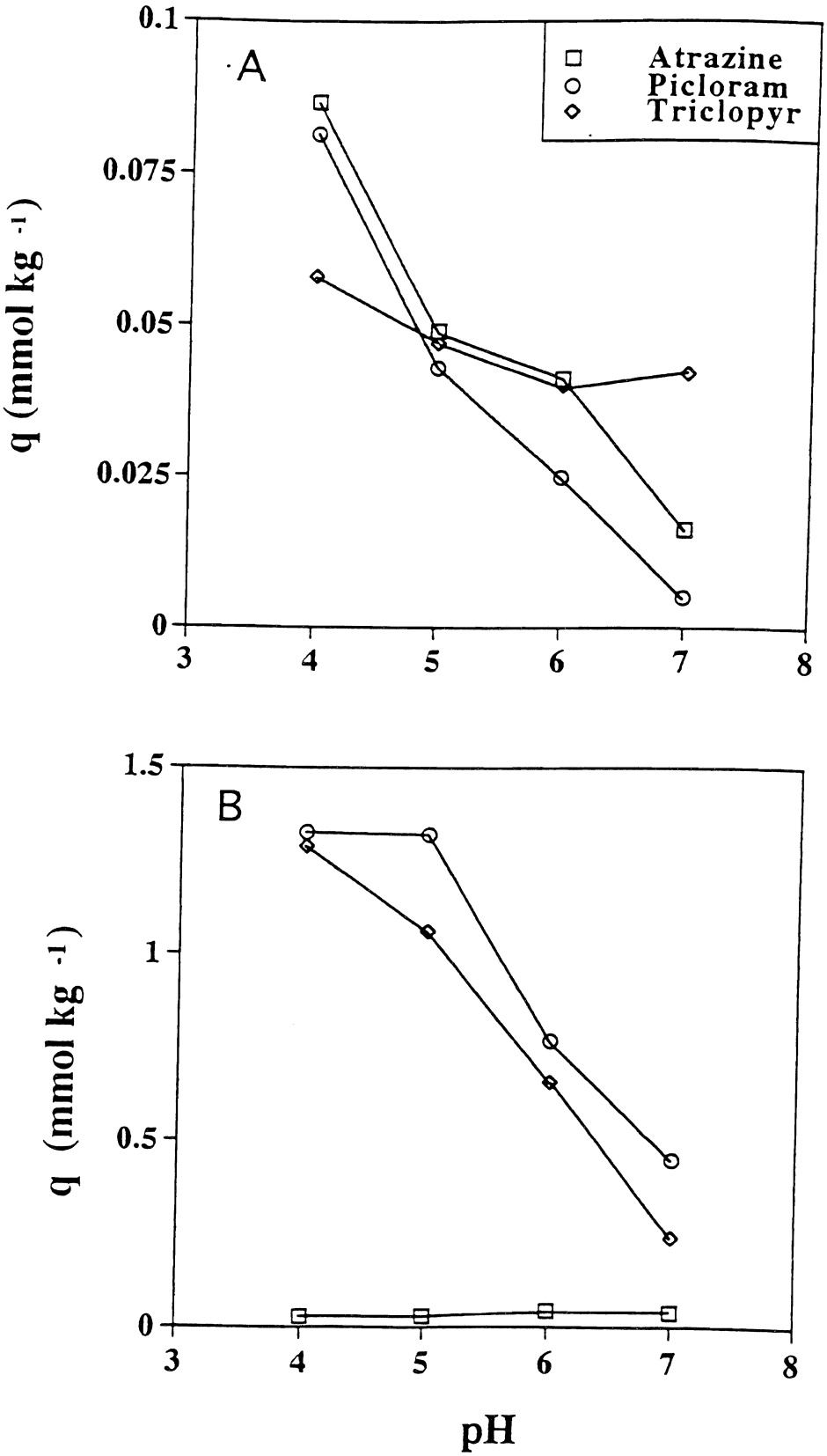


Figure 2. Adsorption edge of atrazine, picloram, and triclopyr onto A. birnessite and B. ferrihydrite from pH 4 to 7.

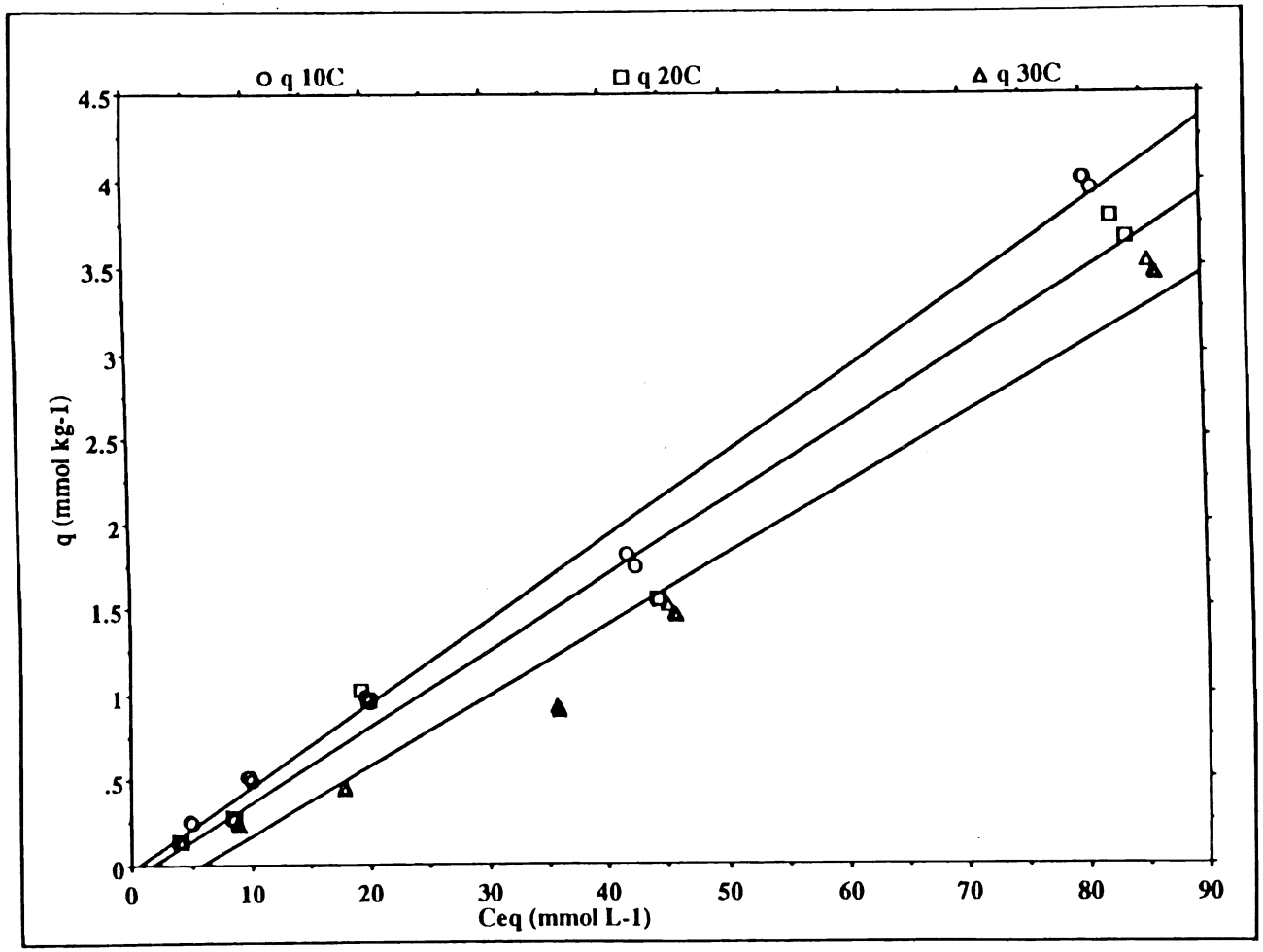


Figure 3. Adsorption of triclopyr onto ferrihydrite with changing temperature and constant pH (5.0).

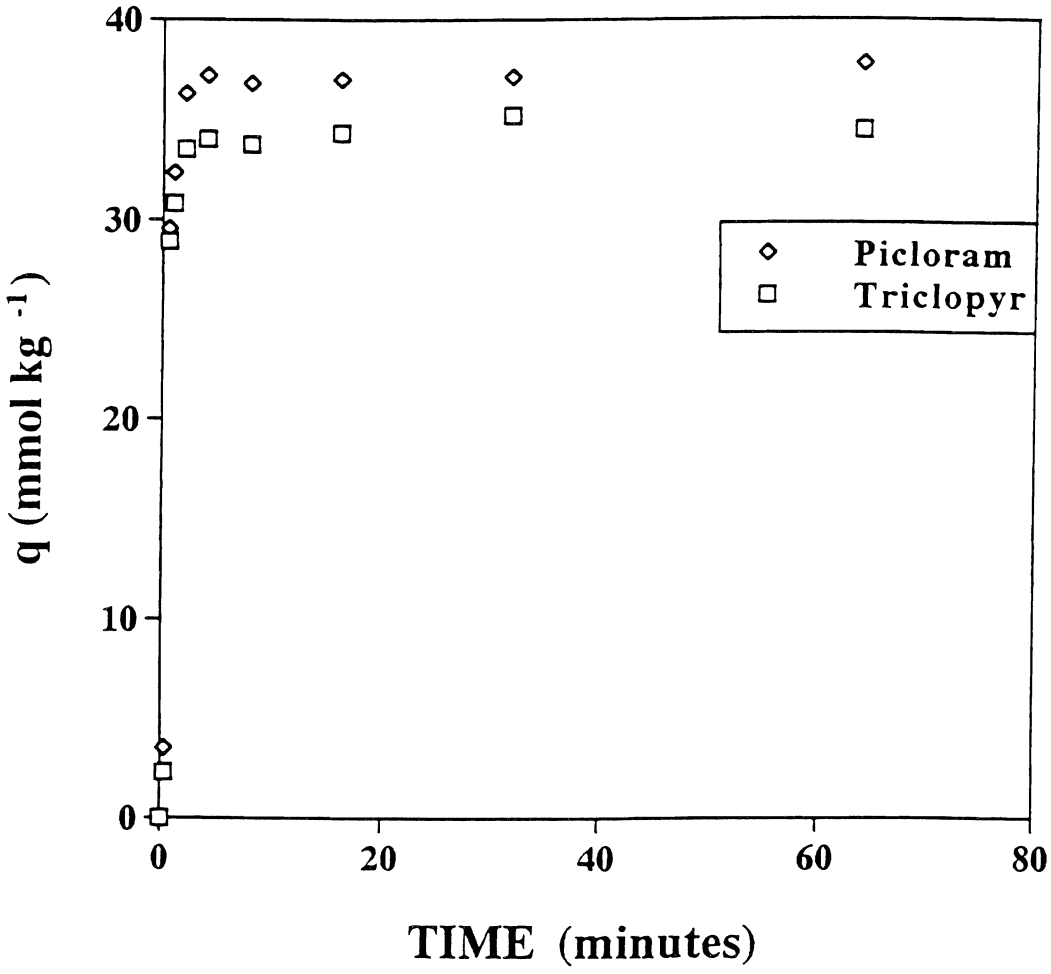


Figure 4. Kinetics of picloram and triclopyr adsorption onto ferrihydrite at pH 5.0 and 20°C.

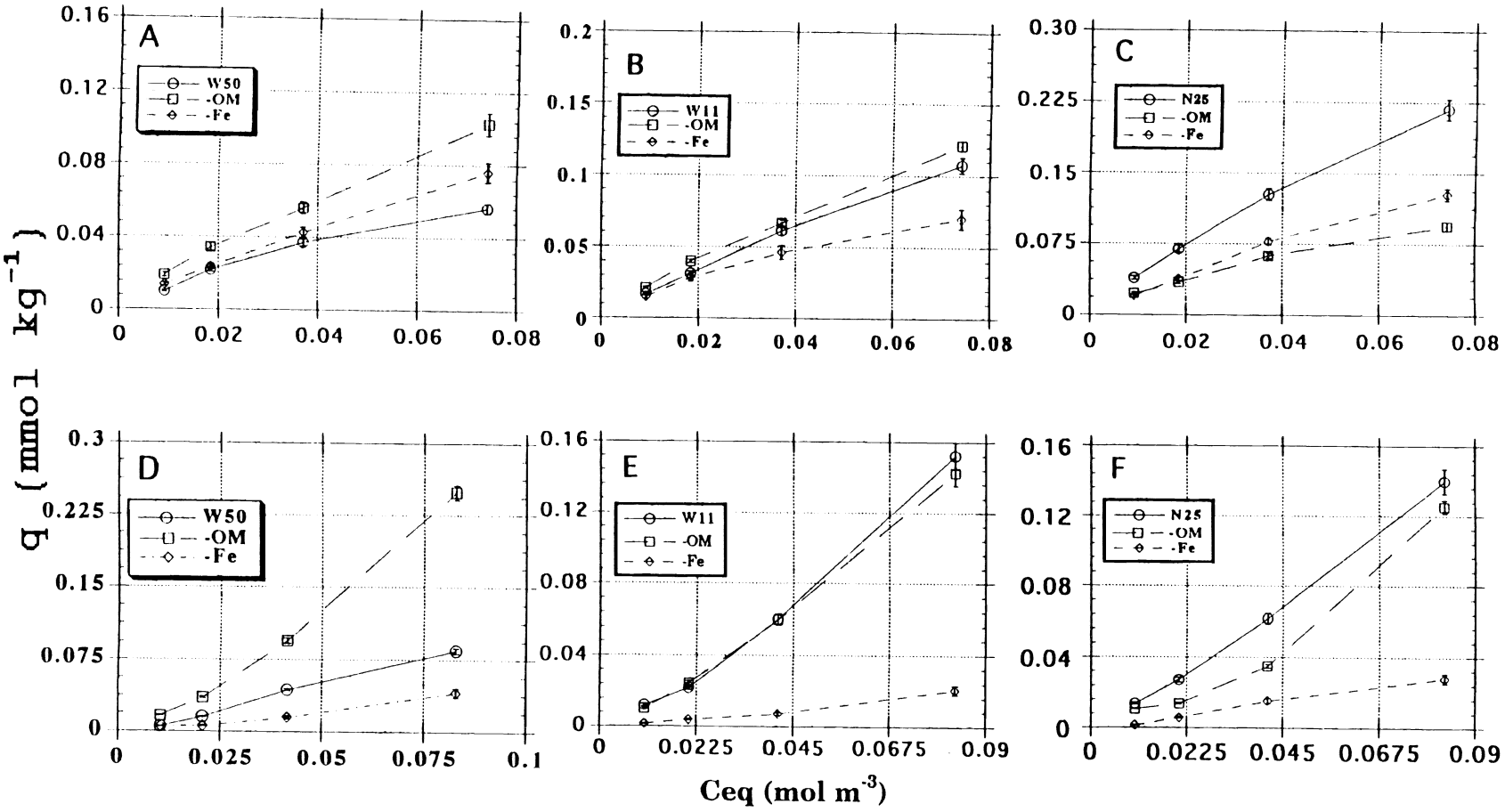


Figure 5. Sorption of atrazine (A, B, and C) and picloram (D, E, and F) onto Whitmore 50 and 11 cm, and New York Flats soils, respectively.

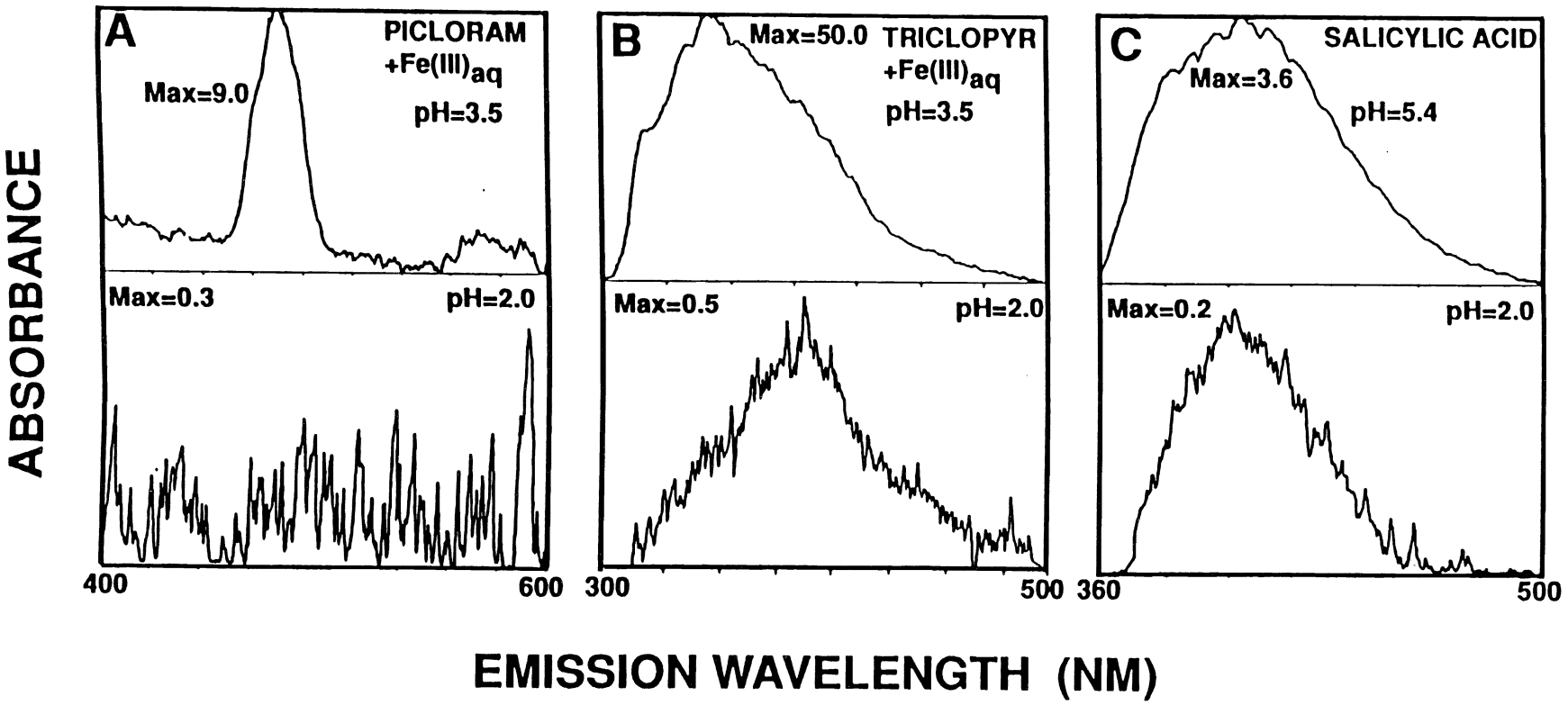


Figure 6. Effects of pH on fluorescence for picloram, triclopyr and salicylic acid (A, B, and C, respectively) with low pH in the bottom frame and high pH in the upper frame, in the presence of Fe (III).

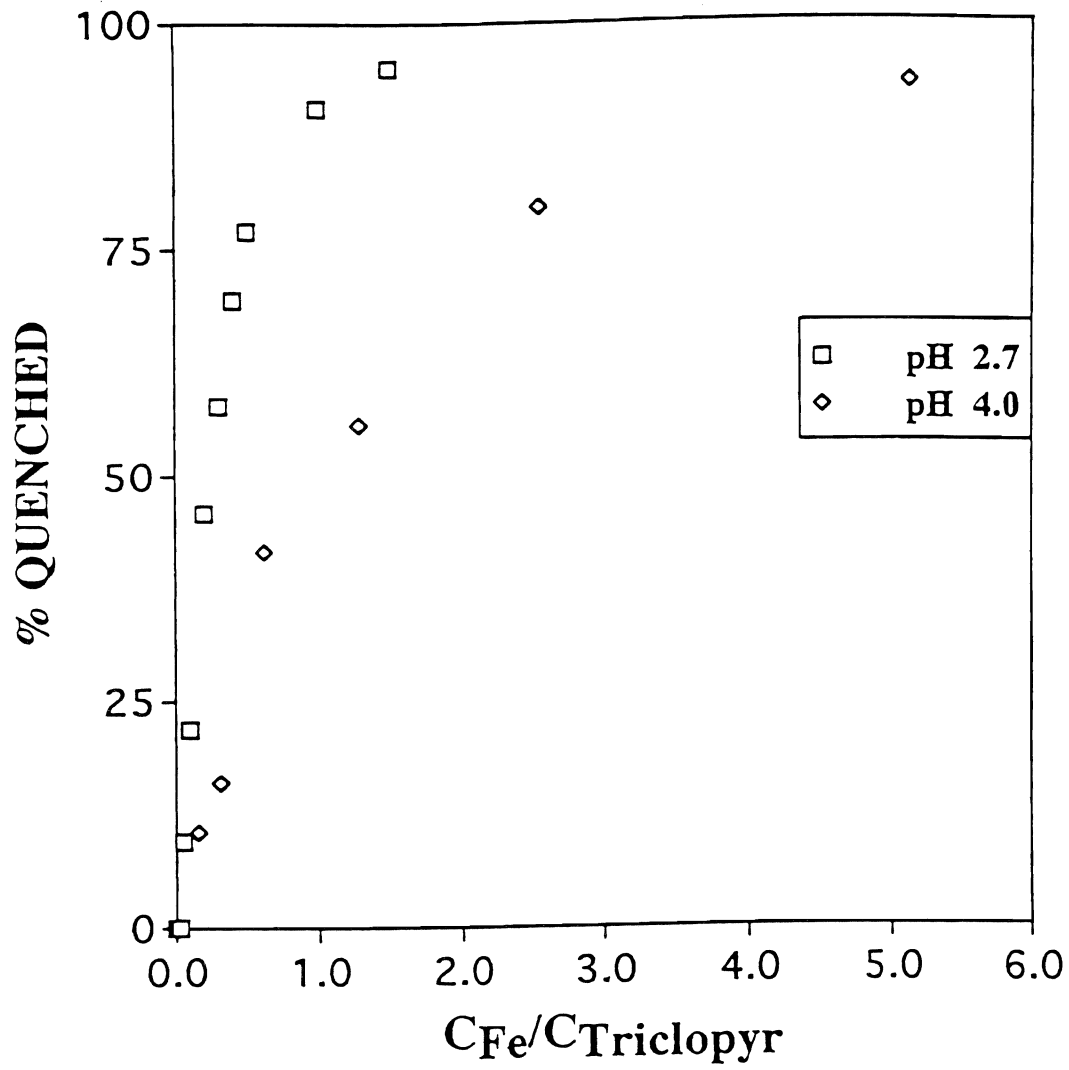


Figure 7. Titration curves of percent fluorescence quenched versus Fe (III)/triclopyr concentration ratio at pH 2.7 and 4.0.

# Pesticide Transport Via a Soil Particulate Carrier Mechanism and Interactions with Polymers

J. LETEY AND W. J. FARMER
*Department of Soil and Environmental Sciences, Riverside Campus*

## Summary

Transport of napropamide was studied in disturbed columns of Hanford sandy loam, Domino sandy clay loam, and Tujunga loamy sand. Carbon-14 labeled napropamide solution was applied to the soil surface and then subjected to simulated rainfall. Experimental conditions were designed to prevent mineral particulate transport through the soil column. Napropamide was measured in the initial leachate, and the concentration decreased gradually with cumulative leaching. No preferential flow occurred in the disturbed columns. The leachate had a yellow-orange color, possibly associated with dissolved organic matter (DOM), and the discoloration reduced gradually with cumulative leaching. The presence of napropamide in the leachate was confirmed by gas chromatography analysis. We speculate that napropamide transport was in association with DOM. During the course of this study, we identified some potential shortcomings of the standard procedures for measuring pesticide concentration in leachates. Whatever components of the soil system that were responsible for the mediated transport of napropamide appeared to interfere with napropamide detection. This requires further investigation. An additional study was conducted to determine whether soil erosion contributes to pesticide transport by furrow irrigation. Results indicate that fine particulates in the runoff can enhance the transport of pesticides from the field. Use of polymers or other means of reducing erosion should be effective in decreasing pesticide transport in the field.

**Key Words:** napropamide, dissolved organic matter, leachate, erosion

## Project Objectives Addressed in 1993-94

1. Evaluate the migration of pesticide through soil via a clay carrier mechanism for various soil characteristics and water qualities.
2. Evaluate the surface transport of pesticides by particulate movement in furrow irrigation with and without polymer treatment.

## Objective 1

### Research Plan and Procedures

Based on current knowledge, rapid and deep flow of pesticides in the vadose zone may be attributed to preferential flow of water via macropores. The same phenomena may be the result of transport of soil particulates or DOM to which pesticides are adsorbed. The objective of this study was to evaluate the transport of a pesticide through soil via a carrier mechanism. The study followed a 3-phase evolutionary process whereby the detailed experimental design of succeeding phases was predicated on the results of earlier phases. For clarity of communication, the experimental details and results of each phase will be reported separately followed by overall conclusions.

**Phase One Study**. The goal during the first phase was to create particulate transport through a soil column and to determine whether the particulate transport facilitated the movement of a pesticide. All studies were conducted in the laboratory on sieved soils packed 150 mm deep in plexiglass columns 76 mm in diameter. A funnel with a sharp rim 67 mm in diameter was placed in the column with its stem protruding through the enclosed bottom. The space between the column wall and the conical part of the funnel was filled with coarse sand. An outlet was drilled into the column bottom to release water flowing along the column wall. A perforated plexiglass plate was placed 3 mm below the funnel rim. A 0.5-mm mesh screen was placed over the perforated plate to retain soil. The leachate through the central portion of the soil column was collected through the funnel stem, while the leachate along the wall was collected through the outlet in the column bottom.

Hanford sandy loam was used in phase one (see Table 1 for some soil properties). Soils were collected from the 0-15 cm layer, air-dried, and sieved through a 1-mm screen. The sieved soil was poured into the column while tapping on the column walls to create a resultant bulk density of 1.5 g $cm^{-3}$.

Carbon-14 labeled napropamide [2-α-naphthoxy-N,N-diethylpropionamide] was the pesticide investigated. Unlabeled napropamide was mixed with $^{14}C$-labeled napropamide in 20 ml acetone to produce a $^{12}C$:$^{14}C$ ratio of 130:1. This solution was sprayed on 215 g of soil in a flask which was frequently rotated to wet the soil evenly. The flask containing the acetone-napropamide mixture was rinsed with 20 ml acetone four times and the rinsate was also sprayed on the soil. The soil was then allowed to dry for 24 h in the hood and was turned several times during the day. A 1-cm thick layer of

napropamide-treated soil was placed over untreated soil in the experimental column. The treated layer was covered with approximately 0.5 cm of untreated soil to reduce $^{14}C$ activity in the runoff water.

Distilled water applied through a rainfall simulator was used to facilitate development of fine particulates which could be transported through the soil column. The rainfall simulator delivered water from hypodermic needles in a manner to prevent drops from continuously hitting the same spot. The simulated rain intensity was 33 mm $h^{-1}$. Loss of soil by splash from the column was prevented by extending the column walls 30 cm above the soil surface. An outlet hole and tube were used to collect runoff and prevent ponding on the soil surface. Leachates were periodically collected. The leachates were shaken and a 1-ml sample was placed in Budget Solve cocktail and the C-14 activity measured in a Beckman LS5000 TD liquid scintillation counter. The remaining leachate was centrifuged, the supernatant poured off, and the solid particulates dried and weighed.

Twenty-four hours after termination of the experiment, samples were taken from the soil column at 20-mm intervals. Samples were removed through holes that had been drilled in the column wall for this purpose. The $^{14}C$ activity was measured on soil samples collected at each depth. The experiment was repeated three times.

**Results of Phase One Study.** The concentrations of napropamide and soil particulates in the leachate are plotted as a function of cumulative leachate in Figs. 1 and 2, respectively. Both the napropamide and soil particulate concentrations were highest in the initial leachate and decreased with increasing leachate volume. The distribution of napropamide in the soil column is illustrated in Fig. 3. Note that napropamide had been leached downward in the soil column, but it had not reached the bottom of the column.

The presence of both particulates and napropamide in the initial leachate suggests that the soil particulates served as a carrier for the adsorbed napropamide. This hypothesis is further supported by the concentrations of both napropamide and soil particulates decreasing with additional leachate. The conclusion from the phase one study was that soil particulates served as a carrier for napropamide transport through the soil column.

**Phase Two Study.** The next set of experiments was designed to get supporting evidence of the soil particulate carrier hypothesis. In this case, the experiments were designed to prevent soil particulate flow through the column and presumably prevent the early breakthrough of napropamide in the leachate.

In this case, the study was extended to include Domino sandy clay loam and Tujunga loamy sand, as well as Hanford sandy loam (see Table 1 for some characteristics of these soils). The air-dried soils were sieved and packed in the same columns as described in Phase One. The resultant bulk densities were 1.4 g $cm^{-3}$ for Domino and 1.3 g $cm^{-3}$ for Tujunga soil. These soil columns

were initially leached with Riverside, California, tap water prior to addition of napropamide. The initial leachings were to remove particulates and were continued until the leachate was clear. The soil columns were then allowed to dry in an oven at 45°C until they reached the initial weight after packing with air-dried material. No cracking or pulling away from the cylinder wall was observed following drying.

Carbon-14 labeled and nonlabeled napropamide were mixed in a ratio of 1:80 to a total concentration of 600 mg $L^{-1}$ by dissolving the napropamide in a small amount of acetone and mixing with water. The napropamide solution was then dripped over the soil surface to create an equivalent application of 8 kg $ha^{-1}$. The acetone and water were then allowed to evaporate in a hood for 24 h.

The same procedures were used as in Phase One except steps were taken to mitigate particulate formation. A fiberglass screen was placed just above the soil surface to intercept the raindrops and dissipate the energy. Also, NaCl and $CaCl_2$ were added to tap water to create a water having an electrical conductivity of 1 dS $m^{-1}$ and a sodium adsorption ratio of 2. The more saline water was to promote flocculation rather than dispersion. The experiment was replicated three times for each soil.

**Results of Phase Two Study**. The procedure to eliminate particulate transfer through the column was successful and no particulates were observed in the leachate. The leachate, however, was discolored and the intensity of the discoloration was observed to decrease with increasing volume of leachate.

Relationships between the napropamide concentration in the leachate and the cumulative leachate volume are presented in Fig. 4 for the three soils. Note that the concentrations were highest in the initial leachate and decreased with increasing leachate volume.

The distribution of $^{14}C$ in the Hanford sandy loam soil column (data not presented) was about the same as depicted in Fig. 3 for the Phase One Study. The downward movement of $^{14}C$ activity in the Tujunga soil was slightly less than the Hanford and the least amount of movement occurred in the Domino soil.

The results of the PhaseTwo Study were perplexing. The same pattern of $^{14}C$ distribution in the leachate was observed with and without solid particulates (Figs. 1 and 4). The leachate discoloration indicated the presence of soluble organic matter or other colloidal material which may have facilitated the rapid transport of napropamide through the soil column. Another possibility was the presence of $^{14}C$ labeled impurities which were water-soluble and not adsorbed to the soil. The Phase Three Study was undertaken to investigate this possibility.

**Phase Three Study**. The company supplying the $^{14}C$-labeled napropamide indicated the sample was 99% napropamide with approximately 1% being other chemicals. The labeled material was analyzed through gas chromatography and found to be 99% pure, thus verifying that no degradation had occurred. Nevertheless, the fraction of $^{14}C$ coming through the soil column in the leachate was very low and could have been the result of a small fraction of water-soluble $^{14}C$ labeled impurities.

The $^{14}C$ napropamide in hexane was extracted with water. Only the material in the hexane was used for the phase three experiments. The water-soluble impurities in the water phase were discarded. Additionally, the leachates from the experimental columns were analyzed for napropamide concentration by gas chromatography (GC) as well as $^{14}C$ analysis. Except for using the "purified" napropamide application of distilled rain water and GC analysis of leachate, the experimental conditions of Phase Three were identical to Phase Two. In Phase Three, the napropamide was applied to the soil columns in hexane rather than in aqueous solution and the hexane evaporated.

**Results of Phase Three Study**. The napropamide concentration in the leachate as determined by $^{14}C$ analysis is plotted as a function of cumulative leachate in Fig. 5 for the Phase Three Study. Napropamide was detected in the initial leachate and the concentration tended to decrease with additional leaching. The results from the Phase Three Study were similar to the Phase Two Study except that the concentrations in the leachate were somewhat higher under Phase Three. For Phase Three, the amount of napropamide in the leachate as determined by $^{14}C$ analysis was 1.4, 1.1, and 5.7% of that applied to Hanford, Domino, and Tujunga soils, respectively. Presence of napropamide in the leachate was verified by GC analysis. Therefore, the presence of $^{14}C$ in initial as well as subsequent leachates is not the result of $^{14}C$ labeled impurities or degradation products.

No solid particulates were observed in the Phase Three leachate. However, the leachate had a yellow-orange discoloration. We assume that the transport of napropamide in our studies may be attributed to the effect of DOM on napropamide mobility, and that the gradual decrease in napropamide concentration with cumulative leachate is consistent with the gradual decrease in leachate discoloration.

## Discussion

Napropamide was found in the initial leachate of every experiment we conducted. These results cannot be explained on the basis of preferential flow, whereby some of the water flows rapidly through large pores or channels. The wetting front observed through the plexiglass container walls advanced uniformly through the column. Preferential flow along the column walls was not observed either visually or by the funnel technique for collecting leachate at the bottom. Preferential flow can occur in the field and preferential flow can

contribute to relatively rapid, deep movement of low concentrations of pesticides. However, our results indicate that preferential flow is not necessary to create the commonly-observed field phenomena. Dissolved organic matter and possibly mineral particulates with which the pesticide is associated can serve as a carrier, creating transport that is inconsistent with transport theory that does not include the carrier mechanism.

## Objective 2

Several studies have been reported on the amount of pesticide in runoff from fields. Investigators who separated the sediment from the runoff water and then analyzed the pesticide associated with each phase typically found higher concentrations of pesticide in the sediment than in the water. However, because the ratio of water to sediment was so large, the total amount of pesticide in the water greatly exceeded that associated with sediment. Observations such as these led to the conclusion that erosion control practices, unless they control water as well as sediment losses, can be expected to have very little effect on runoff losses of pesticides, except those having very low solutilities or ionic pesticides with extreme clay-binding capabilities.

Adsorbed chemicals on sorbed particulates would be expected to desorb as the ratio of water to solids increases. Thus, it is probable that desorption occurs after the soil becomes entrained in the runoff water, or after runoff water is collected by the investigators prior to separation of sediment from solution, such that most of the measured pesticide is in the water phase. Thus, the major question remains regarding the effectiveness of erosion control practices that prevent soil particles from becoming entrained in runoff water for reducing pesticide transport from the field. The answer to this question is important. If the particulates do not significantly contribute to pesticide in runoff, then erosion control would not be effective in reducing pesticide transport from the field.

Treatment of irrigation water with high molecular weight polymers has been found to be effective in reducing erosion from furrow-irrigated fields. Sediment reduction in runoff water, however, has many advantages but whether one of them is pesticide load reduction is presently unknown. A laboratory study was initiated to identify the relationship between erosion and pesticide transport. The following is a report of that study.

### Research Plan and Procedures

A miniature furrow was created in the laboratory by placing soil in a flume. The flume was 50 cm long and 4 cm wide. A $90^{o}$ angle aluminum trough was attached to each end of the flume to introduce water to the furrow and collect runoff. Seven cm of quartz sand were placed on the bottom of the flume and covered with soil to fill the flume. Soil was removed to create a furrow with dimensions coincident to the angled aluminum placed at each end of the flume. The soil at the bottom of the furrow was 3 cm above the sand.

Holes and drainage tubes were connected at the bottom of the flume to collect any water percolating through the soil and sand. The flume was placed at a 0.5% slope.

Soil from the Ap horizon of a Hanford sandy loam (coarse-loamy, mixed, nonacid, thermic Typic Xerorthents) was used in the study. The soil was air-dried and passed through a 6-mm sieve. The soil was poured into the flume over the sand and lightly tapped. Soil was then removed to create the V-shaped furrow.

Water was introduced to the flume through a pump with a rheostat to adjust flow rate. Preliminary studies were done to determine the appropriate water flow rate to create sediment transport. The erosion was initially high and decreased quickly with time for any given flow rate. Thus, to create erosion throughout the experiment the flow rate was incrementally increased with time. The following flow regime was established. An initial flow rate of 0.22 L $min^{-1}$ was maintained for 4 min after the water reached the end of the furrow. Thereafter, the flow rate was increased at successive 2-min intervals to 1.1, 1.9, and 2.7 L $min^{-1}$.

To accomplish Objective 2, napropamide [2-a-naphthoxy)-N,N-diethylpropionamide] was the pesticide investigated. A concentrated (2 g $L^{-1}$) labeled and non-labeled solution of napropamide was mixed, and in later experiments, 40 g $L^{-1}$ of KBr was added to the solution as an independent tracer. The soil surface was wetted with the solution to create a napropamide treatment equivalent to 8 kg $ha^{-1}$. The soil surface was then dried in a hood for 24 h.

Distilled water and distilled water plus 10 mg $L^{-1}$ of polymer were used for the experiment. Distilled water was used to promote dispersion and enhance erosion, whereas the polymer was used to flocculate and decrease erosion. The polymer was a high molecular weight (10-15 mg $mol^{-1}$) polyacrylamide with an intermediate level of anionic charge.

Water was introduced to the flume and all of the runoff was collected for the first 4 min after runoff began. Thereafter, the flow rate was increased every 2 min as described above. Three samples were collected at predetermined times during each 2-min increment. A total of 10 samples were collected for each run. Each sample was mixed and 1 mL of suspension was taken for $^{14}C$ analysis. The sample was placed in Budget Solve cocktail and the activity measured by a Beckman LS5000TD liquid scintillation instrument. The remaining suspension was centrifuged and a 1-mL sample of the supernatant was analyzed for $^{14}C$ activity by the same procedure. The samples were then dried and the weight of solids was measured. These procedures were followed for the two irrigation waters on each of three replicate runs per irrigation water.

A second set of three runs with each water was conducted; however, there was some modification in analysis of the samples. Bromide was introduced as a separate tracer in the second set of runs. Therefore, 2 mL from each sample were used to determine Br concentration using an Alpkem Model RFA-300 rapid flow analyzer. As before, 1 mL of suspension was used for $^{14}C$ analysis. A measurement on the amount of fine particulates, rather than total sediment load, was done on the last set of samples. The runoff samples were stirred and allowed to settle for 5 min, after which 6 mL of suspension from the top were siphoned and placed into colorimeter tubes. The optical transmittance was measured at 410 nm wavelength in the colorimeter. A calibration curve between optical transmittance vs. the concentration of particulates in suspension was created.

## Results and Disucssion

The relationship between amount of napropamide and weight of particulates in a given sample is illustrated in Fig. 6 for the various replications of distilled water and polymer-treated water. No consistent trend between the amount of napropamide and particulates occurred.

The average $^{14}C$ activity of the solution with suspended particles was an average of 4% higher than the activity of the supernatant solution created by centrifugation. Thus, approximately 96% of the napropamide was associated with the water phase. However, because the water content was 3 to 4 orders of magnitude greater than the solids, the computed concentration of napropamide adsorbed on solids ($\mu g\ g^{-1}$) was greater than the concentration in water ($\mu g\ mL^{-1}$).

The results from the first set of runs were consistent with those from field studies. Although the pesticide concentration on solids was higher than in water, almost all of the pesticide was in water at the time of analysis. Reduction in erosion would appear to be relatively ineffective in reducing pesticide transport because no significant relationship between the amount of particulates and the amount of pesticide removed was evident. However, since the soil used was a sandy loam, most of the eroded particulates were sand particles. Sand particles adsorb very little pesticide, and this observation prompted the second set of runs whereby the amount of fines in the runoff was measured. Furthermore, bromide, which was not adsorbed, was introduced with the pesticide as an independent tracer.

The bromide concentration in the runoff is presented as a function of cumulative runoff in Fig. 7. The results were as expected: highest concentrations were in the initial runoff and decreased rapidly toward zero with increased runoff.

The relationship between the amount of napropamide and fines in runoff samples is illustrated in Fig. 8 for the various runs. The two data points on each graph which lie above the other data points and obviously do not fit the

relationship are from the first runoff collected. These samples would be highly charged by napropamide initially situated at the soil surface which was easily solubilized. An error was made in sample collection on one of the replicates (Pam 4 and DW 5), which explains why only two rather than three high data points appear on the graphs.

Excluding the high data points for the first runoff collected, a linear relationship existed between the amounts of napropamide and fines collected in the runoff. These results would be consistent with napropamide being adsorbed to the fine particulates in the runoff water.

Different levels of fine particulate erosion were achieved by two means: application of polymer to the water and the flow dynamics. The water flow rate in the furrow was increased three times and three samples were collected for each flow rate. Consistently, the first sample collected after the increase in flow rate contained higher levels of particulates which decreased with succeeding sampling.

A regression analysis was conducted excluding the two data points from the first runoff samples. The regression equation for distilled water was $y = 59.9 + 2.93x$ ($r^2 = 0.744$), where y is the amount of napropamide and x is the amount of fines in each sample. The regression equation for the polymer-treated water was $y = 126 + 3.81x$, ($r^2 = 0.876$). Only two of the polymer-treated runoff water samples had fines totaling more than 50 mg. A regression analysis excluding the two samples with more than 50 mg fines produced the equation $y = 127 + 3.56x$ ($r^2 = 0.378$). Note that the equations with and without the excluded data points were very similar.

The amount of napropamide associated with a given amount of fines is higher for the polymer-treated water than for distilled water. One of the effects of the polymer was to flocculate fines which get into suspension and cause them to settle out. Even though the fines were flocculated, and by our methods of analysis would not appear as fines, nevertheless those flocculated fines that were carried off the soil before settling would transport adsorbed pesticide.

As would be expected for a non-adsorbing chemical such as bromide, there was no relationship between bromide removed and the amount of fines (data not presented). The average percentage of bromide applied and napropamide removed in the runoff are presented in Table 2. Note that there is essentially no difference in bromide removed from the distilled and polymer-treated waters. The main effect of polymer treatment was to reduce the erosion of fines, which would not affect the transport of non-adsorbed soluble chemicals such as bromide. The percent removal of napropamide was higher than bromide in each case, suggesting that there was an additional mechanism for napropamide transport. Specifically, it was the transport of fine particulates onto which the napropamide was adsorbed. Also note that there was a higher percentage of napropamide removed with distilled water than with polymer-treated water. Again, this is an effect of the polymer-treated water reducing the transport of fines carrying the napropamide.

The results could indicate that fine particulates in runoff can enhance the transport of pesticides from the field. An approximate 7-fold increase in napropamide removal was observed in going from no particulates to the highest observed particulate removal. These results cannot be quantitatively transferred to the field because of differences in furrow length and flow dynamics. Nevertheless, the mechanisms should remain the same in both cases. Pesticide adsorbed on particulates which get suspended into the water can desorb and be removed in the runoff. Pesticide adsorbed to particulates which remain intact in the soil matrix are less likely to contribute much to the runoff. As the pesticide desorbs from the intact soil matrix it should be carried into the soil with the infiltrating water. Field studies are required to further verify and quantify the beneficial effects of erosion control for decreasing pesticide runoff from fields.

Table 1. Some characteristics of the soils studied.

| Soil type series | Classification | Sand | Silt | Clay | CEC | Organic carbon | pH |
|---|---|---|---|---|---|---|---|
| | | ----------%---------- | | | (cmol(+) $kg^{-1}$ soil) | % | |
| Hanford sandy loam | Typic Xerorthent | 67.1 | 25.8 | 7.1 | 4.5 | 0.43 | 6.1 |
| Domino sandy clay loam | Xerollic Calciorthid | 50.5 | 24.3 | 25.2 | 15.4 | 0.52 | 8.0 |
| Tujunga loamy sand | Typic Xeropsamment | 82.4 | 13.9 | 3.7 | 2.3 | 0.71 | 7.9 |

Table 2. Average percent of bromide applied and napropamide removed in the runoff.

| | Bromide | Napropamide |
|---|---|---|
| Distilled water | 9.6 | 19.3 |
| Polymer-treated | 9.4 | 12.9 |

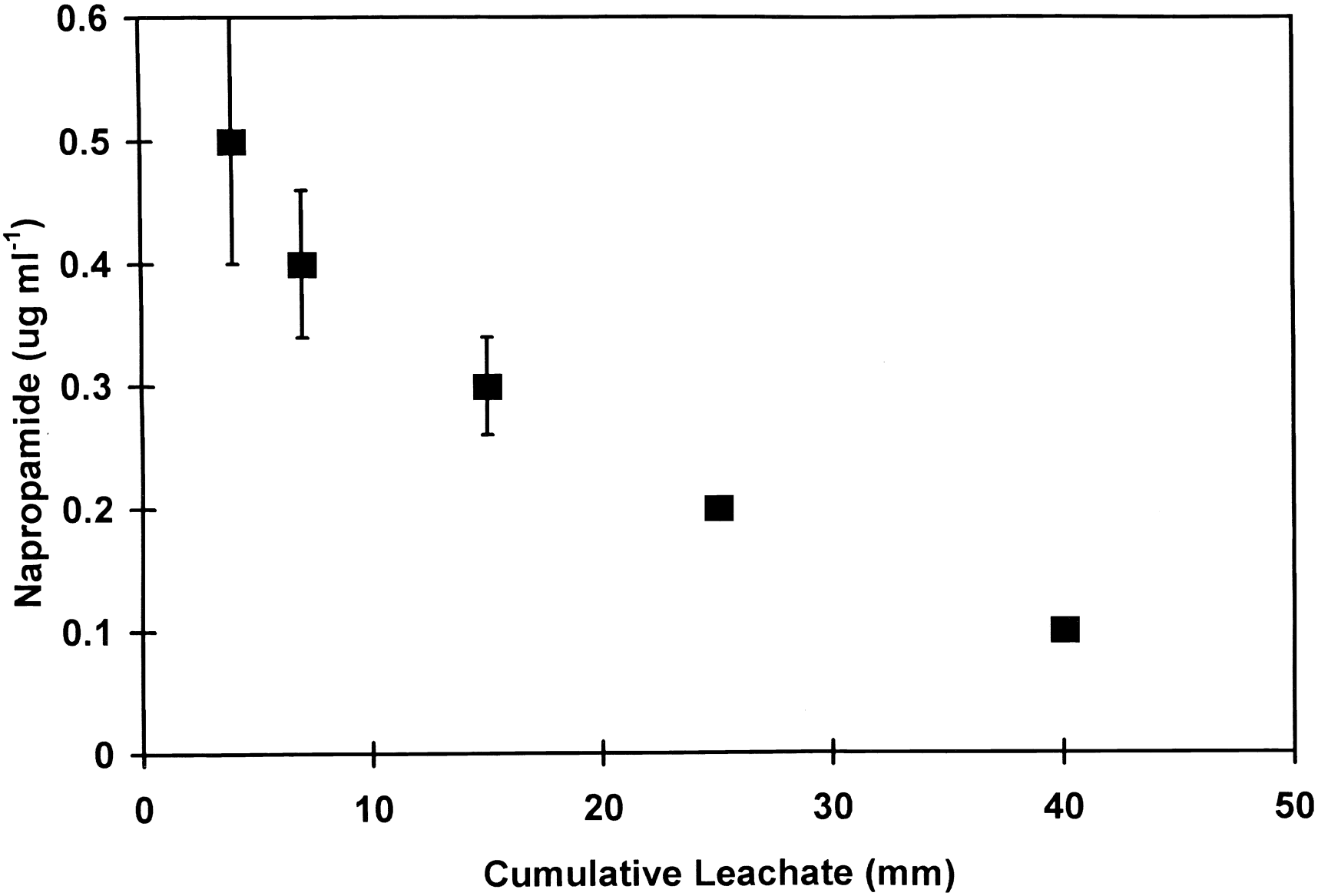


Figure 1. Concentration of napropamide in the leachate as a function of cumulative leachate.

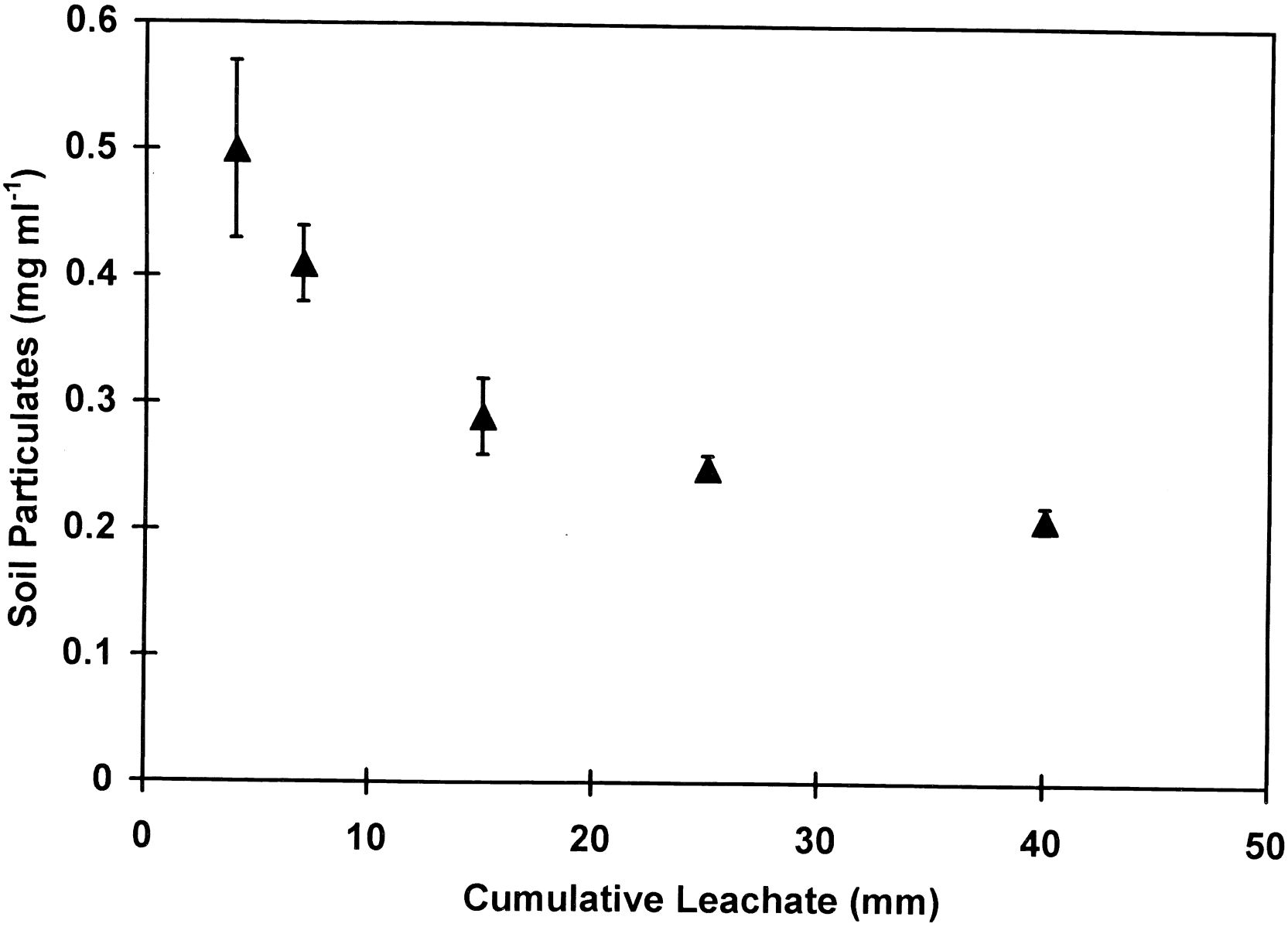


Figure 2. Concentration of soil particulates in the leachate as a function of cumulative leachate.

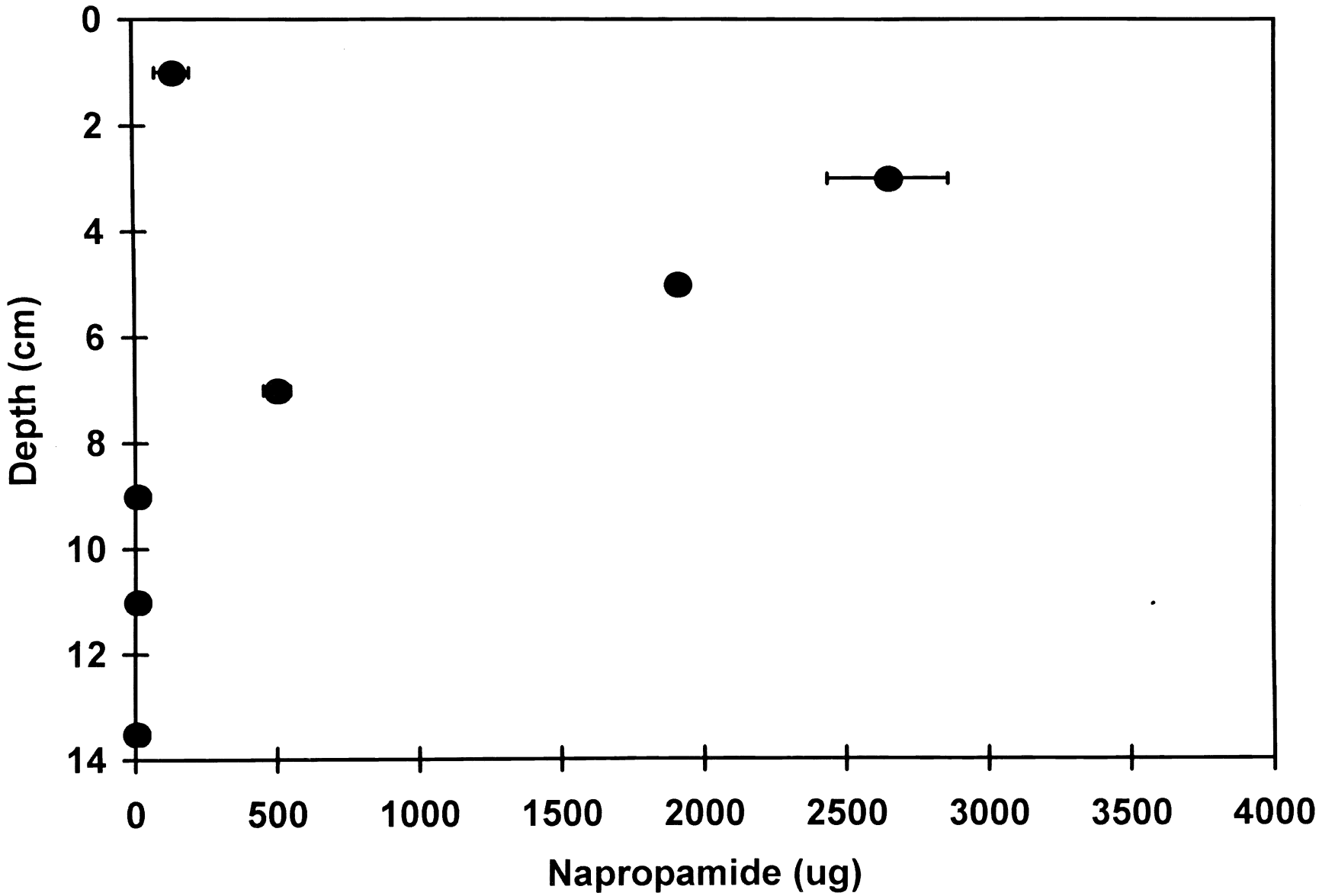


Figure 3. Napropamide distribution in the soil column at the end of the experiment.

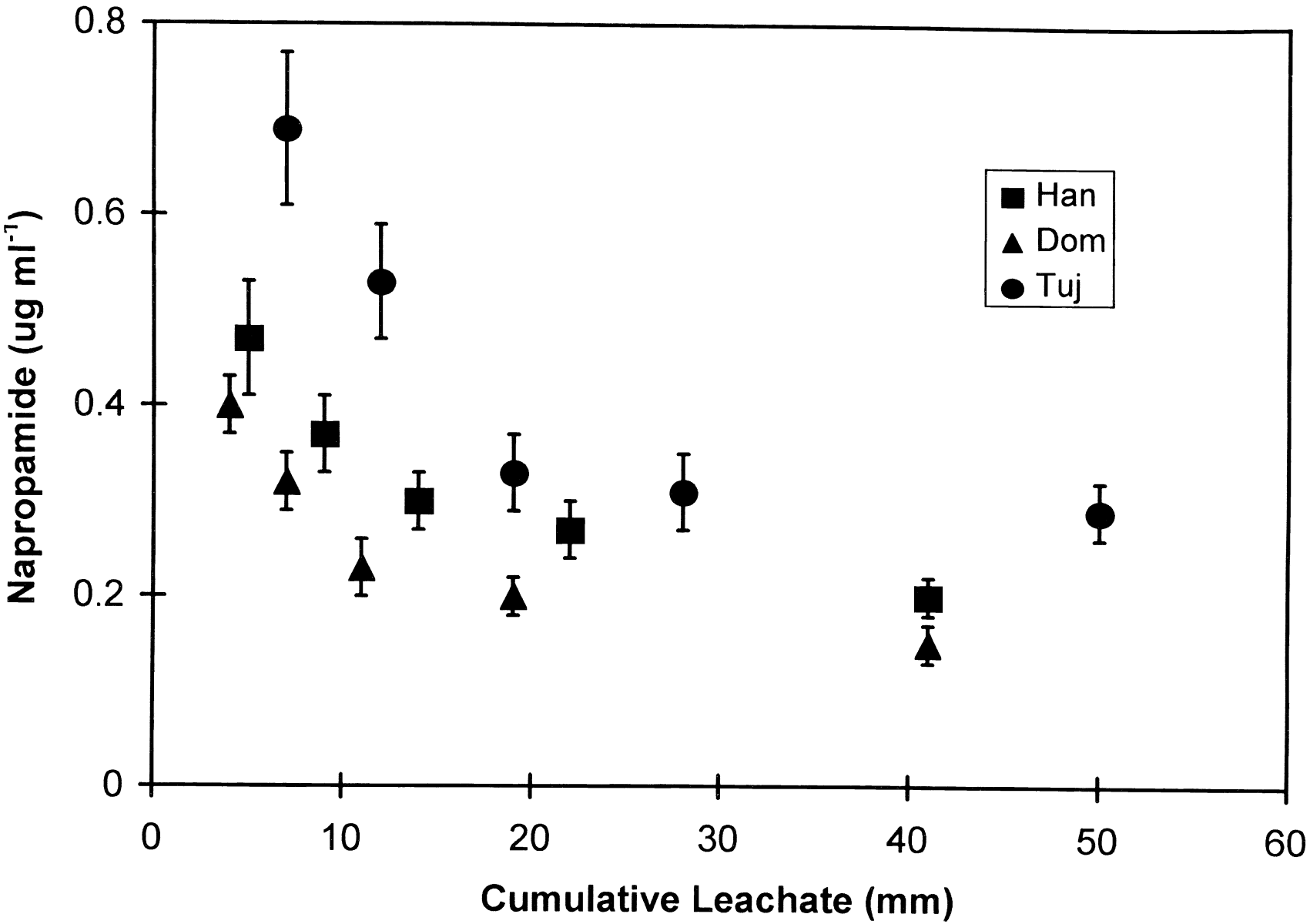


Figure 4. Concentration of napropamide in the leachate as a function of cumulative leachate for Hanford (Han), Domino (Dom), and Tujunga (Tuj) soils for Phase Two experiment.

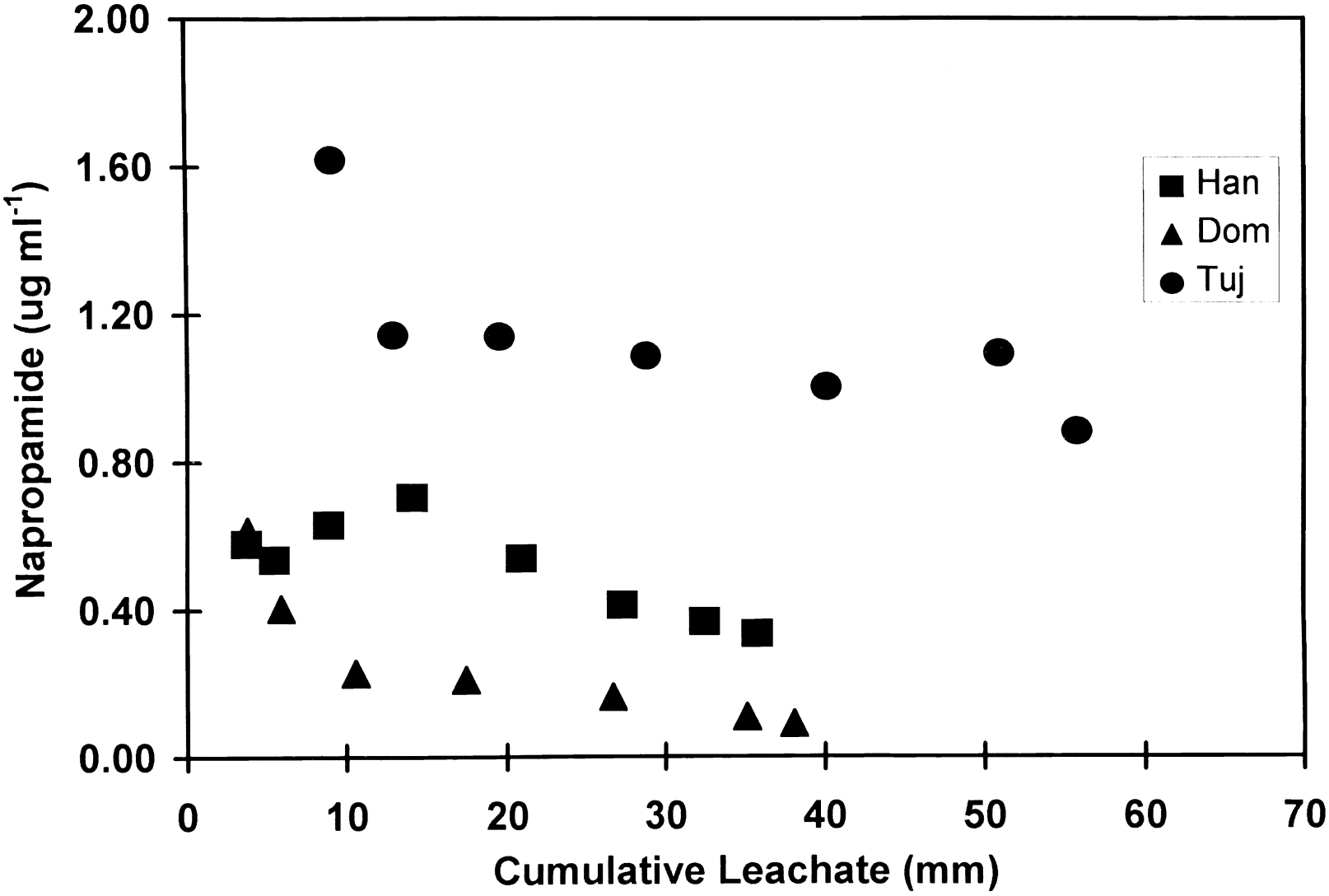


Figure 5. Concentration of napropamide in the leachate as a function of cumulative leachate for Hanford (Han), Domino (Dom), and Tujunga (Tuj) soils for Phase Three Study.

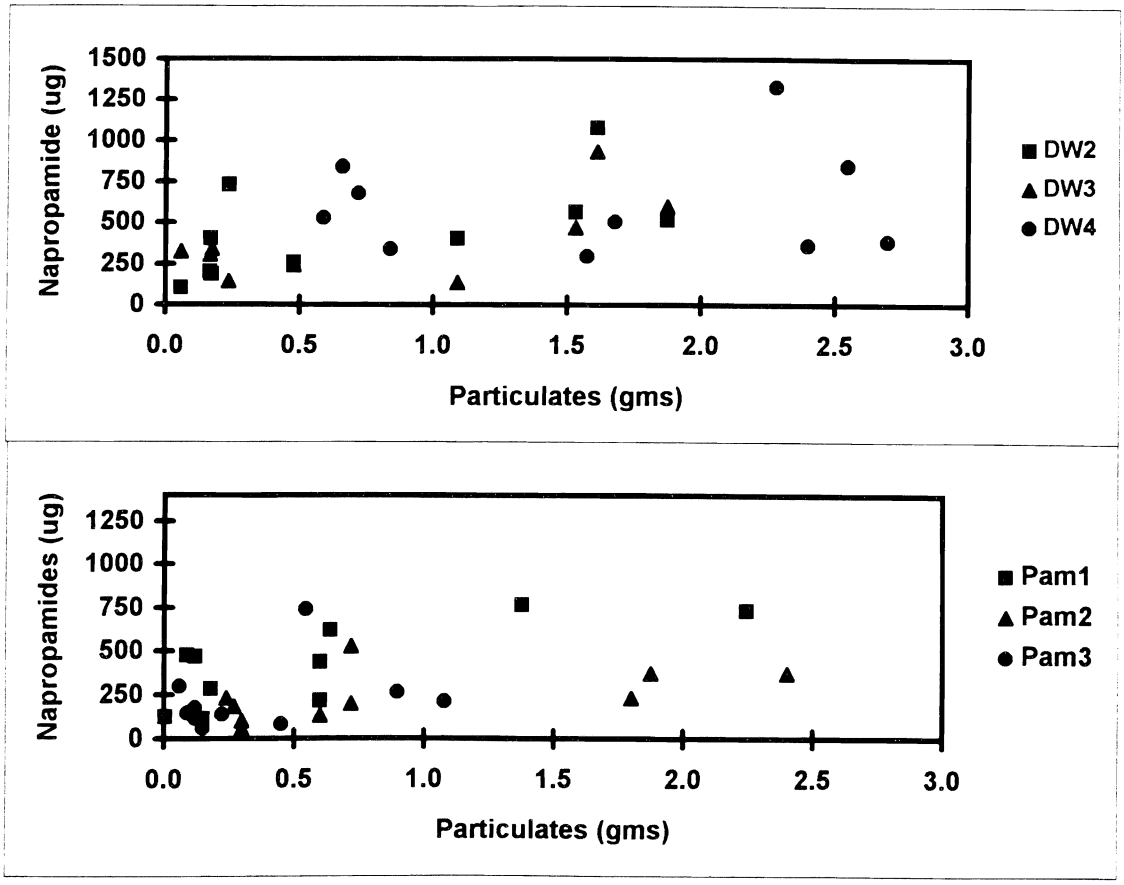


Figure 6. Relationships between amount of napropamide and soil particulates in runoff for individual replicates of distilled water (DW) and polymer treated-water (Pam).

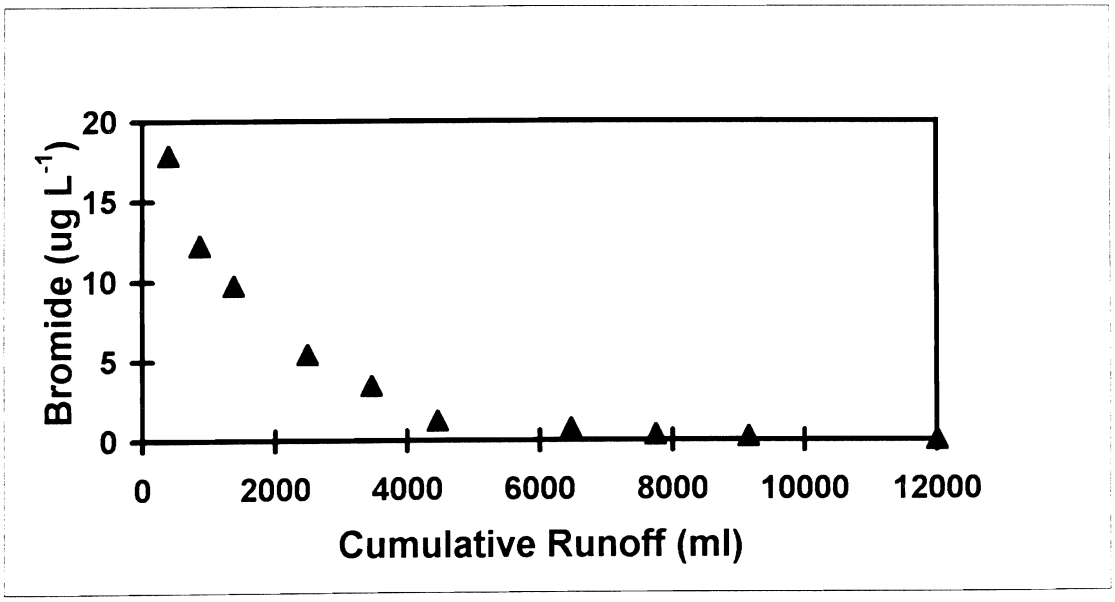


Figure 7. Bromide concentration in runoff as a function of cumulative runoff.

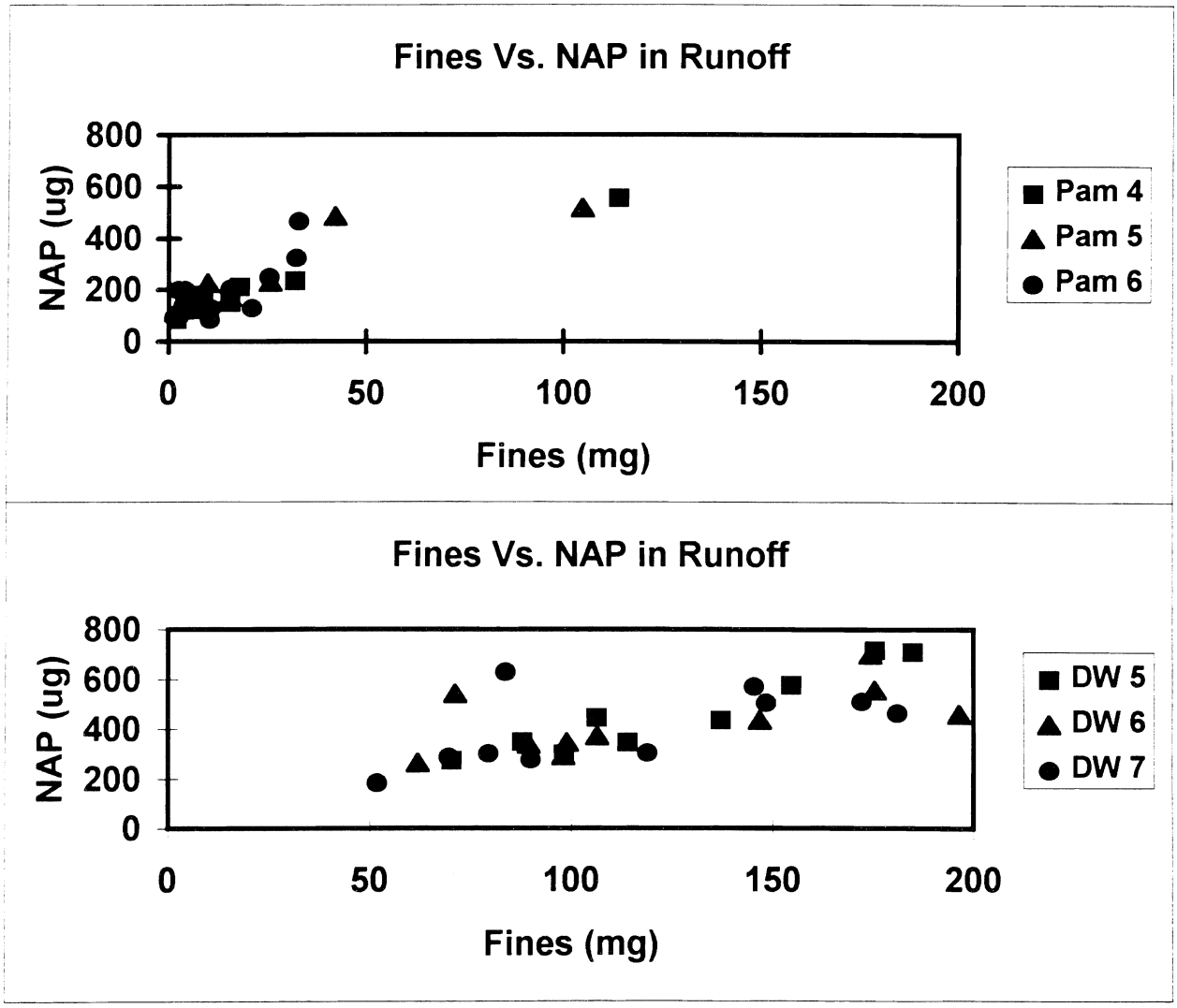


Figure 8. Relationships between amount of napropamide and soil fines in runoff for individual replicates of distilled water (DW) and polymer-treated water (Pam).

# Kinetics of Metal Fixation at Soil Carbonate Mineral Surfaces

WILLIAM H. CASEY[1] AND PETER A ROCK[2]
[1]*Department of Land, Air and Water Resources, Davis Campus*
[2]*Department of Chemistry, Davis Campus*

## Summary

Industrial metal extraction releases 7,000 to 70,000 metric tons per year of base metals (lead, copper, zinc, cadmium) to the aquatic environment. Currently there are more than 31,000 metal-contaminated hazardous waste sites in the United States (Moore and Luoma, 1990). The loading to soil from municipal waste treatment is also substantial in the form of incinerator flyash and discarded metal batteries. This waste is harming the population. In 1984, 17 percent of preschool children in the United States had elevated blood lead levels (Driscoll et al., 1992). Much of this metal contamination ends up in carbonate minerals (e.g., Fuller and Davis, 1987) because calcareous, western soils are rich in $CaCO_3$ (10-50 weight percent). Understanding the rates and pathways for metal fixation into minerals is important for predicting the environmental fate of metals in soils.

This research project has two major goals. First, we want to evaluate the rates of incorporation of toxic metals into carbonate mineral surfaces. Second, we want to instruct students within the Department of Land, Air and Water Resources at the University of California, Davis, in an electrochemical approach to determining thermodynamic properties of minerals and aqueous solutions because it avoids many of the disadvantages of conventional solubility experiments. Progress toward accomplishing these goals was achieved by constructing computer-monitored electrochemical cells that are used to determine (i) the rates of approach to equilibrium for a solution in contact with a carbonate mineral, and (ii) the mean ionic activity coefficients for electrolytes in the mixed-electrolyte system $CaCl_2$-$CdCl_2$, which are needed to analyze $Cd^{2+}$(aq) incorporation into calcites.

**Key Words**: thermodynamics, electrochemistry, geochemistry, soil chemistry, solubilities.

## Project Objectives Addressed in 1993-94

The first goal of this research project is to evaluate the rates of reactions between metals and carbonate mineral surfaces using specially designed electrochemical cells that allow for continuous recording of the solution saturation state. Our second goal is to instruct students in the Department of Land, Air and Water Resources (LAWR) at U.C. Davis in a new approach to determining thermodynamic properties for minerals.

## Research Plans and Procedures

Rates of Solid Recrystallization

Experiments show that many divalent metals rapidly adsorb onto the surfaces of calcite but that the amount of metal that can be desorbed decreases with time. This result is interpreted to indicate that the metal is either fixed into the crystal lattice or that a continuous surface precipitate forms that is resistant to dissolution. The electrochemical double cell method allows us to monitor directly the thermodynamic activity of one metal-carbonate component (e.g., $CdCO_3$) in equilibrium with the aqueous solution and at the surface of a calcite solid solution phase. After adding a carbonate solid to an electrochemical cell but before any reaction takes place (t=0), the cell potential corresponds to the Gibbs energy of transferring $CaCl_2$ from the pure $CaCl_2$ solution in the reference cell to the $CaCl_2$-$CdCl_2$ mixture:

$$Cd(Hg,\ 2\text{-phase})|CdCO_3(s),CaCO_3(s)|CaCl_2(aq)|Hg_2Cl_2(s)|Hg(l)\ -$$

$$-\ Hg(l)|Hg_2Cl_2(s)|CaCl_2(aq),\ CdCl_2(aq)|CaCO_3(s),CdCO_3(s)|Cd$$

$$(Hg,\ 2\text{-phase}) \qquad (1)$$

If the solid recrystallizes to a different composition (e.g., $Ca_xCd_{1-x}CO_3$), the cell potential will change with time to the equilibrium potential for the cell:

$$Cd(Hg,\ 2\text{-phase})|CdCO_3(s),CaCO_3(s)|CaCl_2(aq)|Hg_2Cl_2(s)|Hg(l)\ -$$

$$-Hg(l)|Hg_2Cl_2(s)|CaCl_2(aq),CdCl_2(aq)|Ca_xCd_{1x}CO_3(s),CdCO_3(s)|Cd$$

$$(Hg,\ 2\text{-phase}) \qquad (2)$$

The time variation of the cell potential gives us the rate of formation of the solid solution:

$$CaCO_3(s) + xCaCl_2(aq) + (1\text{-}x)CdCl_2(aq) = Ca_xCd_{1-x}CO_3(s) + CaCl_2(aq) \quad (3)$$

because the equilibrium potential for Eq. (3) is known from other sources (e.g., Wagman et al., 1982; Rock et al., 1994).

If incorporation of $CdCO_3$ into the mineral lattice is via solid-state diffusion, the cell will record a parabolic change in $CdCO_3$ activity with time. Conversely, if the surface recrystallizes to a surface precipitate, the cell potential will change nonlinearly with time, but the cell potential will not correspond to a miscible $CdCO_3$-$CaCO_3$ mixture and may be irreversible. Similar cells can be designed for other carbonate solid-solution minerals (e.g., $Ca_xSr_{1-x}CO_3(s)$ or $Ca_xMg_{1-x}CO_3(s)$).

Direct Determination of Activity Coefficients in Mixed-Electrolyte Solutions

If no reaction takes place in cells given by Eq. (1), the cell potential yields the mean ionic activity coefficient of $CdCl_2$ (or other metal-chloride salts) in the $CaCl_2$+$CdCl_2$ mixture. This feature allows for direct measurement of important thermodynamic parameters describing aqueous solutions without appeal to complicated models of the solute speciation.

For the above example of $CdCl_2$+$CaCl_2$ solutions, values for $\gamma_{\pm,CaCl_2}$ and $\gamma_{\pm,CdCl_2}$ can be determined in the mixed $CaCl_2$-$CdCl_2$ solutions through cells of the type:

$$Cd(Hg)|CaCl_2(aq,m_1),\ CdCl_2(aq,m_2)|Hg_2Cl_2(s)|Hg(l) \qquad (4)$$

The equation for the net cell reaction is:

$$Cd(Hg) + Hg_2Cl_2(s) = CdCl_2(aq) + Hg(l) \qquad (5)$$

Application of the Nernst equation to the net cell reaction yields

$$E = E^\circ - \frac{RT}{2F} \ln\left[m_2(2m_1 + 2m_2)^2\, \gamma^3_{\pm,CdCl_2}\right] \qquad (6)$$

from which $\gamma_{\pm,CdCl_2}$ values can be calculated. A mixture of these electrolytes ($CaCl_2$ and $CdCl_2$) is highly nonideal and, because no independent values exist for $\gamma_{\pm,CaCl_2}$ and $\gamma_{\pm,CdCl_2}$ in the mixed $CaCl_2$-$CdCl_2$ solutions, the accuracy of models of the thermodynamic activities in Cd-containing soil solutions is difficult to assess. Knowledge of values for $\gamma_{\pm,CaCl_2}$ and $\gamma_{\pm,CdCl_2}$ is also important to our study of the rates of formation of calcium-carbonate solid-solution minerals via Eq. 1.

## Results

Rates of Solid Recrystallization

Cells have been designed to record the approach toward equilibrium of electrolyte solutions and solid carbonate minerals. As an example, the time-course in voltages for the cell given by:

$$Cd(Hg)|CdCO_3(s),Ca_{0.91}Mg_{0.08}CO_3(s)|CaCl_2(aq),$$

$$MgCl_2(aq)|Hg_2Cl_2(s)|Hg(l) \qquad (7)$$

is shown in Fig. 1. The solid powder used in this experiment was formed by recrystallizing $CaCO_3$ and $MgCO_3$ in a welded gold capsule at high temperatures and pressures. The resulting solid is a single-phase material with homogeneous composition. Horizontal lines are given on the figure that correspond to the cell voltages that would result if the $Ca_xMg_{1-x}CO_3(s)$ recrystallized to either pure calcite or an ideal solution of $MgCO_3$ and $CaCO_3$.

Activity Coefficients in $CaCl_2$+$CdCl_2$ Solutions

A series of cells given by Eq. (4) were constructed with electrolyte solutions having differing molalities of $CaCl_2$ and $CdCl_2$, but near-constant ionic strength. The results of these preliminary experiments are given in Table 1. The cell voltages yield values for $\gamma_{\pm,CdCl_2}$ in the mixed $CaCl_2$-$CdCl_2$ electrolyte solution (Table 1).

## Discussion

Rates of Recrystallization

The voltage variation shown in Fig. 1 illustrates the fact that information about both reaction kinetics and equilibria can be determined using these electrochemical cells. As expected, the voltages of electrochemical cells with the $Ca_xMg_{1-x}CO_3$ solids vary considerably during the first few weeks of reaction, consistent with recrystallization of the solids. In fact, the $Ca_xMg_{1-x}CO_3$ solids were chosen for study because of geochemical evidence for metastability. Most biogenic marine carbonate minerals are magnesium calcites ($Ca_xMg_{1-x}CO_3(s)$) where x varies between 0.98 and 0.80. The thermodynamics of mixing in the $CaCO_3$-$MgCO_3$ system is, however, highly nonideal. High-magnesium calcites tend to recrystallize during early diagenesis to eliminate magnesium from the structure. Thus, pore fluids in carbonate sediments are commonly enriched with dissolved magnesium relative to sea water (see Morse and Mackenzie, 1990). This magnesium enrichment is attributed to spontaneous recrystallization of high-magnesium calcites with time, as we observed in the electrochemical cells (Fig. 1) .

The electrochemical data (Fig. 1) indicate that the recrystallization is sensitive to the solution and solid compositions. Small changes in the $MgCl_2$ concentration of the cell electrolyte, or the value of x in the $Ca_{1-x}Mg_xCO_3$ solid, can yield dramatically different reaction products. In the case of $Ca_{0.92}Mg_{0.08}CO_3$ (Fig. 1), the voltage changes nonlinearly with time in the early stages of an experiment and achieves a value close to that for an ideal solution. In contrast, the voltage for an electrochemical cell that includes $Ca_{0.94}Mg_{0.06}CO_3$(s) and an electrolyte solution containing a lower concentration of $MgCl_2$, achieve voltages that approximately correspond to equilibrium with pure calcite (Fig. 1, lower diagram). Additional work is needed to elucidate these reactivity trends, but it is clear that these electrochemical cells can be used to determine both kinetic and thermodynamic data about solid stabilities.

We are considering several design improvements. Specifically, we are designing the cell to allow continuous flow of the electrolyte solution, slow stirring of the electrolyte solution, and continuous monitoring of the $CO_2$ activity.

Activity Coefficients in $CaCl_2$+$CdCl_2$ Solutions

Many geochemical problems require the modeling of high-ionic strength brines. Calculations of activity coefficient corrections in these solutions were highly inaccurate until an ion-ion interaction approach was developed (e.g., Pitzer, 1991). Central to this approach is a virial expansion that relates the electrolyte activity coefficients to parameters that account for electrostatic, pairwise, triplewise, etc. interactions with other solutes. The primary data to evaluate these interaction parameters are based on measurements of mean ionic activity coefficients in mixed electrolyte solutions.

The data compiled in Table 1 are the measured values for $\gamma_{\pm,CdCl_2}$ in mixed $CdCl_2$-$CaCl_2$ solutions, in spite of the environmental importance of $CdCl_2$ solutions. We have verified that Harned's Rule holds for this mixed electrolyte solution. Harned's Rule (see Robinson and Stokes, 1959; p. 438) states that, empirically, the logarithm of the activity coefficient of one electrolyte in a mixture is linearly proportional to the concentration of the second electrolyte at constant ionic strength. Verification of Harned's Rule for the mixed $CdCl_2$-$CaCl_2$ electrolyte solution is illustrated in Fig. 2 in which the logarithm of $\gamma_{\pm,CdCl_2}$ is correlated with the molality of $CaCl_2$. This strong correlation is important because both $\gamma_{\pm,CaCl_2}$ and $\gamma_{\pm,CdCl_2}$ can be estimated from cells such as those given by Eq. (4).

## References


Driscoll W., Mushak P., Garfias J. and Rothenberg S. J. 1992 . Reducing lead in gasoline-Mexico's experience. Environ. Sci. and Technol. 26:1702-1705.

Fuller C. C. and Davis J. A. 1987. Processes and kinetics of $Cd^{+2}$ adsorption by a calcareous aquifer sand. Geochim. Cosmochim. Acta. 51:241-254.

Moore J. N. and Luoma S. N. (1990) Hazardous wastes from large-scale metal extraction. Environ. Sci. and Technol. 24:1279-1285.

Morse, J. W. and Mackenzie, F. T. 1990. Geochemistry of Sedimentary Carbonates. Developments in Sedimentology. 48, pp. 707. Elsevier.

Pitzer, K. S. 1991. Ion interaction approach: theory and data correlation. In: Activity Coefficients in Electrolyte Solutions, pp. 75-153, 2nd ed., CRC Press.

Robinson, R. A. and Stokes, R. H. 1959. Electrolyte Solutions. Butterworths Scientific Publications.

Rock, P. A., Casey, W. H., McBeath, M. M. and Walling, E. M. 1994. A New Method for Determining Gibbs Energies of Formation of Metal-Carbonate Solid Solutions: The $Ca_xCd_{1-x}CO_3(s)$ System at 298°K and 1 bar. Geochim. Cosmochim. Acta. (in press).

Wagman, D. D., Evans, W. H., Parker, V. B., Schumm, R. H., Halow, I., Bailey, S. M., Churney, K. L. and Nuttall, R. L. 1982. The NBS tables of chemical thermodynamic properties: selected values for inorganic and $C_1$ and $C_2$ organic substances in SI units. J. Phys. Chem. Ref. Data, 11: (Supplement 2), 392 pp.

Table 1. Values for $\gamma_{\pm,CdCl_2}$ in $CaCl_2$-$CdCl_2$ solutions are from cells given by Eq. (4). The concentrations are reported at precisions that are higher than significant in order to minimize the truncation and round-off errors. The $E^o$ value for this cell is 0.61970 V, using data from Wagman et al. (1982).

| Cell | $m_1$ | $m_2$ | E/V | $m_1+m_2$ | $-\ln(\gamma_{\pm,CdCl_2})$ |
|---|---|---|---|---|---|
| A1 | 0.022938 | 0.073970 | 0.7513 | 0.096908 | 1.4551 |
| A2 | 0.046475 | 0.049903 | 0.7553 | 0.096378 | 1.4241 |
| A3 | 0.070002 | 0.025438 | 0.7629 | 0.095440 | 1.3903 |
| A4 | 0.009312 | 0.088653 | 0.7495 | 0.097944 | 1.4759 |
| A5 | 0.085034 | 0.010159 | 0.7738 | 0.097965 | 1.3656 |
| B1A | 0.035453 | 0.006056 | 0.7889 | 0.095193 | 1.0478 |
| B1B | 0.036857 | 0.005990 | 0.7889 | 0.042509 | 1.0494 |
| B19 | 0.044860 | 0.054361 | 0.7513 | 0.042847 | 1.3681 |
| B3 | 0.010864 | 0.023025 | 0.7771 | 0.099221 | 1.0355 |
| B13D | 0.078387 | 0.002319 | 0.7912 | 0.033889 | 1.2150 |
| B13B | 0.010906 | 0.068524 | 0.7540 | 0.079430 | 1.3671 |

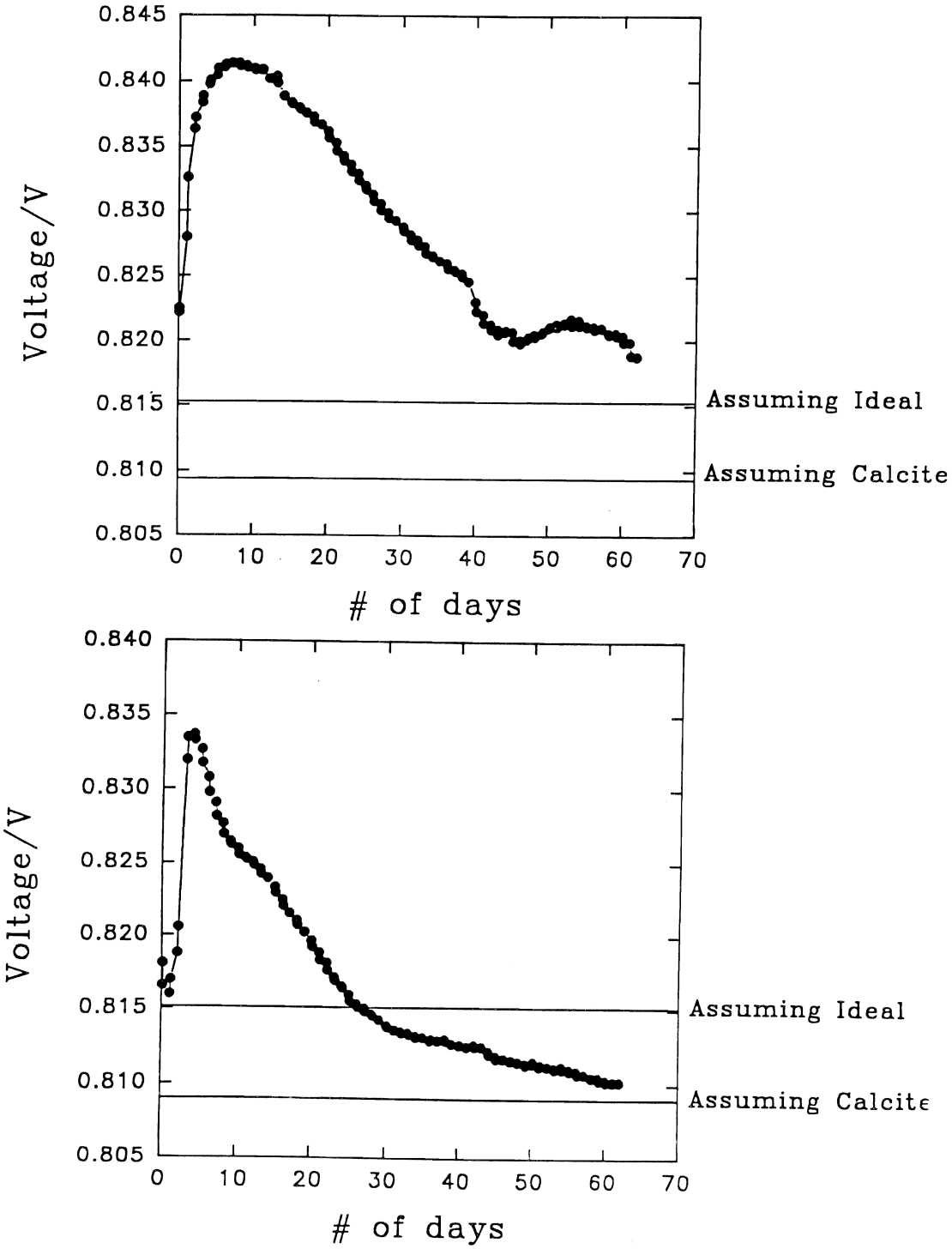


Figure 1. Voltage as a function of time for cells of the type: $Cd(Hg)|CdCO_3(s),Ca_xMg_{1-x}CO_3(s)|CaCl_2(aq,m_1)$, $MgCl_2(aq,m_2)|Hg_2Cl_2(s)|Hg(l)$. In the top diagram, x=0.92, $m_1$=0.093803 and $m_2$=0.008727. In the lower diagram, x=0.94, $m_1$=0.096772 and $m_2$=0.005835. The horizontal lines are the cell voltages predicted for equilibrium with pure calcite (x=1.0) and an ideal solution of $MgCO_3$ and $CaCO_3$ to yield the $Ca_xMg_{1-x}CO_3$ solid.

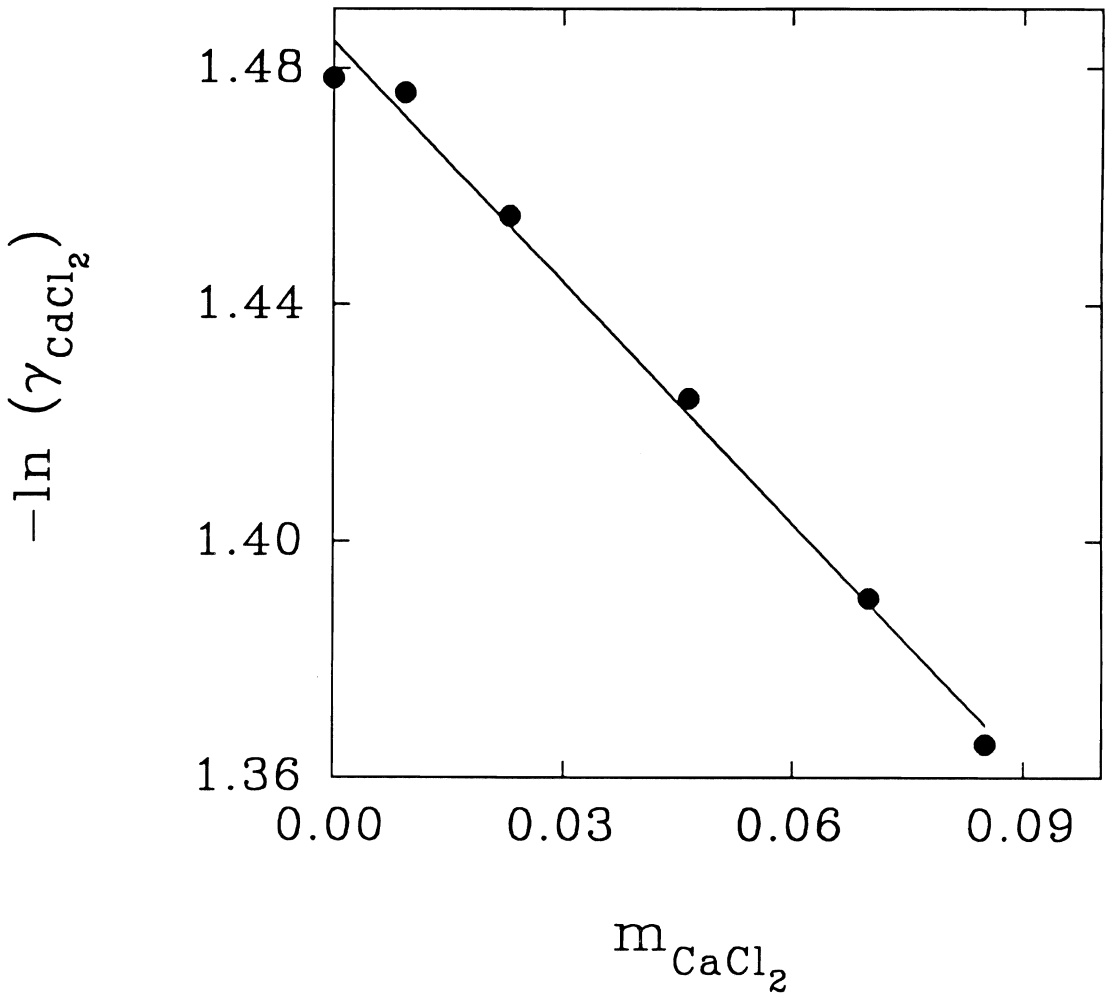


Figure 2. Values of the logarithm of $\gamma_{\pm,CdCl_2}$ as a function of the molality of $CaCl_2$ in solution. The voltages correspond to cells of the type given by Eq. (4).

# NMR Relaxation and Self-Diffusion Measurements of Water Imbibed in Porous Matrices

MICHAEL A. ANDERSON AND ZEINA HINEDI

*Department of Soil and Environmental Sciences, Riverside Campus*

## Summary

Nuclear Magnetic Resonance (NMR) provides a noninvasive tool to probe the molecular organization of water in heterogeneous porous matrices. In a porous matrix, the relaxation rate of water is enhanced with respect to that of bulk water due to van der Waals interactions effective over near neighbor distances, (≈3 Å), at the water-grain interface. The distribution of pore sizes can be determined from laboratory measurement of $^1$H NMR longitudinal relaxation in water-saturated porous media. The NMR measurement consists of exciting the spin system in the water and recording its relaxation back to equilibrium over the delay time ($t$) which can vary from 10 ms to more than 5000 ms. The measured relaxation rate is a linear combination of the bulk relaxation rate and the relaxation rate at the surface weighted by the surface-to-volume ratio which holds the pore size information. In a porous matrix (e.g. porous silica, soils), which consists of a collection of pores where fluid relaxes at different rates, the contribution of all the relaxation rates to the magnetization decay is weighted by the volume of fluid that relaxes at each rate. In this one-year project, carried out in water-saturated packed beds of porous silica beads, short decay times translated into intraparticle pore sizes that agreed with reported pore sizes of the silica beads used. Decay times on the order of 1000 ms correspond to water present in interparticle pores. In an admixture of silica beads with different intraparticle pore sizes, NMR was unable to distinguish between 60Å and 150Å pore sizes, yielding an intermediate 130Å pore size. We used scanning electron microscopy to examine the surface micromorphology of individual magnetic and nonmagnetic Borden aquifer material grains. The dimension of the intraparticle pores observed on a magnetite particle corresponded to the smaller pore size measured by NMR methods. We are therefore attributing part of the intraparticle porosity in the Borden aquifer to iron and manganese oxides. We attribute the larger pore size detected by NMR to interparticle porosity. In the second series of experiments, we used Pulsed Field Gradient Spin Echo NMR (PFG-SE NMR) to measure self-diffusion of water in Eustis soil. The time-dependent diffusion coefficient of a fluid in a porous matrix holds valuable information about the microgeometry of the restricting pores. At short diffusion times, the mean square displacement calculated from the PFG-NMR measurement corresponds to the maximum displacement within an average pore. At long diffusion times, the true macroscopic diffusion coefficient is obtained from the PFG-NMR measurement.

**Key Words:** NMR T1 relaxation, PFG-SE NMR diffusion, RMSD, Eustis soil

## Project Objectives Addressed in 1993-94

(1) Use NMR relaxation methods to investigate and characterize the porosity of soil water.
(2) Measure the self-diffusion coefficient of water in Eustis soil using PFG-SE NMR techniques to study pore microgeometry and tortuosity.

## Research Plan and Procedures

**Background.** Fate and transport of pollutants in terrestrial and aquatic ecosystems are influenced by the heterogeneity of the sorbent matrix. In modeling solute transport, assumptions regarding sorption mechanisms and the microgeometry of sorbents must be made. Experimental data are needed to calibrate the parameters that describe the pore structure and hydraulic properties. There is, however, a lack of process-based molecular level characterization of the sorbent matrices that describe the microenvironment where sorption takes place. Soils and aquifer materials include organic and inorganic phases, each endowed with its own characteristic porosity. Coatings and cementation processes that coalesce various constituents into aggregates result in the formation of a continuum of heterogeneous pores. For modeling solute transport, the pore space in soils and sediments may be discretized into mobile and immobile regions (van Genuchten and Wierenga, 1976 and 1977; Sardin et al., 1991). The mobile region is where advective-dispersive transport occurs, and the immobile region serves as sink/source for sorption/desorption of solutes.

Depending on the material being studied and the purpose for which the porosity is being evaluated, different tools are used for porosity evaluation. In soil science, attempts were made to define porosity with respect to transport phenomena of water and methods of measurement. (Luxmoore, 1981; Bouma, 1981). In Luxmoore's pore size classification, pores < 10 μm are designated as micropores; pores between 10-1000 μm are designated as mesopores; and pores > 1000 μm are designated as macropores. In the chemistry and colloid science literature, when sorption mechanisms are being studied, a different scale for evaluating porosity prevails. Gregg and Sing (1967) defined pores < 0.002 μm as micropores, pores between 0.002-0.05 μm as mesopores, and pores > 0.05 μm as macropores.

Methods for pore structure analysis include optical/electron microscopy, gas adsorption/condensation, and mercury porosimetry. There are disadvantages and limitations inherent in each of these methods. In microscopy, a large number of two-dimensional data are needed to yield macroscopic-type information about pore volume distribution. Both gas adsorption and mercury porosimetry measure the smallest constriction, S, in a porous matrix, not the pore radius. All three methods are applicable to dry

samples. Nuclear magnetic resonance relaxation methods for evaluating porosity, on the other hand, measure the "true" pore volume-to-surface area ratio and can be used in the presence of water or any saturating fluid containing a NMR-sensitive nucleus.

The same setup used to evaluate porosity can be used to measure self-diffusion with Pulsed-Field Gradient Spin Echo NMR (PFG-SE NMR). The time-dependent self-diffusion coefficient of water in porous matrices holds important information pertaining to the microgeometry of the constricting pores.

**Pore Size Distribution from Longitudinal Relaxation Measurements.** The spin-lattice (longitudinal) relaxation ($T_1$) of the overall spin ensemble refers to the exchange of energy between the proton nuclear spins in water and their surroundings. In a porous matrix, the relaxation rate of water is enhanced due to van der Waals interactions effective over near neighbor distances $\lambda$ (3 Å) at the water-grain interface. The NMR measurement consists of exciting the spin system in the water and recording its relaxation back to equilibrium over the delay time ( $t$ ) which can vary from 10 ms to more than 5000 ms. The measured relaxation rate is a linear combination of the bulk relaxation rate ($1/T_b$) and the relaxation rate at the surface ($1/T_s$) weighted by the surface-to-volume ratio (s/v), which holds the pore size information. In a porous matrix (e.g. porous silica, soils), which consists of a collection of pores where fluid relaxes at different rates, the contribution of all the relaxation rates ($1/T_i$) to the magnetization decay A(t) is weighted by the volume ($w_i$) of fluid that relaxes at each rate:

$$A(t) = \sum_i w_i \exp\left(-\frac{t}{T_i}\right) \Big/ \sum_i w_i \qquad (1)$$

where

$$\frac{1}{T_i} = \frac{1}{T_b} + \frac{\lambda}{T_s}\frac{m}{l}$$

In its continuum form, equation (1) can be written as follows

$$A(t) = \int_0^\infty P(l) \exp\left[-t\left(\frac{1}{T_b} + \frac{\lambda}{T_s}\frac{m}{l}\right)\right] dl \qquad (2)$$

where

$P(l)$ is defined as the probability distribution that a molecule of liquid is in a pore with the size range $l + dl$ and $l$ is the pore size
$1/T_b$ is the relaxation rate of the bulk water
$1/T_s$ is the relaxation rate at the interface
The volume and the surface of a pore are proportional to $l^3$ and $l^2$, respectively, and $s/v = m/l$, where $m$ depends on the geometry of the pore.

**Measurement of Self-Diffusion by NMR Methods.** Self-diffusion can be inferred from its effect on NMR relaxation; however, using a PFG-NMR sequence allows direct measurement of self-diffusion. The NMR method detects self-diffusion over a time period ranging from a few milliseconds to a few seconds, which translates into distances in excess of a few hundred Angstroms (Å). This method, thus, lends itself to investigations of structural features in a broad range of synthetic and natural porous matrices. The PFG sequence is an elaboration of the transverse relaxation measurement carried out in the presence of a pair of gradient pulses. Because of the diffusive motion of the water molecules that occurs between the first and the second gradient pulse, the refocusing of the NMR signal is incomplete and results in an attenuation of the spin echo. The ratio of the echo amplitude before the application of the gradient to that at variable gradient timing parameters gives a measure of the ensemble average molecular translation.

For isotropic, unrestricted self-diffusion, the relative echo intensities are given by the following expression, derived by Stejskal and Tanner (1965):

$$\frac{M}{M_0} = R = \exp\left[-\gamma^2 G^2 \delta^2 \left(\Delta - \tfrac{1}{3}\delta\right) D\right] \qquad (3)$$

where

M is the echo amplitude

$\Delta$ is the time interval between 90° and 180° rf pulses (s)

$\delta$ is the duration of the gradient pulse (s)

$\gamma$ is the magnetogyric ratio of the nucleus at resonance ($Tesla^{-1}\ s^{-1}$)

G is the magnitude of the gradient pulse ($Tesla\ m^{-1}$)

D is the diffusion coefficient ($m^2\ s^{-1}$)

The time-dependent diffusion coefficient of a fluid in porous media as measured by NMR holds valuable information about the microgeometry of the restricting pores.

The self-diffusion coefficient measured in equation (3) is equivalent to the diffusion coefficients expressed by:

Einstein's relation

$$r^2 = 6Dt \qquad (4)$$

where

$r^2$ is the mean square displacement
t is the observation time

and

Fick's second law of diffusion.

$$\frac{\partial C}{\partial t} = D\frac{\partial^2 C}{\partial r^2} \qquad (5)$$

where

C is the concentration of a tracer molecule

Porous Silica. Two types of porous silica of comparable particle size and varying pore sizes were purchased from Alltech (Deerfield, IL) and used without further treatment in our studies. Their physical characteristics are listed in Table 1. The silica materials were admixed in the proportions listed in Table 2 to produce specific pore size distributions. The admixtures were packed into 5mm NMR tubes, evacuated, then saturated with an electrolyte solution (0.005M $CaSO_4$, 0.02%$NaN_3$) under a $CO_2$ atmosphere.

**NMR Experiments.** Porous matrices of geological origin, characterized for use in numerous solute transport studies by this group, (Hinedi et al., 1993) and others Ball and Roberts, 1990) were used in our NMR relaxation experiment (Borden aquifer material, collected near a sand quarry located at the Royal Canadian Air Force Base, Borden, Ontario) and PFG- NMR diffusion experiment (Eustis soil, collected from a site located on the campus of the University of Florida, Gainesville, FL). The physical and chemical properties of the soil and aquifer material are listed in Tables 3 and 4, respectively.

Relaxation measurements. The longitudinal relaxation data were collected on a Joel FX200 NMR using the inversion recovery pulse sequence. The computer code CONTIN (Provencher, 1982) was used to obtain a regularized relaxation distribution from equation (2).

Pulsed-Field Gradient Spin-Echo NMR diffusion measurements . The water self-diffusion NMR measurements in the Eustis soil were run on a MSL200 spectrometer using a PFG-SE sequence.

## Results and Discussion

### NMR Relaxation Experiment

Pore size distributions in silica beads. Nuclear relaxation measurements of water in silica beads with known pore sizes revealed two relaxation peaks. (Data not shown). The longer relaxation time is attributable to interparticle water. The shorter relaxation time, which yielded pore sizes comparable to those reported in the porous Davisil silica product literature, is attributed to intraparticle pores (Fig. 1). The pore sizes can be obtained by solving equation (1) or (2). The analytical solution of equation (1) agreed with the numerical solution of equation(2) for the pore sizes corresponding to the two relaxation rates and the fractions of the water relaxing at each rate. Table 5 summarizes results of the numerical solution of equation (2) for the intraparticle pore sizes in the two Davisil silica materials and their admixture. In the admixture (1/1 by

weight), prepared with Davisil silica beads having the same particle size but two different intraparticle pore sizes (60Å and 150Å, respectively), the NMR experiment did not distinguish between them and yielded an intermediate pore size of 130Å (Fig. 1).

Assignment of pore sizes in the Borden aquifer material. The pore size distribution as determined from NMR relaxation of the water of saturation in the Borden aquifer (Hinedi et al., 1993) was found to be comparable to pore sizes evaluated by nitrogen adsorption and mercury porosimetry methods for the same aquifer material (Ball et al., 1990). The average pore sizes previously reported (Hinedi et.al., 1993) in the Borden aquifer material after 3 days of saturation are comparable to those in Fig. 3.

Scanning Electron Microscope (SEM) pictures showing a magnetite grain reveal that indeed the dissolution pits on the surface of the magnetite particle are on the order of a micrometer, which corresponds to the smaller pore size measured by NMR methods (Hinedi et al., 1993). It has been suggested that the source of the intraparticle porosity in the Borden aquifer was due to calcium carbonate coating (Ball et al., 1990). Based on NMR and SEM data, we contend that the iron and manganese oxides in the Borden aquifer material are another source of intraparticle porosity. Our observation is consistent with the one made by Johnson and Amy (1995) regarding the association of the magnetically susceptible mineral fraction (iron oxides etc.) with substantially higher surface area and fraction of organic matter compared to the nonmagnetic fraction. While the NMR evaluation of the porosity in the Borden material revealed a single intraparticle porosity domain, the persistence of that domain after magnetic separation suggests that the porosity scale of the two microporous fractions are not different enough to be distinguishable by NMR. We attribute the larger pore size detected in our NMR measurements to interparticle porosity. In addition, a comparison between the relative inter- and intra-particle pore population before and after demagnetization suggests that the magnetic fraction is particulate in nature and is characterized by both inter- and intra-particle porosity. The intraparticle porosity associated with the nonmagnetic fraction, on the other hand, is associated with coatings which lack the interparticle porosity character.

## NMR Diffusion Experiment

The PFG-NMR measurement provides a direct estimate of the self-diffusion coefficient in a porous matrix. The straight line showing the behavior of bulk water in Fig.4 is characterized (equation 4) by a slope of $(6Do)^{1/2}$ for water diffusing at $Do=2.98x10^{-9}$ $m^2s^{-1}$ and is plotted for comparison between unrestricted self-diffusion of water in the absence and presence of a porous matrix.

Using equation (4), a mean square displacement of 55 μm (Fig. 4) is calculated from a diffusion time of 300 ms and a corresponding diffusion coefficient of 1.67 $m^2s$ as D/Do starts becoming asymptotic to the diffusion time

axis . The mean square displacement thus calculated corresponds to the maximum displacement within an average pore. Pulsed Field Gradient-NMR methods, however, are $T_1$-biased and tend to overestimate the average pore size. This phenomenon occurs because, at longer observation times, signals from smaller pores with shorter relaxation time $T_1$ are lost. At longer diffusion times, the loss of NMR signals from small pores would bias the ratio of D/Do towards higher values. Nuclear magnetic resonance relaxation methods are better suited for pore size distribution evaluation.

At long diffusion times, the true macroscopic diffusion coefficient, also referred to as $D_{eff}$, and containing information of tortuosity, rather than pore size, is obtained from the reduced echo amplitude data. As the diffusing water molecules probe the connectivity of the pore space, the diffusion coefficient approaches the long-range interpore diffusivity and D/Do approaches $\tau^{-1}$, the inverse of the tortuosity of the pore space (Bear, 1972).

$$\frac{D}{D_0} = \frac{1}{\tau} \qquad (6)$$

The tortuosity in the sandy Eustis soil, as calculated by equation 6, is equivalent to $\tau^{-1} = 0.4$, which is consistent with tortuosity values measured in sandy soils (Shackelford and Daniel, 1991).

## Conclusions

The NMR relaxation of water imbibed in a packed bed of porous particulate matter (e.g. silica beads, soils, aquifer material) exhibits a bimodal distribution reflecting the existence of inter- and intra-particle porosity domains. The NMR relaxation method for pore size distribution characterization was evaluated for silica beads with different pore sizes and their admixtures. It was found that the pore sizes determined by NMR methods were comparable to sizes determined from nitrogen adsorption methods. In admixtures of silica beads with different pore sizes, NMR yielded an intermediate pore size. Pore size distribution measurements were made in the Borden aquifer materials before and after magnetic separation in an effort to assign porosity domains to various mineral phases. Intraparticle porosity was found to be attributable to particulate oxides (Fe, Mn) and calcium carbonate coatings. The self-diffusion coefficient of water measured by PFG-NMR methods provided information about tortuosity in the Eustis sandy soil.

## References


Ball, W. P., C. H. Buehler, T. C. Harmon, D. M. Mackay, and P. V. Roberts. 1990. Characterization of a sandy aquifer material at the grain scale. J. Contam. Hydrol. 5:253-295.

Bear, J. 1972. Dynamics offluids in porous media. Chapt. 4. American Elsevier Publ. Co., New York.

Bouma, J. 1981. Comment on "Micro-, Meso-, and Macroporosity of Soil". Soil Sci. Soc. Am. J. 45:1244-1245.

Gregg, S. J. and K. S. W. Sing. 1982. Adsorption, surface area and porosity. (Ed. 2) Academic Press, New York.

Hinedi, Z. R., Z. J. Kabala, T. H. Skaggs, D. B. Borchard, R. W. K. Lee, and A. C. Chang. 1993. Probing Soil and Aquifer Material Porosity with Nuclear Magnetic Resonance. Water Resour. Res. 29:3861-3866.

Johnson, W. P. and G. L. Amy 1995. Facilitated transport and enhanced desorption of polycyclic aromatic hydrocarbons by natural organic matter in aquifer sediments. Environ. Sci. Technol. 29:807-817.

Luxmoore, R. J. 1981. Micro-, Meso- and Macroporosity of Soil. Soil Sci. Soc. Am. J. 45:671-672.

Provencher, S. W. 1982. CONTIN: A general purpose constrained regularization program for inverting noisy linear algebraic and integral equations. Comput. Phys. Commun. 27:229-242.

Sardin, M., D. Schweich, F. J. Leij, and M. T. van Genuchten. 1991. Modeling the Nonequilibrium Transport of Linearly Interacting Solutes in Porous Media: A Review. Water Resour. Res. 27:2287-2307.

Shackelford, C. D. and D. E. Daniel. 1991. Diffusion in saturted soil. I. Background. J. Geotech. Eng. 117:467-484.

Stejskal, E. O. and J. E. Tanner. 1965. Spin diffusion measurements: Spin echos in the presence of a time dependent field gradient. J. Chem. Phys. 42:288-292.

van Genuchten, M.T. and P. J. Wierenga. 1976. Mass transfer studies in sorbing porous media I: Analytical Solutions. Soil Sci. Soc. Am. J. 40:473-480.

van Genuchten, M.T. and P. J. Wierenga. 1977. Mass transfer studies in sorbing porous media II: Experimental evaluation with Tritium ($^3H_2O$). Soil Sci.Soc.Am.J. 41:272-278.

Table 1. Physical Characteristics of model porous silica material

| Porous Matrix | Pore Size (Å) | Particle Size μm | Pore Volume mL/g |
|---|---|---|---|
| **Davisil** | 60 | 149-250 | 0.76 |
| | 150 | 149-250 | 1.1 |
| **Unibead** | <100 | 180-250 | NA |

Table 2. Weight fractions in admixutes of porous silica

| Porous Matrix | Weight Fraction |
|---|---|
| Davisil 60Å | 1 |
| Davisil 150Å | 1 |
| Davisil 60Å/150Å | 1/1 |

Table 3. Physical properties of the soil and aquifer material used in the study

| Porous Matrix | Sand % | Silt % | Clay % | Organic C % |
|---|---|---|---|---|
| Eustis | 95.5 | 3.2 | 1.3 | 0.39 |
| Borden | 100 | | | 0.02 |

Table 4. Chemical properties of the soil and aquifer material used in the study

| | Total Elemental Analysis, $mg.kg^{-1}$ | | | |
|---|---|---|---|---|
| **Porous Matrix** | Fe | Ca | Si | Al |
| Eustis | 663 | 438 | 403,000 | 2,240 |
| Borden Aquifer | | | | |
| Before Demagnetization | 16,700 | 44,640 | 310,000 | 56,430 |
| After Demagnetization | 2,520 | 35,230 | 301,000 | 51,660 |

Table 5. Numerical Solution of the parameters in eq. 2 for different silica materials

| **Porous Matrix** | $f^{intra\text{-}particle}$ | Pore Size Å |
|---|---|---|
| **Davisil 150Å** | 0.27 | 160 |
| **Davisil 60Å** | 0.18 | 64 |
| **Davisil 60Å/150Å** | 0.40 | 130 |

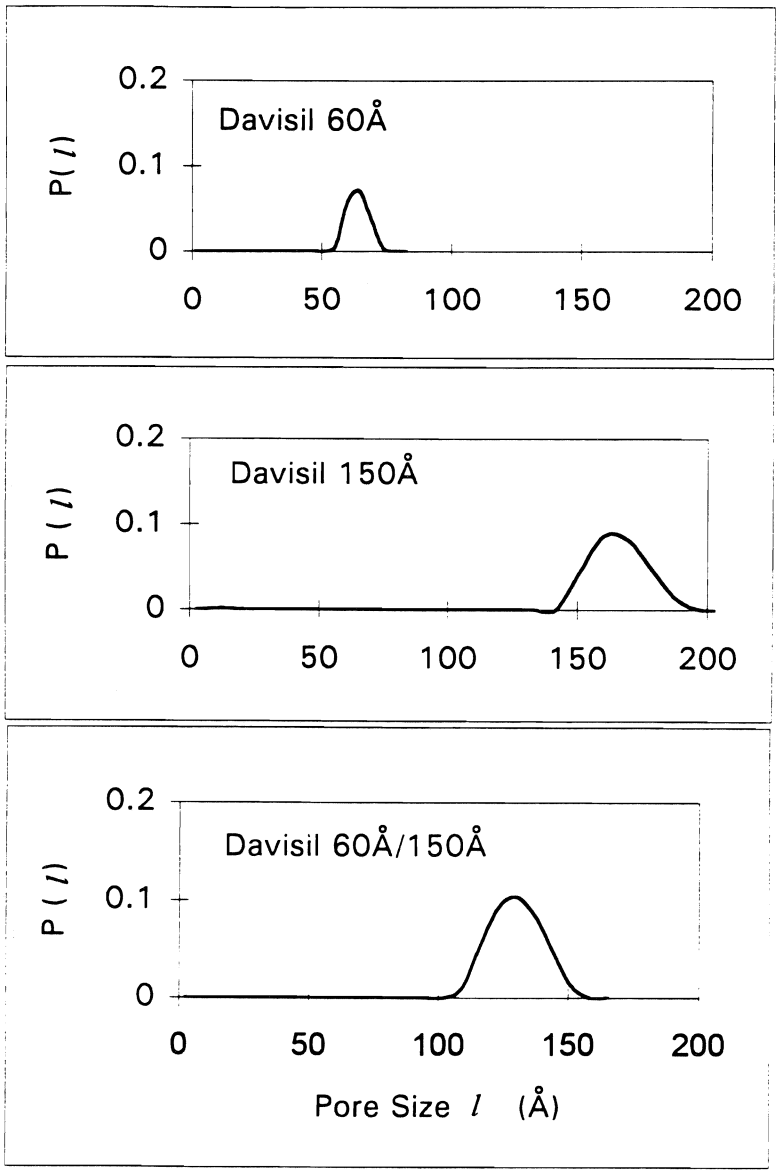


Figure 1. Intraparticle porosity in Davisil silica beads.

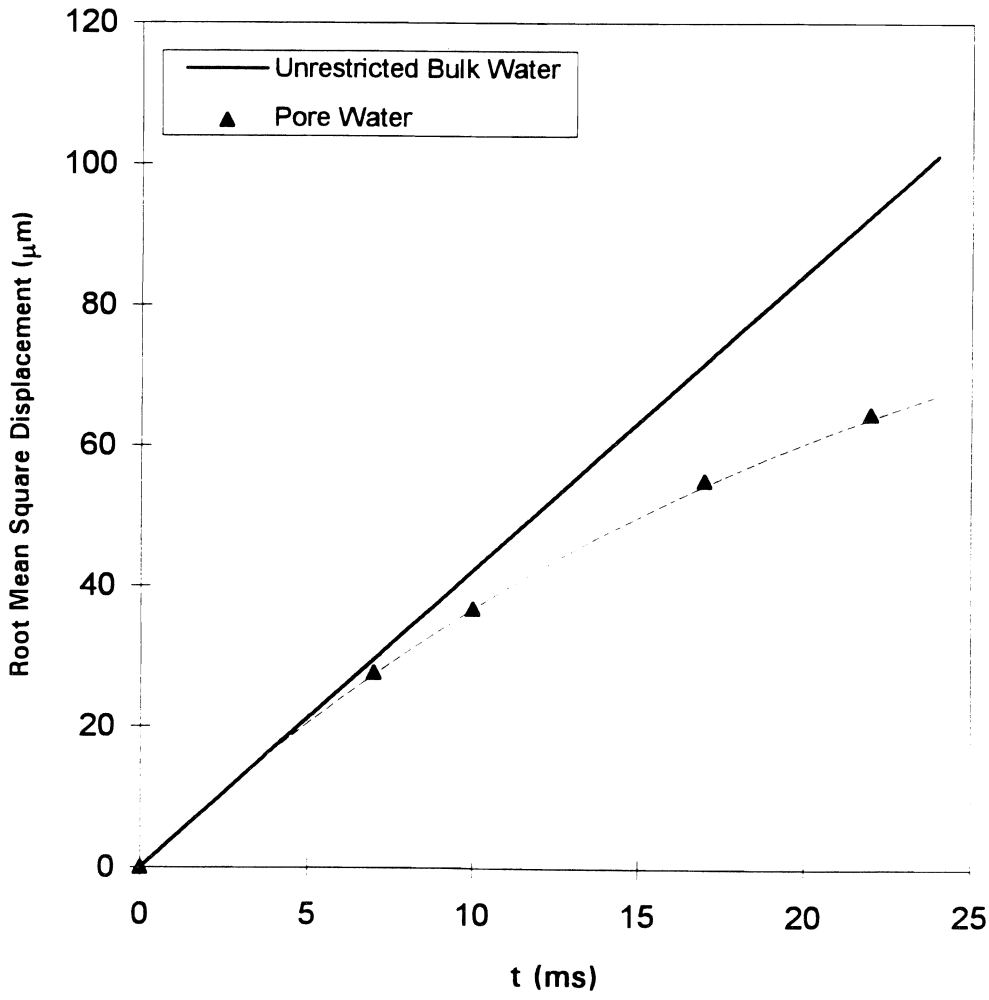


Figure 4. Mean square displacement for water in the Eustis soil.

# Dissolution of Nonaqueous Phase Liquids in Soil

WILLIAM A. JURY AND MICHAEL A. ANDERSON
*Department of Soil and Environmental Sciences, Riverside Campus*

## Summary

Nonaqueous phase liquids (NAPLs) such as oil products move through the soil by capillary forces, gravitational attraction, and forces induced by movement of other phases. As the NAPL moves, part of it becomes immobilized in the porous medium, either as films coating the particles or as ganglia trapped in the pore spaces. Once a chemical has reached residual saturation in a soil, the only way it can move within the medium is as a dissolved consituent of the flowing water or as a vapor if the soil is unsaturated (Schwille, 1988).

The rate of removal of residual NAPLs by dissolution into the surrounding flowing water determines how much of the surrounding water volume will ultimately be contaminated (Schwille, 1988). Obviously, it would be highly desirable to have a way of determining in advance the extent to which a particular NAPL will be removed from a spill volume by dissolution.

Although various models have been developed for the dissolution process, all of them depend on the interfacial contact area between the NAPL and the surrounding water. This feature makes them difficult to adapt to the natural environment where spill geometry is never known with a high degree of precision. Moreover, little experimental work has been conducted to test model hypotheses. In this report we use a modified form of the dissolving spheres model proposed by Geller and Hunt (1993) to describe NAPL dissolution, with and without the presence of surfactants. This model has a significant advantage over other approaches in that it depends on a single calibrated parameter (initial sphere radius). We have tested the model using two types of NAPLs in a series of experiments with and without surfactant addition.

This study reports experimental and theoretical results on the dissolution of NAPLs during leaching from saturated soil. A series of soil column experiments were performed with light and dense NAPLs leached by water and a surfactant solution, in which both column leachate and NAPL concentration in the soil were monitored, the latter by final sectioning of the column after varying amounts of leaching. A numerical transport model was developed based on the concept that the NAPLs were dissolving spheres immobilized in the soil that transferred mass to the solution by radial diffusion. The model was able to simulate dense NAPL dissolution in the column satisfactorily when an initial sphere radius of 0.07 cm was chosen, both for the water and surfactant leaching studies. The model was less successful when the light NAPL experiments were simulated, apparently because of NAPL particle mobilization during leaching. The presence of NAPLs altered solute transport through the columns somewhat, because the water velocity increased in regions where NAPLs blocked part of the pore space.

**Key Words:** chemical transport, surfactants, NAPL, rate process, remediation

## Project Objectives Addressed in 1993-94

1. Measure the dissolution rate constant of different NAPLs in a series of laboratory experiments.
2. Repeat the experiments in a binary mixture containing NAPLs and a surfactant added to speed up the dissolution process.
3. Develop a transport model describing the process.
   All of the objectives have been completed at this time.

## Research Plan and Procedures

## Materials and Methods

*Apparatus*: The column apparatus used for the experiments consisted of a glass column of 7.5 cm I.D. by 10 cm long equipped with aluminum end plates and Teflon© o-rings. Details of the apparatus and support equipment were provided in previous reports.

*Chemicals and porous material*: Two different nonaqueous phase chemicals were used in this study: a light nonaqueous phase liquid (LNAPL) o-xylene (1,2-dimethylbenzene), and a dense nonaqueous phase liquid (DNAPL) o-dichlorobenzene (1,2-dichlorobenzene). Witconol SN90, an ethoxylated alcohol, was selected for the surfactant-enhanced dissolution studies. This surfactant has a minimum effect on aggregate dispersion compared to other surfactants. A surfactant solution of 1% (volume surfactant/volume dionized water) was used in all the surfactant studies, which corresponds to a concentration of 10 mg $L^{-1}$.

The wavelengths used for analysis of the o-xylene and the o-dichlorobenzene with the UV-spectrophotometer, determined after testing, were 260 and 269 nm, respectively. All the water used during the experiments was deaerated, deionized, distilled water that was passed through a resin column (Barnstead, cat. no. D8901) to remove organic contaminants.

The experiments were conducted under water-saturated conditions in a coarse sand of 16 mesh (i.e., passes through a sieve with opening of 0.991 mm in diameter) composed mainly of quartz. For each experiment, the column was packed dry in 1-cm increments to a bulk density of 1.56 g $cm^{-3}$, and approximately 10 pore volumes were passed through the column at the flow rate selected for the experiments before any NAPL was added. A pulse of bromide was sent through the clean column to characterize the transport pathways in NAPL-free soil, after which the NAPL was introduced in the column.

It was difficult to obtain a reproducible, uniform, residual NAPL distribution in the column. The best method found was first to drain the column of its excess water and then to introduce the chemical in the column from the bottom. This method allowed the chemical to distribute throughout the sand column. Once

the chemical reached the top of the column, the excess was displaced with water. The chemical was displaced by applying water from the top for the DNAPL and from the bottom for the LNAPL. Once water appeared in the outflow, two more pore volumes of water were sent through to displace any remaining excess chemical. The chemical remaining in the column was at residual saturation.

*Sampling of the column*: For certain experiments, the chemical remaining in the column was analyzed before the dissolution process was completed. Just before sampling, the temperature was lowered by immersing the column in a bucket of ice. Then, the column was opened and sampled in 1-cm increments. The whole sampling procedure was completed within 10 minutes, and loss of the chemical by volatilization was minimal. The efficiency of the extraction method was 95% for o-xylene and 105% for o-dichlorobenzene.

*Water dissolution experiments*: Water dissolution experiments were conducted with both o-xylene and o-dichlorobenzene. After residual saturation was achieved in the column, deaerated water was added from the top and the outflow concentration was monitored. The outflow concentration was measured directly using the uv-spectrophotometer in the DNAPL experiments, since the outflow concentration was always at or below the water saturation value. For the LNAPL, outflow samples of about 10 ml were taken periodically using a gas-tight syringe and injected in 10 ml of methanol. This method was continued until the outflow concentration reached the water solubility value, after which the concentration was measured automatically. Three different experiments were conducted with the LNAPL. The first one consisted of continuous leaching of the residual LNAPL until the outflow concentration fell below detection limits. The second experiment was very similar, except that it was stopped when one-third of the chemical mass had been removed by dissolution and the distribution of the chemical remaining in the sand column was determined through column sampling. The third experiment consisted of the dissolution of LNAPL initially placed in the top 5 cm of the column. Only one water dissolution experiment was performed with the DNAPL, consisting of continuous leaching until one-third of the chemical mass was removed. At that point, the experiment was stopped and the column sampled.

*Enhanced removal with surfactant Witconol SN90*: In the surfactant studies, residual saturation of the chemical in the column was obtained as described previously. Once residual saturation was reached, the surfactant solution was introduced from the top of the column at the same flow rate as the previous experiments. Columns were then leached with the surfactant and sampled at various times. The analysis of the sand samples was conducted according to the method described in the previous section. When possible, the outflow was sampled in 30 minute intervals, then diluted in 250 mL volumetric flasks using methanol and analyzed using the UV-spectrophotometer. A number of surfactant dissolution experiments were conducted.

## One-Dimensional Transport and Dissolution Model

In previous years we developed and presented transfer function and mixing cell models of the transport and dissolution process. Although these models had the advantage of simplicity and ease of computation, they were applicable only to the early and intermediate stages of dissolution, because they could not take into account the influence of declining NAPL volume on mass transfer. In this year's research we developed and tested a numerical model that is able to describe all stages of the dissolution process in a physical manner. The approach is based on a conceptual model developed by Geller and Hunt (1993), in which the NAPL volume is treated as a network of identical spheres.

*Dissolving NAPL Spheres*: We assume that the medium is comprised of identical spheres of NAPL that always maintain a film of saturated concentration around them, but dissolve over time. The first step to understanding this problem is to solve the following model.

*Saturated Sphere in a Uniform Medium*: To envision the dissolution rate of a sphere, we first calculate the flux from a sphere of radius R that is always at a concentration $C^*$, which diffuses into an infinite medium of initially uniform concentration $C_0$. Thus, for r > R we solve

$$\frac{\partial C}{\partial t} = \frac{D}{r^2} \frac{\partial}{\partial r} \left(r^2 \frac{\partial C}{\partial r}\right) \tag{1}$$

subject to

$$C(R,t) = C^* \tag{2}$$

$$C(r,0) = C_0 \tag{3}$$

$$C(\infty,t) = C_0 \tag{4}$$

This has the solution (Carslaw and Jaeger, 1959)

$$C(r,t) = C_0 + (C^* - C_0) \frac{R}{t} erfc\left(\frac{r-R}{\sqrt{4Dt}}\right) \tag{5}$$

and the flux at the sphere's boundary is

$$J(R,t) = -D\left\{\frac{\partial C}{\partial r}\right\}_{r=R} = \frac{D(C^* - C_0)}{R}\left[1 + \frac{R}{\sqrt{\pi Dt}}\right] \tag{6}$$

Of more interest is the rate of mass loss ,Q(t), from the sphere

$$Q(t) = 4\pi R^2 J(R,t) = 4\pi RD(C^* - C_0)[1 + \frac{R}{\sqrt{\pi Dt}}] \qquad (7)$$

*Application to NAPL Dissolution*: The result for a single sphere does not translate unaltered to the transport problem, because the fluid flowing by the sphere is continually changing in concentration and the size of the spheres is decreasing from dissolution. Nevertheless, with some approximations and adjustments, the model can be adapted to the transport-dissolution problem.

The first approximation is that instead of a uniform initial concentration $C_0$ we use the local solute concentration $C_t(z,t)$ which is continually changing because of fluid movement. The effect produced by fluid movement is somewhat like starting over again with a new initial concentration for every pore volume. Therefore, the time parameter in (7) does not evolve but continually resets to zero. We can produce an approximate representation of this process by averaging Q over a time step $\Delta t$ while ignoring the slowly changing values of R and $C_0$. This produces

$$\bar{Q} \approx 4\pi RD(C^* - C_0)[1 + \frac{2R}{\sqrt{\pi D\Delta t}}] \qquad (8)$$

Now we assume that our NAPL mass is comprised of N identical spheres of initial radius R in the soil volume $V_S$, uniformly distributed with a density of $\xi(N)$ spheres per volume. The one-dimensional CDE solute transport equation for this system is

$$\frac{\partial C}{\partial t} + 4\pi R(z,t)\mathcal{D}\xi(N)[1 + \frac{2R(z,t)}{\sqrt{\pi D\Delta t}}](C - C^*) = D\frac{\partial^2 C}{\partial z^2} - V\frac{\partial C}{\partial z} \qquad (9)$$

where D is the local diffusion coefficient for the dissolved organics in soil water, D is the macroscopic longitudinal dispersion coefficient, and the notation R(z,t) is used to denote the dissolution of the spheres at a given depth in the soil.

The dissolution process can be modeled with the NAPL mass balance equation, which may be written for an individual sphere as

$$\rho_N \frac{\partial V_N}{\partial t} = -\bar{Q} = 4\pi R(z,t)\mathcal{D}[1 + \frac{2R(z,t)}{\sqrt{\pi\mathcal{D}\Delta t}}](C(z,t) - C^*) \qquad (10)$$

where $V_N$ is the volume of the sphere. Plugging in the volume formula and rearranging, we obtain

$$\frac{\partial R(z,t)}{\partial t} = \frac{\mathcal{D}}{\rho_N R(z,t)}[1 + \frac{2R(t)}{\sqrt{\pi \mathcal{D} \Delta t}}](C(z,t) - C^*) \tag{11}$$

Note that we can write (9) as

$$\frac{\partial C}{\partial t} = h(R(z,t))(C - C^*) = D\frac{\partial^2 C}{\partial z^2} - V\frac{\partial C}{\partial z} \tag{12}$$

where

$$h(R(z,t)) = 4\pi R(z,t)\mathcal{D}\xi(N)[1 + \frac{2R(z,t)}{\sqrt{\pi \mathcal{D} \Delta t}}] \tag{13}$$

is the mass transfer coefficient for the system. As the spheres dissolve, h becomes smaller, which will decrease the release of mass to the solution, thereby allowing NAPL located downstream to begin dissolving before the NAPL upstream is completely dissolved.

Inspection of (11) reveals that the radius will increase its shrinking rate as the radius decreases, and the concentration gradient should also increase as the overall transfer to the dissolved phase decreases. However, the rate of decrease in volume will slow as time progresses.

*Parameter Identification*: The local value of D is just the liquid diffusion coefficient, modified to account for the effects of the porous medium. Since the volumetric NAPL content $\eta_0$ is observable or can be estimated, we can relate it to the NAPL sphere density $\xi(N)$ and the initial radius $r_0$ by the formula

$$\frac{4\pi\, r_0^3 \xi(N)}{3} = \eta_0 \tag{14}$$

or, alternatively, in terms of the initial NAPL mass density $\Omega_0 = \rho_N \eta_0$ (mass of NAPL/volume of soil). Thus, the only parameter that cannot be estimated independently is the initial sphere radius $r_0$.

*Reformulation in Terms of NAPL Mass Density Ω:* Since the radius cannot be observed, it is useful to reformulate the dissolution equation (10) in terms of the measurable macroscopic NAPL mass density variable

$$\Omega = \rho_N \eta = \rho_N V_N \xi(N) = \rho_N \eta_0 \frac{V_N}{V_0} = \Omega_0 \frac{V_N}{V_0} = \Omega_0 (\frac{R}{r_0})^3 \tag{15}$$

This can be substituted into (10) for R, with the result

$$\frac{\partial \Omega}{\partial t} = (A\Omega^{1/3} + B\Omega^{2/3})(C(z,t) - C^*) \tag{16}$$

where

$$A = 3\eta_0^{2/3} r_0^{-2} \mathcal{D} \rho_N^{-1/3} \tag{17}$$

$$B = \frac{6\eta_0^{1/3} r_0^{-1} \mathcal{D} \rho_N^{-2/3}}{\sqrt{\pi \mathcal{D} \delta t}} \tag{18}$$

With this change, the solute transport equation (12) can be written as

$$\frac{\partial C}{\partial t} + \frac{1}{\theta} - \frac{\partial \Omega}{\partial t} = D\frac{\partial^2 C}{\partial z^2} - V\frac{\partial C}{\partial z} \tag{19}$$

Equations (16)-(19) are solved numerically, subject to the following initial and boundary conditions:

$$J_s(0,t) = 0 \tag{20}$$

$$\frac{\partial C}{\partial z}(L,t) = 0 \tag{21}$$

$$\Omega(z,0) = \rho_N \eta_0 \tag{22}$$

$$C(z,0) = C_i \tag{23}$$

## Results and Discussion

**Effect of NAPLs on Solute Movement.** Pulses of bromide were periodically sent through columns with and without NAPLs to determine if the transport process was being disrupted by NAPLs blocking the pores, and if the transport properties changed over time as the NAPL dissolved. Figure 1 shows the outflow concentrations from pulses sent through a column filled with a LNAPL at various times during leaching. The Mobile-Immobile Water Model (MIM) (van Genuchten and Wierenga, 1976) fit the data the best, and the decrease in apparant velocity shows that as the leaching process progresses, more of the void space is occupied by water and the mean solute velocity decreases somewhat.

**Outflow Concentration During Dissolution with Water.** Figure 2 shows the solute concentration leaving the column for the LNAPL o-xylene as a function of the number of pore volumes leached. The outflow concentration for o-xylene in the first part of the dissolution experiment was erratic and above the

solubility value of the chemical in water. This erratic behavior may be caused by the escape of some droplets of non-dissolved chemical from the column. Geller and Hunt (1993) observed a similar phenomenon for toluene, a closely related LNAPL.

**Residual NAPL Saturation During Dissolution with Water.** Experiments where the resident NAPL saturation was measured after a specified amount of chemical was leached out of the column were performed with both the LNAPL and the DNAPL. The outflow concentration for both the LNAPL and the DNAPL remained at or above water solubility when the experiment was stopped. The results for the final chemical distribution in the sand column were analyzed using the dissolving sphere model. For the DNAPL, the results are presented in Fig. 3. For a given water content, all the parameters in the model were kept fixed, except for the initial radius of the NAPL spheres, $r_0$, which fit the data best when assigned a value of 0.045 cm. The dispersivity was fixed at 0.1 cm, which gives values for the diffusion-dispersion coefficient D close to the values evaluated with the tracer pulses. The values for the local diffusion coefficients of o-xylene and o-dichlorobenzene were estimated following Schwarzenbach et al. (1993). The effect of the soil was taken into account by multiplying the diffusion coefficient by a tortuosity factor estimated using the Millington-Quirk relationship. For $\theta = 0.41$, the values obtained for each chemical are 0.3026 $cm^2\ d^{-1}$ for o-xylene and 0.2576 $cm^2\ d^{-1}$ for o-dichlorobenzene. Once we calibrated the model on the DNAPL from this experiment, the model was used to simulate all other DNAPL runs in water. The resulting agreement is quite good and significantly better than we were able to achieve with any other model.

The same analysis was performed with the LNAPL (Fig. 4), this time producing an optimum agreement when a value $r_0 = 0.06$ cm was chosen and the water solubility of the chemical was set at the average value (219 mg $L^{-1}$) of the outflow during the leaching period prior to sampling (see Fig. 2). In both cases, the model predictions were not very sensitive to radius size, as long as the value selected was of the same order as the largest pore size. Since our sand was screened to exclude particles larger than 1.18 mm diameter, initial radius values of the order of 0.5 mm are reasonable approximations for a NAPL trapped in our sand.

**Surfactant-Assisted NAPL Dissolution.** The removal of both chemicals from the sand column was greatly increased when a surfactant solution of 1% SN90 was added at the inlet end as compared to clean water. Table 1 summarizes the results obtained for both chemicals with different times of leaching with the surfactant solution. Figure 5 shows the DNAPL residual saturation for various pore volumes of leaching with the surfactant solution, and Fig. 6 shows the corresponding outflow concentration as a function of pore volumes leached. The removal of the DNAPL from the column seems to be more efficient after 6-11 pore volumes of surfactant solution were passed through the column. From the outflow analysis, we see an increase in the rate of the mass of chemical removed after 6 pore volumes. From Fig. 5, the removal seems to be less efficient after 11 pore volumes. For the 2 and 6 hours of

washing, the removal seems to be gradual and the shapes of the curves are similar to the ones for the dissolution experiment in water, with an increase in solubility. At 9 hours, the distribution of the chemical remaining in the column increases more linearly with depth. It seems that after 6 pore volumes, the chemical is not only removed by solubilization in the surfactant solution, but it is also mobilized (Fig. 6). This can also be seen from the percentage of chemical removed from the column (Table 1).

The results for the LNAPL are different and are presented in Figs. 7 and 8. The removal of o-xylene by the surfactant solution is much less efficient than that of o-dichlorobenzene. This can be seen in Table 1 where, for 5.6 and 8.4 pore volumes of leaching with SN90,1%, 23.4% and 54.7%, respectively, of o-dichlorobenzene were removed from the column, while only 11.9% and 46.3%, respectively, of o-xylene were removed. The distribution of the remaining o-xylene in the column (Fig. 7) seems to stay the same with depth, except for a decrease in the amount remaining as the number of pore volumes of surfactant solution increases. The top layer of the column contains more chemical, which is attributed to the density of the chemical. Some of the chemical removed near the top of the column tends to float and accumulate close to the first layer. From the analysis of the outflow, the removal of the LNAPL by the surfactant seems to increase exponentially with time of washing.

The medium used for the experiments did notcontain any clay and silt particles, so that dispersion of the particles and blockage of the pores due to the surfactant were never observed. The mobilization of the chemical might not be as high if the texture of the contaminated soil is fine. But, for sandy aquifer remediation, this method seems to be very efficient.

## Conclusions

From this research we were able to draw a number of conclusions about NAPL dissolution.

1. This study revealed substantial differences between the behavior of LNAPLs and DNAPLs. The LNAPL immobilized only after hundreds of pore volumes of leaching, and even then was not completely trapped during the leaching process. In contrast, the DNAPL quickly immobilized and remained in place during virtually the entire leaching process.

2. The dissolving spheres model was very successful at describing DNAPL dissolution in water when an initial sphere radius of 0.045 cm was chosen, which is large enough to be immobilized within the pore size of the sand sample chosen. The model was also successful in describing the LNAPL dissolution with an initial NAPL radius of 0.06 cm, provided that an average value was used for the solubility based on the outflow concentration prior to sampling.

3. The dissolving spheres model was also reasonably successful at describing DNAPL dissolution in the surfactant when an initial sphere radius of 0.045 cm was chosen, provided that the solubility was raised to a high level.

4. The NAPL increased the speed of solute movement somewhat in the column experiments, implying that the water velocity increased in regions where the NAPL filled part of the pore space. It is not clear what effect this would have in a multidimensional flow field where the water could migrate around the NAPL-contaminated zone.

5. The dissolving spheres model is easily adaptable to two-dimensional flow and transport problems, where the dissolution of finite volumes of NAPL can be simulated as a function of NAPL size and shape. We are currently studying this problem.

## References


Carslaw, H. S. and J. C. Jaeger. 1959. Conduction of Heat in Solids. Oxford University Press, London.

Geller, J. T. and J. R. Hunt. 1993. Mass transfer from nonaqueous phase organic liquids in water-saturated porous media. Water Resour. Res. 29:833-845.

Schwarzenbach, R. P., P. M. Gschwend and D. M. Imboden, 1993. Environmental Organic Chemistry, John Wiley & Sons, New York.

Schwille, F., 1988. Dense Chlorinated Solvents in Porous and Fractured Media: Model Experiments. Lewis Publications, Chelsea, MI, 146 pp.

van Genuchten, M.Th. and P. J. Wierenga, 1976: Mass transfer studies in sorbing porous media. 1. Analytical solutions. Soil Sci. Society of America J. 40, 473-480.

Table 1. Summary of the surfactant experiments.

| Chemical | Reference number | Leaching time (hrs) | Pore volumes | Initial amount of chemical (mL) | Amount remaining (mL) | Percentage removed (%) |
|---|---|---|---|---|---|---|
| ODCB | 22 | 2 | 1.87 | 23.1 | 20.1 | 13.0 |
| | 18 | 6 | 5.60 | 20.4 | 13.5 | 33.8 |
| | 23 | 6 | 5.60 | 18.4 | 14.1 | 23.4 |
| | 26 | 9 | 8.41 | 22.3 | 10.1 | 54.7 |
| | 25 | 9 | 8.41 | 19.8 | 7.4 | 62.6 |
| | 24 | 12 | 11.21 | 21.1 | 2.7 | 87.3 |
| | 20 | 16 | 14.95 | 18.8 | 2.0 | 89.4 |
| | 17 | 33 | 30.83 | 27.3 | 2.4 | 91.2 |
| | 21 | 36 | 33.63 | 23.8 | 0.3 | 98.7 |
| OX | 28 | 6 | 5.60 | 32.9 | 29.0 | 11.9 |
| | 29 | 9 | 8.41 | 33.7 | 18.1 | 46.3 |

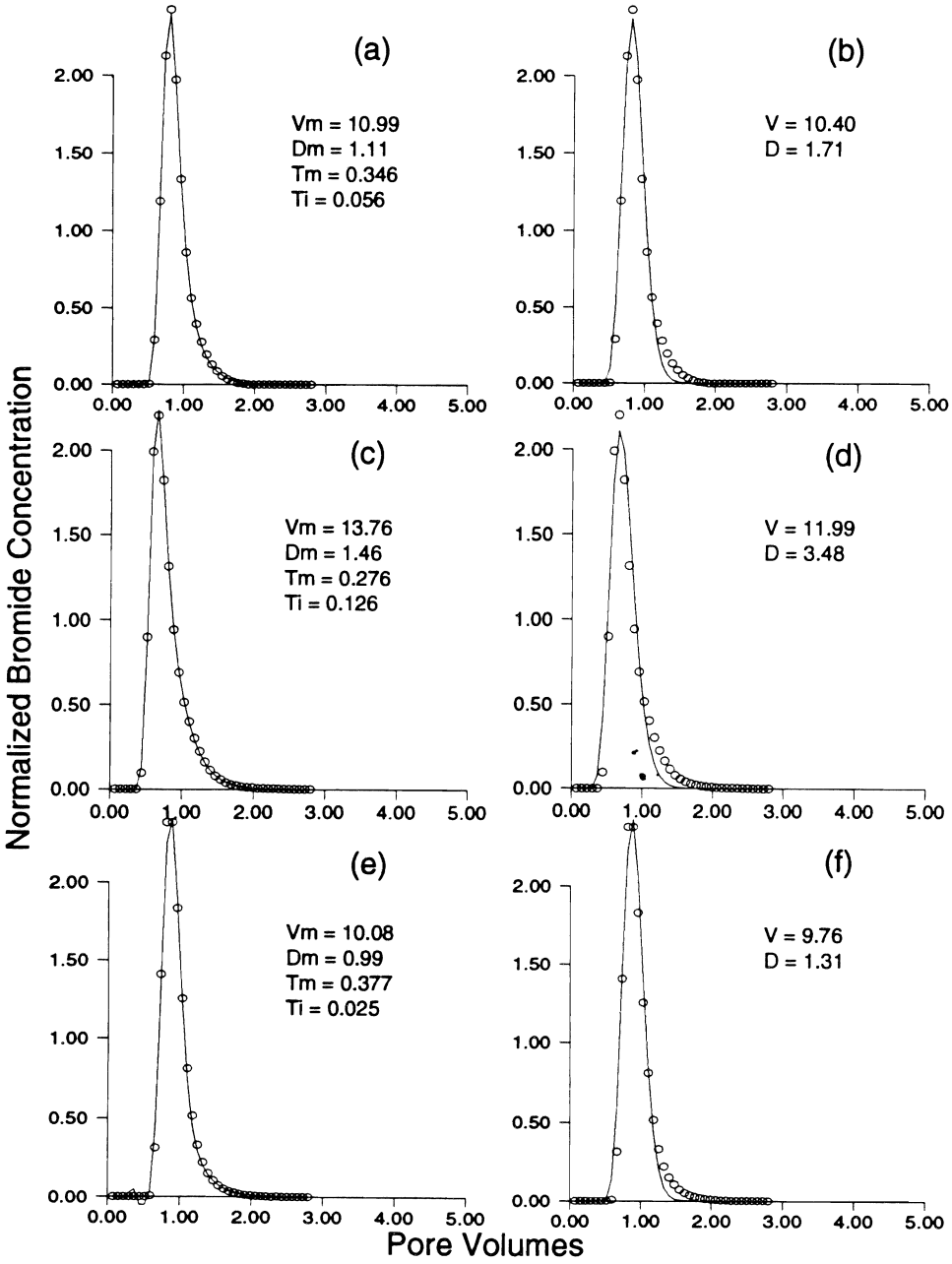


Figure 1. Analysis of the tracer pulses of Br- for Column 4. The breakthrough curves in (a) and (b) are from the same pulse in the clean column; (c) and (d) are after 38 pore volumes of water and (e) and (f) are after 312 pore volumes of water. The results in (a), (c) and (e) were analyzed using the MIM; the results in (b), (d) and (f) were analyzed using the CDE. The solid line represents the model.

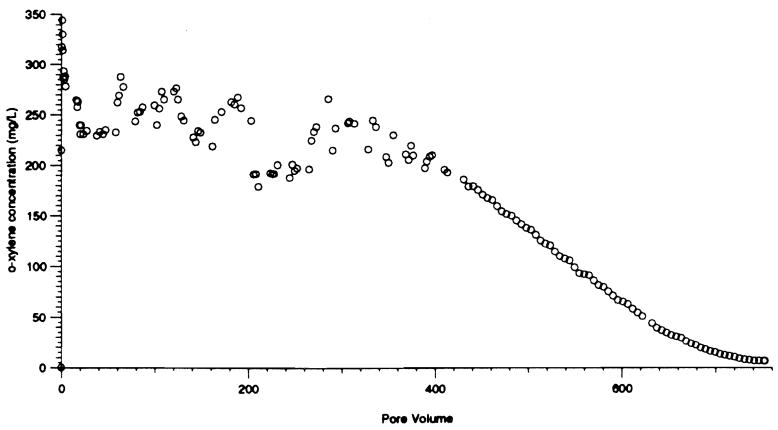


Figure 2. Outflow concentrations for the dissolution of o-xylene in water.

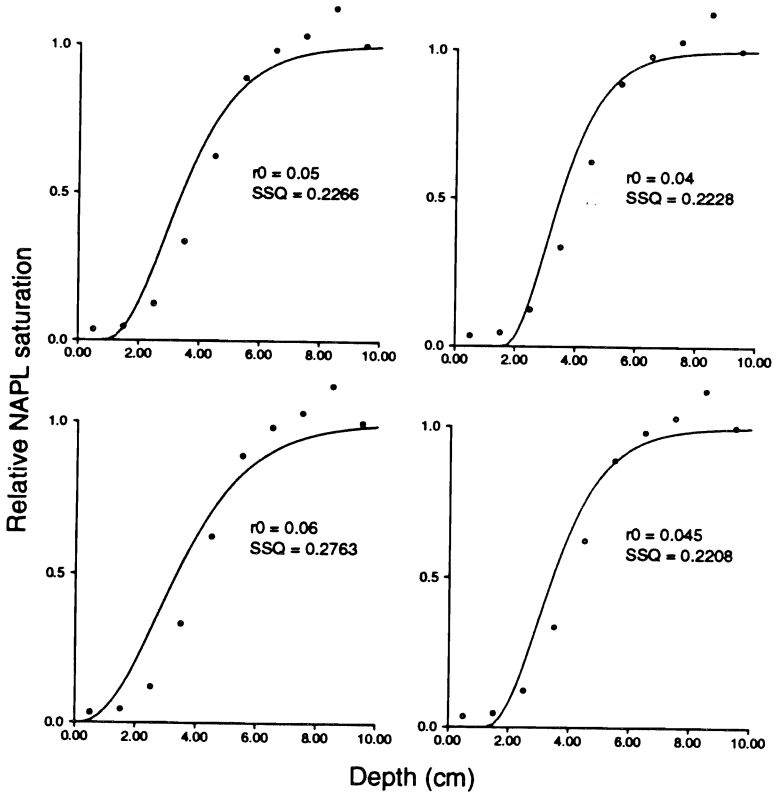


Figure 3. O-dichlorobenzene distribution in a sand column after 403 pore volumes of water. Initial residual saturation: 0.0533. The solid line is the result for the model using $J_w$ = 91 cm day$^{-1}$, V = 9.35 cm hr$^{-1}$, D = 0.93 cm$^2$ hr$^{-1}$, $D^s_{org}$ = 0.26 cm$^2$ day$^{-1}$, and $\theta$ = 0.41. $r_0$ is the initial sphere radius in the model (cm).

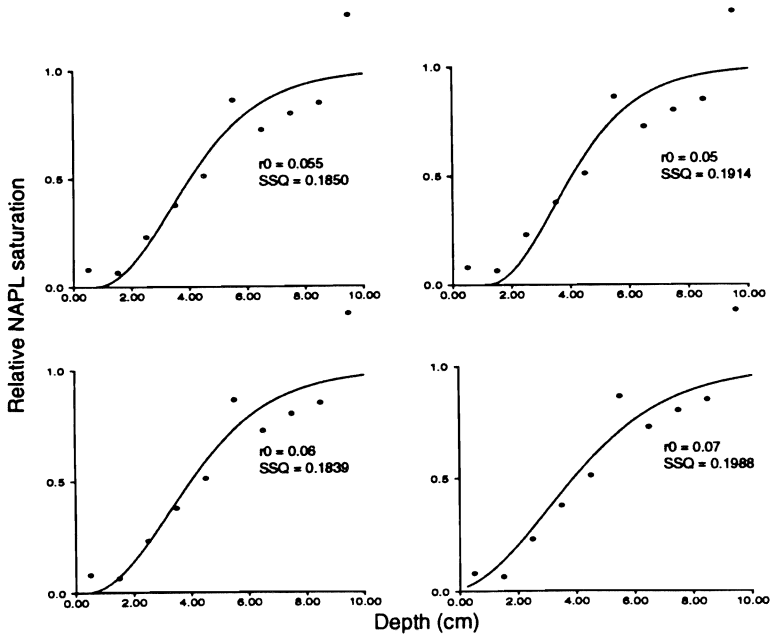


Figure 4. O-xylene distribution in a sand column after 216 pore volumes of water for different values of initial NAPL radius $r_0$. (Column 27) Initial residual saturation: 0.0502. The solid line is the result for the model using $J_w$ = 91 cm day$^{-1}$, V = 9.35 cm hr$^{-1}$, D = 0.94 cm$^2$ hr$^{-1}$, $D^s_{org}$ = 0.30 cm$^2$ day$^{-1}$, and $\theta$ = 0.41.

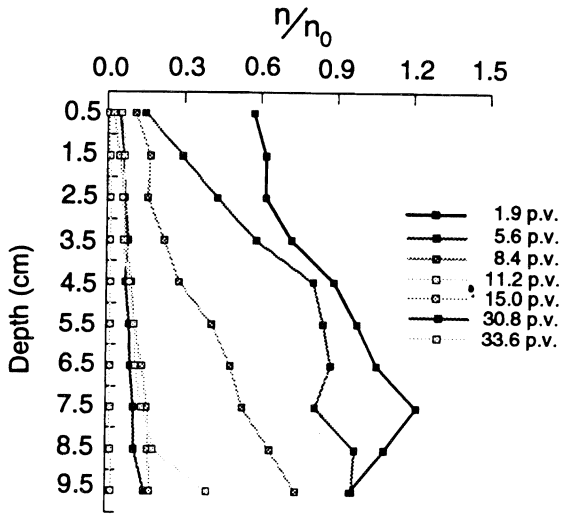


Figure 5. O-dichlorobenzene distribution in the column after different pore volumes (pv) of washing with the solution of SN90 1%.

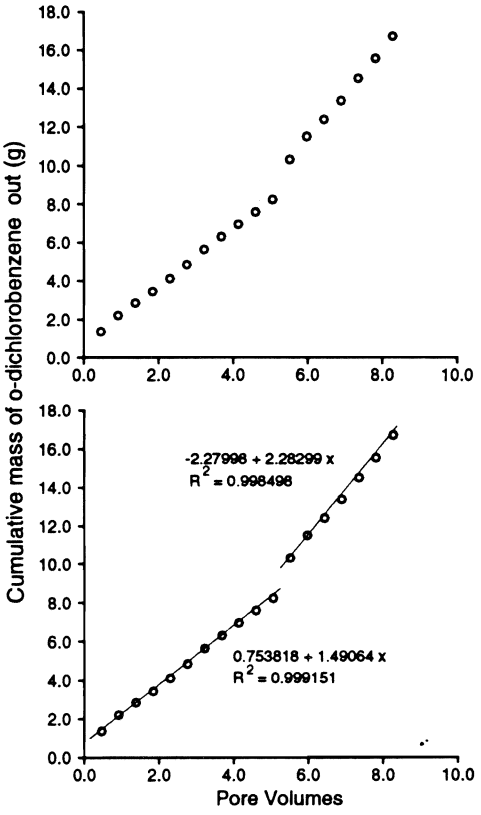


Figure 6. Outflow analysis for the surfactant washing of o-dichlorobenzene.

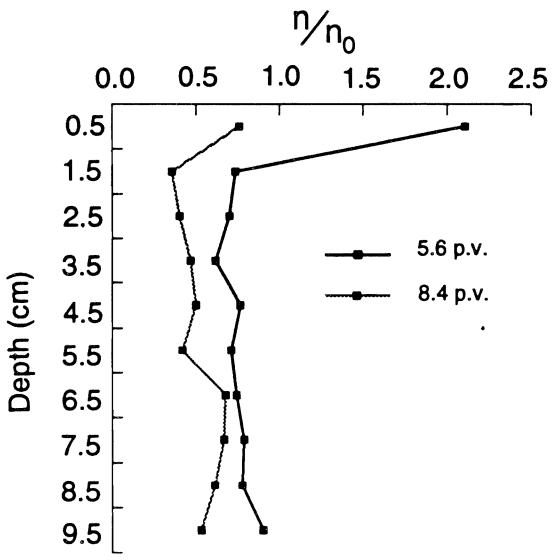


Figure 7. O-xylene distribution in the column after 5.6 and 8.4 pore volumes of washing with the solution of SN90 1%.

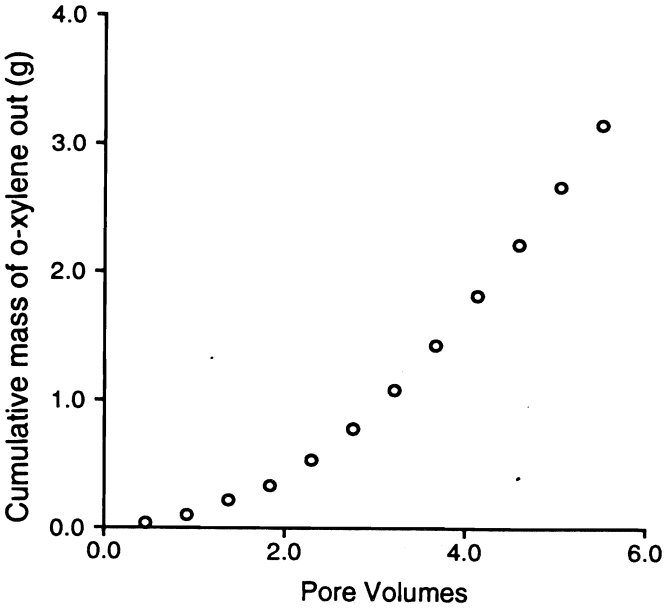


Figure 8. Outflow analysis for the surfactant washing of o-xylene.

# Characterizing Organic Chemical Sorption-Desorption Hysteresis with a Two-Site, Rate-Limited Mass Transfer Model

WILLIAM A. JURY AND WALTER J. FARMER
*Department of Soil and Environmental Sciences, Riverside Campus*

## Summary

This study was conducted to reconcile an apparent inconsistency between the simazine laboratory sorption isotherm data and the field lysimeter transport experiment reported in Poletika (1993). In this investigation, linear and nonlinear one- and two-stage simazine sorption models were fitted to sorption and desorption isotherm laboratory data to obtain parameter estimates for use in the transport model. Once obtained, the calibrated sorption model was combined with the parameterized outflow concentration record from a mobile Br tracer to represent rate-limited sorption and transport of the simazine added simultaneously with the Br. The calibrated model did an excellent job of representing the final simazine profile in the soil, particularly with the nonlinear model. This result is in contrast to a single-stage adsorption model, which reached poor agreement with the field profile when laboratory-measured sorption parameters were used. The results demonstrate the compatibility of field and laboratory experiments on pesticide movement, and also indicate that sorption isotherms may require substantially longer to reach equilibrium than is customarily allowed in current protocols.

**Key Words:** chemical transport, pesticide transport, adsorption, batch equilibrium isotherm

## Project Objectives Addressed in 1993-94

The following objectives for this project were stated in the proposal submitted to the Kearney Foundation last year:

1. To develop organic chemical transport models, using linear and nonlinear two-stage adsorption;
2. To use existing experimental information on adsorption-desorption hysteresis of Simazine in the study of Poletika (1993) to develop an estimation method for determining the parameters in the two-stage model,
3. To use the fitted parameters in the transport model to predict the movement of Simazine measured by Poletika, and to reinterpret the pesticide transport observed by ElAbd (1984);
4. To use the two-stage model to evaluate the information actually measured in a typical adsorption isotherm determination, and to compare the predictions of a transport model using that information with the behavior predicted by the two-stage model;
5. To use the two-stage model to make predictions about what would actually happen in an adsorption-desorption isotherm measurement with different equilibration times;
6. To make adsorption-desorption isotherm measurements to test predictions made in step 5.

Of these objectives, all have been completed at this time except for the last one, which is in progress and will be completed without additional funding.

## Research Plan and Procedures

**Background.** The sorption isotherm is a standard tool for the characterization of organic partitioning between the dissolved and the sorbed phases. It is a plot of the mass of chemical per solution volume dissolved at equilibrium versus the mass of chemical sorbed per unit mass of soil matrix. Sorption isotherms are commonly measured in so-called batch experiments, in which soil is added to a volume of solution in which the chemical of interest has been dissolved. The resulting suspension is shaken continually until equilibrium is believed to be achieved. After measuring the solution concentration of the chemical, the mass sorbed is calculated from the mass balance, and the two phase concentrations are entered as a point on the sorption isotherm. For many years, periods between 1 and 48 hours were generally considered sufficient for equilibration (Rao and Davidson, 1980; Calvet, 1980). In particular, kinetic studies conducted on simazine adsorption in a number of soils showed that equilibrium adsorption levels were reached in this time period, especially in soils low in organic C (Talbert and Fletchall, 1965; Day et al., 1968; Williams, 1968).

Many organic chemicals have shown pronounced hysteresis between sorption and desorption loops of the isotherms. Although apparent hysteresis has also been explained by biodegradation (Koskinen et al., 1979), or by

sorption to nonfilterable organic matter (Gschwend and Wu, 1985), there is now increasing evidence that in many cases hysteresis is an experimental artifact caused by slow sorption kinetics (Boesten and van der Pas, 1988; Miller and Pedit, 1992), implying that equilibrium may not be attained in many batch experiments. The conventional assumption that equilibrium is attained in 24 hr or less is due at least in part to the fact that the sorption of organic chemicals proceeds at two time scales, in which a rapid initial uptake (minutes or hours) is followed by a much slower approach to equilibrium (days, weeks, or even months) (Wu and Gschwend, 1986; Brusseau and Rao, 1989a; Ball and Roberts, 1991).

Nonattainment of equilibrium in a batch experiment will have two major consequences. First, the measured partition coefficient will be smaller than the true one, resulting in an overestimation of organic chemical mobility in soil. Second, additional spreading (i.e., early or late arrival), which will be significant if the pore water velocity is large compared to the time scale of equilibration, is not accounted for in an equilibrium approach.

In this study we evaluated the ability of various linear and nonlinear nonequilibrium sorption models to predict, without curve fitting, the simazine concentration profiles measured by Poletika (1993). He used a single-site rate-limited linear adsorption model to represent simazine transport through a field lysimeter containing undisturbed, unsaturated soil and achieved good agreement, but only when a value for the sorption coefficient was used that was greatly in excess of the one measured in a batch isotherm lab measurement using 24-hour equilibration times. In our study, independent estimation of all parameters was achieved by analysis of the inert tracer experiment and the sorption-desorption isotherms measured by Poletika (1993).

**Materials and Methods.** The project used data obtained from the dissertation field and laboratory study of Poletika (1993), which will be briefly summarized here. Batch and field experiments were performed with Tujunga loamy sand (organic carbon content: 0.5-0.7% by weight; bulk density: 1.45 kg $L^{-1}$ in top 0.2 m.

*Batch experiment*: 20 mL of 0.01 N $CaCl_2$ containing 0.015, 0.06, 0.15, 0.6, and 1.5 mg $L^{-1}$ $^{14}C$-labeled simazine were added to Teflon tubes each containing 10 g of oven-dried equivalent of soil. The tubes were shaken for 24 h and then centrifuged. Ten mL of the supernatant solution were removed, analyzed for simazine by liquid scintillation counting and replaced by 10 mL of simazine-free 0.01 N $CaCl_2$. The tubes were shaken for another 24 h and centrifuged. Again, 10 mL of supernatant solution were removed, analyzed for simazine, and replaced by 10 mL of 0.01 N simazine-free $CaCl_2$.

*Transport experiment*: By digging out the underlying soil, a lysimeter with 0.8 m x 0.8 m surface area and a vertical extent of 0.3 m was constructed at the field site. Sixty-four fiberglass capillary wick solution samplers, each covering an area of 0.1 m x 0.1 m, were installed underneath the lysimeter to collect the drainage water. After the lysimeter was draining at a nearly steady rate of 20

mm $d^{-1}$, a pulse input of 4 mm of a solution containing 1598 mg $L^{-1}$ bromide and 0.37 mg $L^{-1}$ simazine was applied. During the following ten days drainage water was collected four to five times daily and analyzed for both solutes. While this time period was sufficient to measure the complete breakthrough of the bromide pulse, only negligible amounts of simazine could be detected. The total amount of drainage water collected was 197 mm. During the 10-d breakthrough experiment, no measurable degradation occurred. This was verified with soil samples spiked with simazine which had been buried adjacent to the lysimeter at the 0.15 m depth. After the end of the breakthrough experiment, ten locations in the lysimeter were chosen in a random manner for final sampling. At these locations 0.1 m x 0.1 m soil samples were taken in 2.5 cm depth increments and analyzed for simazine by repeated methanol/water extraction.

**Parameter Estimation.** Parameters of the sorption-desorption models tested in this study were estimated by minimizing the sum of squared residuals using the Levenberg-Marquardt algorithm (Press et al., 1988). We used both an additive (AEM) or multiplicative error model (MEM), the latter minimizing the sum of squared residuals of the log-transformed data and model.

**Sorption Equations.** The basic hypothesis behind our two-stage sorption model is that the sorbent can be subdivided into two regions (I and II) of different accessibility. While region I is in direct contact with the bulk solution, region II exchanges only with region I. In soil, where organic chemicals are mainly sorbed on organic matter, sorbents may be envisioned as separate particles or as coatings on mineral surfaces. Assuming a Freundlich type equilibrium adsorption at the surface between bulk solution and region I yields the following sorption rate equations:

$$f\frac{\partial S_1}{\partial t} = \alpha_1(kC^m - S_1) - a_2(S_1 - S_2) \qquad (1)$$

$$(1-f)\frac{\partial S_2}{\partial t} = a_2(S_1 - S_2) \qquad (2)$$

where $C$ (mg $L^{-1}$) denotes the concentration of dissolved chemical; $S_1$ and $S_2$ (mg $kg^{-1}$), the concentrations of sorbed chemical in region I and region II (mg $kg^{-1}$ soil), respectively; $f$ the fraction of region I sites; $k$ ($mg^{1-m}$ $L^m$ $kg^{-1}$), the Freundlich distribution coefficient, and $m$ (dimensionless) the Freundlich exponent. The rate coefficients $\alpha_1$ and $\alpha_2$ ($d^{-1}$) are given by:

$$\alpha_1 = A_1^* k_1^* \quad \alpha_2 = A_2^* k_2^* \qquad (3)$$

where $A_1^*$ and $A_2^*$ are the specific surface areas ($m^2$ $kg^{-1}$ soil) between bulk solution and region I and between region I and region II, while $k_1^*$ and $k_2^*$ (kg $m^{-2}$ $d^{-1}$) are lumped mass transfer coefficients. The total mass of solute per unit soil volume is given by:

$$C_t = \theta C + \rho S \tag{4}$$

where $\rho$ and $\theta$ denote bulk density and volumetric water content, respectively, and

$$S = f S_1 + (1 - f)S_2 \tag{5}$$

If the sorption to region I sites is fast compared to the time scale of the experiment, we can assume equilibrium between bulk solution and region I sites, so that

$$S_1 = kC^m \tag{6}$$

while (2) remains unchanged. In the following, we will refer to this model as the two-stage, one-rate model. Note that it is equivalent to the adsorption-desorption model of Brusseau et al. (1989), if we set $m = 1$ and $\alpha_2 = (1 - f)k_2$ where $k_2$ denotes the desorption rate constant in their model (Brusseau et al., 1991). We will refer to the model defined by (1) and (2) as the two stage-two rate model. Note that both the two-stage, one-rate and the two stage-two rate models predict the same equilibrium concentration in the solid phase, namely:

$$S = S_1 = S_2 = kC^m \quad (t \rightarrow \infty) \tag{7}$$

**Batch Experiment.** If decay is negligible, the mass balance in a closed batch system can be stated as:

$$\frac{dC_t}{dt} = 0 \tag{8}$$

By combining (8), (4)-(6), and the sorption rate equation (2), the two-stage, one-rate model may be written as:

$$(\rho f m k C^{m-1} + \theta)\frac{\partial C}{\partial t} = \frac{\alpha_2}{(1-f)}[C_t - \theta C - \rho k C^m] \tag{9}$$

which is subject to the initial condition:

$$C(0)=C_0 \tag{10}$$

Similarly, after combining (1), (2), (4), (5), and (8), the two stage-two rate model can be written as:

$$\frac{\partial C}{\partial t}=\frac{\alpha_1}{f\theta}[C_t-\theta C-\rho(1-f)S_2-\rho fkC^m] \tag{11}$$

$$\frac{\partial S_2}{\partial t}=\frac{\alpha_2}{\rho f(1-f)}[C_t-\theta C-\rho S_2] \tag{12}$$

Equations (11)-(12) are subject to the initial phase conditions:

$$C(0) = C_0 \qquad S_2(0) = S_{20} \tag{13}$$

The linear forms (i.e., m = 1) of (9) and (11)-(12) were solved analytically, and the nonlinear forms numerically by Runge-Kutta integration (Press et al., 1988).

**Lysimeter experiment.** Assuming that the convective-dispersive hypothesis holds, the soil is homogeneous, water flux and water content are constant, and decay is negligible, we may write the chemical transport equation in the lysimeter as:

$$\frac{\partial C_t}{\partial t}=D\theta\frac{\partial^2 C}{\partial z^2}+J_w\frac{\partial C}{\partial z} \tag{14}$$

where z is the vertical coordinate (positive downwards); D is the dispersion coefficient ($cm^2\ d^{-1}$); and $J_w$ is the water flux density ($cm\ d^{-1}$). Combination of (14) with (4), (5), and (6) yields the final transport equation for the two-stage, one-rate model:

$$(\theta+\rho fkmC^{m-1})\frac{\partial C}{\partial t}+\rho(1-f)\frac{\partial S_2}{\partial t}=D\theta\frac{\partial^2 C}{\partial z^2}+J_w\frac{\partial C}{\partial z} \tag{15}$$

which is coupled with the sorption rate equation (2) for the term $\partial S_2/\partial t$. Similarly, the transport equation for the two stage-two rate model is derived by combining (14) with (4) and (5):

$$\theta\frac{\partial C}{\partial t}+\rho f\frac{\partial S_1}{\partial t}+\rho(1-f)\frac{\partial S_2}{\partial t}=D\theta\frac{\partial^2 C}{\partial z^2}+J_w\frac{\partial C}{\partial z} \qquad (16)$$

which is coupled with the sorption rate equations (1) and (2) for $\partial S_1/\partial t$ and $\partial S_2/\partial t$. Initial and boundary conditions are given by

$$C(z,0) = 0 \qquad (17)$$

and

$$J_w C(0,t)-D\theta\left.\frac{\partial C(z,t)}{\partial z}\right|_{z=0+}=\begin{cases} J_w C_i & \text{if } 0<t<t_i \\ 0 & \text{otherwise}\end{cases} \qquad (18)$$

$$\lim_{z\to 0} C(z,t) = 0 \qquad (19)$$

where $C_i$ and $t_i$ are the concentration and time span of the input pulse, respectively.

The linear forms of (15)-(16) were solved in Laplace space with (18) approximated by a Dirac delta function. The results were inverted numerically with the Talbot algorithm (Jury and Roth, 1990). The nonlinear forms ($m \neq 1$) of (15)-(16) were solved numerically using a fully implicit finite difference scheme, in combination with the Newton-Raphson algorithm to solve (15). The transport equations were coupled with the relevant sorption rate equations by iteration.

## Results and Discussion

### Sorption-Desorption Isotherm

Although the sorbed concentrations $S_1$ and $S_2$ cannot be measured individually, Fig. 1 (upper panel) illustrates the sorption progress in time predicted by the linear form of the two stage-two rate model. The concentration in solution has been normalized to the initial concentration $C_0$, the sorbed concentrations to their mutual equilibrium concentration given by (7). At early times, the solute is rapidly sorbed to region I sites, significantly exceeding the final $S_1$ equilibrium concentration, while for longer times the solute is mainly redistributed between the sorption sites. Accordingly, these stages of the sorption process are reflected in a short and rapid decrease of dissolved

concentration followed by a long, slow decrease. The middle panel of Fig. 1 shows the effect of an interruption of the sorption process to begin the desorption procedure. Initially, the solute withdrawn from the system is mainly taken from region I sites while the sorption to region II sites continues. After approximately five days, the flux between region I and region II reverses and the system slowly approaches an equilibrium state. As can be seen from the lower panel of Fig. 1, the sorption-desorption process appears to be hysteretic if plotted as an isotherm using the values reached after 24 h, a phenomenon noted earlier by Selim et al. (1976).

The amount of time required to approach 95% of the final equilibrium value of the linear two-stage, one-rate model for a given set of parameters is shown in Fig. 2. The asymptotic approach to the equilibrium state makes it necessary to define a practical equilibration time. We chose the period after which the apparent distribution coefficient, defined as S(t)/C(t), attained 95% of its equilibrium value $k$. To indicate what combination of $k$ and $\alpha_2$ might be encountered in practice, we included the two regression lines established by Brusseau and Rao (1989b) after analysis of literature data. These authors grouped the compiled data into two types (I and II), denoting hydrophobic and nonhydrophobic organic chemicals, respectively.

Figure 2 shows that for equilibration roughly between one and 50 d would be required for a Type II chemical, and from less than 0.1 to more than 100 d for a Type I chemical. If the regression equations are used to estimate the rate coefficient from a distribution coefficient measured in a sorption experiment, Fig. 2 or (9) can be used to check if the time period of the sorption experiment was really sufficient to yield an equilibrium distribution coefficient as assumed. For example, analyzing data originally published by van Genuchten et al. (1977), Brusseau et al. (1989b) used a distribution coefficient derived from a 24 h batch experiment to estimate the rate coefficient with the Type II regression equation. According to their model, however, equilibrium (within 95%) would have been reached only after a period of 4.3 days. After 24 h, the distribution coefficient would have attained only 45% of the observed value. Hence, the parameterization results of Brusseau et al. (1989b) are not consistent with their model. This inconsistency may also be present in the regression lines if some of the literature data for the distribution coefficient $k$ were actually nonequilibrium values.

## Applications

*Batch Experiment*: Prior to working with the two-stage models, we fit the single-stage (RLS) model ($a_2 \rightarrow \infty$) to the sorption-desorption isotherm of Poletika (1993). Although in principle the single-stage model is able to produce hysteretic sorption-desorption isotherms neither the linear nor the nonlinear model was able to fit the measured data with any degree of precision. Moreover, the agreement between the sorption-desorption measurements and the isotherm calculated with the sorption parameters obtained by Poletika (1993) from the transport experiment was very poor. Subsequently, we focused our attention exclusively on the two-stage models.

Sorption parameters were estimated by fitting (1)-(2) to the measured sorption-desorption isotherms. Figure 3 and Table 1 show the results for the linear sorption models. Since the best fits of both two-stage, one-rate and two stage-two rate models are very similar, we present in Fig. 3 only those of the two-stage, one-rate model. It can be seen that the AEM fit results in an increasing underestimation of sorption with decreasing concentration. The MEM fit reveals the same shortcoming, although the residuals are better balanced over the range of measured concentrations. Obviously, the systematic deviation is caused by the inability of the linear models to account for the nonlinearity of the measured sorption isotherm.

The agreement between measured and sorbed concentrations can be improved substantially by including sorption nonlinearity, i.e., allowing $m$ to take values smaller than one. Table 2 and Fig. 4 show the results of the nonlinear model fit to the sorption-desorption isotherm. Figure 4 shows the excellent fit of the two-stage, one-rate model (AEM) both in cartesian and logarithmic coordinates. The MEM assumption leads to similar results (Table 2). Since the two-stage, one-rate model is a special case of the two stage-two rate model, it is not surprising that the additional optimization of $\alpha_1$ further reduces the sum of squares. The slight decrease, however, is accompanied by considerably increased parameter uncertainties reflected in low $t$-ratios and high parameter correlations (Table 2). At the 5% level, the fit of the full two stage-two rate model is not significantly superior to the fit of the partial two-stage, one-rate model.

*Field Experiment:* The transport parameters were estimated by fitting the flux pdf of the convective-dispersive model to the measured bromide breakthrough curve as explained in Poletika (1993). This curve was obtained by averaging the concentrations measured by the 64 wick solution samplers and normalizing the concentration-time curve to unit area. Apart from the small tailing of the measured curve, fitted and measured curves agree well (Fig. 5). The optimized parameter values are V = 6.76 cm $d^{-1}$ and D = 3.28 $cm^2$ $d^{-1}$. Division of the averaged flux density $J_w$ = 1.97 cm $d^{-1}$ by the pore water velocity V yields the volumetric water content, $\theta$ = 0.29 $cm^3$ $cm^{-3}$. These are the parameter values used in all simulations presented below.

We have now determined values for all quantities necessary to test the simulation models introduced in the theory section. In summary, these values were set by the experimenter ($C_i$); measured ($\rho$); or estimated from separate experiments (V, D, $\theta$ from the inert tracer experiment and $\alpha_1$, $\alpha_2$, $f$, $k$ and $m$ from the batch study). No parameter values were taken from the literature or estimated from the outcome of the simazine transport experiment itself.

Before discussing the nonequilibrium models, we first present the concentration profiles obtained with local equilibrium sorption (LES) models. In the LES I run we used the Freundlich parameters estimated by Poletika (1993) from the batch sorption data ($k$ = 0.38, $m$ = 0.85 for $S$, $C$ measured in mg $kg^{-1}$, mg $L^{-1}$, respectively). However, the analysis of the batch data presented above

suggests that equilibrium had not been reached during this sorption experiment. Therefore, comparative simulations (LES II) were run assuming the equilibrium isotherm of the two-stage, one-rate model to hold true (averages: k = 0.66, m = 0.88). For the linear forms the isotherms were linearized by defining an effective $k_{eff} = S(C_0)/C_0$, where $C_0$ is the input simazine concentration. Figure 6 shows that none of the computed profiles resembles the measured profile. Note also that even though *m* is close to unity, simulations based on nonlinear and linearized isotherms yield quite different results, in contrast to an assumption often made in soil science. This result is not surprising since dilution and mixing processes tend to lower the simazine solution concentration well below the input concentration, thereby causing greater attenuation if the isotherm is nonlinear.

Simazine concentration profiles computed with the linear forms of the two stage models are shown in the upper panel of Fig. 7 together with the measured simazine profile. It can be seen that the linear models substantially overestimate the displacement of the simazine pulse. As in the batch experiment, failure is attributed to the inability of the linear models to cope with the nonlinearity of the measured sorption isotherm. As shown in Fig. 3, the linear models increasingly underestimate sorption with decreasing solute concentrations. Since this deviation is less severe under the MEM assumption than under the AEM assumption, the former results in a slower solute displacement and therefore in a better agreement between simulated and measured simazine profile. It should be noted, however, that despite their only moderate performance, the linear nonequilibrium models already represent a major improvement compared to the LES model.

The simazine concentration profiles computed with the nonlinear forms of the two-stage models are displayed in the lower panel of Fig. 7. All of them show an excellent agreement with the measured profile. The two-stage, one-rate model gives more accurate results than the models in the upper part of the lysimeter while the reverse holds true in the lower part. Both models fail to predict the slight increase in concentration near the outlet end of the lysimeter. The concentrations at the bottom of the lysimeter, however, are probably influenced by the drainage device as suspected by Poletika (1993). Although the AEM assumption yields slightly better results, the influence of the error assumption made in the parameter estimation procedure has only a minor influence upon the outcome of the transport simulations. It should be pointed out, however, that the two methods differed considerably when we included in the parameter estimation procedure the highest desorption isotherm of Poletika (1993), whose initial concentration was much higher than the concentration of the input pulse applied in the transport experiment. Concentration profiles calculated with parameters estimated under the MEM assumption still agreed very well with the measurements, while the AEM assumption led to considerable disagreement.

## Conclusions

This study removes the apparent inconsistency between the laboratory isotherm measurements and the field lysimeter experiment on simazine transport of Poletika (1993). The foremost conclusion is that the simazine isotherm measurements were not at equilibrium, and therefore the isotherm slope obtained from a 24 h equilibration period could not be used to deduce the final effective retardation factor value.

An essential goal of any transport model is to represent a process using independently determined values for its parameters. In this study kinetic sorption parameters for a number of different models were estimated independently from the field experiment using laboratory batch experiments, and were combined with parameters determined from a concurrent tracer experiment to predict the final simazine profile in the field lysimeter. Based on our results we conclude the following:

1. The field data cannot be described with a linear or nonlinear equilibrium sorption model.

2. Although the linear nonequilibrium sorption models perform comparatively better, they are not really compatible with both field and laboratory data.

3. The nonlinear two-stage sorption models produce a considerably better representation of both field and laboratory data than any of the other models tested, including the single-stage sorption model. Since they do not differ significantly in performance, the simpler one-rate model is recommended for applications of the duration of our field study (10 d).

4. Based on the estimate given in our Fig. 2, the time required for the batch samples to approach 95% equilibrium is the order of 10 d for this pesticide and soil. Since this is a long enough time to create experimental problems in measuring the true equilibrium sorption coefficient, and since nonequilibrium sorption is necessary to model the data over the same time period in a field study, we recommend running kinetic studies or sorption-desorption measurements over shorter time periods and fitting the two-stage, one-rate model to the resulting data.

5. We do not expect the same model to work in all soils. Our soil had negligible stagnant water (Poletika, 1993), so that a single rate process was required to represent the transfer from bulk solution to the interior sorption sites of the solid phase. In more structured soils, we would expect a second rate process for the transfer between the mobile and the immobile water. In such a case, the water tracer would reveal the presence of the immobile water, and a multiprocess nonequlibrium model such as that used by Brusseau et al. (1989) could be employed.

## References


Ball, W. P. and P. V. Roberts. 1991. Long-term sorption of halogenated organic chemicals by aquifer material. 1. Equilibrium. Environ. Sci. Technol. 25: 1223-1237.

Boesten, J.J.T.I. and L.J.T. van der Pas. 1988. Modeling adsorption/desorption kinetics of pesticides in a soil suspension. Soil Sci. 146:221-231.

Brusseau, M. L. and P.S.C. Rao. 1989a. Sorption nonideality during organic contaminant transport in porous media. CRC Crit. Rev. Environ. Control. 19:33-99.

Brusseau, M. L. and P.S.C. Rao. 1989b. The influence of sorbate-organic matter interactions on sorption nonequilibrium. Chemosphere, 18:1691-1706.

Brusseau, M. L., R. E. Jessup, and P.S.C. Rao. 1989. Modeling the transport of solutes influenced by multiprocess nonequilibrium. Water Resour. Res. 25:1971-1988.

Brusseau, M. L., R. E. Jessup, and P.S.C. Rao. 1991. Nonequilibrium sorption of organic chemicals: Elucidation of rate-limiting processes. Environ. Sci. Technol. 25:134-142.

Calvet, R. 1980. Adsorption-desorption phenomena. p. 1-31. *In* R. J. Hance (ed.), Interactions between herbicides and the soil. Academic Press., London.

Day, B. E., Jordan, L. S., and V. A. Joliffe. 1968. The influence of soil characteristics on the adsorption and phytotoxicity of simazine. Weed Science. 1:209-213.

ElAbd, H., 1984. Spatial variability of the pesticide distribution coefficient. Ph.D Thesis, University of California, Riverside, 100 p.

Gschwend, P. M. and S. Wu. 1985. On the constancy of sediment-water partition coefficients of hydrophobic organic pollutants. Environ. Sci. Technol. 19:90-96,

Jury, W. A. and K. Roth. 1990. Transfer functions and solute movement through soil. Birkhaeuser Verlag, Basel, Switzerland.

Koskinen, W. C., G. A. O'Connor, and H. H. Cheng. 1979. Characterization of hysteresis in the desorption of 2,4,5-T from soils. Soil Sci. Soc. Am. J. 43:871-874.

Miller, C. T. and J. A. Pedit. 1992. Use of a reactive surface-diffusion model to describe apparent sorption-desorption hysteresis and abiotic degradation of lindane in a subsurface material. Environ. Sci. Technol. 26:1417-1427.

Poletika, N. 1993. Transport of bromide, simazine, and Ms-2 coliphage in unsaturated soil. Ph.D Thesis, University of California, Riverside, 135 p.

Press, W. H., B. P. Flannery, S. A. Teukolsky, and W. T. Vetterling, 1988. Numerical recipes in C, The art of scientific computing, Cambridge University Press, New York,

Rao, P.S.C. and J. M. Davidson. 1980. Estimation of pesticide retention and transformation parameters required in nonpoint source pollution models. p. 23-67 *In* M. R. Overcash and J. M. Davidson, (eds.) Environmental impact of nonpoint source pollution. Ann Arbor Science Publishers, Ann Arbor, Michigan, USA.

Selim, H. M., J. M. Davidson, and R. S. Mansell. 1976. Evaluation of a two-site adsorption-desorption model for describing solute transport in soils. Summer Computer Simulation Conf., Washington, D.C., USA. Simulation Councils, Inc., La Jolla, California, USA.

Talbert, R. E., and O. H. Fletchall. 1965. The adsorption of some s-Triazines in soils. Weeds. 13:46-52.

van Genuchten, M.Th., P. J. Wierenga, and G. A. O'Connor. 1977. Mass transfer studies in sorbing porous media: Experimental evaluation with 2,4,5--T. Soil Sci. Soc. Am. J. 41:278-285.

Williams, J. D. H. 1968. Adsorption and desorption of simazine by some Rothamsted soils. Weed Res. 8:327-335.

Wu, S. and P. M. Gschwend. 1986. Sorption kinetics of hydrophobic organic compounds to natural sediments and soils. Environ. Sci. Technol. 20:717-725.

Table 1: Results of parameter estimation for linear models. Units for $\alpha_1, \alpha_2, k$ are $d^{-1}$, and L $kg^{-1}$

| Sorption Model | Error Model | Sum of Squares | Parameter | Estimate | Approx. Std.Err. | $t$ Ratio | Correlation Matrix | | | |
|---|---|---|---|---|---|---|---|---|---|---|
| 2S1R | Additive | 5.52E-5 | $\alpha_2$ | 0.121 | 0.015 | 7.9 | 1.00 | | | |
| | | | $f$ | 0.381 | 0.013 | 28.7 | 0.38 | 1.00 | | |
| | | | $k$ | 0.839 | 0.044 | 19.1 | -0.91 | -0.69 | 1.00 | |
| | Multiplicative | 5.13E-3 | $\alpha_2$ | 0.121 | 0.031 | 3.9 | 1.00 | | | |
| | | | $f$ | 0.414 | 0.020 | 20.7 | -0.85 | 1.00 | | |
| | | | $k$ | 1.021 | 0.108 | 9.4 | -0.84 | -0.29 | 1.00 | |
| 2S2R | Additive | 5.42E-5 | $\alpha_1$ | 1.205 | 0.562 | 2.1 | 1.00 | | | |
| | | | $\alpha_2$ | 0.119 | 0.070 | 1.7 | 0.99 | 1.00 | | |
| | | | $f$ | 0.465 | 0.048 | 9.8 | 0.69 | 0.77 | 1.00 | |
| | | | $k$ | 0.926 | 0.197 | 4.7 | -0.96 | -0.98 | -0.86 | 1.00 |
| | Multiplicative | 5.01E-3 | $\alpha_1$ | 0.877 | 1.055 | 0.8 | 1.00 | | | |
| | | | $\alpha_2$ | 0.070 | 0.116 | 0.6 | 1.00 | 1.00 | | |
| | | | $f$ | 0.433 | 0.346 | 1.3 | 0.98 | 0.99 | 1.00 | |
| | | | $k$ | 1.356 | 1.293 | 1.1 | -0.99 | -1.00 | -1.00 | 1.00 |

Table 2: Results of parameter estimation for nonlinear models Units for $\alpha_1, \alpha_2, k$ are $d^{-1}$, and $mg^{1-m}L^m\ kg^{-1}$

| Sorption Model | Error Model | Sum of Squares | Parameter | Estimate | Approx. Std.Err. | $t$ Ratio | Correlation Matrix | | | | |
|---|---|---|---|---|---|---|---|---|---|---|---|
| 2S1R | Additive | 1.22E-5 | $\alpha_2$ | 0.164 | 0.013 | 12.7 | 1.00 | | | | |
| | | | $f$ | 0.447 | 0.010 | 43.4 | 0.24 | 1.00 | | | |
| | | | $k$ | 0.698 | 0.022 | 31.7 | -0.67 | -0.84 | 1.00 | | |
| | | | $m$ | 0.892 | 0.010 | 87.7 | 0.11 | -0.67 | 0.57 | 1.00 | |
| | Multiplicative | 1.23E-3 | $\alpha_2$ | 0.145 | 0.027 | 5.4 | 1.00 | | | | |
| | | | $f$ | 0.508 | 0.017 | 30.5 | -0.07 | 1.00 | | | |
| | | | $k$ | 0.620 | 0.048 | 12.9 | -0.54 | -0.68 | 1.00 | | |
| | | | $m$ | 0.868 | 0.014 | 62.5 | 0.05 | -0.70 | 0.74 | 1.00 | |
| 2S2R | Additive | 1.08E-5 | $\alpha_1$ | 1.355 | 0.321 | 4.2 | 1.00 | | | | |
| | | | $\alpha_2$ | 0.099 | 0.032 | 3.1 | 0.98 | 1.00 | | | |
| | | | $f$ | 0.506 | 0.040 | 12.5 | 0.89 | 0.91 | 1.00 | | |
| | | | $k$ | 0.793 | 0.101 | 7.9 | -0.97 | -0.97 | -0.97 | 1.00 | |
| | | | $m$ | 0.893 | 0.096 | 9.3 | -0.09 | 0.02 | 0.13 | 0.15 | 1.00 |
| | Multiplicative | 1.10E-3 | $\alpha_1$ | 1.228 | 0.625 | 2.0 | 1.00 | | | | |
| | | | $\alpha_2$ | 0.069 | 0.055 | 1.3 | 0.99 | 1.00 | | | |
| | | | $f$ | 0.536 | 0.156 | 3.4 | 0.97 | 0.98 | 1.00 | | |
| | | | $k$ | 0.752 | 0.276 | 2.7 | -0.98 | -0.98 | -0.99 | 1.00 | |
| | | | $m$ | 0.870 | 0.013 | 66.0 | -0.05 | 0.02 | -0.06 | 0.16 | 1.00 |

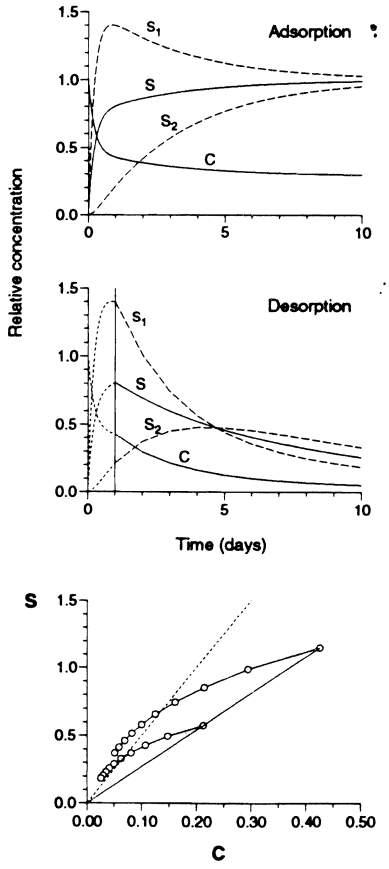


Figure1. Simulated dissolved and sorbed concentrations as a function of time during sorption (upper panel) and desorption (middle panel), together with the sorption-desorption isotherm produced by using 24 h equilibration periods at each step (lower panel) predicted by the linear two stage-two rate model. The dotted line on the lower panel is the true equilibrium isotherm.

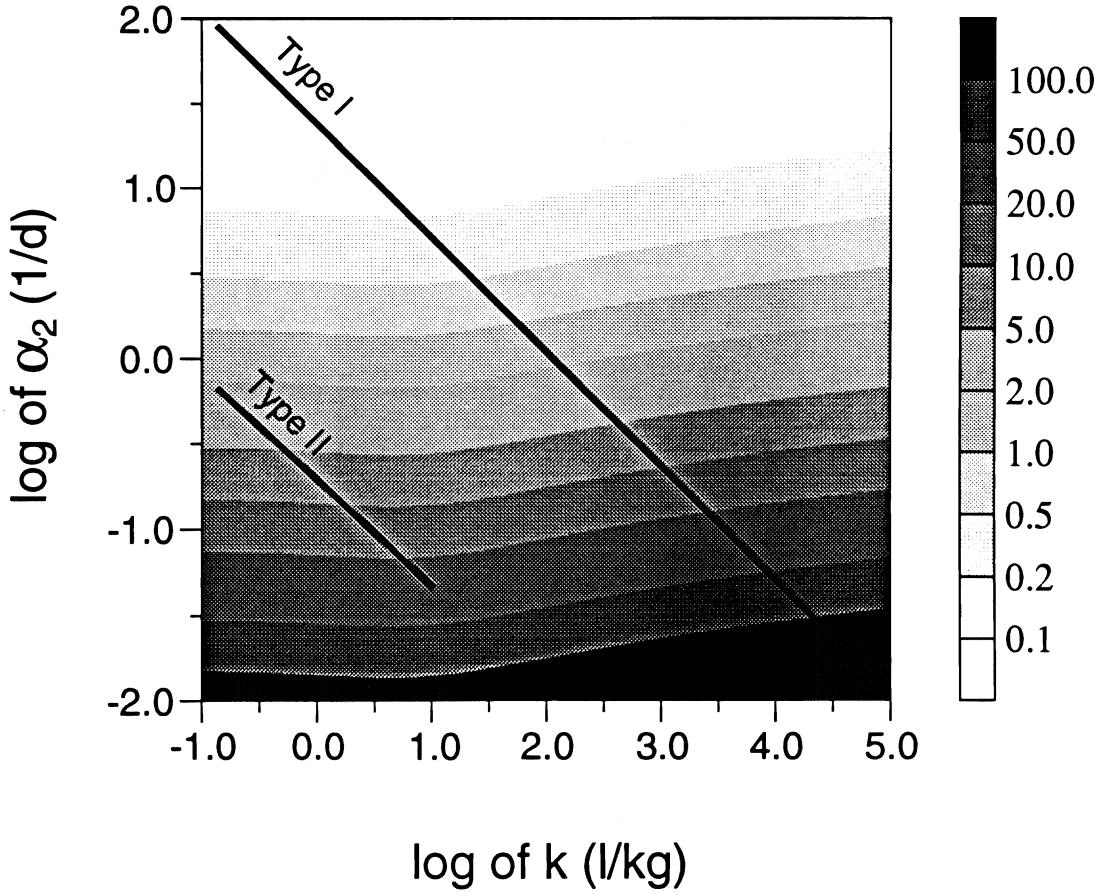


Figure 2. Time (days) required for the apparent distribution coefficient, defined as S(t)/C(t), to reach 95% of its equilibrium value in a simulated batch experiment predicted by the linear two-stage, one-rate model (soil-solution ratio 0.5 g $mL^{-1}$, f=0.5). The solid lines are the (appropriately converted) regression lines given by Brusseau and Rao (1989b).

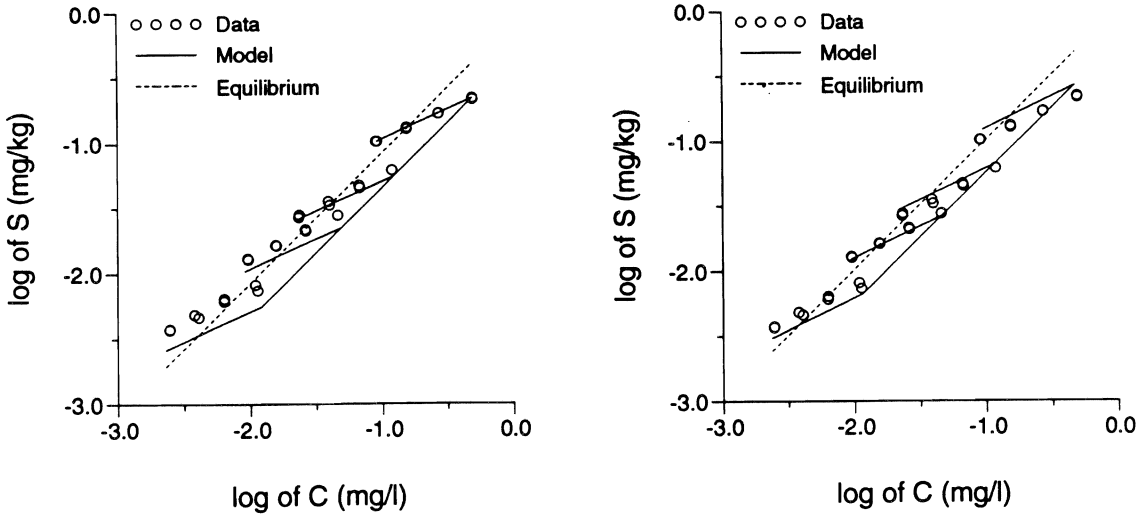


Figure 3. Linear form of the two-stage, one-rate model fitted to the measured simazine sorption-desorption isotherm assuming AEM (left) or MEM (right). Equilibrium line: S=kC.

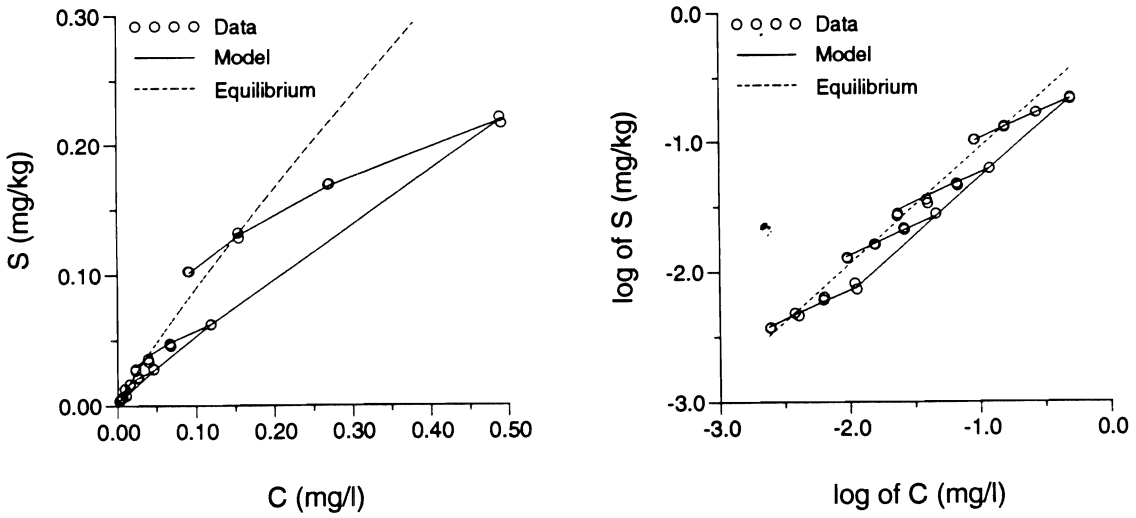


Figure 4. Nonlinear form of the two-stage, one-rate model fitted to the measured simazine sorption-desorption isotherm assuming AEM in cartesian (left) and logarithmic coordinates (right). Equilibrium line: $S=kC^m$.

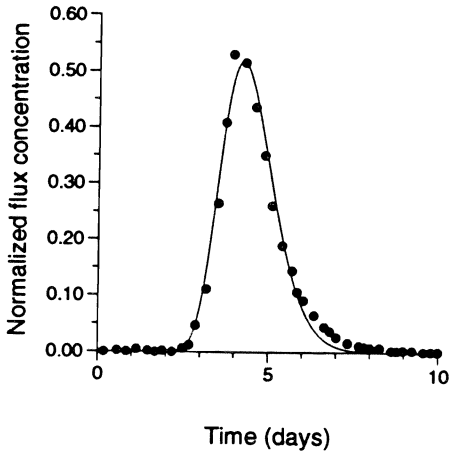


Figure 5. Measured (points) and fitted (solid line) bromide flux pdfs.

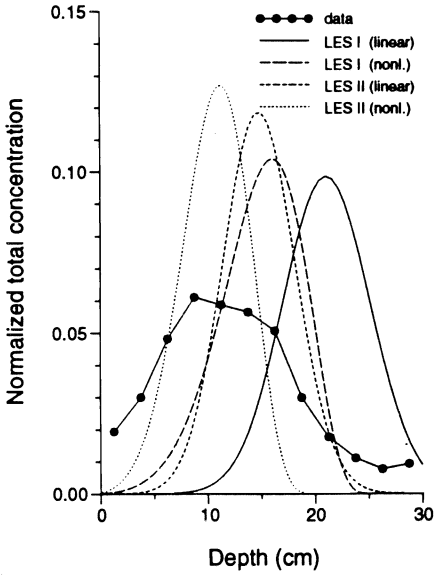


Figure 6. Measured area averaged simazine concentrations and model predictions obtained with linear and nonlinear forms of the local equilibrium sorption (LES) model.

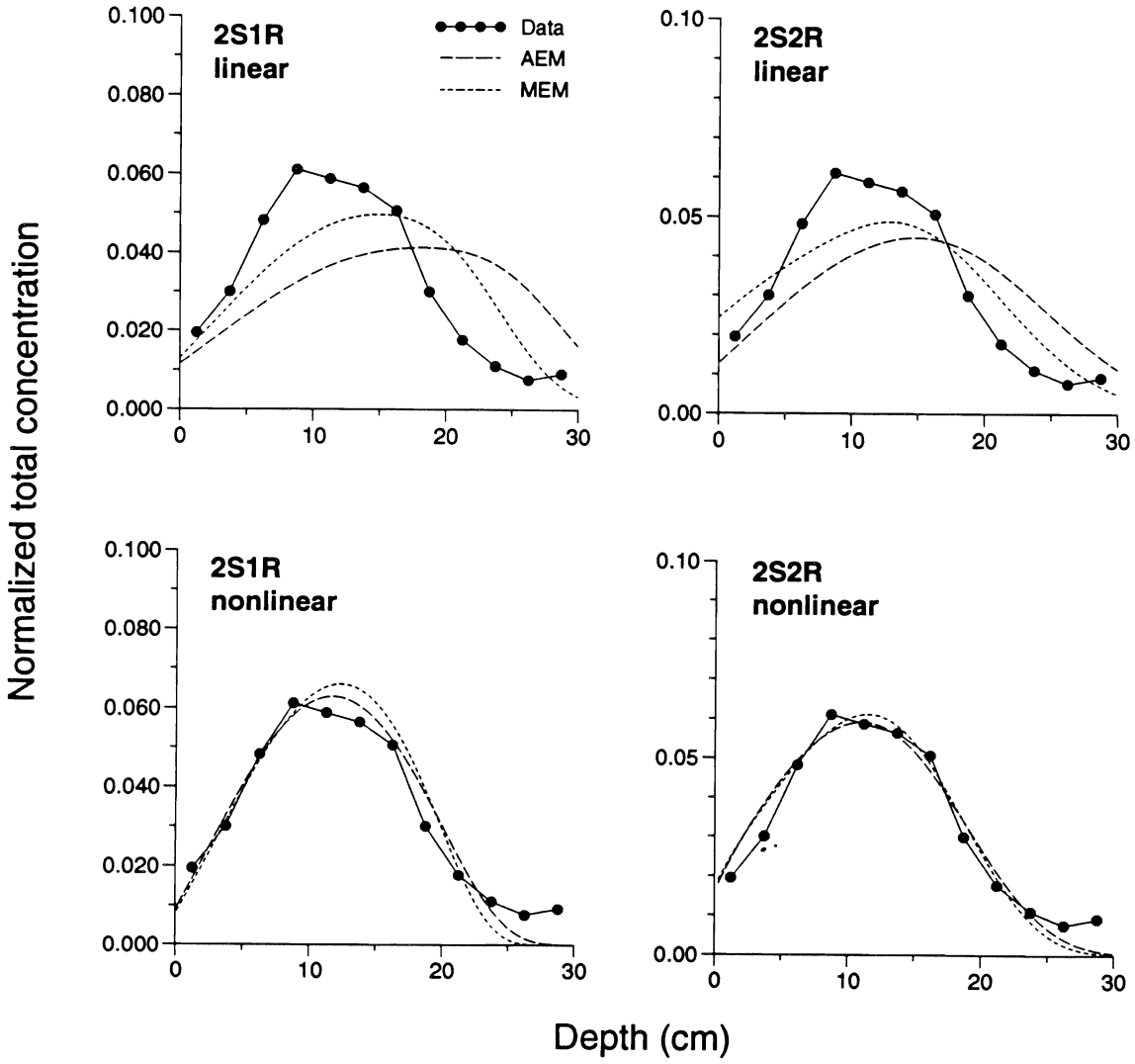


Figure 7. Measured area-averaged simazine concentrations and model predictions obtained with linear and nonlinear forms of the two-stage, one-rate (2S1R) and two stage-two rate (2S2R) models. Transport parameters (V, D) were obtained from the measured bromide breakthrough curve. Sorption parameters ($\alpha_1$, $\alpha_2$, *f*, *k*, *m*) were estimated from batch sorption-desorption experiments under the additive (AEM) or the multiplicative error assumption (MEM).

# Deterministic Fractal Modeling of the Spatial Patterns of Soil Contaminants

CARLOS E. PUENTE
*Department of Land, Air and Water Resources, Davis Campus*

## Summary

This research dealt with the geometric quantification of the concentration patterns that are observed when a pollutant migrates within the soil. In particular, this research focused on the mathematical description of vertically-averaged two-dimensional concentration patterns as seen in actual sites. The objective of this research was to test whether the two-dimensional geometrical features (contours) observed in pollutant concentration fields could be properly described via fractal-multifractal representation. This work was comprised of two phases: first, the making of a catalog of contour shapes that could be generated as transformations of multifractal measures via fractal fuctions; and, second, the use of such a catalog to fine-tune some of its pages to describe contamination data as measured on the Borden site in Ontario, Canada.

Our results illustrate that actual plumes may indeed be described geometrically, employing the fractal-multifractal framework. Not only was it possible to generate plausible plume evolutions employing the procedure, but also excellent fits of the chloride and bromoform plumes were obtained for the Borden site. These results point toward a future application of the methodology for studying pollution dynamics from the whole plume rather than from its first moments, as is currently done when employing sophisticated stochastic procedures. The results suggest the feasibility of describing three-dimensional plumes by means of a similar approach.

**Key Words:** pollution transport, contaminant transport, fractals, multifractals.

## Project Objectives Addressed in 1993-94

1. Determination of fractal-multifractal parameters to fit contamination data from the Borden site.

## Research Plan and Procedures

Proper description (interpolation, estimation, prediction, simulation, etc.) of hydrologic (geophysical) information (in space and time) is crucial for the understanding and quantification of the phenomena at hand and its consequences. A common trait of these data sets, typical in pollution studies, is that they are *complex*. They exhibit "heterogeneities", "anisotropies", and "intermittencies", which preclude a simple mathematical description. The typical approach for many years has been to understand such variability based upon well-founded physical principles, i.e. partial differential equations that express conservation laws. When deterministic, physically-based approaches fail (for instance, due to improper knowledge of parameters or boundary conditions), a common technique has been to develop approaches based on probability theory.

Instead of concentrating on data sets per-se, state of the art stochastic procedures focus on "relevant statistics" of the patterns at hand (i.e. means, variances, spatial correlations, extremes, etc.). Assumptions like stationarity and ergodicity are often used to aid in the development of theories, even though it is common to have phenomena which provide buy a single spatial pattern (i.e. as in groundwater properties). Despite the substantial progress throughout the years, the problem of understanding and predicting soil pollution still remains. Although state of the art stochastic methods provide a viable representation of complex data, more often than not (given their assumptions) they result in "smoothed", "distorted", and/or "unreal" representations of observed patterns. All these approximations may be unacceptable if prevailing dynamic conditions are sufficiently nonuniform and nonlinear.

This work attempted to capture explicitly the geometrical features observed in pollution studies, i.e. "shades of concentrations". The idea was to reproduce the "complex", "jagged", and "intricate" patterns as deterministic fractal transformations of turbulence-related distributions (multifractal probability measures) (Puente, 1992). The basis for the representation is the belief that the geometric effects may be properly filtered out by proper encoding , which then would allow us to see the evolution of the plume based upon few surrogate parameters. Capturing geometry may be the key because, after all, the observed patterns are mere reflections of ongoing physicochemical mechanisms.

This research concentrated during its first two years on the determination of suitable parameter sets which would allow a fractal-multifractal description of pollution patterns defined over the plane, (i.e. vertically-averaged concentration patterns). A brief summary of the way the representation is achieved is explained pictorially in Fig. 1. This figure shows how to combine a multifractal

measure (dx) with a fractal interpolating function (f) to arrive at a derived measure (dy). The measure in y is obtained by looking at all possible ways in which y = f(x), adding up the measures of all relevant events in x. The measure dy may be used to describe a complex pattern defined over a line in space. Both the function f and the parent measure dx are parameterized in a very parsimonious way (Puente, 1992). This leads to a compact description of the measure dy which could otherwise be thought of as a complex and even stochastic object. (See Fig. 1).

The procedure is generalized so that fractal interpolating function f is a "wire" in three dimensions, such that it produces a derived joint measure over the plane y - z. These joint measures are the ones that are used to describe pollution patterns over the plane. The following are the surrogate parameters that are needed in order to generate derived joint measures: (a) *interpolating points*, by which the function f passes; (b) *scalings and rotations*, which determine the degree of variability and orientation of the function f between interpolating points; and (c) *multifractal parameters*, which dictate the shape of the parent measure dx (Barnsley, (1988); Puente and Klebanoff, (1994).

## Results

Figure 2 shows some examples of derived measures which illustrate the kinds of patterns that could be generated. As may be seen, some of them result in patterns that may describe concentration profiles or soil properties. Others may not apply to pollution but clearly are related to other geophysical phenomena. All measures shown in Fig. 2 are generated only via 8 surrogate parameters. Except pattern (h), which is appropriate for classical diffusion, all figures are quite irregular and seemingly "random" (i.e. they could be studied according to stochastic attributes like correlations, spectrum, multifractal spectrum, etc.). They completely deterministic.

Figure 3 shows that parameters have been identified for the creation of plausible pollution simulations (from a point source). These simulations were obtained via the fractal-multifractal procedure, and the changes seen (clockwise) from frame to frame are due only to the variation again of 8 surrogate parameters. As the procedure is continuous with respect to fractal-multifractal parameters, it is expected that when applied to real data the surrogate parameters of nearby patterns will be close to one another.

Figure 4 shows 10 frames (clockwise) of chloride concentration patterns as measured at the Borden site. Figure 5 shows the best fits that were obtained employing the fractal-multifractal methodology. Table 1 includes the scalings and rotations for all days considered, while Fig. 6 shows the evolution of the interpolating points. All multifractal parameters were found equal (i.e. $p_1=p_2=1/2$), leading to multifractality only when points in the $x$ coordinate are not equally spaced.

## Discussion

We have identified plausible fractal-multifractal combinations which result in patterns that nicely resemble observed pollution profiles or soil properties. The fractal-multifractal procedure is quite flexible and allows encoding of connected data sets as well as extremely disconnected and erratic sets. All of this is accomplished by means of a very few surrogate parameters (8 for the profiles shown).

The results in Figs. 4 and 5 and others at the same site for bromoform show that the fractal-multifractal approach leads indeed to a very accurate description of the original plume. As may be seen in table 2, the fit is very good not only visually but also in terms of spacial moments typically used when employing stochastic theories of pollution transport. Figure 6 exhibits the time evolution of the interpolating points (i.e. the first three columns of Table 1). As may be seen, the movement and growth of the plume are nicely captured by means of these surrogate parameters, i.e. as the plume moves and grows with the y - z locations. Observe also that the plume dispersion nicely captured by these parameters, with more growth vertically than horizontally. (See Fig. 5).

As may be seen in Table 1, there is no significant variability in terms of the scaling parameters (their range is between -1 and 1). When the magnitude of the scaling parameters tends to 1, the derived joint measures may be shown to be Gaussian and therefore elliptical (Puente and Klebanoff, 1994). The obtained values in Table 1, all above 0.8, would seem to imply a high degree of "ellipticity" for the plume, but care must be exercised in interpreting variations in these parameters, as there are examples which are not even unimodal (day 647). As seen in Table 1, the rotations did not vary greatly as time passed. This fact is in agreement with the observation that the plume center of mass basically traveled along a line in space which corresponds to the longitudinal axis of the plume (Freyberg, 1986).

These results indicate that application of the methodology to pollution dynamics will improve understanding of contaminant transport in soils in the future. Given that the spatial moments of the plume may be obtained analytically in terms of the surrogate parameters, a link may be stablished between the most current stochastic theories and the fractal-multifractal representation. But more importantly, given that a compact description of the plume is at hand, there is hope for providing a theory that describes the dynamics of the whole plume, rather than only of its moments. Work with other contaminants and at other sites will be necessary before such a theory could be developed. The succes of the ideas in two dimensions suggests that a similar approach could also work in three dimensions. Future research will concentrate on such issues and on a complete physical representationof the surrogate parameters.

## References

Barnsley, M.F. 1988. Fractals Everywhere. Academic Press.

Freyberg, D.L. 1986. A natural gradient experiment on solute transport in a sand aquifer. 2. Spatial moments and the advection and dispersion of nonreactive tracers. Water Resour. Res. 13: 2031-2046.

Puente, C.E. 1992. Multinomial multifractals, fractal interpolators, and the Gaussiam distribution, Physics Letters A, 161: 441-447,

Puente, C.E., and A., Klebanoff. 1994. Gaussians everywhere. Fractals 2(1): 65-79,

Table 1. Scalings and rotations for chloride concentrations at the Borden site.

| Day | Scalings | | | | Rotations (degrees) | | | |
|---|---|---|---|---|---|---|---|---|
| | $r_1^{(1)}$ | $r_2^{(2)}$ | $r_1^{(2)}$ | $r_2^{(2)}$ | $\theta_1^{(1)}$ | $\theta_1^{(2)}$ | $\theta_2^{(1)}$ | $\theta_2^{(2)}$ |
| 1 | 0.995 | 0.9 | 0.9 | 0.9 | 20 | -90 | -19 | -70 |
| 9 | 0.995 | 0.9 | 0.9 | 0.9 | 20 | -90 | -19 | -70 |
| 29 | 0.995 | 0.9 | 0.9 | 0.9 | 20 | -90 | -19 | -70 |
| 43 | 0.995 | 0.9 | 0.9 | 0.9 | 20 | -90 | -19 | -70 |
| 63 | 0.995 | 0.85 | 0.85 | 0.85 | 35 | 3 | 45 | -45 |
| 259 | 0.995 | 0.9 | 0.8 | 0.85 | 15 | -68 | -20 | -45 |
| 332 | 0.995 | 0.9 | 0.7 | 0.85 | 15 | -68 | -20 | -45 |
| 381 | 0.995 | 0.9 | 0.8 | 0.85 | 15 | -68 | -20 | -45 |
| 462 | 0.995 | 0.9 | 0.8 | 0.9 | 52 | -88 | -8 | -45 |
| 647 | 0.995 | 0.9 | 0.8 | 0.85 | 15 | -68 | -20 | -45 |

Table 2. First and second order moments for chloride plumes (Fitted and Measured).

| | Measured | | | | | Fitted | | | | |
|---|---|---|---|---|---|---|---|---|---|---|
| Day | Center of Mass | | Spatial moments | | | Center of Mass | | Spatial moments | | |
| | $\bar{x}$ | $\bar{y}$ | $\sigma_x$ | $\sigma_y$ | $\rho$ | $\bar{x}$ | $\bar{y}$ | $\sigma_x$ | $\sigma_y$ | $\rho$ |
| 1 | 0.41 | 0.40 | 1.36 | 1.66 | 0.12 | 0.87 | 0.32 | 1.44 | 2.25 | 0.31 |
| 9 | 0.64 | 0.73 | 1.13 | 1.87 | 0.10 | 1.00 | 0.94 | 1.40 | 2.11 | 0.30 |
| 29 | 3.07 | 1.45 | 1.61 | 2.11 | 0.47 | 3.06 | 3.05 | 3.83 | 4.29 | 0.50 |
| 43 | 4.10 | 1.55 | 1.63 | 1.74 | 0.34 | 5.00 | 1.86 | 2.50 | 2.56 | 0.42 |
| 63 | 5.18 | 1.47 | 1.87 | 1.99 | 0.13 | 6.73 | 3.28 | 3.07 | 4.07 | 0.29 |
| 259 | 23.0 | 11.4 | 3.66 | 3.56 | 0.58 | 22.2 | 11.8 | 3.69 | 4.17 | 0.61 |
| 332 | 28.4 | 14.7 | 4.55 | 3.53 | 0.50 | 28.0 | 13.9 | 3.63 | 3.66 | 0.56 |
| 381 | 32.2 | 16.0 | 4.01 | 3.61 | 0.56 | 32.7 | 17.3 | 4.15 | 3.88 | 0.60 |
| 462 | 38.6 | 16.9 | 4.86 | 3.64 | 0.53 | 40.0 | 17.1 | 4.80 | 3.52 | 0.43 |
| 647 | 53.4 | 24.0 | 5.74 | 3.09 | 0.84 | 54.3 | 24.8 | 6.11 | 4.05 | 0.74 |

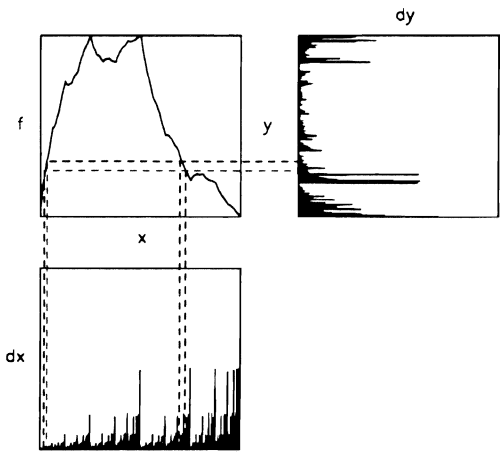


Figure 1. Derived measure via a fractal interpolator and a multifractal measure.

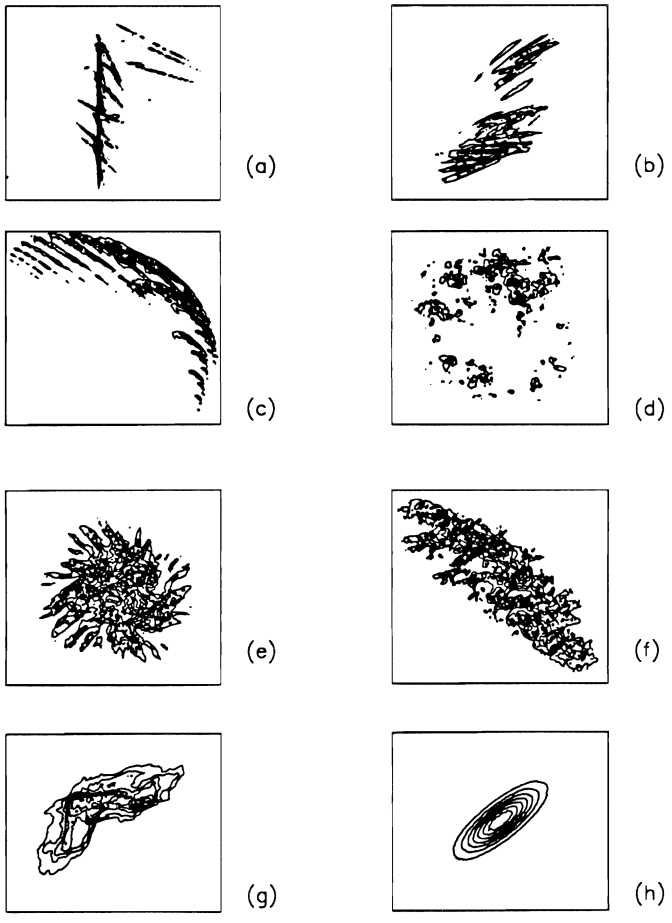


Figure 2. Examples of bivariate derived measures (domain y - z).

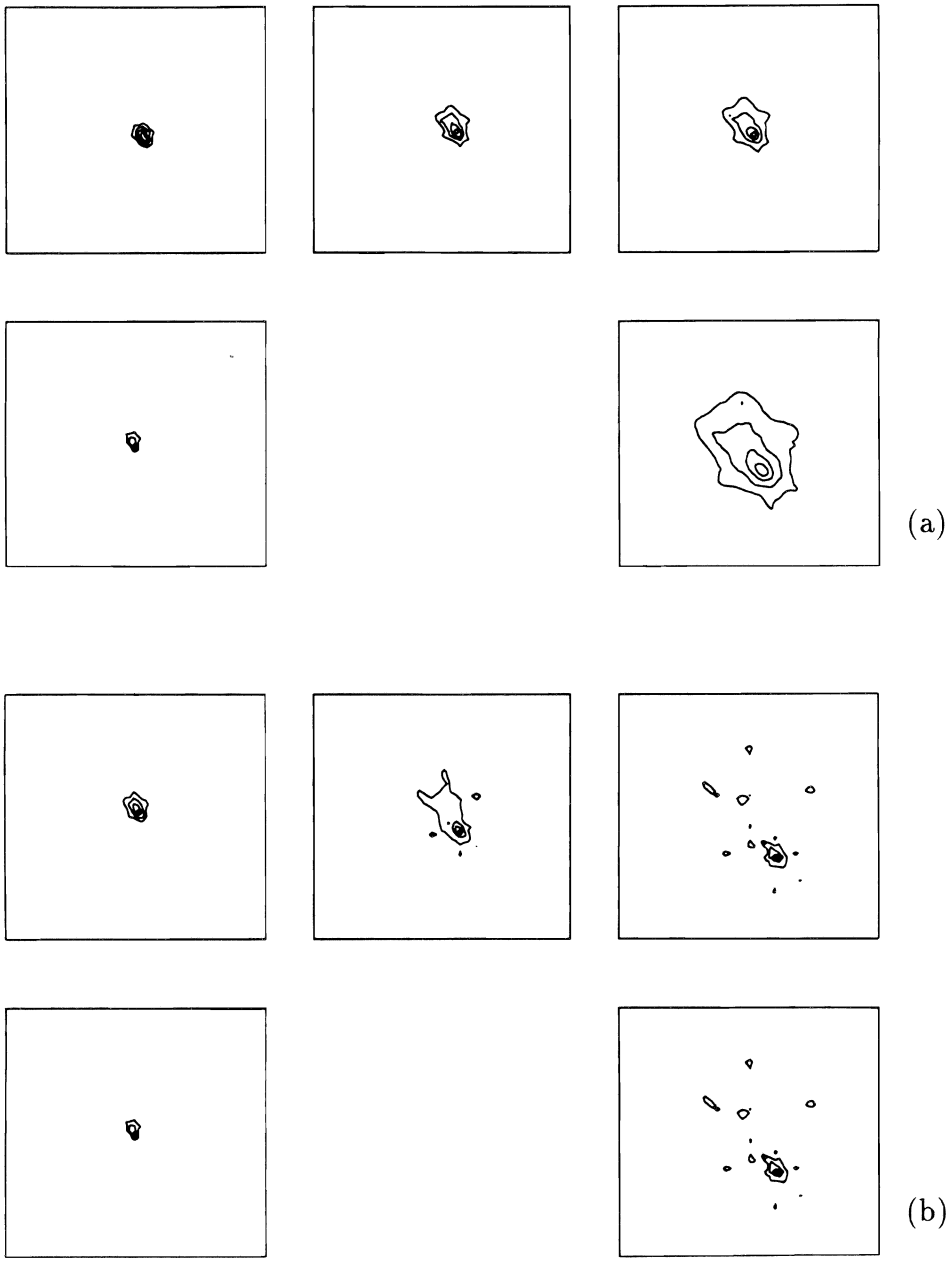


Figure 3. Plausible plume evolutions (clockwise).

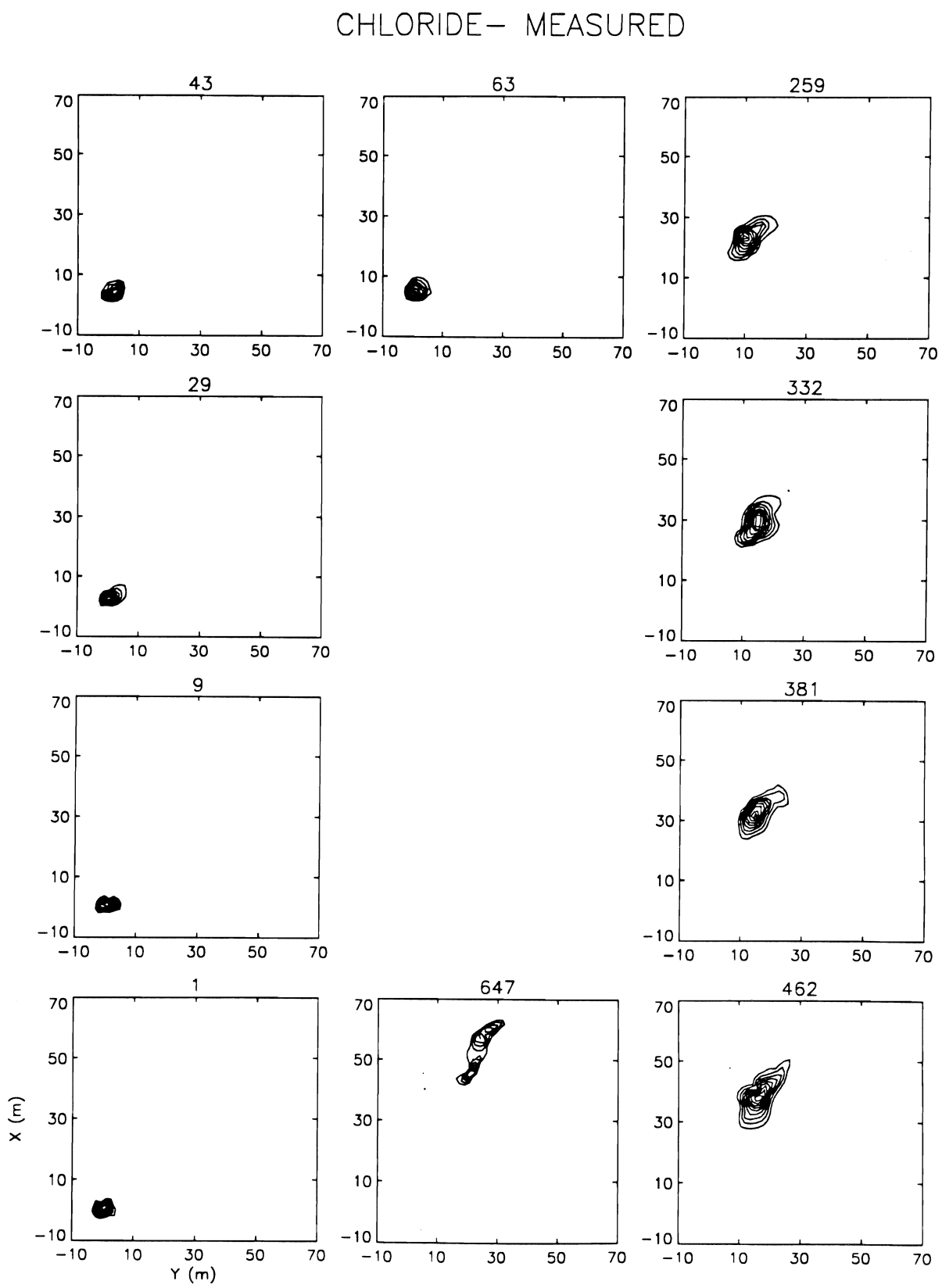


Figure 4. Measured chloride concentrations at the Borden site (clockwise).

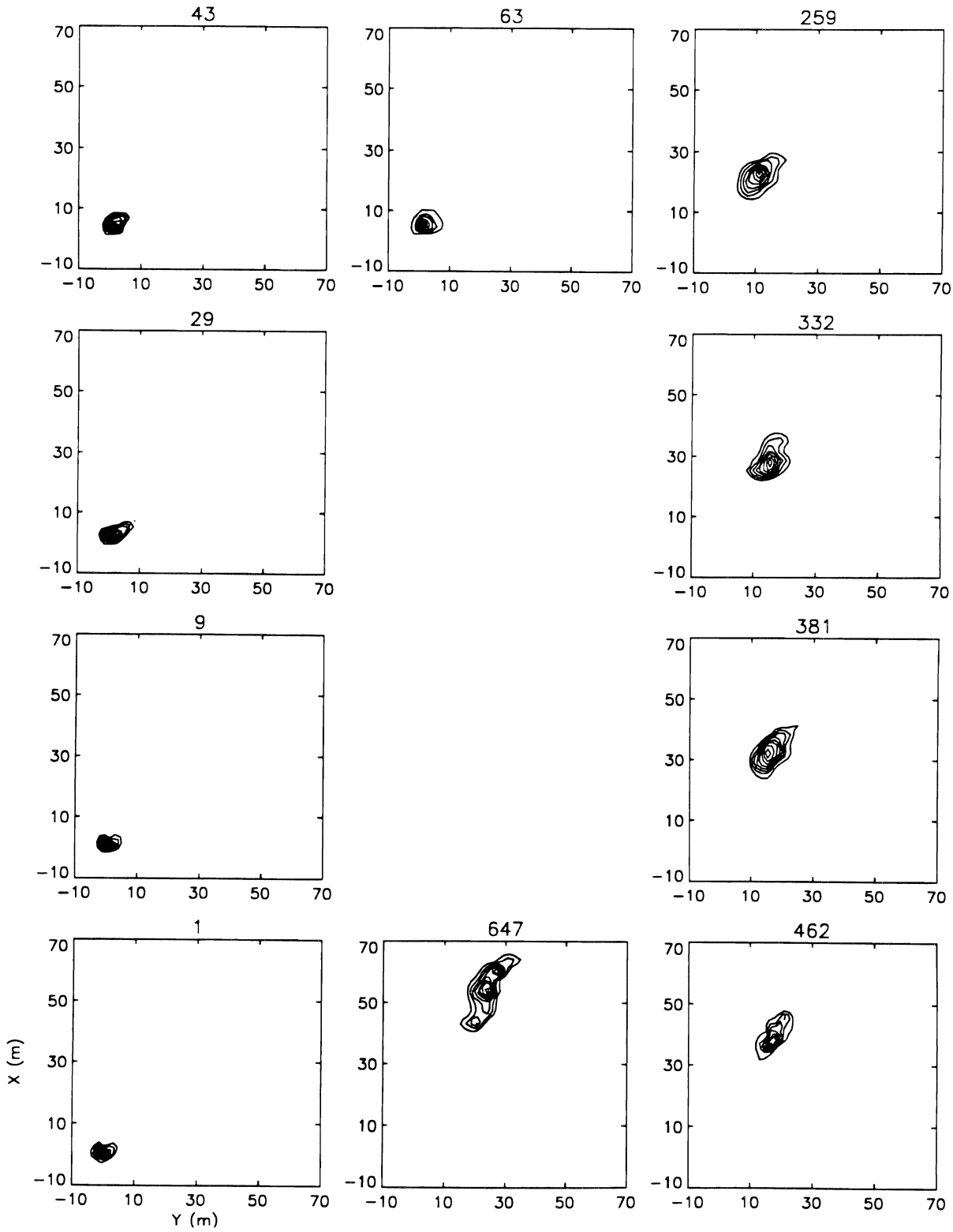


Figure 5. Fitted chloride concentrations at the Borden site (clockwise).

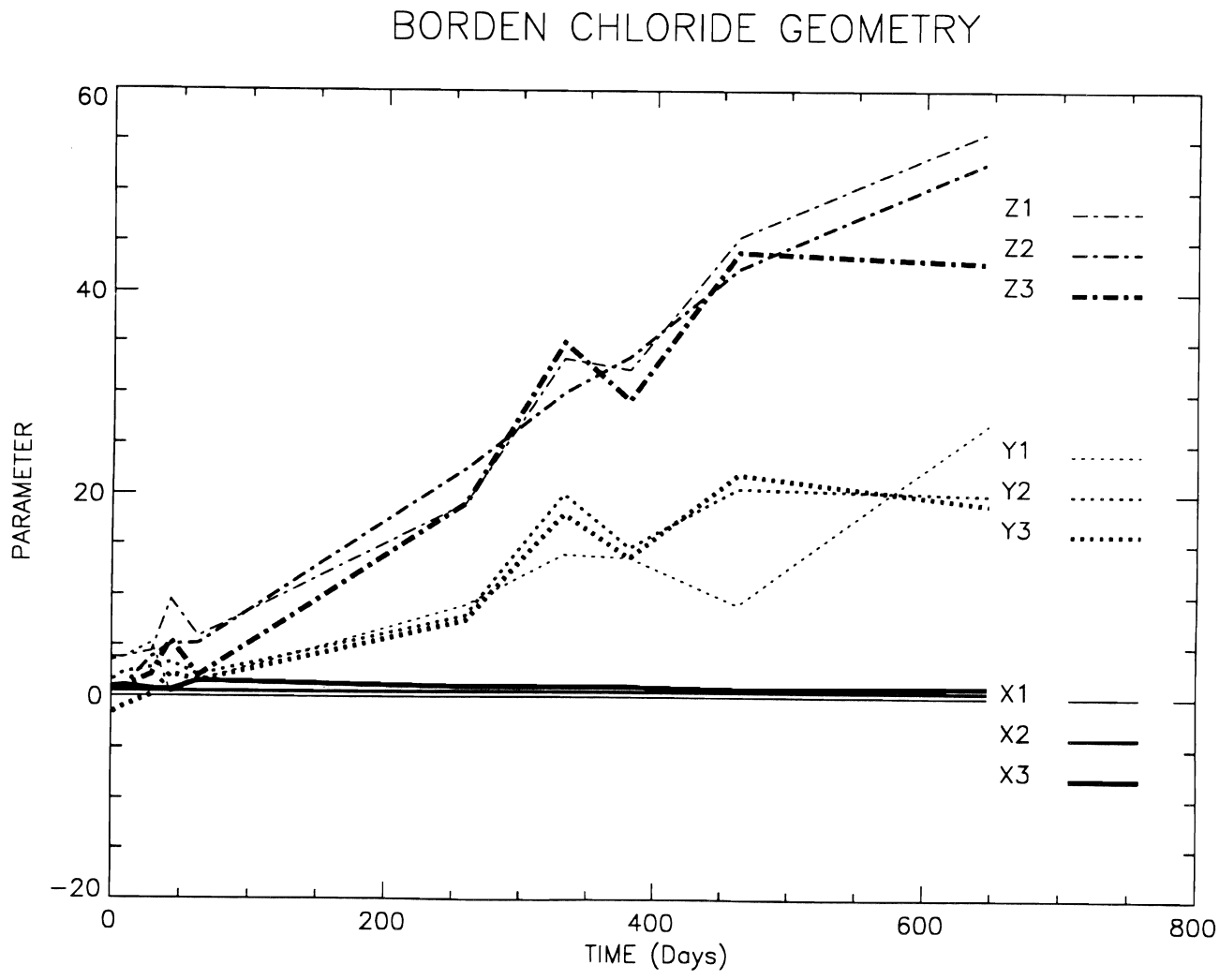


Figure 6. Evolution of fractal-multifractal interpolating points.

# Flow And Transport In Soils With Heterogeneous Hydraulic Conductivity

M. A. MARIÑO[1], H. A. LOAICIGA[2], AND R. B. LEIPNIK[3]
[1]*Dept. of Land, Air & Water Resources, Davis Campus*
[2]*Dept. of Geography, Santa Barbara Campus*
[3]*Dept. of Mathematics, Santa Barbara Campus*

## Summary

Starting with a stochastic differential equation with random coefficients describing steady-state flow, the effective hydraulic conductivity of one-, two-, and three-dimensional aquifers is derived. The natural logarithm of hydraulic conductivity ($\ln K$) is assumed to be heterogeneous, with a spatial trend, and isotropic. The effective hydraulic conductivity relates the mean specific discharge in an aquifer to the mean hydraulic gradient; thus, its importance in predicting Darcian discharge when field data represent mean or average values of hydraulic conductivity or hydraulic head. Effective hydraulic conductivity results are presented in exact form in terms of elementary functions. It was found that in one, two, and three dimensions, for the type of aquifer heterogeneity considered, the effective hydraulic conductivity depends on (1) the angle between the gradient of the trend of $\ln K$ and the mean hydraulic gradient (which is zero in the one-dimensional case); (2) (inversely) the product of the magnitude of the trend gradient in $\ln K$, $b$, and the correlation scale of $\ln K$, $\lambda$; and (3) (proportionally) the variance of $\ln K$, $\sigma_f^2$. The product $b\,\lambda$ plays a central role in the stability of the results for effective hydraulic conductivity.

**Key Words:** effective hydraulic conductivity, heterogeneity, trend, spectral theory, groundwater flow

## Project Objectives Addressed in 1993-94

The work reported herein addresses the first objective of the project, i.e., the determination of effective, spatially variable hydraulic conductivity of heterogeneous saturated soils. A methodology is presented for the determination of effective hydraulic conductivity in one, two, and three dimensions.

## Results

The effective hydraulic conductivity is an important parameter since it represents an average or ensemble mean of aquifer properties (Sposito et al., 1986). Theoretically, it relates an ensemble specific discharge to an ensemble hydraulic gradient. Practically, it relates measurable, field-scale variables (specific discharge, hydraulic gradient) to field-scale aquifer parameters. If the effective hydraulic conductivity is identifiable from measurable parameters and characteristics of the groundwater flow regime, then it can be useful in calibrating groundwater flow models and in implementing stochastic models of flow and transport that rely on "effective" (that is, ensemble means) parameters.

Consider the stochastic differential Eq. describing steady-state groundwater flow in an aquifer with random hydraulic conductivity $K(\mathbf{x})$ ($\mathbf{x}$ represents a three-dimensional coordinate vector and tensorial index notation is used with $i = 1, 2,$ or 3 depending on aquifer dimensionality):

$$\frac{\partial}{\partial x_i}\left[K(\mathbf{x})\,\frac{\partial \phi(\mathbf{x})}{\partial x_i}\right] = 0 \qquad (1)$$

in which $\phi(\mathbf{x})$ is the hydraulic head and $K(\mathbf{x})$ is a stochastic parameter whose distribution is conveniently expressed in terms of the natural logarithm of hydraulic conductivity, $Y = \ln K$. $Y$ is composed of a deterministic and spatially variable trend $T$ plus a zero-mean random noise $f$ with specified spatial statistical structure. Specifically, $Y(\mathbf{x}) = T(\mathbf{x}) + f(\mathbf{x})$. The hydraulic head, $\phi(\mathbf{x})$, is modeled as the sum of a deterministic mean $H(\mathbf{x})$ and a zero-mean random noise $h$, i.e., $\phi(\mathbf{x}) = H(\mathbf{x}) + h(\mathbf{x})$. Loaiciga et al. (1993) showed that based on these (mean plus perturbation) decompositions of hydraulic head and $\ln K$, as well as on Eq. (1), one arrives at a couple of partial differential Eqs. of which the first (Eq. 2) governs the distribution of mean hydraulic head ($H$) and the second (Eq. 3) governs the perturbations of hydraulic head, $h$ ($b_i = \partial T / \partial x_i$ and $E$ denotes expectation in Eqs. (2) and (3)):

$$\frac{\partial^2 H}{\partial x_i \partial x_i} + b_i \frac{\partial H}{\partial x_i} + E\left\{\frac{\partial f}{\partial x_i}\,\frac{\partial h}{\partial x_i}\right\} = 0 \qquad (2)$$

and

$$\frac{\partial^2 h}{\partial x_i \partial x_i} + b_i \frac{\partial h}{\partial x_i} + \frac{\partial f}{\partial x_i}\frac{\partial H}{\partial x_i} + \left\{ \frac{\partial f}{\partial x_i}\frac{\partial h}{\partial x_i} - E\left( \frac{\partial f}{\partial x_i}\frac{\partial h}{\partial x_i} \right) \right\} = 0 \qquad (3)$$

Eqs. (2) and (3) are a system of coupled partial differential Eqs.. Methods for the solution of these Eqs. have been examined by Christakos et al (1993). One approach (the "small perturbation" approach; see, e.g., Gelhar (1993)) decouples the two Eqs. by neglecting the products of perturbations in the right-hand side of Eq. (3). Spectral methods are then useful to transform the simplified form of Eq. (3) to the frequency domain from which it can be integrated to yield, for example, the variance of hydraulic head (Bakr et al., 1978).

Loaiciga et al. (1993, 1994) have shown that the relationship between the complex-valued processes $dZ_h(\mathbf{k})$ and $dZ_f(\mathbf{k})$ is given by the following expression (where **J** is the mean hydraulic gradient vector whose components are $J_i = \partial H / \partial x_i$; **b** is the ln$K$ trend gradient vector (with components $b_i = \partial T / \partial x_i$, and $k^2 = \mathbf{k}\cdot\mathbf{b}$):

$$dZ_h(\mathbf{k}) = \frac{\left[ j k^2 - \mathbf{k}\cdot\mathbf{b} \right] [\mathbf{k}\cdot\mathbf{J}]}{\left[ \left(k^2\right)^2 + (\mathbf{k}\cdot\mathbf{b})^2 \right]} dZ_f(\mathbf{k}) \qquad (4)$$

The relevance of Eq. (4) to the effective hydraulic conductivity becomes clear if one considers Darcy's law for the specific discharge $q_i$:

$$q_i = - K \frac{\partial \phi}{\partial x_i} \qquad (5)$$

Replacing the hydraulic head $\phi$ by $H + h$ and the hydraulic conductivity K by $e^{T+f}$ in Eq. (5), expanding the exponential $e^f$ by a Taylor series up to first-order terms, and taking expectations of the resulting Eq. (5), one obtains the following Eq. relating the mean specific discharge $\overline{q}_i$ to the mean hydraulic gradient $J_i$ and the covariance of the ln$K$ perturbation $f$ and the partial derivative of the head perturbation $h$:

$$\overline{q}_i \approx - e^T \left[ J_i + E\left( f \frac{\partial h}{\partial x_i} \right) \right] \qquad (6)$$

The covariance of perturbations in Eq. (6) can be obtained by a Fourier transform of its corresponding spectrum $\Phi_{fh_i}$:

$$E\left( f \frac{\partial h}{\partial x_I} \right) = \int_{\mathbf{R}} \Phi_{fh_i}(\mathbf{k})\, d^3\mathbf{k} \qquad (7)$$

in which **R** is the complete three-dimensional space and

$$\Phi_{fh_i}(\mathbf{k}) = E\left[dZ_f(\mathbf{k})\, dZ^*_{h_i}(\mathbf{k})\right] \tag{8}$$

in which

$$dZ^*_{h_i}(\mathbf{k}) = -jk_i\, dZ^*_h(\mathbf{k}) \tag{9}$$

In Eq. (9), $dZ_h^*(\mathbf{k})$ is the complex conjugate of $dZ_h(\mathbf{k})$, and the latter was given in Eq. (4) in function of the complex-valued process $dZ_f(\mathbf{k})$. From Eq. (4), the cross-spectrum of Eq. (8) becomes (using the fact the spectrum of ln$K$ is given by $\Phi_{ff}(\mathbf{k}) = E\left[dZ_f(\mathbf{k})\, dZ_f^*(\mathbf{k})\right]$):

$$\Phi_{fh_i}(\mathbf{k}) = \frac{jk_i\left[jk^2 + \mathbf{k}\cdot\mathbf{b}\right][\mathbf{k}\cdot\mathbf{J}]}{\left[\left(k^2\right)^2 + (\mathbf{k}\cdot\mathbf{b})^2\right]}\,\Phi_{ff}(\mathbf{k}) \tag{10}$$

It is seen from Eq. (6) for the mean specific discharge and from Eqs. (7) and (10) that the effective hydraulic conductivity relating the mean specific discharge to the mean hydraulic gradient depends on the form of the spectrum of ln$K$ in one, two, and three dimensions. In addition to the heterogeneous model for ln$K$ already presented, it is assumed that the covariance of ln$K$ is exponential, i.e., $\sigma_{ff}(\tau) = \sigma_f^2 \exp\left(-|\mathbf{t}|/\lambda\right)$, where **t** is the separation vector, and $\lambda$ is the correlation scale of ln$K$).

## The Mean Specific Discharge in One-, Two-, and Three-Dimensional Domains

A General Expression for the Mean Specific Discharge Starting with Eqs. (6), (7) and (10) it is possible to derive the mean specific discharge in terms of the spectrum of ln$K$. For the assumed exponential covariance model $\sigma_{ff}(\mathbf{t})$, the spectrum of ln$K$ can be derived by means of the Fourier transform relating spectra to covariances: $\Phi_{ff}(\mathbf{k}) = (2\pi)^{-n} \int_{\mathbf{R}_n} \exp\left(-j\mathbf{k}\cdot\mathbf{t}\right) \sigma_{ff}(\mathbf{t})\, d^n\mathbf{t}$, where $n$ is the flow dimensionality ($n$ = 1, 2, or 3) and $R_n$ is the complete $n$-dimensional space. The following spectrum for ln$K$ results:

$$\Phi_{ff}(\mathbf{k}) = \frac{\sigma_f^2\, \lambda^{q-1}}{\kappa_{q-1}\left(1 + k^2\lambda^2\right)^{q/2}} \tag{11}$$

where $q$ = 2, 3, and 4 for one-, two-, and three-dimensional domains, respectively, and $\kappa_{q-1} = \pi$, $2\pi$, and $\pi^2$ for one-, two-, and three-dimensional domains, respectively.

Based on Eqs. (6) and (11), a generic expression for the mean specific discharge is given by the following Eq.:

$$\bar{q}_i \approx - e^T \left[ J_i + \frac{j \sigma_f^2 \lambda^{q-1}}{\kappa_{q-1}} \int_{\mathbf{R}_{q-1}} \frac{k_i \left[ j k^2 + \mathbf{k} \cdot \mathbf{b} \right] \left[ \mathbf{k} \cdot \mathbf{J} \right]}{\left[ \left( k^2 \right)^2 + (\mathbf{k} \cdot \mathbf{b})^2 \right] \left( 1 + k^2 \lambda^2 \right)^{q/2}} d^{q-1}\mathbf{k} \right] \quad (12)$$

where $q$ takes the values 2, 3, and 4 for one-, two-, and three-dimensional flow domains, respectively, as before, $\kappa_{q-1}$ takes the values $\pi$, $2\pi$, and $\pi^2$ for $q$ = 2, 3, and 4, respectively, and $\mathbf{R}_{q-1}$ denotes the complete $q$-1-dimensional space, for $q$ = 2, 3, 4.

The One-Dimensional Case Integrating Eq. (12) for a one-dimensional space (i.e., $q$ = 2 in Eq. (12)) leads to the following mean specific discharge:

$$\bar{q} \approx - e^T \left[ 1 - \frac{\sigma_f^2}{b\lambda + 1} \right] J \quad (13)$$

in which $J$ is the mean hydraulic gradient, and $b = dT/dx$ is the gradient of the trend in ln$K$. It is clear from Eq. (13) that the one-dimensional hydraulic conductivity is given by:

$$K_e = e^T \left[ 1 - \frac{\sigma_f^2}{b\lambda + 1} \right] \quad (14)$$

It is seen from Eq. (14) that the condition for nonnegative effective hydraulic conductivity is $\sigma_f^2 < b\lambda + 1$, and that a singular point exists at $b\lambda = -1$. (Gutjahr et al., 1978, presented an alternate expression for one-dimensional effective hydraulic conductivity leading to different stability conditions.) Notice then how in the presence of a trend in ln$K$, the restriction on the variance of ln$K$ perturbation involves the critical product of parameters $b\lambda$. It is also possible to show by the spectral method that the variance of hydraulic head becomes arbitrarily large when $b\lambda \rightarrow -1$. Since the correlation scale is a positive parameter, this condition can only arise when the trend gradient in ln$K$ is negative and equal to $1/\lambda$. A plausible explanation for the instability of the stochastic results at $b\lambda = -1$ is that as the gradient of the trend of ln$K$ approaches the critical value $-1/\lambda$, the hydraulic conductivity declines over spatial scales equivalent to the correlation scale to a value small enough to prevent flow for finite hydraulic gradients. The expression in Eq. (14) also

shows that, since the trend $T$ is in general spatially variable, so is the effective hydraulic conductivity. If the trend of $\ln K$ can be adequately identified from data, it is possible to construct a spatially dependent effective hydraulic conductivity field directly from Eq. (14). In two-, and three-dimensional domains this is potentially useful in calibrating numerical models of groundwater flow and mass transport. Most of the hydraulic head and aquifer properties data collected in the field represent averages or "effective" values over extended spatial domains. Numerical simulation models are also coarse and discrete spatial approximations to continuous processes. It seems reasonable, therefore, that in seeking calibration parameters for such numerical simulation models, to focus on the theoretical effective conductivity relating the mean or average groundwater flow discharge to the mean hydraulic gradients. Average effective hydraulic conductivities over finite-difference cells and finite elements can be calculated (e.g., by integration) from the continuous-space function $K_e$.

Effective Hydraulic Conductivity in Two and Three Dimensions When $b\lambda > 1$, the two-dimensional expression for effective hydraulic conductivity can be shown to be

$$K_e(x, y) = e^{T(x,y)}\left[1 - \frac{\sigma_f^2 \lambda^2}{2\pi}\left(L_1 \cos^2\theta + L_2 \sin^2\theta\right)\right] \tag{15}$$

When $b\lambda < 1$, the corresponding two-dimensional expression is

$$K_e(x, y) = e^{T(x,y)}\left[1 - \frac{\sigma_f^2 \lambda^2}{2\pi}\left(L_1 \cos^2\theta + L_2 \sin^2\theta\right)\right] \tag{16}$$

in which:

$$L_1 = \frac{2\pi}{b^2\lambda^4}\left[\left(1 + \frac{1}{1 - (b\lambda)^2}\right)E[u] - \frac{(b\lambda)^2}{1 - (b\lambda)^2}K[u]\right] \tag{17}$$

$$L_2 = \frac{2\pi}{b^2\lambda^4}\left[(b\lambda)^2 K[u] - 2E[u]\right] \tag{18}$$

where

$$K[u] = \frac{\pi}{2}\left[1 + 2h(u) + 2h^4(u) + 2h^9(u) + \cdots\right]^2 \tag{19}$$

$$E[u] = (1 - u^2)\left(u\frac{dK[u]}{du} + K[u]\right) \tag{20}$$

$$h(u) = \frac{1}{2}I(u) + \left(\frac{1}{2}\right)^3 I^5(u) + 15\left(\frac{1}{2}\right)^9 I^9(u) + 150\left(\frac{1}{2}\right)^{13} I^{13}(u) + \cdots \tag{21}$$

$$I(u) = \frac{1 - \left(1 - u^2\right)^{1/4}}{1 + \left(1 - u^2\right)^{1/4}} \tag{22}$$

For $b\lambda < 1$, the argument $u = \left[1 - \frac{1}{(b\lambda)^2}\right]^{1/2}$ while

for $b\lambda < 1$, the argument $u = \left[1 - (b\lambda)^2\right]^{1/2}$.

When $b\lambda = 1$, the two-dimensional effective hydraulic conductivity simplifies to (in this case $L_1 = -L_2 = \pi^2/\lambda^2$):

$$K_e(x, y) = e^{T(x,y)}\left[1 - \frac{\sigma_f^2 \pi}{2}\left(2\cos^2\theta - 1\right)\right] \tag{23}$$

The effective hydraulic conductivity in three dimensions is (where $m = b\lambda$):

$$K_e = e^T\left\{1 - \frac{\sigma_f^2 \lambda^3 b^3}{\pi}\left[\left(4\cos^2\theta - 2\sin^2\theta\right)\frac{\pi}{m^6}\left[\ln(1+|m|) + \frac{|m|}{4}\,\frac{\left(m^2 - 2|m| - 4\right)}{1+|m|}\right]\right.\right.$$

$$\left.\left. -2\sin^2\theta\left[\frac{\pi}{2m^4}\ln(1 + |m|) - \frac{\pi}{4|m|^3\,(1 + |m|)}\right]\right] \tag{24}$$

## Discussion

All the expressions for effective hydraulic conductivity have the generic form:

$$K_e(x, y) = e^{T(x,y)}\left[1 - \sigma_f^2\,\Xi(b, \lambda, \theta)\right] \tag{25}$$

where $\theta$ is the angle between the gradient of the trend in ln$K$, $\mathbf{b}$, and the mean hydraulic gradient, $\mathbf{J}$; $T(x, y)$ is the trend in ln$K$; and $\Xi$ is a function of aquifer parameters ($b = |\mathbf{b}|$, the correlation scale I, and q), and depends on the flow-domain dimensionality. For example, for one-dimensional domains, $\Xi = 1/(b\lambda + 1)$. Eq. (25) shows that the effective conductivity in the presence of trends of ln$K$ is equal to the geometric mean $e^T$ times a factor introduced by the stochastic analysis $\left(= 1 - \sigma_f^2\,\Xi\right)$ that depends on aquifer parameters. Nonnegativity of $K_e$ requires that

$$\sigma_f^2 < \frac{1}{\Xi\,(b,\,\lambda,\,\theta)} \qquad (26)$$

Eqs. (26) represents a generalization of the condition $\sigma_f^2 < 1$ widely used in stochastic groundwater analyses relying on the small-perturbations assumption.

Since the trend of ln$K$ is generally space-dependent, the effective conductivity is also, in general, heterogeneous. According to Eq. (25), $K_e$ is isotropic, although it depends on the angle between the vector gradient of the trend $T$ and the mean hydraulic gradient, both of which are, in general, spatially variable. For each location **x**, $K_e$ (**x**) represents a spatial average centered at that point. If areal or volumetric averages of hydraulic conductivity are needed, say, for the purpose of calibrating numerical models that rely on spatial discretizations, the effective conductivities given here can be averaged over a domain $\Omega$ by carrying out the integration $(1/\Omega)\int_{\Omega} K_e\, d\Omega$.

Numerical implementation of Eq. (25) requires the trend $T(x, y)$, which must be identified from ln$K(x, y)$ data. Trend identification consists essentially of fitting suitable functions to spatially indexed data. Having the trend $T(x, y)$, its vector gradient **b** follows directly by differentiation with respect to spatial coordinates. The variance of ln$K$, $\sigma_f^2$, can be obtained from the second moment of the residuals $f = \ln K - T$, or jointly with the correlation scale $\lambda$ by estimation methods such as maximum likelihood (Hoeksema and Kitanidis, 1985; Loaiciga and Mariño, 1987). The correlation scale can also be estimated by variogram analysis if a geostatistical estimation method is considered adequate for that purpose. In regards to the angle $\theta$, its value depends on the trend of ln$K$ as well as on the orientation of the mean hydraulic gradient vector at any point, **J**. Contour maps of hydraulic head and piezometric head data are key to calculating the angle $\theta$ through the flow domain. Two examples illustrating the calculation of $K_e$ are presented next.

Calculations of Effective Hydraulic Conductivities in Two and Three Dimensions

Sudicky (1986) presented hydraulic conductivity data acquired during the Borden aquifer tracer experiment; these data were further analyzed by Woodbury and Sudicky (1991). Figure 1a shows a plot of the hydraulic conductivity data along cross section A-A' of the Borden experiment. This plot was composed from 720 $K$ values collected along a vertical cross-section 20 m long and 1.80 m deep; along the horizontal coordinate, $K$ was determined at 1.0 m intervals; the vertical sampling spatial frequency was 1 sample every 0.05 m. Figure 1b shows the plot of ln$K$, a decreasing trend in both $K$ and ln$K$ can be observed with the highest gradient approximately oriented from north (near the surface, where $K$ and ln$K$ appear to be highest) to south (along the deepest side of the cross-section) in the plots of Figures 1a and 1b. In order to "filter out" the effective conductivity from the ln$K$ field, a third-order polynomial trend was fitted to the ln$K$ data, $T(x, y) = -4.12 + 0.152x - 1.06y - 0.0170x^2$

$+ 0.515y^2 - 0.0946xy + 0.000408x^3 + 0.00524x^2y$, where $\mathbf{x} = (x, y, z)$, with all spatial dimensions in meters; modeling the ln$K$ data as isotropic led to a correlation scale estimate of approximately 1 m; $\sigma_f^2$ was estimated to be about 0.30. Based on the approximate orientation of groundwater velocity at the Borden site reported in the series of papers that described the Borden experiment (Freyberg, 1986), the angle $\theta$ between the ln$K$ trend gradient **b** and the mean hydraulic gradient **J** could be calculated at every location. Figure 2 shows the effective hydraulic conductivity (in cm/s) for section A-A' estimated by the Eqs. developed for two-dimensional domains (Eqs. (15), (16) and (23)). In Fig. 2, the decline in effective hydraulic conductivity with depth from the surface is apparent. Pronounced variations in $K_e$ occur along the longitudinal direction at shallow depths. The longitudinal variability in $K_e$ decreases considerably with depth. The effective hydraulic conductivity is a deterministic and continuous function, hence its rather smooth shape in Fig. 2, quite in contrast to the irregular distribution of $K$ and ln$K$ in Figs. 1a and 1b.

Figures 3a and 3b show the plots of $K$ and ln$K$, respectively, for cross-section B-B' of the Borden aquifer experiment as reported by Sudicky (1986). The sampling intervals along the longitudinal and vertical sides were 1m and 0.05 m, respectively, with the longitudinal dimension having a total length of 13 m and the vertical one being 1.80 m. The trend of ln$K$ for section B-B' was estimated to be a fourth-order polynomial $T(x, y) = -3.93 + 0.0215x - 1.49y^2 - 0.364xy + 0.663xy^2 + 0.432y^4 - 0.218xy^3$; the correlation scale and variance of ln$K$ were estimated to be, respectively, 1.0 m and 0.28, quite similar to the cross-section A-A' data, which is not surprising given that both cross-sections were located within the same type of geological material and in close proximity. Figure 4 shows the effective hydraulic conductivity (in cm/s) for cross-section B-B'. There is an overall declining trend in $K_e$ with depth, and its variability along the longitudinal direction is more pronounced than that calculated for cross-section A-A' in Fig. 2.

The results for $K_e$ in Figs. 2 and 4 demonstrate the methods for deriving the effective hydraulic conductivity in two-dimensional domains. Our results are approximate, since, for example, Sudicky (1986) identified different horizontal and vertical anisotropies for Sections A-A' and B-B'. In fact, the analysis of the hydraulic conductivity data from the Borden site as being two-dimensional is somewhat arbitrary since the two cross-sections are, evidently, part of a three-dimensional aquifer. Nevertheless, the experimental design leading to the collection of $K$ data along planar sections lends itself well for the two-dimensional analysis proposed in this work.

Figure 5 shows the three-dimensional plot of vertically averaged hydraulic conductivity (in cm/s) in a semiconsolidated, fractured, claystone aquifer of the Casmalia Hills, Santa Barbara County, California, extensively studied by Hudak (1991). The heterogeneous nature of this random realization (plotted from thousands of granulometric field measurements) is clear, with values ranging over three orders of magnitude. In three dimensions, the ln$K$ field was fitted by a second-order polynomial (quadric surface) to yield a trend $T(x, y, z) = -50.6 + 0.0556y + 0.252z + 0.000003x^2 - 0.000019y^2 - 0.000065xz -$

0.000132$yz$, where $\mathbf{x}' = (x, y, z)$, with all spatial dimensions in meters. $\sigma_f^2$ and $\lambda$ were estimated at 14.24 and 16.25 m, respectively. The variance $\sigma_f^2$ has an unusually large value, at least an order of magnitude larger than that estimated at the Borden aquifer. This surprisingly large variance is, at least theoretically, incompatible with the small-perturbations approach to stochastic groundwater analysis adopted in this report. The Casmalia data can be considered, therefore, a borderline test case for the results developed herein. Typically, better "behaved" data sets are advisable to work with the methods and results developed in this work.

A computer program was written for Eq. (24) to calculate the effective hydraulic conductivity assuming a constant direction of the mean hydraulic gradient (inferred from piezometric data presented by Hudak, 1991). To illustrate some of the results obtained, Figs. 6 and 7 show the plots of effective hydraulic conductivity (in m/day, to enhance the graphical display) for fixed depths $z = 60$ *m* and $z = 90$ *m* for the entire planar domain $(x, y)$. It is clear some sort of an east-west "ridge" in $K_e$, that seems to be accentuated with depth. Because of the extremely large variance of ln$K$, we suspect that calculations based on Eq. (24) unduly reduced the calculated $K_e$ over certain sections of the aquifer; thus, the relatively uniform (with low values) distribution of effective hydraulic conductivity over extensive areas of Figs. 6 and 7. In spite of these difficulties, in this case brought about by unusually large geological variability, the authors are confident that data sets with less variability in ln$K$ can be adequately analyzed with our results to extract the effective hydraulic conductivity. The authors are pursuing further data analyses, besides the two data sets examined in this work, to test further the theoretical findings of this report.

## Conclusions

A method has been developed for calculating the effective hydraulic conductivity in one-, two-, and three-dimensional groundwater flow domains. Starting with the assumption of an isotropic and trend-heterogeneous ln$K$, equations for effective hydraulic conductivity were developed and tested with two data sets.

It was found that the effective hydraulic conductivity is spatially variable and isotropic. Assuming an exponential covariance for ln$K$, it was determined that the effective hydraulic conductivity is continuous in two-, and three-dimensional aquifers for all values of the parameter product $b\lambda$. In one dimension, a discontinuity in $K_e$ exists at $b\lambda = -1$. A discontinuity exists at $b\lambda = 0$, regardless of aquifer dimensionality. However, given the assumption of a trend in ln$K$, this discontinuity is prevented by our choice of model for ln$K$.

The results of effective hydraulic conductivity in two and three dimensions show that this "ensemble" parameter depends on the flow regime and on aquifer parameters. The flow regime determines $K_e$, somewhat indirectly, through the angle formed by the ln$K$ trend gradient and the mean

hydraulic gradient. The magnitude of the $\ln K$ trend gradient, $b$, the variance of $\ln K$, $\sigma_f^2$, and the correlation scale of $\ln K$, $\lambda$, are aquifer parameters that directly affect $K_e$. In one dimension, the effective hydraulic conductivity depends on $\sigma_f^2$, $\lambda$, and $b$ exclusively.

A general condition for the feasibility of $K_e$, according to our results in one-, two-, and three-dimensional domains, is that the variance of $\ln K$ satisfies the inequality $\sigma_f^2 < 1/\Xi(b, \lambda, \theta)$, where the function $\Xi$ depends on flow-domain dimensionality, and it was given for one, two, and three dimensions. It was found that the effective hydraulic conductivity is proportional to the geometric mean $e^T$, where $T$ is the trend in $\ln K$; the proportionality factor is $1 - \sigma_f^2 \Xi$.

## References


Bakr, A. A., L. W. Gelhar, A. L. Gutjahr, and J. R. MacMillan. 1978. Stochastic analysis of spatial variability in subsurface flows, I, Comparison of one- and three-dimensional flows. Water Resources Research 14(2):263-271.

Christakos, G., C. T. Miller and D. Oliver. 1993. Stochastic perturbation analysis of groundwater flow. Spatially variably soils, semi-infinite domains and large fluctuations. Stochastic Hydrology and Hydraulics 7: 213-239.

Freyberg, D. L. 1986. A natural gradient experiment on solute transport in a sand aquifer. 2. Spatial moments and the advection and dispersion of nonreactive tracers. Water Resources Research 22(13): 2031-2046.

Gelhar, L. W. 1993. Stochastic subsurface hydrology. Prentice-Hall, Englewood Cliffs, N.J.

Gutjahr, A. L., L. W. Gelhar, A. A. Bakr, and J. R. MacMillan. 1978. Stochastic analysis of spatial variability in subsurface flows, 2. Evaluation and application. Water Resources Research 14(5):953-959.

Hoeksema, R. J. and P. K. Kitanidis. 1985. Analysis of the spatial structure of properties of selected aquifers. Water Resources Research 21(4): 563-572.

Hudak, P. F. 1991. Analytical methods for regional-scale groundwater monitoring network design and numerical verification. Ph.D. Dissertation, University of California, Santa Barbara.

Loaiciga, H. A., and M. A. Mariño. 1987. The inverse problem for confined aquifer flow: identification and estimation with extensions. Water Resources Research 23(1): 92-104.

Loaiciga, H. A., R. B. Leipnik, M. A. Mariño, and P. F. Hudak. 1993. Stochastic groundwater flow analysis in heterogeneous hydraulic conductivity fields. Mathematical Geology 25(2): 161-176.

Loaiciga, H. A., R. B. Leipnik, P. F. Hudak, and M. A. Mariño. 1994. Effective hydraulic conductivity of nonstationary aquifers. Stochastic Hydrology and Hydraulics. 8(1): 1-17.

Sposito, G., W. A. Jury, and V. K. Gupta. 1986. Fundamental problems in the stochastic convection-dispersion model of solute transport in aquifers and field soils. Water Resources Research 22(11): 77-88.
Sudicky, E. A. 1986. A natural gradient experiment on solute transport in a sand aquifer: spatial variability of hydraulic conductivity and its role in the dispersion process. Water Resources Research 22(13): 2069-2082.
Woodbury, A. L. and E. A. Sudicky. 1991. The geostatistical characteristics of the Borden aquifer. Water Resources Research 27(4): 533-546.

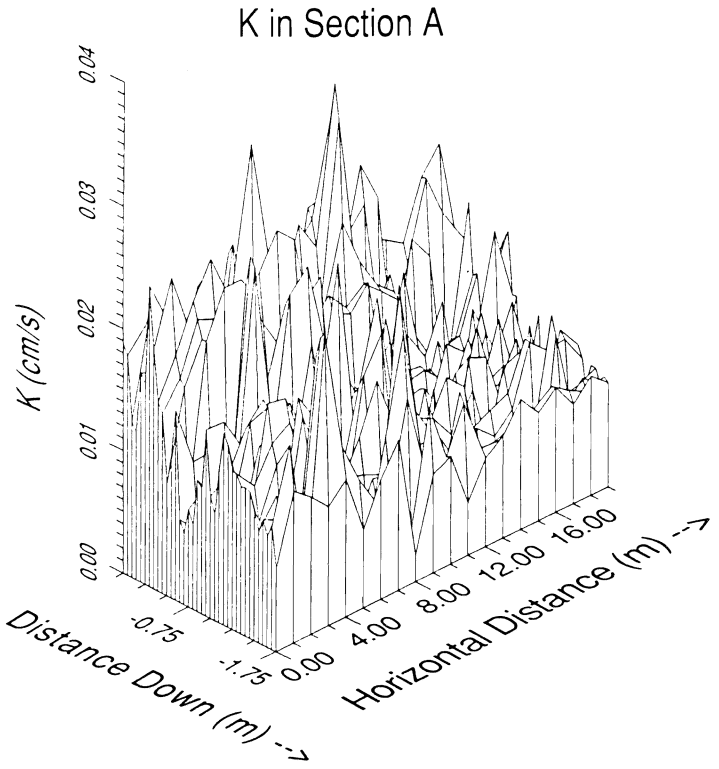


Figure 1a. Plot of hydraulic conductivity data (cm/s) for section A-A' of Borden aquifer (Sudicky, 1986)

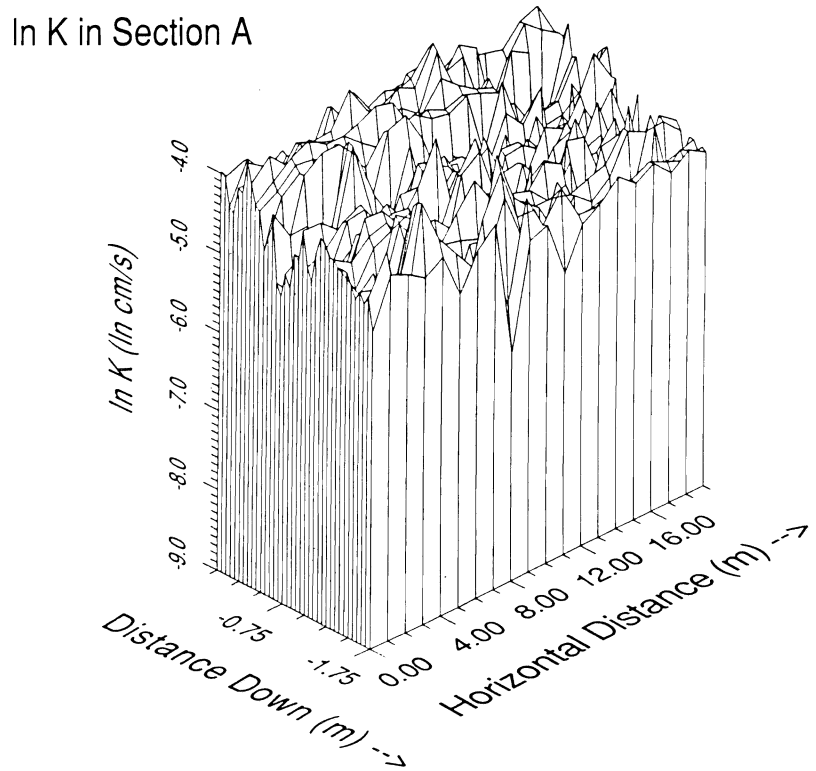


Figure 1b. Plot of ln*K* data cross-section A-A' of Borden aquifer (Sudicky, 1986)

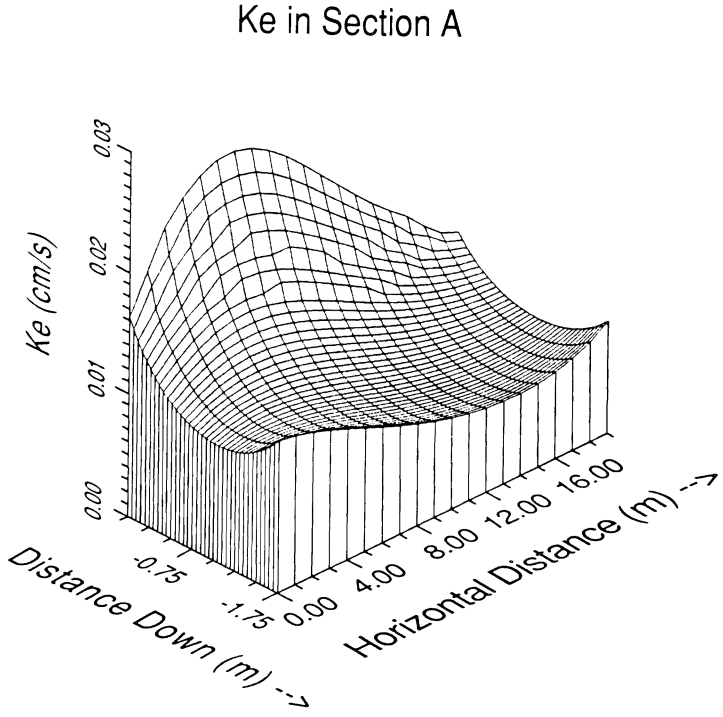


Figure 2. Effective hydraulic conductivity for section A-A' of Borden aquifer (in cm/s)

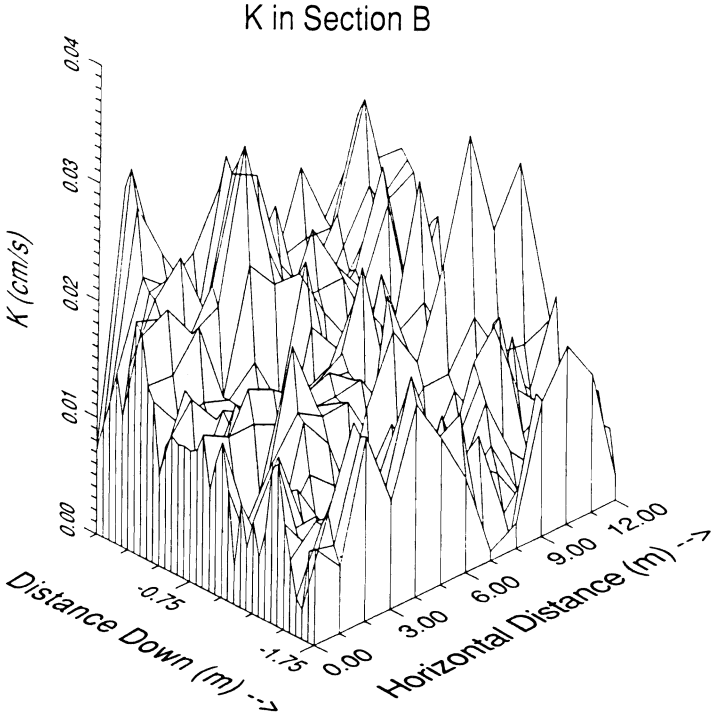


Figure 3a. Plot of hydraulic conductivity data (cm/s) for section B-B' of Borden aquifer (Sudicky, 1986)

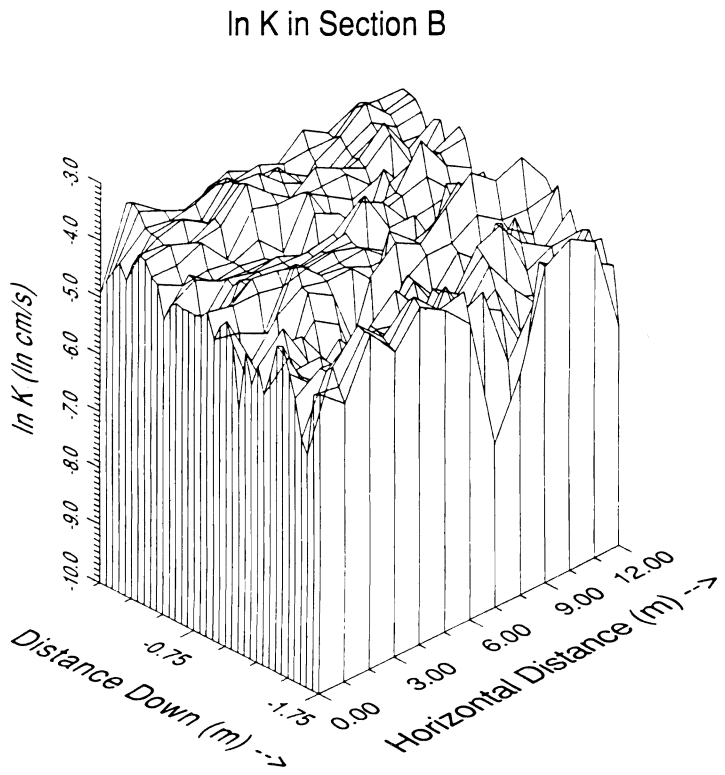


Figure 3b. Plot of ln*K* data for section B-B' of Borden aquifer (Sudicky, 1986)

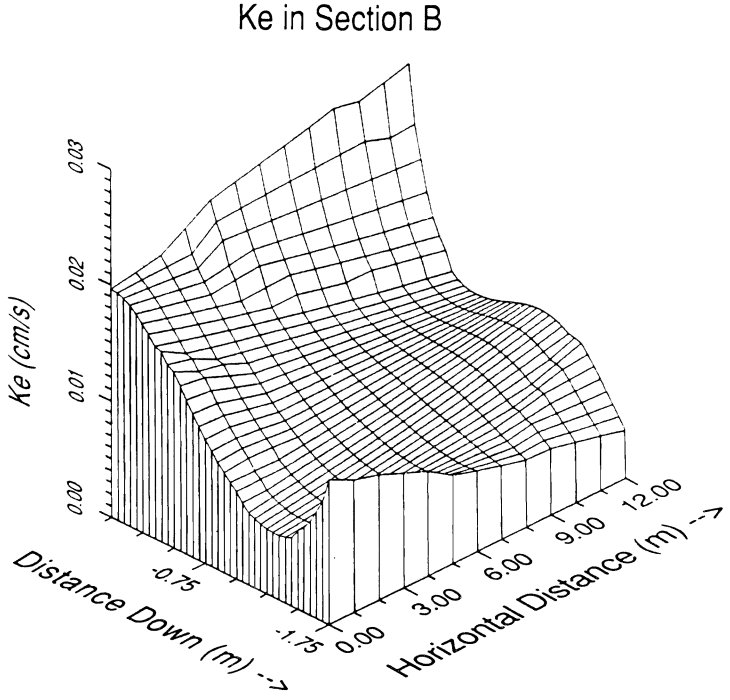


Figure 4. Effective hydraulic conductivity (cm/s) for section B-B' of Borden aquifer

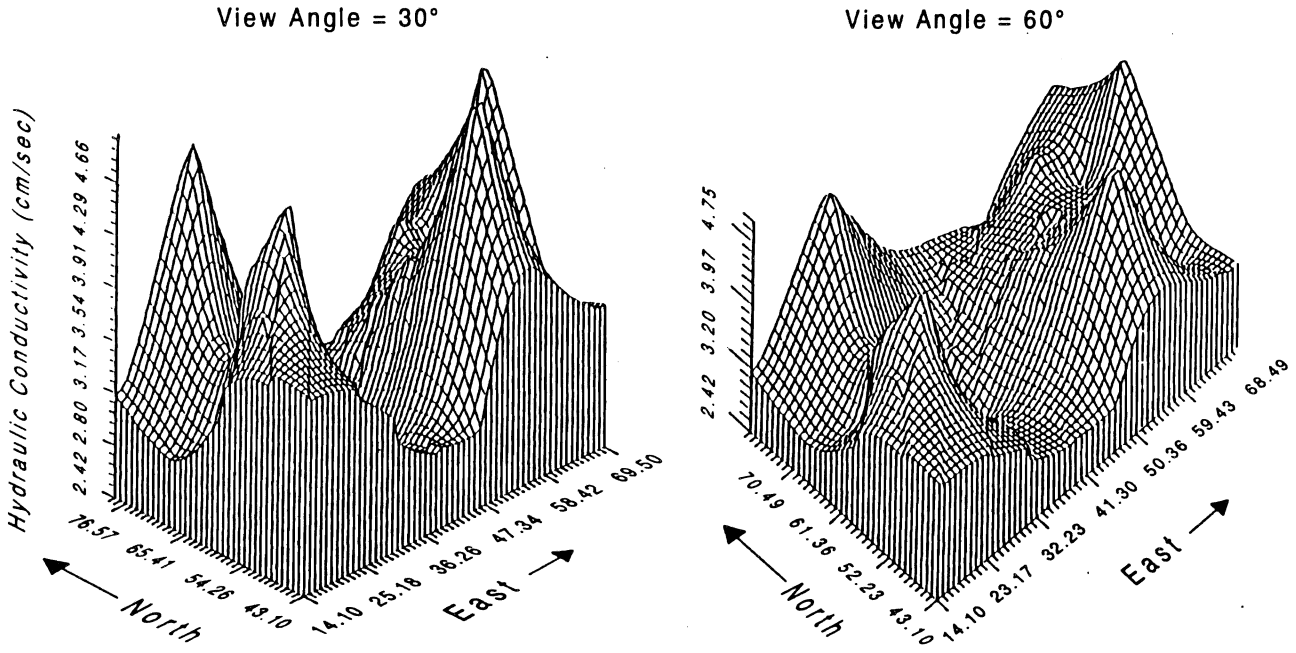


Figure 5. Two three-dimensional views of vertically averaged hydraulic conductivity (cm/s) for the semiconsolidated claystone of the Casmalia Hill aquifer, Santa Barbara County, California (Hudak, 1991)

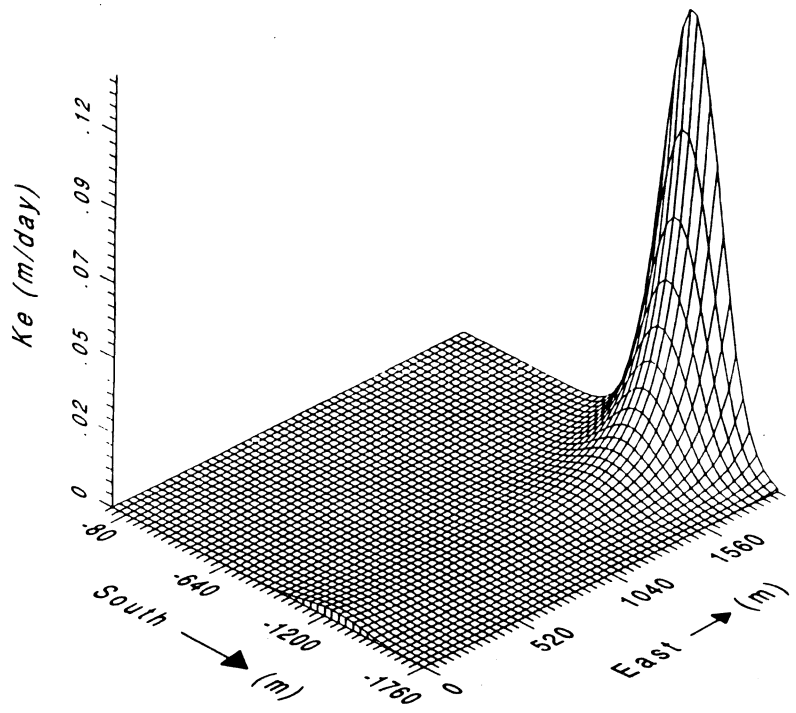


Figure 6. Effective hydraulic conductivity (m/d) at depth $z$ = 60 $m$ at the Casmalia aquifer.

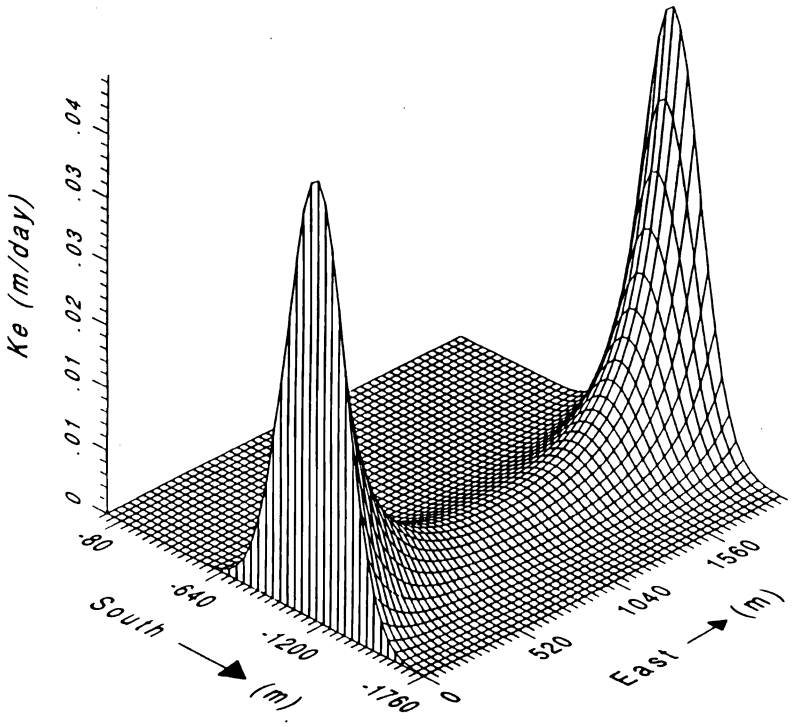


Figure 7. Effective hydraulic conductivity (m/d) at depth $z$ = 90 $m$ at the Casmalia aquifer.

# Application of Industrial X-Ray Computed Tomography to Transport of Organic Solvents and Pesticides in Soils

JAN W. HOPMANS[1], VOLKER CLAUSNITZER[1], DONALD R. NIELSEN[1], AND JOHN S. STEUDE[2]

[1]*Department of Land, Air and Water Resources, Davis Campus*

[2]*Scientific Measurements, Inc., Austin, Texas*

## Summary

Movement of industrial and agricultural chemicals as subsurface contaminants is usually described by the convection-dispersion equation, including terms for adsorption and degradation. However, in many cases poor agreement is found between measured and predicted contaminant concentrations (Gish et al., 1986). Very often, unaccounted soil heterogeneities are cited as probable cause for the deviations.

This two-year project investigates the transport of soluble and nonaqueous phase liquids (NAPL) through porous media on a scale small enough to resolve spatial heterogeneities found within the sampled volumes commonly used for determination of soil hydraulic and transport parameters. High-resolution X-ray computed tomography is applied as a nondestructive measurement technique to variably saturated samples to characterize transport processes in terms of spatial and temporal variation of these parameters.

**Key Words:** Multiphase transport, porous media, image analysis

## Project Objectives Addressed in 1993-94

1. Develop methodology for two- and three-dimensional visualization of phase distribution in porous media with multiple fluid phases present.
2. Test and develop the software necessary to extract maximum information from scanner output.

## Research Plan and Procedures

Scanner

Scans were performed at Scientific Measurement Systems, Inc. (SMS) in Austin, TX. By using a microfocus X-ray emitter (125 kV, 0.08 A, 10 mm focal spot size) in combination with an aerial detector, 30 horizontal "slices" could be scanned simultaneously (Fig. 1). At this resolution, object size is limited to diameters not exceeding 1 cm. The areal detector consists of a rectangular array of 1000 ¥ 1000 individual detector cells each measuring 20 mm ¥ 20 mm. The focal spot size, i.e., the diameter of the X-ray fan at the emitter, and the size of the detector cells set a physical limit to the resolution that can be obtained. An object, typically centered between emitter and detector array, will cast a "shadow" at the detector array that is bigger than itself. Considering this magnification effect, the smallest "unit" to be identified inside a cross section would be approximately 15 mm wide for our system (assuming a theoretical no-noise image).

The object is held in place by a high-precision linear positioning system within 1 mm both horizontally and vertically.

A compromise had to be found between scanning time and image quality, i.e., the amount of noise in the attenuation values. After several initial tests we selected a procedure with 720 rotation increments of 0.5 degrees. Each position was scanned for 1 sec. Thus, a volumetric representation of an approximately 0.5 mm vertical range of the object could be obtained within 20 min. This seemed appropiate for static objects but may still be too slow for many flow experiments where significant changes occur over much shorter periods and hence would only be detectable as blurs.

Image Reconstruction and Visualization

Volume data of relative attenuation values representing the scanned object as a set of two-dimensional images (one for each horizontal cross section) were to be reconstructed by SMS using SUN workstation equipment and proprietary software. The new microfocus/multislice technology and the pertaining volume reconstruction algorithm still being of experimental nature at SMS, this step proved particularly prone to delay. At this point, reconstruction is complete for the top third of the respective scanned volume of the NAPL experiments.

The binary data files as shipped by SMS (each defining one horizontal slice) had to be converted into a format accessible to visualization software. We

chose the flexible Hierarchic Data Format (HDF), developed at the National Center for Supercomputing Applications (NCSA), because it produces hardware-independent, compact (i.e., binary) data files and is well documented and readily available as a public-domain utility. HDF files can be used directly as input for both commercial (e.g., SPYGLASS) and various public-domain software products. Computer code was developed to transfer SMS's files into HDF files containing volumetric data sets, clipping in the horizontal plane as necessary.

We tested a variety of software tools for data visualization on a Silicon Graphics Indigo workstation. The public-domain programs VIS-5D and 4d2, developed by the University of Wisconsin Space Science and Engineering Center and at NCSA, respectively, were selected for their 3D graphical capabilities. While being the more powerful tool, VIS-5D required creating an additional data conversion program to match its input format. The source code was modified to accommodate our rather large volumetric data sets and to avoid interpolation between image pixel values which would obstruct the actual resolution obtained by the tomographic procedure. For 2D slice-image analysis, we used the program "Transform" by SPYGLASS, Inc.

Experimental Procedures

Having tested bead sizes ranging from 200 mm to 1 mm, we decided to compromise between realistic particle size and good particle image resolution by using 500 mm glass beads of nearly perfect sphere-shape, obtained from Jaygo, Inc. Beads were packed in sample holders made from plastic tubing of 4.5 mm inner diameter and approximately 0.8 mm wall thickness. The sample holder was firmly attached to the linear positioning table of the scanner.

To establish whether the new technology could distinguish individual fluid phases and the respective interfaces in porous media, we added small amounts (two drops of approximately 0.015 ml each) of water and carbon tetrachloride ($CCl_4$) to the bead packs, both in individual samples and combined. $CCl_4$ was chosen as the NAPL for the high X-ray attenuation, relative to water, provided by the chlorine nuclei. Scans of the dry samples were taken before introducing the liquids to serve as references for subsequent image subtraction.

A linear relationship between solute concentration of a sample and attenuation values has been reported repeatedly for medical X-ray CT systems (e.g., Steude, 1990). We had previously confirmed this result for a high-energy industrial SMS scanner of 100 mm spatial resolution using 0-10% sodium-iodide (NaI) solution ($R^2 > 0.99$). We now tested the same solution range for the microfocus device. Glass capillaries were filled with pure water, 1.25%, 2.5%, 5%, and 10% NaI solution, attached inside one of the sample holders, and scanned.

To investigate the potential of X-ray-based microtomography for dynamic experiments, we conducted a "stepwise" miscible-displacement experiment using a water-saturated sample and 10% NaI solution as a pulse. Reference scans

were taken before (at water saturation) and after the experiment (the sample was flushed by five pore volumes of 10% NaI solution and then scanned at assumed NaI saturation). Image reconstruction for the sequence of eight scans is currently underway.

## Results and Discussion

Figure 2 shows the near-linear relationship found between attenuation values and solute concentration inside the glass capillaries; however, with $R^2 = 0.986$ the linearity was less distinct than the one previously obtained with the 100-mm resolution / one-slice technology (Hopmans et al., 1993). The data points were obtained by averaging over the liquid-filled cross section of each glass capillary (approximately 600 pixels). The error bars thus give an indication of the noise level within one slice.

Figures 3A and B show a cross section of the bead pack with air-filled pores and a line graph of attenuation values parallel to the x-axis at y = 4 mm, respectively. Note that the attenuation values for the air between the beads are higher than for the air outside the sample. Clearly, this is an artifact of the procedure that can obstruct phase distinction within the pore space. As a means to reduce this effect, we subtracted the attenuation values of the "dry" scan (Fig. 3A) from those of the subsequent "wet" scan (not shown). Ideally, the artifacts would be subtracted as well and only the difference, i.e., the introduced liquid phase, would be left. In Fig. 4, cross sections of $CCl_4$-ganglia and -films can be identified as the bright parts of the picture. Both the beads and the container effectively disappeared from the image.

Phase boundaries between solid, liquid, and gas phases can be outlined as isosurfaces in three dimensions. However, due to its necessarily interpolative nature, this procedure can produce misleading results---for example, beads may appear smaller when a higher iso-attenuation value is chosen. Thus, attenuation values for each isosurface need to be carefully selected from the histogram of the respective data set. A three-dimensional representation of the dry bead pack within a 0.16 mm vertical range (10 horizontal slices) is given in Fig. 5. Figure 6 depicts a 3D $CCl_4$ distribution for the same spatial range. Please note that isosurfaces are not closed at the upper and lower image boundary, respectively. Image contrast benefits substantially from using color instead of a gray scale as is necessary here.

While providing excellent image contrast, the $CCl_4$ required extra attention as a potential health hazard and, being an aggressive solvent, it proved rather impractical to work with. Therefore, in future experiments, we will use iodine-doped mineral oil as the NAPL. Ongoing efforts focus on measuring solute breakthrough at points within the pore space and aims at further improvement of computerized image analysis.

## References

Gish, T. J., C. S. Helling, and P. C. Kearney. 1986. Simultaneous leaching of bromide and atrazine under field conditions, p. 286-297, in: National Water Well Association. Proc. of The Agric. Impacts on Ground Water -- A Conference, Omaha, NE, Aug. 11-13, 1986.

Hopmans, J. W., D. R. Nielsen, and J. S. Steude. 1993. Application of industrial X-ray computed tomography to transport of organic solvents and pesticides in soils, Annual Report to Kearney Foundation.

Steude, J. S., C. P. Sullivan, R. C. Chaney, M. McKee, and L. E. O'Shea. 1990. Tracer experiments in saturated sand by computed tomography and inductively coupled plasma, in: K. B. Hoddinott and R. O. Lamb, (eds.), Physico-chemical aspects of soil and related materials, Am. Soc. for Testing and Materials STP 1095, Philadelphia, p. 171-184.

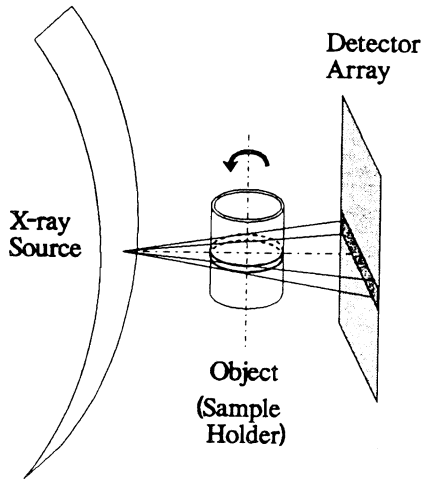


Figure 1. Schematic representation of microfocal scanning system.

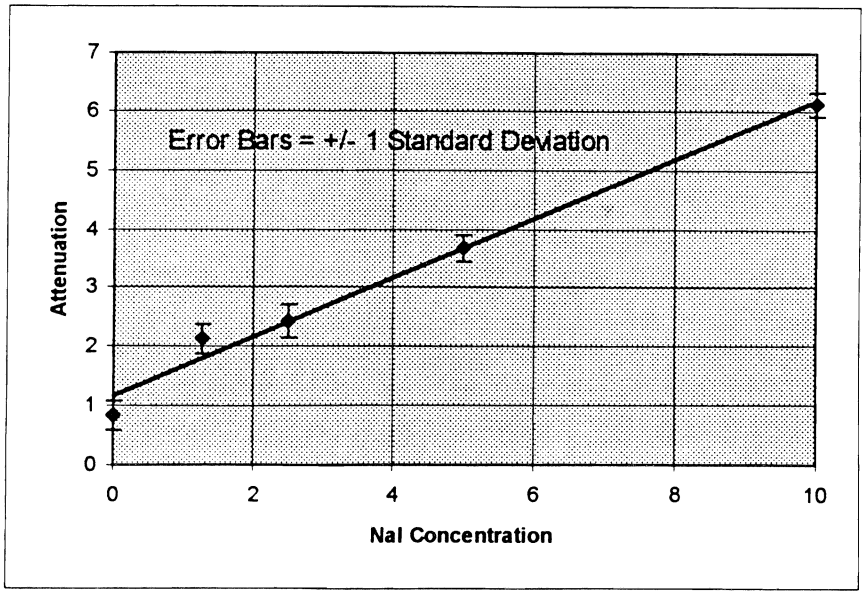


Figure 2. Relationship between solute concentration and attenuation

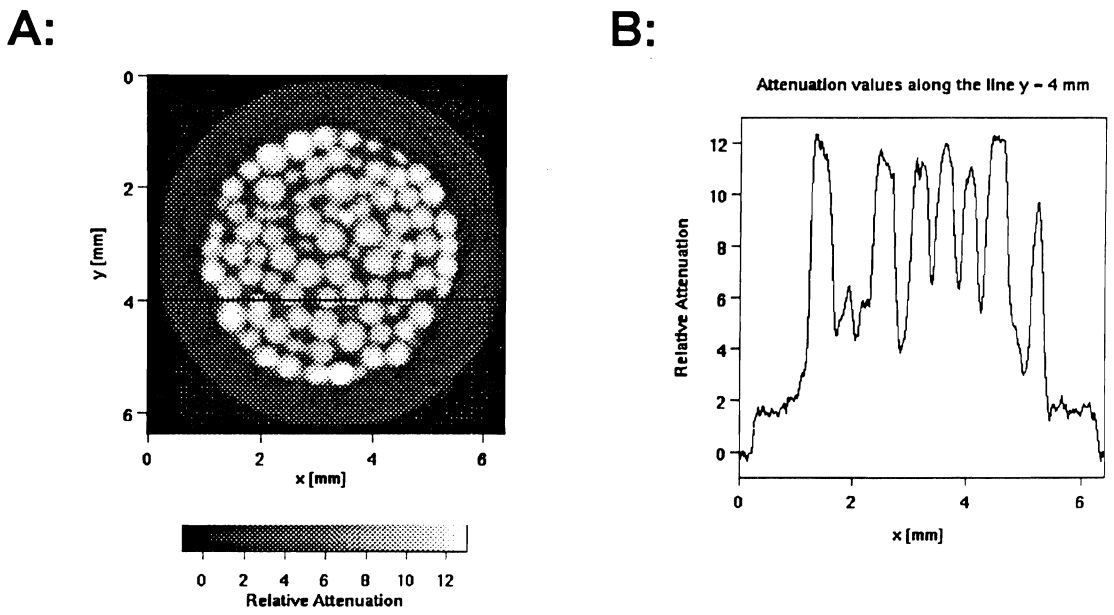


Figure 3. Cross section of dry bead pack (A) and line graph at y = 4 mm (B).

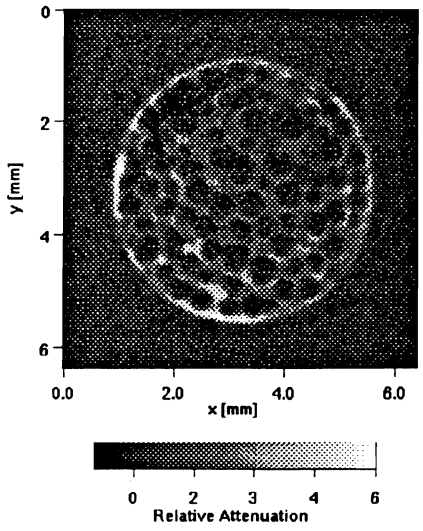


Figure 4. Image obtained by subtracting "dry" from "wet".

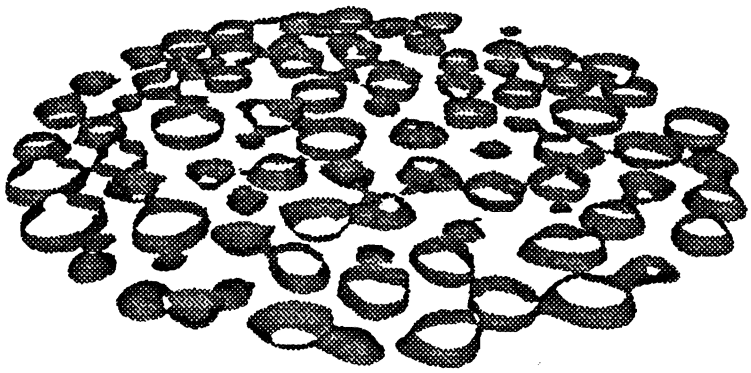

Figure 5. Isosurfaces at attenuation of 2.5, depicting glass-bead–air interfaces in "dry" scan.

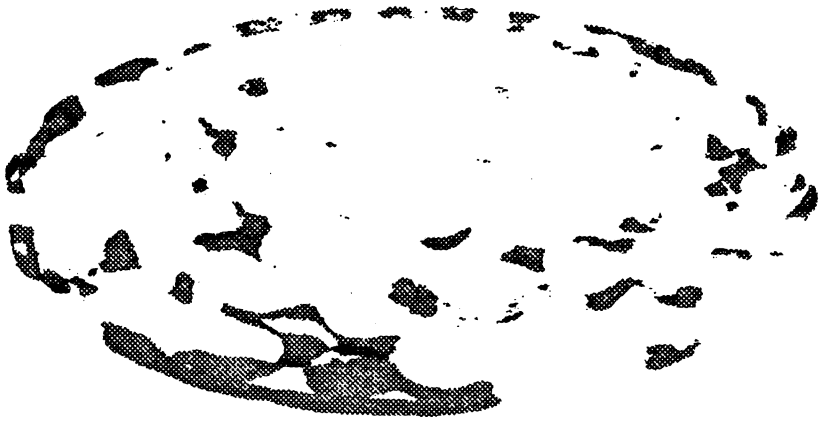

Figure 6. Isosurfaces at attenuation of 10.5, depicting $CCl_4$ after image subtraction.

# Retention and Permeability of Multi-Fluid Soil Systems

SCOTT A. BRADFORD[1], FEIKE J. LEIJ[1], JAN W. HOPMANS[2], PETER J. SHOUSE[3], AND MARTINUS TH. VAN GENUCHTEN[1,3]

[1] *Department of Soil and Environmental Sciences, Riverside Campus*
[2] *Department of Land, Air and Water Resources, Davis Campus*
[3] *U.S. Salinity Laboratory, USDA, ARS, Riverside*

## Summary

Predicting the movement of a nonaqueous phase liquid (NAPL) in the vadose zone requires that the retentive and conductive properties of the soil be known for the aqueous, nonaqeous, and gaseous phases. Theories for the prediction and modeling of capillary pressure ($P_c$) - saturation ($S$) relationships for three-fluid porous media from two-fluid porous media are generally based on the limiting assumptions that the medium (solid) is strongly wetted by one fluid and that the intermediate wetting fluid forms a continuous layer between the wetting and nonwetting fluids. During the first year of this project, two- and three-fluid $P_c$-$S$ relations were measured with an automated setup for samples of blasting sands containing: (i) air and water; (ii) air and oil; (iii) oil and water; and (iv) air, oil, and water. The blasting sands were treated with organosilane compounds to obtain various degrees of hydrophobicity. Mixed wettability media were made up from different fractions of untreated and treated sands. We found a substantial difference between measured and predicted (from scaling and Leverett's assumption) $P_c$-$S$ curves for hydrophobic and mixed wettability media containing oil-water or air-oil-water. The model for predicting $P_c$-$S$ curves of oil-water and hydrophilic air-oil-water media was improved successfully.

**Key Words:** hydraulic properties, capillary pressure, NAPL, wettability, Leverett's assumption, hysteresis.

## Project Objectives Addressed in 1993-94

The general objective of this project is to measure and model the hydraulic functions of multi-fluid porous media containing NAPLs. The activities in this first year consisted of the measurement, modeling, and prediction of $P_c$-$S$ relations for two- and three-fluid soil systems with different wettabilities. In the second year these results will be analyzed further and the permeability of two- and three-fluid media will be investigated.

## Research Plan and Procedures

### Capillary Pressure

The capillary pressure is the pressure drop over the curved interface between the nonwetting and wetting fluids. In air-liquid systems the liquid ($l$), either oil or water, is the wetting fluid and air ($a$) is the nonwetting fluid. The air-liquid capillary pressure, $P_{al}=P_a-P_l$, is always positive. In a two-liquid system with uniform wettability, either water ($w$) or oil ($o$) wets the solid; the other liquid is the nonwetting fluid. The capillary pressure is defined as $P_{ow}=P_o-P_w$ for a water-wet system and $P_{wo}=P_w-P_o$ for an oil-wet system. The definition is less clear for mixed wettability systems. Throughout this report we use $P_c=P_{ow}$ and write $P_c$ as a function of the water saturation, $S_w^{ow}$ (the subscript pertains to the volume of a particular fluid per unit pore volume and the superscript denotes all fluids present).

### Measurement of Two- and Three-Fluid $P_c$-$S$ Relations

Two- and three-fluid $P_c$-$S$ relations were obtained with an automated setup by displacing a known quantity of fluid into or from a soil column (cf. Fig. 1). The column consisted of hydrophobic and hydrophilic ring tensiometers. For fluid systems involving air, the top of the column was allowed to remain open so air was at atmospheric pressure. A data logger controlled stepping motors and solenoid valves, and also registered pressure transducer readings (Fig. 2). The stepping motors adjusted vacuum-pressure regulators, connected to burets filled with water or oil through solenoid valves. The valves were open for establishing a new liquid saturation in the column or closed for achieving an equilibrium fluid distribution. Liquid pressures and saturations were measured with ring tensiometers and burets, respectively, connected to a pressure transducer.

### Fluid and Media Properties

For all $P_c$-$S$ measurements, a column of known volume was filled with the initial wetting fluid and packed with a predetermined mass of a blasting sand mixture to obtain a dry bulk density ($\rho_b$) of 1.71 g/cm$^3$. The porous medium was a mixture of blasting sands containing 12.6 % each of sizes #12 and #16, 25.2% each of sizes #20 and #30, and 8.2 % each of sizes #60, #70, and #90. This distribution corresponds to 25% very coarse sand, 50% coarse/medium

sand, and 25% fine sand according to the USDA textural classification (Soil Survey Staff, 1975). The initial volume of the wetting fluid was considered to be equal to the product of the column volume and porosity; the latter was calculated assuming a specific density of 2.65 g/cm$^3$ (Danielson and Sutherland, 1986). Oil (Soltrol 220, $\rho_o$=0.8 g/cm$^3$) was the initial wetting fluid for air-oil systems, and water was used for all other systems. The fluid interfacial tensions, measured with a du Noüy ring (1919), were $\sigma_{aw}$=72 N/m, $\sigma_{ao}$=24 N/m, and $\sigma_{ow}$=26 N/m.

Treating Media to Obtain Different Wettabilities

To obtain media with different degrees of wettability, blasting sands were treated with organosilane compounds. The sands were added to a 5% solution of an organosilane (octadecyltrichlorosilane, OTS; vinyltriethoxysilane, VTS; or glycidoxypropyltrimethoxysilane, GPTS) in ethanol and mixed in a shaker for 5 hours; the sands were then air dried (Anderson et al., 1991). These organosilanes were selected based on reported values for the solid-air interfacial tensions, $\sigma_{sa}$, of 22.5 N/m for OTS, 25 N/m for VTS, and 42.5 N/m for GPTS (Anderson et al., 1991; Wei et al, 1992) while the value for $\sigma_{\sigma a}$ of the untreated sand was assumed to be 78 N/m just as for fused silica (Hiemenz, 1986). Note that a lower value for $\sigma_{\sigma a}$ reflects an increase in hydrophobicity. Mixed wettability media were obtained by combining untreated and OTS-treated blasting sands; mixtures of 0, 25, 50, 75, and 100% OTS sands were used. The untreated sands were strongly water-wet, while the OTS-treated sands were oil-wet in oil-water systems or water repellent in air-water systems.

## Results and Discussion

Quantifying Wettability

The contact angle ($\phi$) is used to quantify the wettability of solids with uniform wettability. The advancing and receding contact angles ($\phi^A$ or $\phi^R$) of fluid system 2 can be obtained from $P_c$-$S$ data for fluid systems 1 and 2, with complete wetting for system 1, using a scaling relation based upon the Laplace-Young equation:

$$P_{c1}(S_{\theta 1}) = \frac{\sigma_1 \cos(\phi_1^{A,R})}{\sigma_2 \cos(\phi_2^{A,R})} P_{c2}(S_{\theta 2}) = \beta P_{c2}(S_{\theta 2}) \qquad (1)$$

where $\beta$ is a scaling factor to be determined from optimizing $P_c$-$S$ data; $\phi^{A,R}$ is an advancing or receding contact angle; and the effective saturation $S_\theta = (S-S_r)/(1-S_r)$, with $S_r$ as the residual saturation. Note that $\phi_2^{A,R}$ can be determined

from $\sigma_1$, $\sigma_2$, and $\beta$ if $\phi_1^{A,R}=0$. Soltrol was found to completely wet air-oil media for various wettabilities (cf. Fig. 4). Table 1 shows the values of $\phi^A$ and $\phi^R$ obtained with the optimized scaling factor for air-water and oil-water media with uniform wettability (i.e., untreated, GPTS, VTS, and OTS sands).

The contact angle is position-dependent in oil-water media with mixed wettability; its value depends on surface roughness (Morrow, 1976), immobile adsorbed liquid layers (Adamson, 1967), and adsorptive properties of the solid (Anderson, 1986). An alternative method of quantifying the wettability is the United States Bureau of Mines (*USBM*) Method, which uses the principle that work necessary for displacement of the wetting by the nonwetting fluid is less than for the reverse process. The *USBM* wettability index is (Donaldson et al., 1969):

$$I_{USBM} = \log(A_W / A_O) \qquad (2)$$

where $A_w$ is the area under the $P_{ow}$-$S_w^{ow}$ curve for a hydrophilic system ($P_{ow}>0$), and $A_o$ is the area above the $P_{ow}$-$S_w^{ow}$ curve for a hydrophobic medium ($P_{ow}<0$). Figure 3 shows a plot of the calculated values of $I_{USBM}$ versus the fraction of OTS sand. The wettability index, $I_{USBM}$, was determined as: (i) $I_{USBM}^1$ from primary drainage and main imbibition $P_{ow}$-$S_w^{ow}$ data and (ii) $I_{USBM}^2$ from main drainage and imbibition $P_{ow}$-$S_w^{ow}$ data.

Wettability Effects on Air-Liquid Systems

Figures 4 and 5 show the $P_{ao}$-$S_o^{ao}$ and $P_{aw}$-$S_w^{aw}$ curves for drainage and imbibition in 0 and 100% OTS media filled with air-oil and air-water, respectively. All pressures are expressed in cm of water. The $P_{aw}$-$S_w^{aw}$ curve is greatly affected by hydrophobicity (% OTS) in contrast with the $P_{ao}$-$S_o^{ao}$ curve. This is primarily due to the difference in interfacial tension of each liquid with air (i.e., $\sigma_{ao}$=24 N/m and $\sigma_{aw}$=72 N/m). The low value for $\sigma_{ao}$ leads to a low $\phi^{A,R}$; Soltrol can therefore completely wet untreated (hydrophilic) and OTS (hydrophobic) media.

Wettability Effects on Oil-Water Systems

Figure 6 shows the $P_{ow}$-$S_w^{ow}$ curves during primary drainage, main imbibition, and main drainage for the 50 and 100% OTS media. Note that during imbibition $P_{ow}$ at a particular $S_w^{ow}$ decreases as the fraction of OTS sand increases, with $P_{ow}$ becoming negative at $S_w^{ow}$=0.69 and 0.27 for the 50% and 100% OTS media, respectively. The negative $P_{ow}$ is a result of forced imbibition, i.e., water can only displace oil from the pore space when positive pressure is exerted on the oil phase relative to the water phase. The main drainage curve always has a lower $P_{ow}$ than the primary drainage curve for a given $S_w^{ow}$. This feature has, of course, already been reported for air-water systems where it was attributed to air entrapment (e.g., Stonestrom and Rubin, 1989). An explanation for the increased difference for the 100% OTS media is that water (the saturating fluid) may initially prevent oil from wetting the sand

during primary drainage. After oil replaces water as the wetting fluid (primary drainage), the solid is wetted more readily by oil during the subsequent (main) drainage of water. The observed difference between primary and main drainage curves illustrates the importance of the initial saturation conditions.

The $P_{ow}$-$S_w^{ow}$ relation is sometimes measured on an initially water saturated soil column with a hydrophilic capillary barrier at the bottom and an oil reservoir at the top. A change in oil pressure in the reservoir causes water to exit at the bottom ($S_w^{ow}$ decreases), similar to applying a pneumatic head for measuring the soil water retention curve. If water is not the wetting liquid ($P_o > P_w$), changes in water content in the forced imbibition region can not be observed in this manner. A better way of measuring the $P_{ow}$-$S_w^{ow}$ relations has been to apply suction initially to the oil reservoir or, even better because of faster equilibration, to impose the liquid contents and to monitor the pressure subsequently (Figs. 1 and 2).

Empirical Model to Describe Oil-Water $P_c$-S Relations

Parametric models, such as those by Brooks and Corey (1964) and van Genuchten (1980), are commonly employed to describe $P_{ow}$-$S_w^{ow}$ data. These models are only suitable for positive capillary pressures. The $P_c$-$S$ model of van Genuchten was therefore modified to account for negative capillary pressures as:

$$P_{ow} + \gamma = \frac{1}{\alpha}\left[\left(\bar{S}_w^{ow}\right)^{-1/m} - 1\right]^{1/n} \qquad (3)$$

where $\bar{S}_w^{ow}=(S_w^{ow}-S_{rw}^{ow})/(1-S_{rw}^{ow}-S_{ro}^{ow})$ maps $S_w^{ow}=S_{rw}^{ow}$ onto $\bar{S}_w^{ow}=0$, and $S_w^{ow}=1-S_{ro}^{ow}$ onto $\bar{S}_w^{ow}=1$, and the subscript $r$ again denotes a residual value. The parameter $\gamma$ was set equal to the magnitude of the lowest value of $P_{ow}$ so that the value of $P_{ow}+\gamma$ is always greater than or equal to zero. The $P_c$-$S$ model of van Genuchten was then used to describe this $(P_{ow}+\gamma)$-$\bar{S})_w^{ow}$ relation. Table 2 shows the measured values of $S_{rw}^{ow}$, $S_{ro}^{ow}$, and $\gamma$ determined from the measured mixed wettability $P_{ow}$-$S_w^{ow}$ curves; $S_{ro}^{ow}$ and $\gamma$ were set equal to zero during primary drainage. Table 2 also shows the fitted values of $\alpha_{PD}$, $\alpha_{MI}$, $\alpha_{MD}$ (denoting the values for $\alpha$ during primary drainage, main imbibition, and main drainage curves), and $n$ (note that $m=1-1/n$) for the $P_{ow}$-$\bar{S}_w^{ow}$ curves. Parameter optimization was done according to Marquardt (1963). The coefficient of regression between measured and fitted values ($R$) was always greater than 0.965.

## Predicting Two-Fluid $P_c$-S Relations

Scaling $P_c$-$S$ data for a particular two-fluid medium is common for obtaining $P_c$-$S$ relations for other two-fluid systems involving the same porous medium. Figures 7a and 7b show the observed and predicted $P_{ao}$-$S_o^{ao}$ and $P_{ow}$-$S_w^{ow}$ curves for the OTS sand during drainage and imbibition. The predictions in Fig. 7a were obtained from scaling the $P_{aw}$-$S_w^{aw}$ curve using the ratios $\sigma_{ao}/\sigma_{aw}$ and $\sigma_{ow}/\sigma_{aw}$, respectively. The scaling in Fig. 7b was based on the ratio of interfacial tensions *and* contact angles (i.e., $\sigma_{ao}/\sigma_{aw}{}^{*}\cos(\phi_{saw}^{A,R})$ and $\sigma_{ow}\cos(\phi_{sow}^{A,R})/\sigma_{aw}{}^{*}\cos(\phi_{saw}^{A,R})$, respectively). The superscript * indicates the more realistic value for (oil) contaminated water. Note that the scaling in Fig. 7b, in contrast with Fig. 7a, results in a closer agreement between predicted and observed OTS $P_c$-$S$ data.

The conventional scaling is more appropriate for air-liquid systems, where the solid is wetted preferentially by the liquid, than for oil-water systems, where the solid may be wetted by both oil and water. Scaling according to Eq.(1) can not account for both positive (spontaneous imbibition) and negative (forced imbibition) capillary pressures. An alternative approach is to shift the $P_c$-$S$ model as well:

$$P_{ow}(\bar{S}_w^{ow}) = \frac{\sigma_{ow}}{\sigma_{ao}} P_{ao}(\bar{S}_o^{ao}) - \gamma \qquad (4)$$

where $\bar{S}_o^{ao}=(S-S_{ro}^{ao})/(1-S_{ro}^{ao}-S_{ra}^{ao})$ while $\sigma_{ow}/\sigma_{ao}$ and $\gamma$ account for the differences between the systems in interfacial tensions and wetting properties, r espectively. The $P_{ao}$-$\bar{S}_o^{ao}$ relationship was used for scaling instead of $P_{aw}$-$\bar{S}_w^{aw}$ because the relatively low $\sigma_{ao}$ compared to $\sigma_{aw}$ suggests that the solid is wetted better by oil than water. The relationship between $\gamma$ and the hydrophobicity/wettability (i.e., the % OTS) is shown in Fig. 8. Values for $\gamma$ were obtained by fitting the $(\sigma_{ow}/\sigma_{ao})P_{ao}$-$\bar{S}^{ao}$ data to the $P_{ow}$-$\bar{S}_w^{ow}$ curves during main drainage and imbibition. Figure 9 shows a comparison of the predicted and measured $P_{ow}$-$\bar{S}_w^{ow}$ relations during main drainage and imbibition for the 25% and 75% OTS media. The regression formulas shown in Fig. 8 were used to predict $\gamma$ during drainage (D) and imbibition (I).

## Three-Fluid $P_c$-S Relations

For three-fluid systems with a continuous intermediate fluid, a pressure drop occurs over the oil-water and air-intermediate fluid interfaces. Figure 10a shows the $P_{ow}$-$S_w^{aow}$ (left side) and $P_{ow}$-$S_o^{aow}$ (right side) curves for the untreated sand while Fig. 10b shows the $P_{ao}$-$S_{tl}^{aow}$ curve. The total liquid saturation is defined as $S_{tl}^{aow}=S_o^{aow}+S_w^{aow}$. The oil-water and air-oil capillary pressures are unique functions of the wetting fluid and total liquid saturations, respectively.

For a discontinuous intermediate fluid layer, a pressure drop occurs over the oil-water, air-water, and air-oil interfaces. Figure 11a shows the $P_{ow}$-$S_w^{aow}$ (left side) and $P_{ow}$-$S_w^{aow}$ (right side) curves for the (100%) OTS medium, while Fig. 11b and 11c show the $P_{ao}$-$S_{tl}^{aow}$ and $P_{aw}$-$S_{tl}^{aow}$ curves, respectively. The capillary pressures $P_{ow}$, $P_{ao}$, and $P_{aw}$ depend on both $S_w^{aow}$ and $S_o^{aow}$. However, $P_{ow}$ and $P_{aw}$ are mainly functions of $S_w^{aow}$, while $P_{ao}$ is mainly a function of $S_o^{aow}$. A change in $S_w^{aow}$ (constant $S_o^{aow}$) or $S_o^{aow}$ (constant $S_w^{aow}$) leads to changes in the air saturation; $P_{ao}$ and $P_{aw}$ are therefore mainly functions of $S_o^{aow}$ and $S_w^{aow}$, respectively. Since water does not spread well on oil in hydrophobic media, in comparison to oil on water in hydrophilic media, air-oil interfaces exist. Changes in $S_w^{aow}$ will obviously cause changes in $S_a^{aow}$; this will affect the air-oil *and* oil-water interfaces, and $P_{ow}$ depends therefore on $S_w^{aow}$.

A similar dependency of three-fluid capillary pressures on fluid saturations was found for the 25, 50, and 75% OTS media. The intermediate fluid for these cases is, obviously, also discontinuous since both water and oil act as the wetting fluid and the intermediate fluid in the same medium. As the fraction of oil-wet sand decreases in the medium, $P_{ow}$ and $P_{aw}$ are higher at a given $S_w^{aow}$, while $P_{ao}$-$S_{tl}^{aow}$ is relatively unaffected. This may be attributed to the energy state of water which, in contrast to that of oil, differs depending on whether water acts as the wetting or intermediate fluid.

Predicting Three-Fluid $P_c$-S Relations

Leverett (1941) predicted three-fluid $P_c$-$S$ curves for a particular medium from measured two-fluid $P_c$-$S$ curves for the same medium according to:

$$P_{ow}(S_w^{ow}) = P_{ow}(S_w^{aow}) \tag{5}$$

$$P_{ao}(S_o^{ao}) = P_{ao}(S_{tl}^{aow}) \tag{6}$$

Three-fluid $P_c$-$S$ relations may also be predicted by scaling and invoking Leverett's assumption. Figure 12a shows the observed $P_{ao}$-$S_o^{ao}$ and $P_{ao}$-$S_{tl}^{aow}$ curves for the untreated sand (left side) and GPTS sand (right side), while Fig. 12b shows the observed $P_{ow}$-$S_w^{ow}$ and $P_{ow}$-$S_w^{aow}$ curves for the untreated sand (left side) and GPTS sand (right side). Note that the three-fluid $P_c$-$S$ curves can be accurately predicted from the measured two-fluid $P_c$-$S$ curves for the hydrophilic media. Figure 13a displays the observed $P_{ao}$-$S_{tl}^{aow}$ curve for the GPTS media and the predicted $P_{ao}$-$S_o^{ao}$ curves obtained by scaling the $P_{aw}$-$S_w^{aw}$ curve according to the previously discussed scaling approaches. Similarly, Fig. 13b shows the observed $P_{ow}$-$S_w^{aow}$ curve for the GPTS media and the predicted $P_{ow}$-$S_w^{ow}$ curves obtained by scaling the $P_{aw}$-$S_w^{aw}$ curve. Note that the scaling results improved by using the contaminated air-water interfacial tension and by including values for the contact angle.

Methods for the prediction of the three-fluid $P_c$-$S$ relations in hydrophobic and mixed wettability media based strictly on eqs. 5 and 6 are generally inadequate. Currently, we are working on improved predictions for such media.

Permeability

An automated steady flux method for the measurement of the unsaturated air-water permeability ($k$)-$P_c$ has been developed at Riverside. Preliminary results suggest that this technique may also be applied for air-oil, oil-water, and air-oil-water systems. The measured $P_c$-$S$ relations also allow the prediction of $k$-$S$ relations. The work in Davis has focused on the numerical modeling of multiphase flow for use in inverse procedures to estimate two- and three-fluid $k$-$P_c$ relations.

## References


Adamson, A. W. 1967. Physical chemistry of surfaces. John Wiley & Sons Inc., New York.

Anderson, R., G. Larson, and C. Smith. 1991. Silicon compounds: register and review 5th edition. Huls America Inc., Piscataway, NJ.

Anderson, W. G. 1986. Wettability literature survey - Part 1: rock/oil/brine interactions and the effects of core handling on wettability. J. Petr. Technol., Oct, 1125-1144

Brook, R. H., and A. T. Corey. 1964. Hydraulic properties of porous media. Hydrology paper No. 3, Colorado State University, Fort Collins, Colorado.

Danielson, R. E., and P. L. Sutherland. 1986. Porosity. Chapter 18. *In* A. Klute (ed.). Methods soil analysis, Part 1, Physical and mineralogical methods. 2nd edition. ASA and SSSA, Madison, WI.

Donaldson, E. C., R. D. Thomas, and P. B. Lorenz. 1969. Wettability determination and its effect on recovery efficiency. Soc. Petr. Eng. J., March, 13-20.

du Noy, P. L. 1919. A new apparatus for measuring surface tension. J. Gen. Physiol. 1:521-524.

Hiemenz, P. C. 1986. Principles of colloid and surface chemistry. Marcel Dekker Inc., New York, New York.

Leverett, M. C. 1941. Capillary behavior in porous solids. Trans. Am. Inst. Min. Metall. Pet. Eng. 142:152-169.

Marquardt, D. W. 1963. An algorithm for least-squares estimation of nonlinear parameters. Journal of Soc. of Indust. Appl. Math. 11:431-441.

Morrow, N. R. 1976. Capillary pressure correlations for uniformly wetted porous media. J. Canadian Petr. Technol., Oct-Dec, 49-69.

Soil Survey Staff. 1975. Soil taxonomy: A basic system of soil classification for making an interpreting soil surveys. *In* USDA-SCS Agric. Handbook 436, U.S. Government Printing Office, Washington, DC.

Stonestrom, D. A. and J. Rubin. 1989. Water content dependence of trapped air in two soils. Water Resour. Res. 25:1947-1958.

van Genuchten, M. Th. 1980. A closed form equation for predicting the hydraulic conductivity of unsaturated soils. Soil Sci. Soc. Am. J. 44:892-898.

Wei, M, R. S. Bowman, J. L. Wilson, and N. R. Morrow. 1992. Wetting properties of silane-treated glass exposed to water, air, and oil. Journal of Colloid and Interface Science 157:154-159.

Table 1. Fitted advancing and receding contact angles for air-water and oil-water systems

| | AIR-WATER | | OIL-WATER | |
|---|---|---|---|---|
| | $\phi^A$ | $\phi^R$ | $\phi^A$ | $\phi^R$ |
| UNTREATED | 32.7 | 0.00 | 51.6 | 0.00 |
| GPTS | 46.6 | 48.2 | 64.7 | 66.8 |
| VTS | 52.2 | 35.6 | 103.3** | 45.9 |
| OTS | 64.8 | 37.6 | 146.0** | 62.1 |

**Note that the van Genuchten model requires a positive $P_c$. Values for $\beta$ for the imbibition of the OTS and VTS sand were obtained by visually estimating a value for oil-water $\phi^A$ which best described the data.

Table 2. Measured ($S_{rw}^{ow}$, $S_{ro}^{ow}$, and $\gamma$) and fitted ($\alpha_{PD}$, $\alpha_{MI}$, $a_{MD}$, and $n$) values obtained from $P_{ow}$-$\bar{S}_w^{ow}$-data according to Eq. 3 as well as the regression coefficient ($R$) for goodness of fit

| %OTS | $S_{rw}^{ow}$ | $S_{ro}^{ow}$† | $\gamma$† cm | $\alpha_{PD}$ 1/cm | $\alpha_{MI}$ 1/cm | $\alpha_{MD}$ 1/cm | $n$ | $R$ |
|---|---|---|---|---|---|---|---|---|
| 0 | 0.194 | 0.190 | 5.900 | 0.0874 | 0.0772 | 0.0563 | 5.0928 | 0.991 |
| 25 | 0.251 | 0.110 | 0.930 | 0.0939 | 0.1519 | 0.1035 | 3.8230 | 0.984 |
| 50 | 0.212 | 0.123 | 3.340 | 0.1023 | 0.2028 | 0.1153 | 3.8528 | 0.980 |
| 75 | 0.220 | 0.131 | 7.642 | 0.1169 | 0.2065 | 0.0949 | 4.5039 | 0.974 |
| 100 | 0.248 | 0.152 | 12.78 | 0.1606 | 0.3020 | 0.0783 | 5.6409 | 0.965 |

† $S_{ro}^{ow}$ and $\gamma$ are set equal to zero during primary drainage

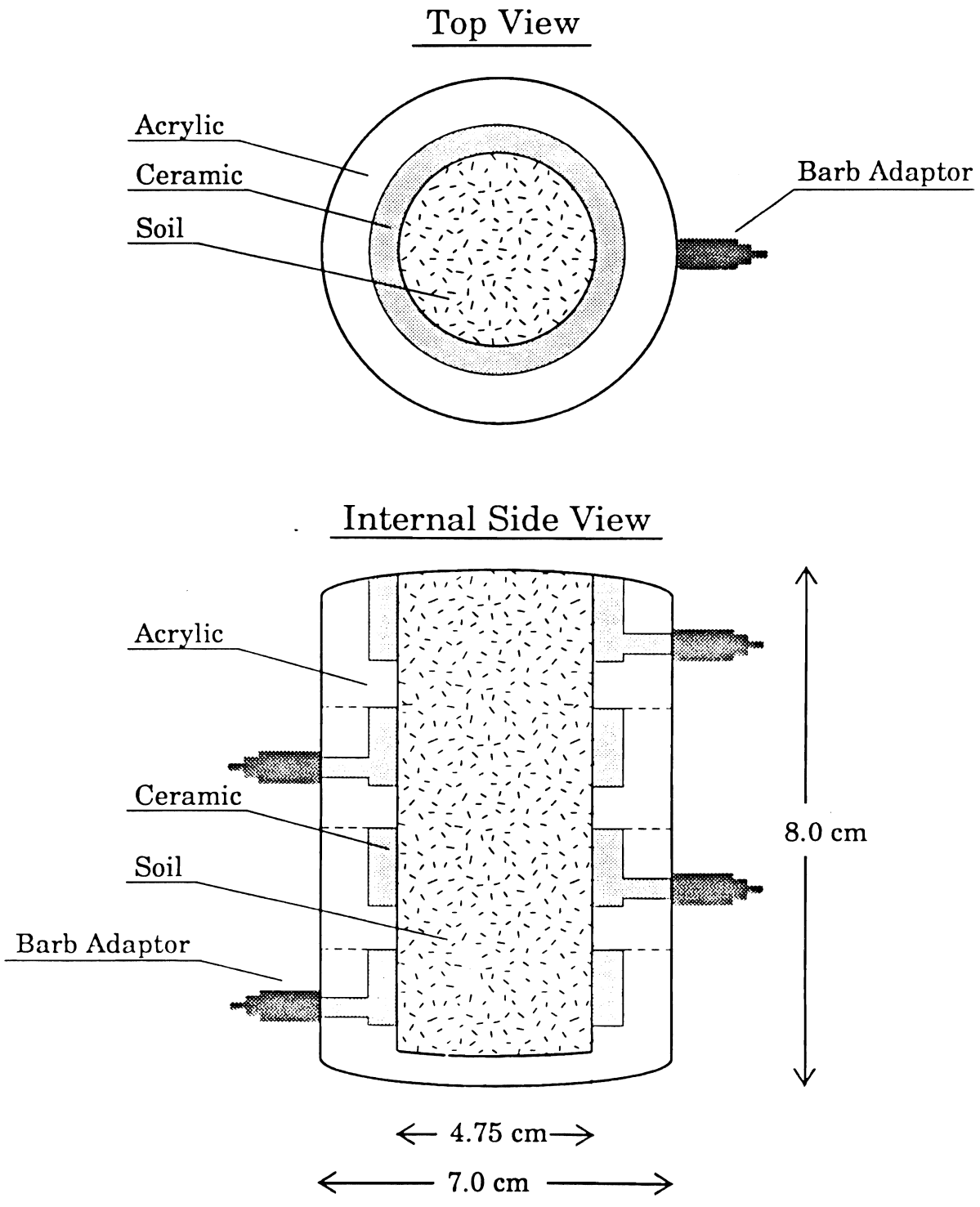


Figure 1. Schematic of soil column consisting of hydrophilic and hydrophobic ring tensiometers for independent control of water and oil phases, respectively.

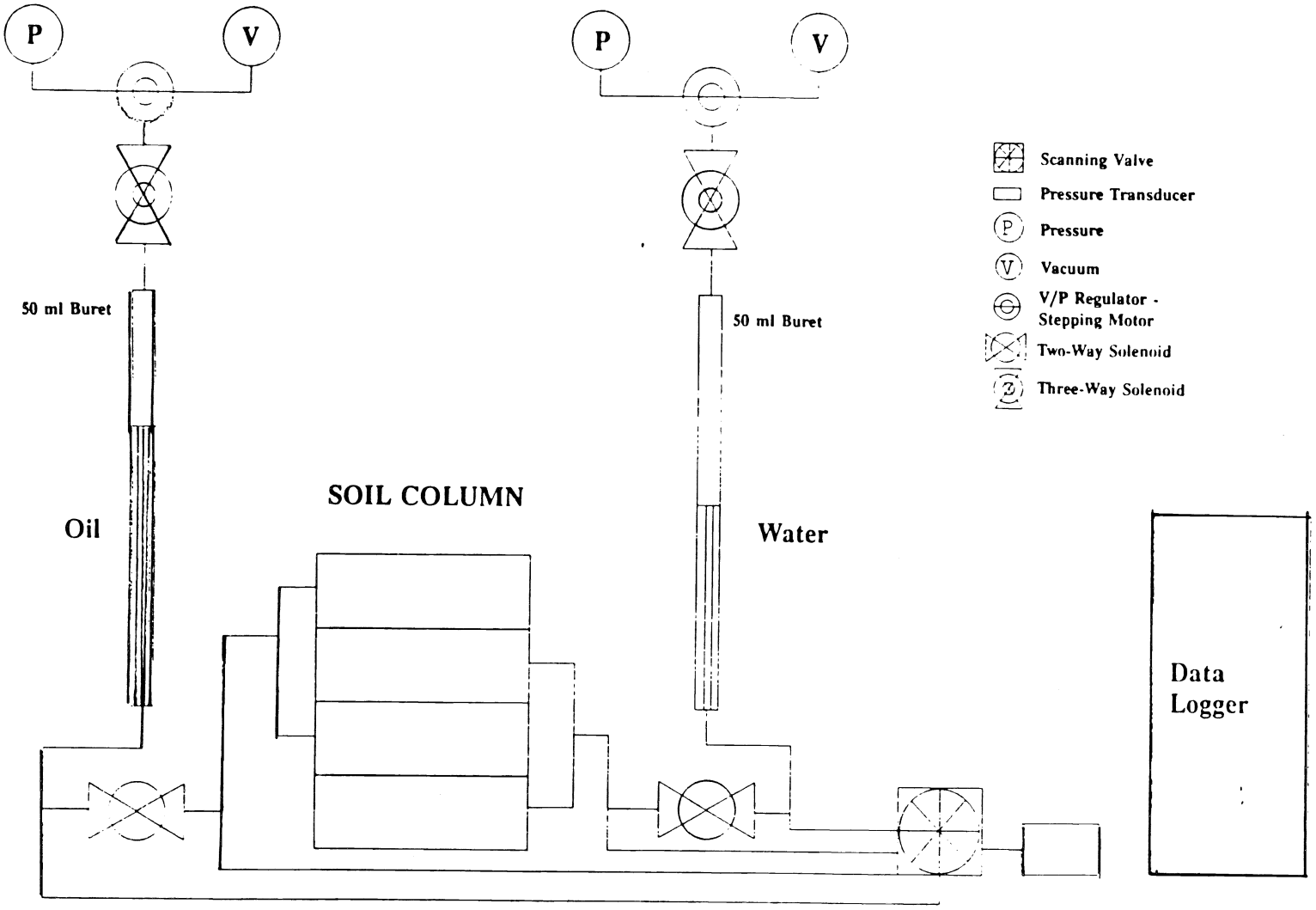


Figure 2. Schematic of automated measurement of the $P_c$-$S$ relations.

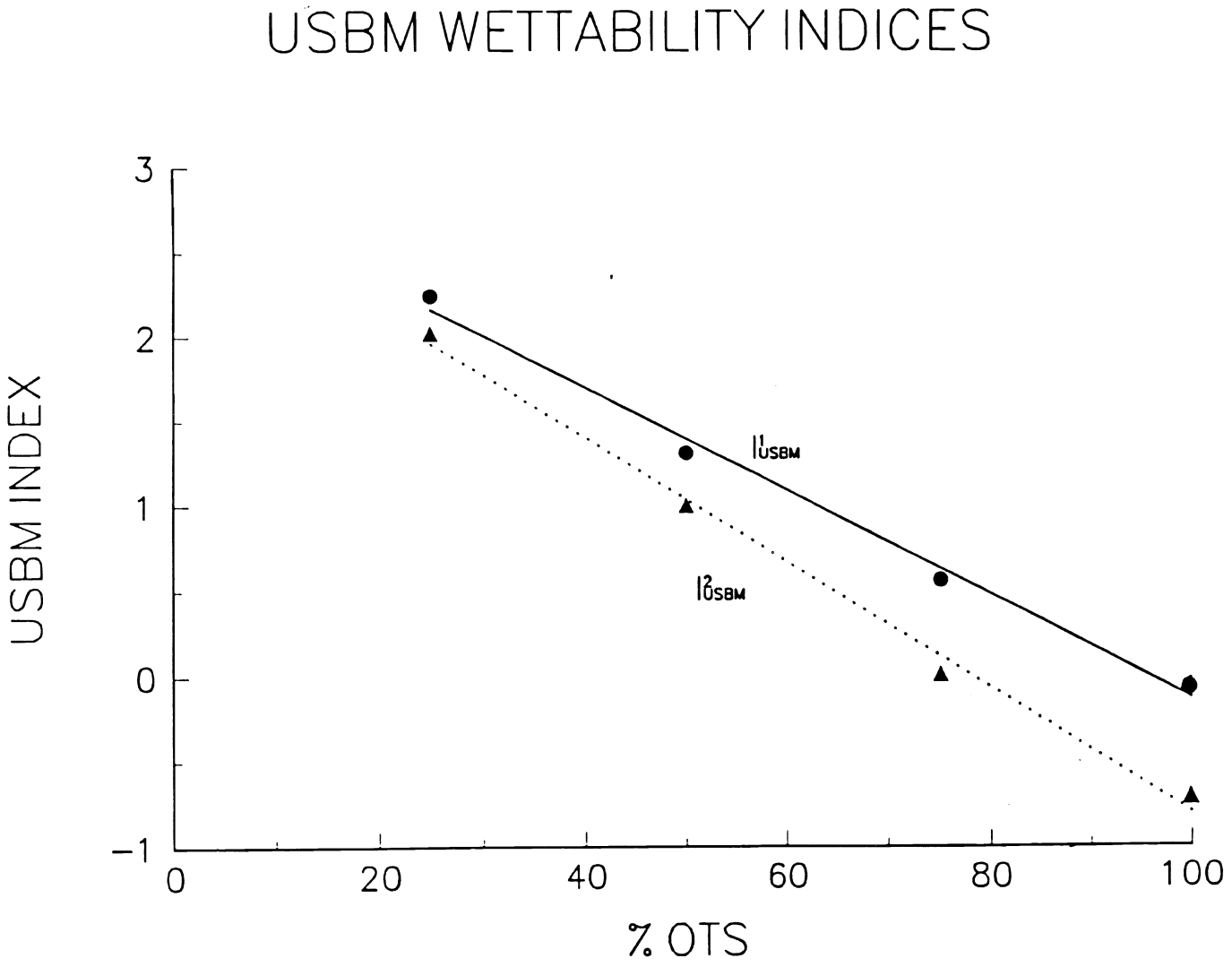


Figure 3. The USBM wettability index, $I_{USBM}$, as a function of the %OTS sand for $P_{ow}$-$\bar{S}_w{}^{ow}$ data; $I_{USBM}{}^1$ and $I_{USBM}{}^2$ are calculated from primary drainage and main imbibition data, and from main drainage and main imbibition data, respectively.

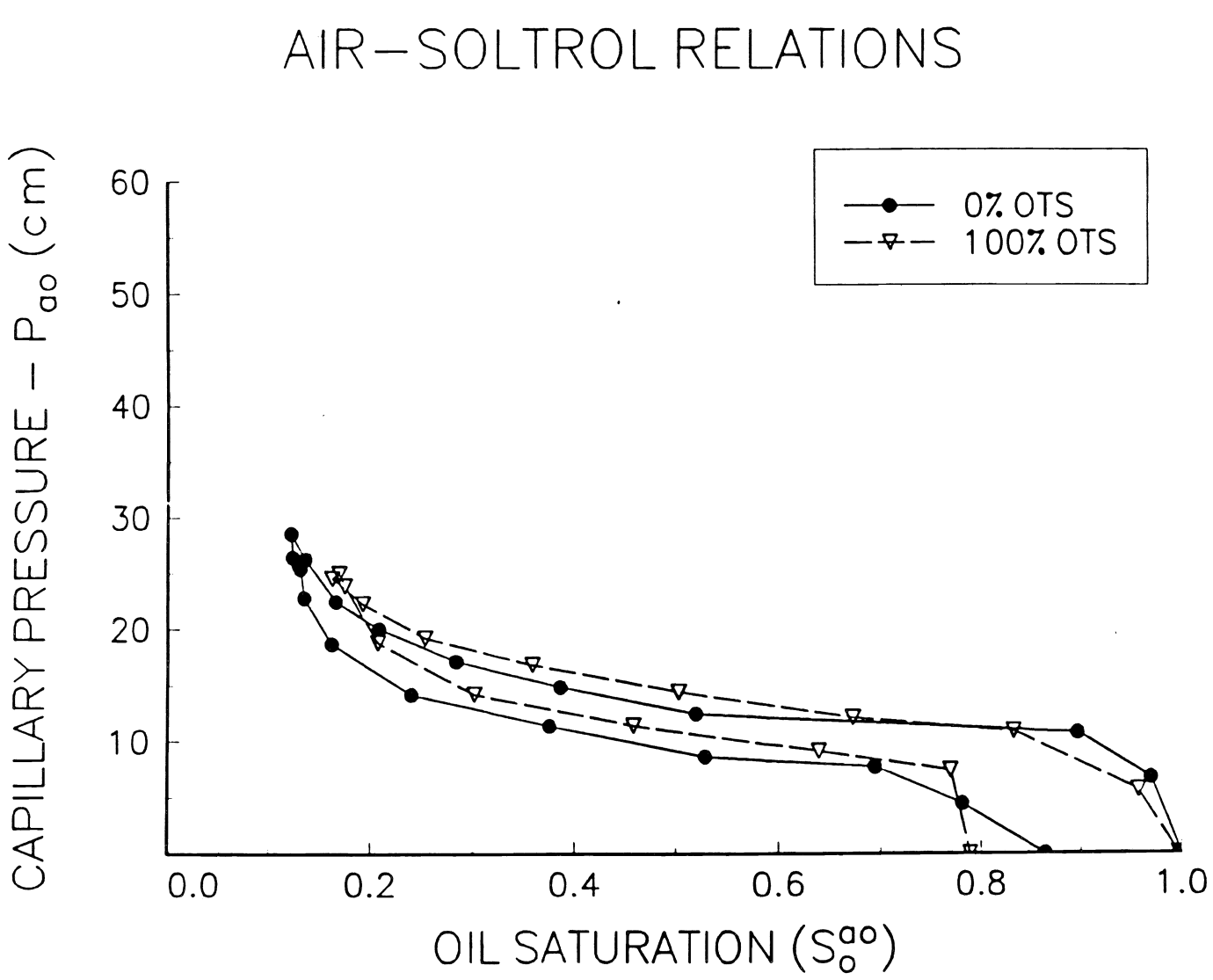


Figure 4. Measured drainage and imbibition $P_{ao}$-$S_o^{ao}$ relations for 0 and 100% OTS media.

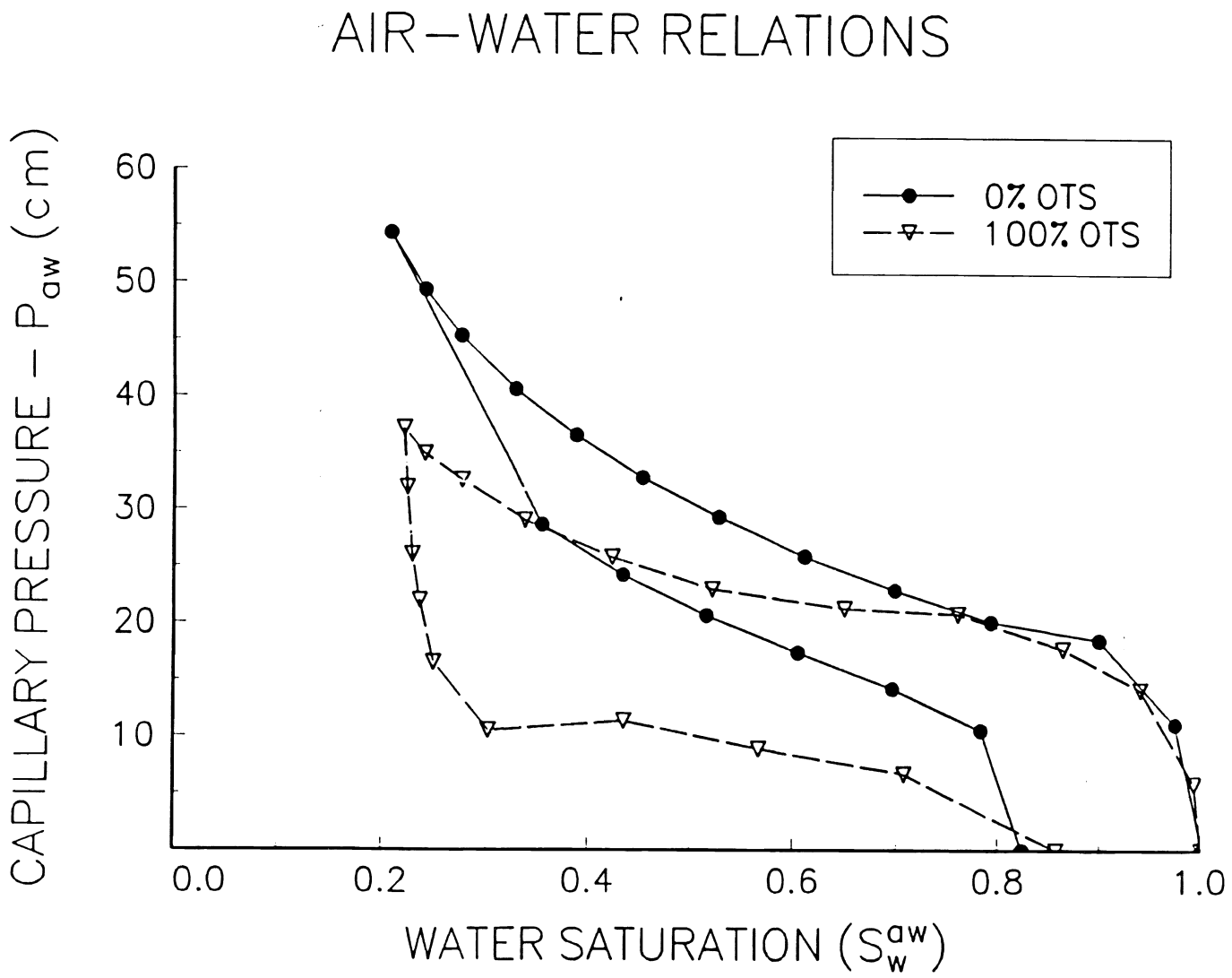


Figure 5. Measured drainage and imbibition $P_{aw}$-$S_w^{aw}$ relations for 0 and 100% OTS media.

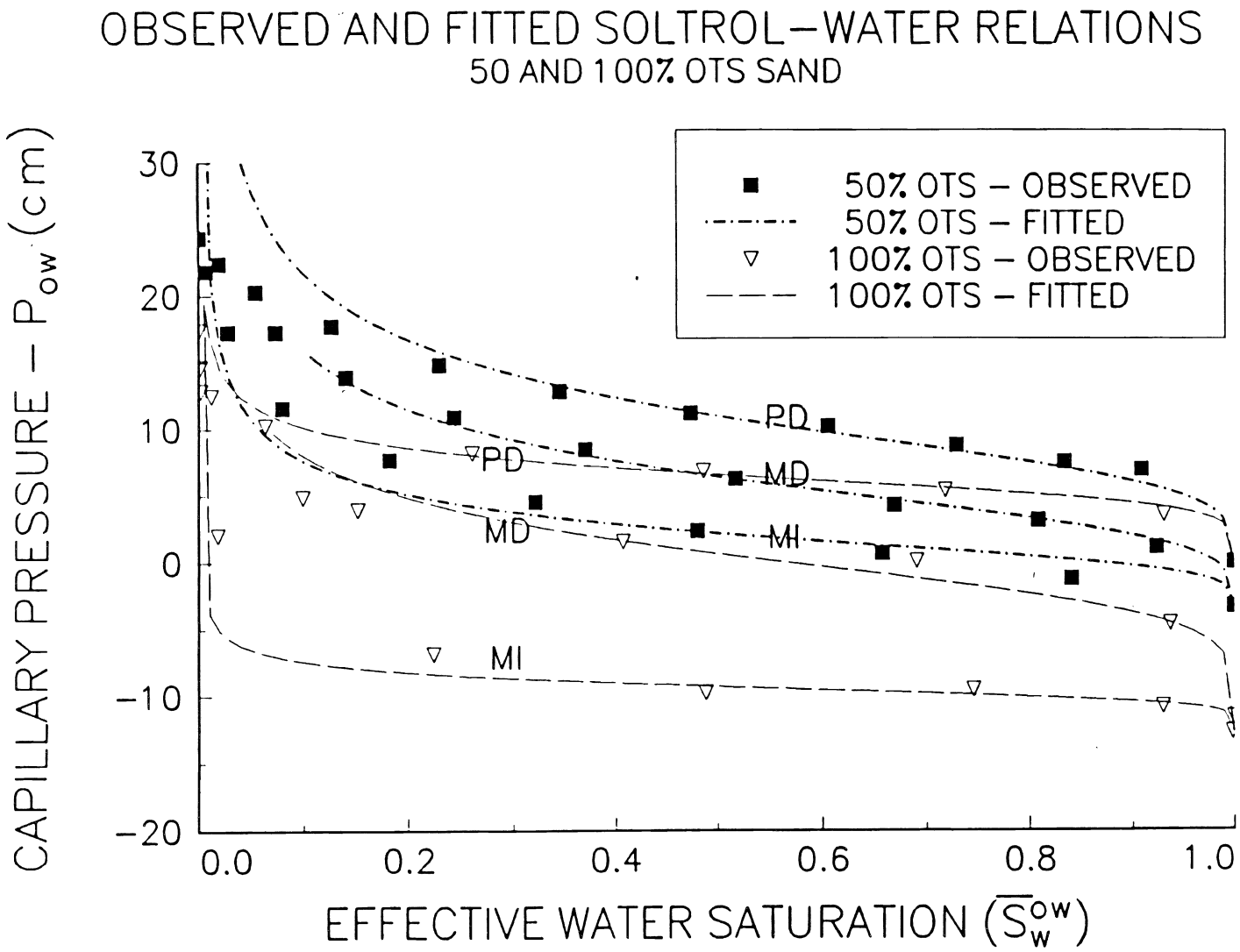


**Figure 6.** Observed and fitted hysteretic $P_{ow}$-$\overline{S}_w{}^{ow}$ relations for the 50 and 100% OTS media.

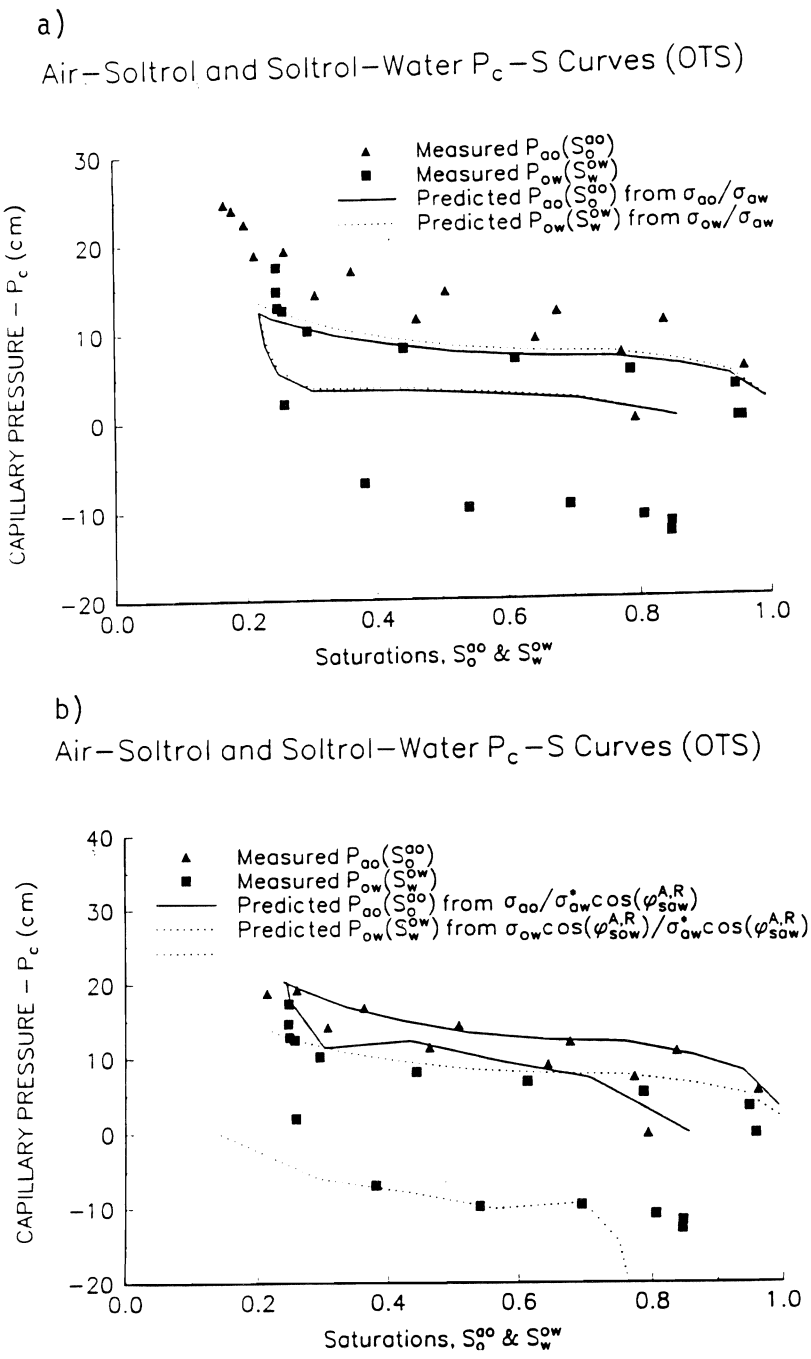


Figures.7a and 7b. Observed and predicted $P_{ao}$-$S_o^{ao}$ and $P_{ow}$-$S_w^{ow}$ curves for OTS sand during drainage and imbibition. The predictions in Fig. 7a were obtained from scaling the $P_{aw}$-$S_w^{aw}$ curve using the ratios $\sigma_{ao}/\sigma_{aw}$ and $\sigma_{ow}/\sigma_{aw}$, respectively. In Fig. 7b the scaling was based on the ratio of interfacial tensions and contact angles (i.e., $\sigma_{ao}/\sigma_{\alpha w}{}^*\cos(\phi_{aw}{}^{A,R})$ and $\sigma_{ow}\cos(\phi_{sow}{}^{A,R})/\sigma_{aw}{}^*\cos(\phi_{saw}{}^{A,R})$, respectively). The superscript * indicates water contaminated by oil.

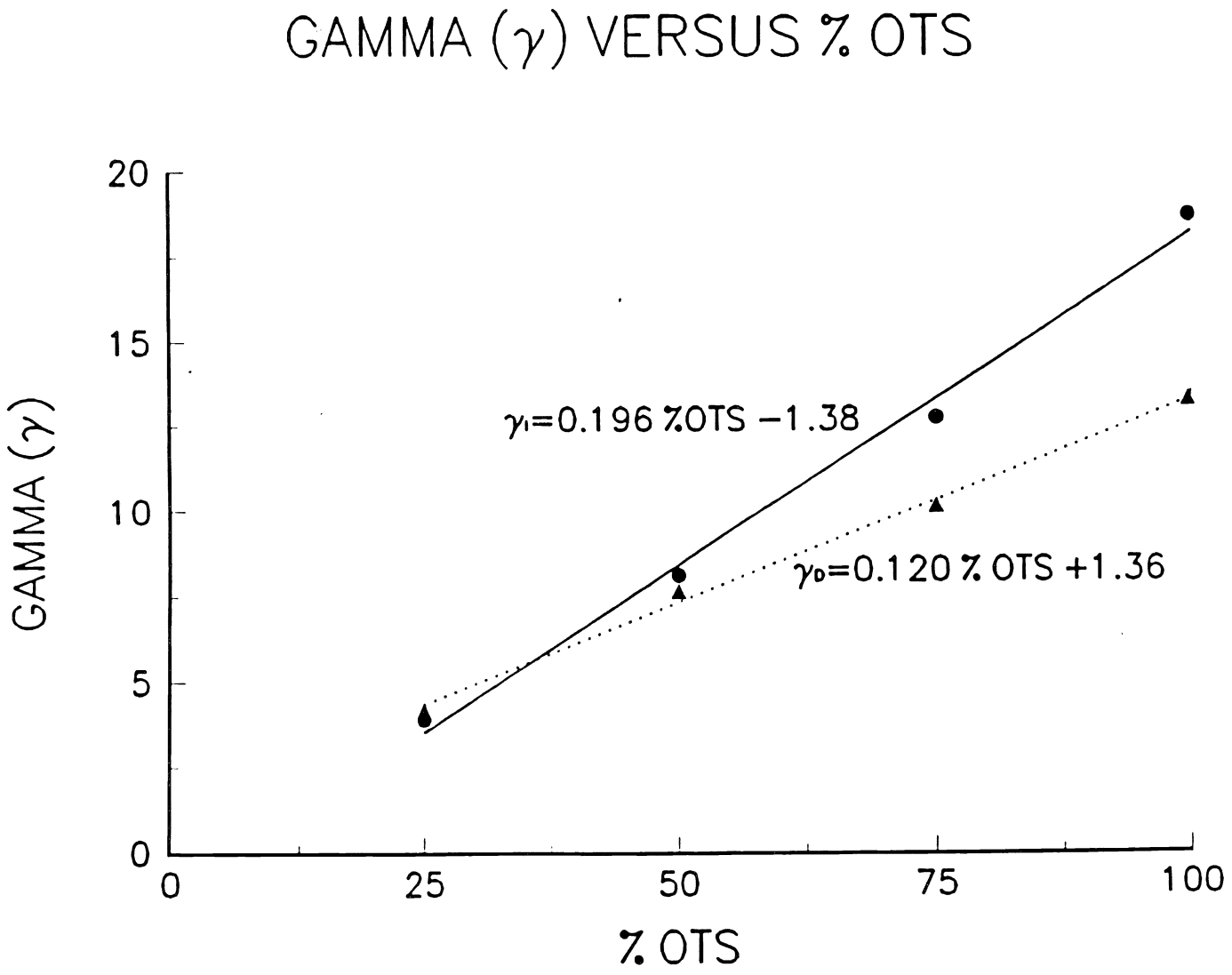


Figure 8. Observed values for $\gamma$ as a function of % OTS during drainage (*D*) and imbibition (*I*). Values for $\gamma$ were obtained by fitting the $(\sigma_{ow}/\sigma_{ao})P_{ao}$-$\overline{S}_o^{ao}$ model according to Eq.(4) to observed $P_{ow}$-$\overline{S}_w^{ow}$ data during main drainage and imbibition.

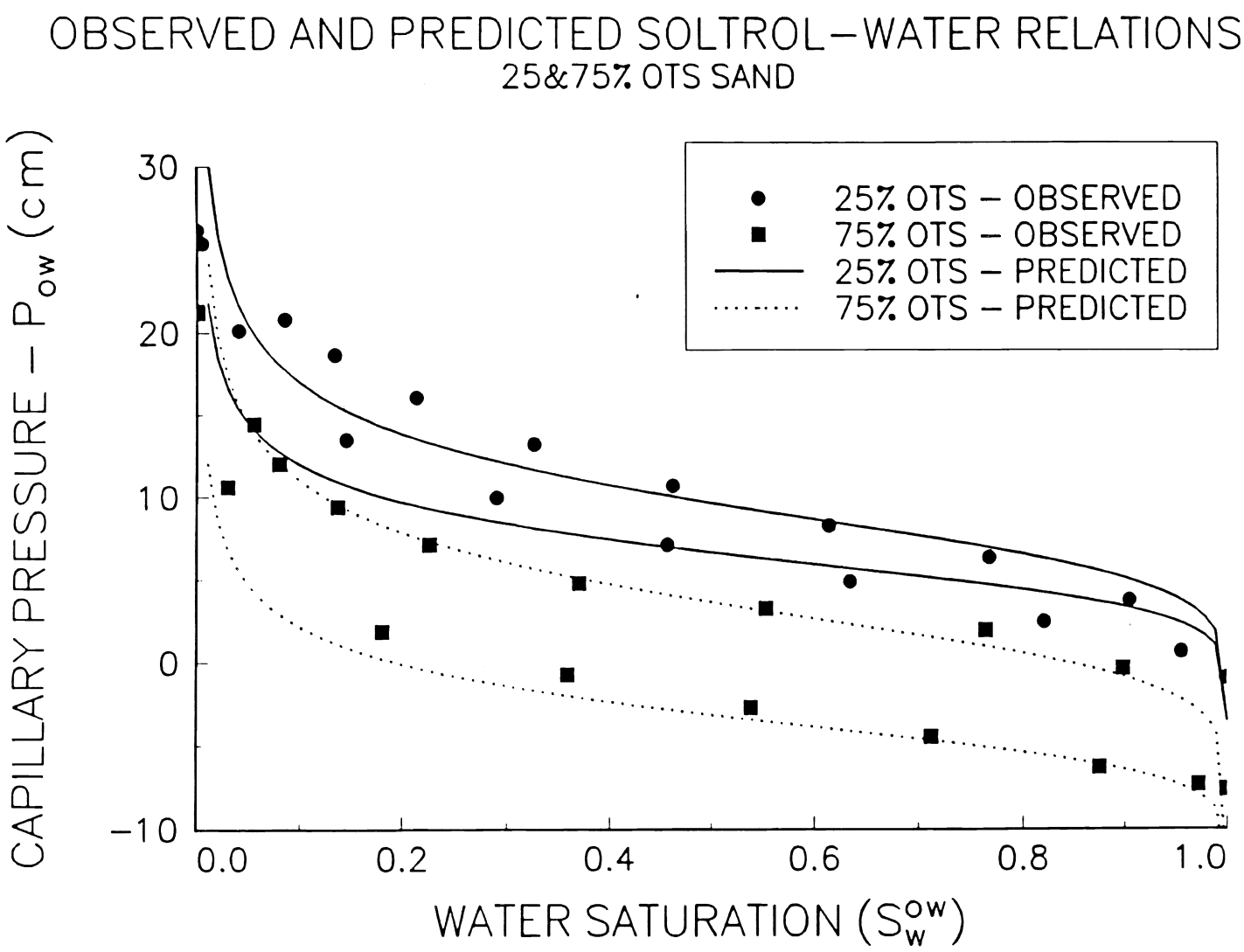


Figure 9. $P_{ow}$-$\bar{S}_w^{ow}$ relations, observed and predicted with Eq. (4), during main drainage and imbibition for the 25% and 75% OTS media. The regression formulas shown in Fig. 8 were used to predict $\gamma$ during drainage (D) and imbibition (I).

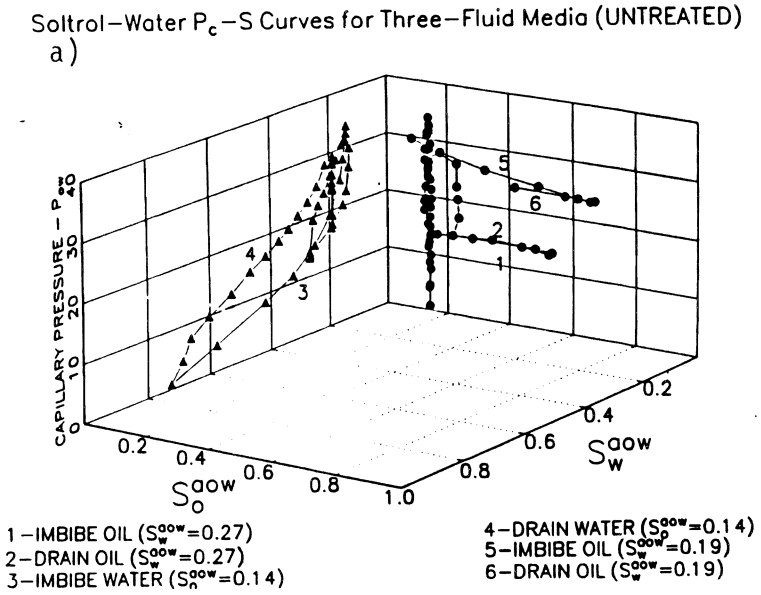


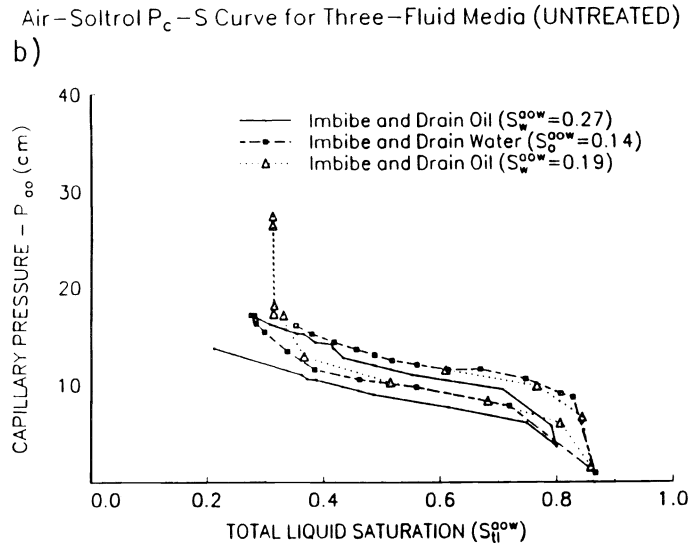


Figures 10a and 10b. Measured three-fluid $P_c$-$S$ relations for the untreated sand, with $P_{ow}$-$S_w^{aow}$ on the left side and $P_{ow}$-$S_o^{aow}$ on the right side of Fig. 10a, and the $P_{ao}$-$S_{tl}^{aow}$ curve shown in Fig. 10b.

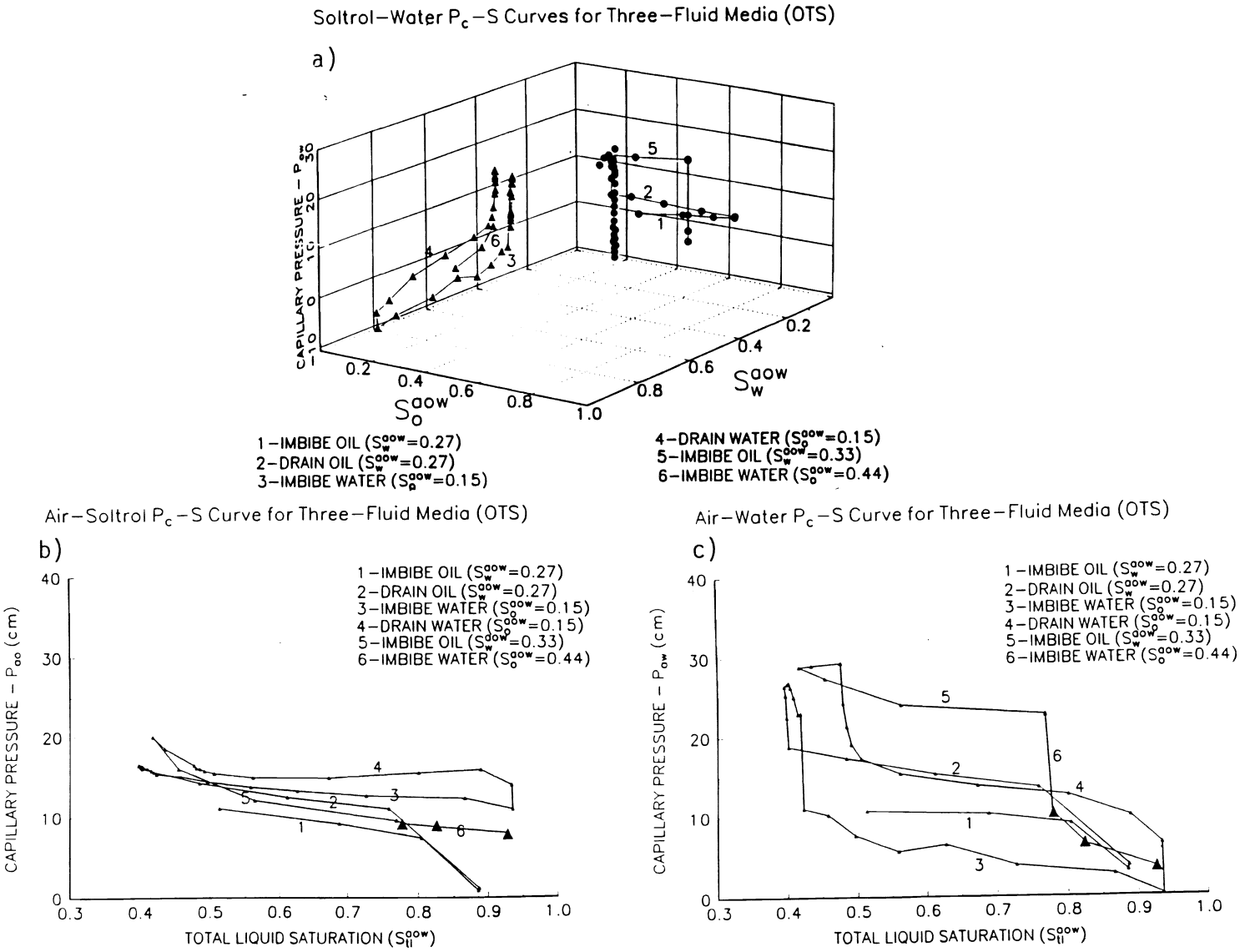


Figures 11a, 11b and 11c. Measured three-fluid $P_c$-$S$ relations for the OTS sand, with $P_{ow}$-$S_w^{aow}$ (left side) and $P_{ow}$-$S_o^{aow}$ (right side) shown in Fig. 11a, and $P_{ao}$-$S_{tl}^{aow}$ and $P_{aw}$-$S_{tl}^{aow}$ shown in Figs. 11b and 11c, respectively.

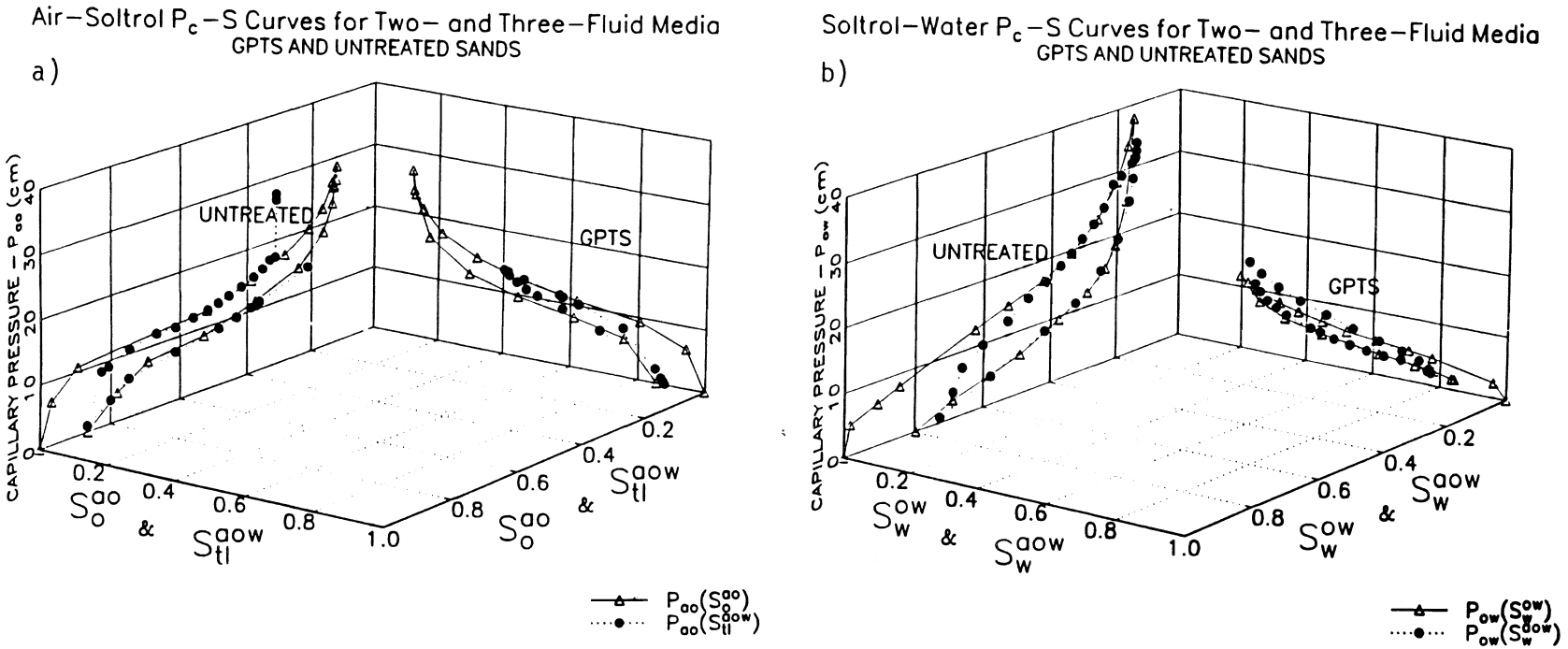


Figures 12a and 12b. Two- and three-fluid air-oil and oil-water $P_c$-$S$ curves for untreated (left side) and GPTS (right side) media, with $P_{ao}$-$S_o^{ao}$ and $P_{ao}$-$S_{tl}^{aow}$ curves shown in Fig. 12a, and $P_{ow}$-$S_w^{ow}$ and $P_{ow}$-$S_w^{aow}$ curves shown in Fig. 12b.

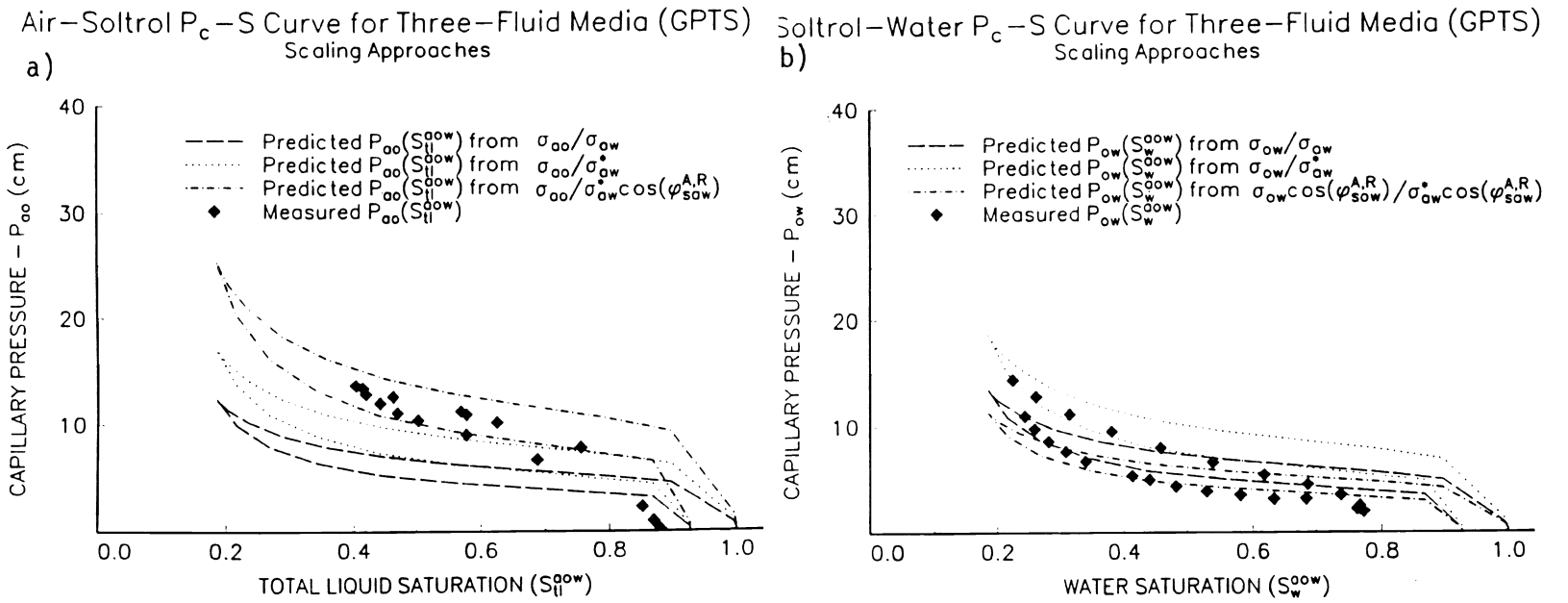


Figures 13a and 13b. Observed and predicted $P_{ao}$-$S_{tl}^{aow}$ (Fig. 13a) and $P_{ow}$-$S_{w}^{aow}$ (Fig. 13b) curves for the GPTS sands. The predictions for the $P_{ao}$-$S_{tl}^{aow}$ curve were obtained by scaling the $P_{aw}$-$S_{w}^{aw}$ curve using (a) $\sigma_{ao}/\sigma_{aw}$, (b) $\sigma_{ao}/\sigma^{*}_{aw}$, and (c) $\sigma_{ao}/\sigma^{*}_{aw}\cos(\phi_{saw}^{A,R})$. The predictions for the $P_{ow}$-$S_{w}^{aow}$ curve were similarly obtained by scaling using (a) $\sigma_{ow}/\sigma_{aw}$, (b) $\sigma_{ow}/\sigma^{*}_{aw}$, and (c) $\sigma_{ow}\cos(\phi_{sow}^{A,R})/\sigma^{*}_{aw}\cos(\phi_{saw}^{A,R})$.

# A Study of the Scale Dependence of Soil Permeability to Air

K. GARBESI, J. OWENS, AND J. HARTE
*Department of Environmental Science, Policy, and Management*
*Berkeley Campus*

## Summary

A technique for measuring soil air-permeability over variable length scales was adapted for use in the field. The technique measures equivalent homogeneous permeabilities along a path between two probes up to a permeability of ~$10^{-9}$ $m^2$. Modifications made to the technique resulted in significant improvement in the signal-to-noise ratio of acquired data, allowing measurements to be made over longer distances and under windier conditions than was possible previously. Excellent data have been acquired at a length scale of 4.5 m. Measurements over considerably larger scales appear feasible. Scale dependence of soil air-permeability was observed in a bare sandy soil up to a length scale of ~1 m—a considerably smaller upper limit than for scale dependence observed earlier at a treed site. However, the magnitude of the scale dependence below the 1m scale is considerably larger than at the earlier treed site. Therefore, it is equally important to account for the effect when predicting advective transport of gas-phase contaminants through soils.

**Key Words:** soil, soil-gas, permeability, heterogeneity, contaminant transport, measurements

## Project Objectives Addressed in 1993-1994

The scientific objective of this work was to investigate the phenomenon of scale dependence of soil permeability to air, its magnitude and prevalence in soils, and its causes. The technical objectives were to (1) adapt a new technique for measuring soil air-permeabilities over variable length scales (Garbesi, 1993) to field applications, (2) determine the range of conditions in which the technique is applicable, (3) improve the signal-to-noise ratio of the acquired data, and (4) extend the length scale and environmental conditions over which measurements can be made.

## Research Plan and Procedures

A recently developed dual-probe dynamic pressure (DDP) technique (patent pending) was adapted for use at field sites. This technique was developed for making *in situ* measurements of soil permeability to air over a range of length scales (~0.5 - 5 m or more). Field tests were conducted of the prototype field system. Modifications were made to the experimental design to improve the signal-to-noise ratio of the acquired data. Sensitivity analysis was conducted of the model used for data interpretation to determine optimal experimental operating parameters and to determine the theoretical range of soil conditions in which the technique is applicable. Field sites were identified for investigation of scale dependence of soil permeability. Two complete sets of measurements were made in two different soils: a sandy soil at a site currently under investigation for gas-phase transport of gasoline components spilled on site; and a sandy loam soil previously used for cultivation of tree seedlings.

## Results

The DDP measurement system uses the propagation time for a sinusoidally oscillating pressure signal to travel from a source to a detector probe as an indicator of the equivalent homogeneous permeability of the path between the probes (see Fig. 1). The distance between the source and detector probes defines the length scale of the measurement. Varying the location of detector probes allows for investigation of permeability over different scales and orientations.

Typically, a 1 kPa-amplitude signal is imposed at the source probe, which can result in pressure oscillations of ~1 Pa several meters away. The pressure signals at the source and detector probes are logged simultaneously while an oscillating pressure signal is imposed at the source. Fast Fourier transform is used to determine the phase shift between the source and detector signals.

A prototype DDP measurement system was constructed for making permeability measurements over different length scales in the field. The field version uses lighter and smaller and less fragile components than the previous version that was run at a permanent facility used to study radon transport through

soils and into basement structures (Fisk et al., 1989; Fisk et al., 1992; Garbesi et al., 1993). The new system is set up to acquire data at 4 detector probes and the source probe simultaneously. The components of the new system are listed in Table 1.

Figure 1 indicates a recent modification to the DDP system which has significantly improved the signal-to-noise ratio in the acquired data. In the previous design, both the source and detector probes were referenced to atmosphere. Because of the small amplitude of the detector probe signals (~1 Pa) at significant distance from the source, a small breeze blowing on the atmosphere side of the pressure transducers can result in significant noise in the acquired detector-probe data. By referencing the probes instead to a reference probe driven into the soil to a depth of ~ 1m and located far from the source and detector probes (≥ 10 m), the noise is greatly reduced, making it possible to make measurements at larger distances from the source probe under windier conditions than was previously possible.

Figure 2 shows an example of the clarity of the raw pressure data acquired using a 0.75-m deep reference probe to damp out atmospheric noise. The measurement was made at the open field site in Ben Lomond, California, described below. The source and detector probes were both located at a depth of 1.5 m, 4.5 m apart. The data were selected from an arbitrary location in the data file without consideration for data quality.

To determine soil air-permeability from a DDP measurement, the observed source-to-detector time lag is matched to a theoretical time lag derived from a model. The model assumes a homogeneous, semi-infinite soil. The technique therefore gives a measure of the equivalent homogeneous permeability for what is inevitably a heterogeneous system. This is a useful measure, however, estimating advective transport of soil-gas contaminants in applications such as the entry of soil-gas radon into houses, where it is often infeasible to make a detailed geostatistical or deterministic assessment of heterogeneity at the site.

The model generates a time lag for given source and detector locations and given soil permeability. Since the time lag is a transcendental function of permeability, the model is run repeatedly at different permeabilities to generate a time lag vs. permeability curve (e.g., Figs. 3a and 3b). Soil permeability is found by reading off the permeability corresponding to the measured time lag.

The sensitivity of the measurements is largest when a large change in time lag (T) results from a small change in permeability (k). That is, large $\partial T / \partial k$ indicates high sensitivity. The model was run to determine the effect of source signal period (an adjustable experimental parameter) on measurement sensitivity. Figures 3a and 3b show plots of T(k) for 40-, 75-, and 120-s periods for the following experimental conditions:

| | |
|---|---|
| source probe depth | 2 m |
| detector probe depth | 2 m |
| distance from source probe to detector probe | 3 m |
| soil porosity | 0.4 |
| atmospheric pressure | $10^5$ Pa |

Figure 4 shows the normalized lag time (the lag time divided by the driving signal period) for the same conditions.

Figures 3a, 3b, and 4 together indicate the advantages of using long driving signal periods. The technique is most sensitive at larger driving periods. In addition, the phase shift remains a fraction of a single driving signal period over a wider range of permeabilities for larger periods. This is important since there is less ambiguity in the data analysis when it is easily established from real-time observation of the source and detector signals that the time lag is less than one period. On the other hand, smaller periods are desirable to minimize the time required to complete a measurement (for good signal-to-noise ratio a single measurement requires taking data for ~30 periods). The compromise between shorter sampling time and greater sensitivity is established by the particular conditions of the site.

Note from Fig. 4a that the upper limit on soil permeability that can be detected using this technique is ~$10^{-9}$ $m^2$. At that permeability the technique is relatively insensitive to changes in source signal frequency; $\partial T / \partial k$ is small for all periods and the absolute time lags are small as well.

Sites were selected for initial study of scale-dependent permeability based on the following criteria: proximity to the University of California, Berkeley; existence of a range of soil types and vegetation covers; usefulness of the measurements in the context of other work. Measurements have been made in two new locations: (1) in sandy soil adjacent to a refueling station at the Alameda Naval Air Station (ANAS), Alameda, CA, at which a large gasoline spill is being studied for gas-phase transport of volatile organics through the unsaturated zone; and (2) in a large open field previously used for the cultivation of tree seedlings. The second plot is near the location of the original DDP measurements in Ben Lomond, California, in which it was determined that soils can display significant scale dependence of permeability (Garbesi, 1993). The native soil is the same in the two Ben Lomond plots, granitic and weathered in place, but the original site is surrounded by mature CA live oak trees, whereas the latter was deforested in the mid-1940s. From the mid-1960s until recently, the site has been used for the cultivation of tree seedlings.

The ANAS site contains two plots suitable for comparison measurements (see Fig. 5). One, adjacent to the refueling station, is essentially bare soil. The second is located under two medium-sized pine trees. Measurements have been made so far at the first of the two plots. We expect to find scale dependence up to a larger length scale in the treed plot, since we hypothesize that high-flow

pathways from decayed tree roots might be the cause of observed scale dependence.

A DDP sampling protocol has been initiated in which permeability measurements are made at different driving signal frequencies at the same probe before conducting a complete investigation of scale dependence. Figure 6 shows the results of permeability measurements made at a single probe at different source signal periods. Note that the estimated permeability increases with period, rolling off and becoming stable at periods greater than ~60 seconds.

We anticipated this effect and believe that it is due to a reduction in the effective air-filled porosity of the soil with increased source signal frequency. The DDP technique yields an indirect measure of permeability (k) via a more direct measure of the pressure diffusivity (D), where

$$D = \frac{kP_a}{em},$$

$P_a$ is the mean atmospheric pressure, m is the dynamic viscosity of air, and e is the air-filled porosity of the soil. Since D, $P_a$, and m are constant for a given experiment, if the effective porosity is a function of the source signal frequency, the apparent value of k will change.

High source signal frequencies (small periods) can give an anomalously low estimate of permeability since the effective porosity of the soil will appear smaller at high frequencies. That is, the high-frequency signal might not have sufficient time to probe the lower permeability regions of soil, resulting in participation of only part of the actual soil porosity in the measurement. As the period is increased, the signal has sufficient time to probe the entire soil volume and the porosity value stabilizes, resulting in stable values of permeability. Note that permeability is actually *defined* in terms of a steady-state experiment *via* Darcy's law:

$$\bar{q} = \frac{k}{m}\nabla P .$$

Here $\bar{q}$ is the volumetric soil gas flux rate (m/s). As the DDP measurement approaches quasi-static conditions for a given soil and scale, the permeability value stabilizes to its true value.

DDP measurements were made at the ANAS site at the array of probes indicated in plot 1 of Fig. 5. All source and detector probes were located at a depth of 1 m except for three probes located at a depth of 0.29 m, with a total source-to-detector distance of 1 m (i.e., the angle between the horizontal at the source location and the detector is $45^{o}$). The air-filled porosity of the soil was determined using standard gravimetric methods from the average of 8 cores obtained from 2 bore profiles going down to ~1.5 m depth .

Figure 7 shows the results of all DDP measurements for which we obtained good signals.[269,270] Scale dependence of permeability is clearly evident. The figure plots DDP estimates of permeabilities at different length scales (open symbols) and the geometric mean permeability determined by small-scale static measurements made at each of the individual probes in plot 1. The vertical bar indicates the full range of values measured using the traditional small-scale single-probe static pressure technique. For comparison, Fig. 8 shows scale dependence originally measured in the treed plot in the granitic soil at the Ben Lomond site.

Recently a complete set of DDP measurements was made at 16 detector probes at the Ben Lomond open-field site over a range of length scales between 0.5 and 4.5 m. Measurements were made using the reference probe to damp out atmospheric noise. Good data were obtained at all probes (see Fig. 2). The data analysis is currently underway.

## Discussion

Significant improvements have been made in the DDP measurement system—especially modifications resulting in significant reduction of signal-to-noise in the acquired data. Measurements recently made at the Ben Lomond open-field site yielded clearly sinusoidal pressure signals at a detector probe located 4.5 m from the source. It is clear from these results that measurements can be made over even larger distances and under windier conditions than previously appeared possible.

Scale dependence of soil permeability is evident at the ANAS site. This result is interesting, since the plot studied had no obvious features at the surface which would lead one to expect scale dependence over significant scales. On the other hand, a comparison of Figs. 7 and 8 agrees with the expectation. Although scale dependence is present in the bare and sandy soil at the ANAS site, permeability rolls off to a constant value at a significantly shorter length scale (~ 1m) than at the Ben Lomond treed site (~3 m). This result is anticipated since the oak tree roots and gophers at the latter site are thought to result in fast-

---

[269]Note that later experience suggests that good data ought to be obtainable on all probes and that it is likely that poor data are a result of obstruction of the probe tip. This problem can be remedied by driving a pointed rod through the probe to break up the soil at the probe tip. In addition, these data were acquired before the modification of using a soil probe for the reference side of the pressure transducers, which in itself dramatically increases the signal to noise ratio.

[270]Note that because the ground water (GW) table has been relatively close to the surface during measurements at the ANAS site, the model should include the level of the GW table as a no-flow boundary condition. The model is currently being updated to include the GW table. The data presented here use the old semi-infinite soil model. Although this might result in a somewhat sytematic bias in the permeability results, it should not have any effect on the finding of scale dependence.

In contrast, at the Ben Lomond site, the water table has always been very deep during our measurements. During measurements for the data presented in Fig. 8, the water table was at 13.8 m. During the more recent set of measurements, it was at 8.5 m.

flow paths many meters in length. The roots of the untended grasses at the ANAS site are unlikely to create large fast flow paths. At that site, burrowing fauna are more likely to be the source of observed scale dependence.

Note, however, that although scale dependence ceases at a smaller length scale at the ANAS site, the *magnitude* of scale dependence between 0.5 m and 1 m is much larger at the ANAS than at the Ben Lomond site. Therefore, small-scale static measurements of permeability, such as those typically made using 1/4" galvanized steel probes used in this study, can result in at least as large an underestimation of advective fluxes of gas-phase pollutants as at the Ben Lomond site.

Regarding future directions, we plan to continue to make improvements in the portability of the DDP field-measurement system. The model will be upgraded to include the effect of the water table, and new soils will be investigated for scale dependence of soil permeability to air. In addition to the measurements presented here, we plan to make measurements in an unvegetated sand dune where we expect little or no scale dependence; in a clayey soil with and without trees; and at the treed plot at the ANAS site.

These continued studies will enable us to anticipate better the existence and magnitude of scale dependence of permeability in soils. Understanding of this effect and the ability to measure it using the DDP system will allow us to design field assessments of advective transport of gas-phase contaminants that should yield much more accurate results than were previously possible. An important application is the entry of soil-gas radon into houses (Revzan et al., 1991; Anderson, 1992; Garbesi et al., 1993). While houses tend to interact with soils on a scale of meters, the typical single-probe, static permeability measurements used to assess transport potential probe the soil at a scale of ~0.1 m. If scale dependence of permeability were not accounted for, such a mismatch in measurement vs. system scale would result in a 20-fold underestimation of advective transport rate of gas-phase contaminants at the ANAS site.

## References


Andersen, C.E. 1992. Entry of Soil-Gas and Radon into Houses. Riso-R-623(EN), Riso National Laboratory, Roskilde, Denmark.

Fisk, W.J., Flexser, S., Gadgil, A.J., Holman, H.Y., Modera, M.P., Narasimhan, T.N., Nuzum, T., Revzan, K.L., Sextro, R.G., Smith, A.R., Tsang, Y.W. and Wollenberg, H.A. 1989 Monitoring and Modeling for Radon Entry into Basements: A Status Report for the Small Structures Project. LBL-27692, Lawrence Berkeley Laboratory: Berkeley, CA.

Fisk, W.J., Modera, M.P., Sextro, R.G., Garbesi, K., Wollenberg, H.A., Narasimhan, T.N., Nuzum, T. and Tsang, Y.W. 1992. Radon Entry into Basements: Approach, Experimental Structures, and Instrumentation of the Small Structures Project. LBL-31864, Lawrence Berkeley Laboratory: Berkeley, CA.

Garbesi, K. 1993 Toward Resolving Model-Measurement Discrepancies of Radon Entry into Houses, Ph.D. Dissertation. LBL-34244, Lawrence Berkeley Laboratory .

Garbesi, K., Sextro, R.G., Fisk, W.J., Modera, M.P. and Revzan, K.L. 1993. Soil-gas entry into an experimental basement: Model-measurement comparisons and seasonal effects, Environmental Science and Technology, 27: 466-473.

Revzan, K.L., Fisk, W.J. and Gadgil, A.J. 1991. Modeling radon entry into houses with basements: Model description and verification. Indoor Air, 1: 173-189.

Table I. Components of DDP Measurement System

| |
|---|
| 1. Notebook computer (486-machine, 16 MByte RAM, with active color monitor) |
| 2. Daqbook 100 (Data acquisition and control interface) |
| 3. Data acquisition software (Labtech Control) |
| 4. 5 pressure transducers (Setra) (2 at ±25 Pa, 2 at ± 63 Pa, 1 at ± 1250 Pa) |
| 5. 2 Mass flow controllers (Sierra Instruments) 0-50 LPM, 0-100 LPM |
| 6. Supply and Exhaust pumps (one each) |
| 7. 6 electronically activated solenoid valves |

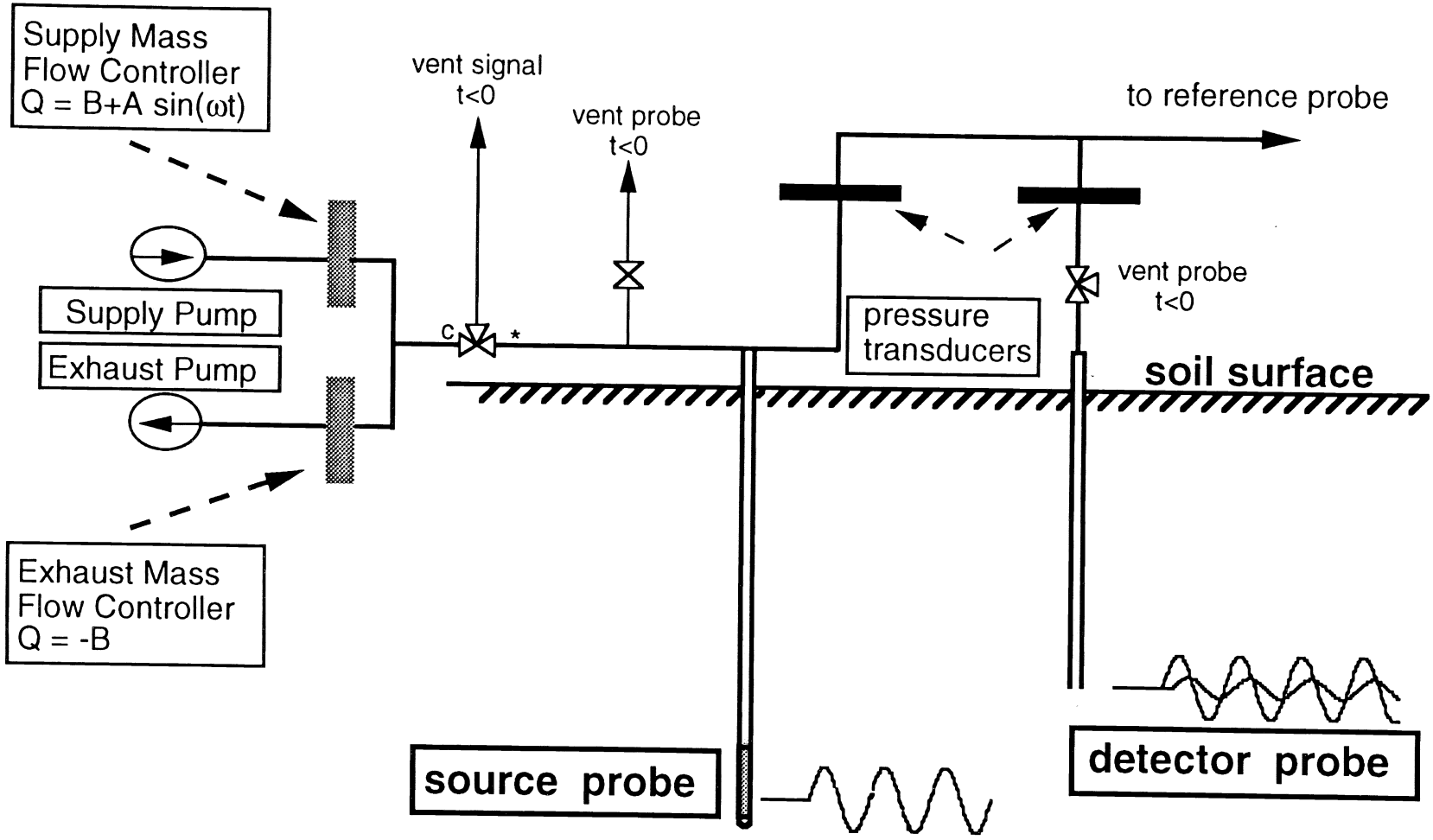


Figure 1. A schematic of the dual-probe dynamic pressure (DDP) system for measuring soil permeability to air over variable length scales. Note that the atmosphere site of both pressure transducers is sent to a reference probe installed in the soil far from the source and detector probes. The purpose is to dampen noise due to atmospheric pressure oscillations.

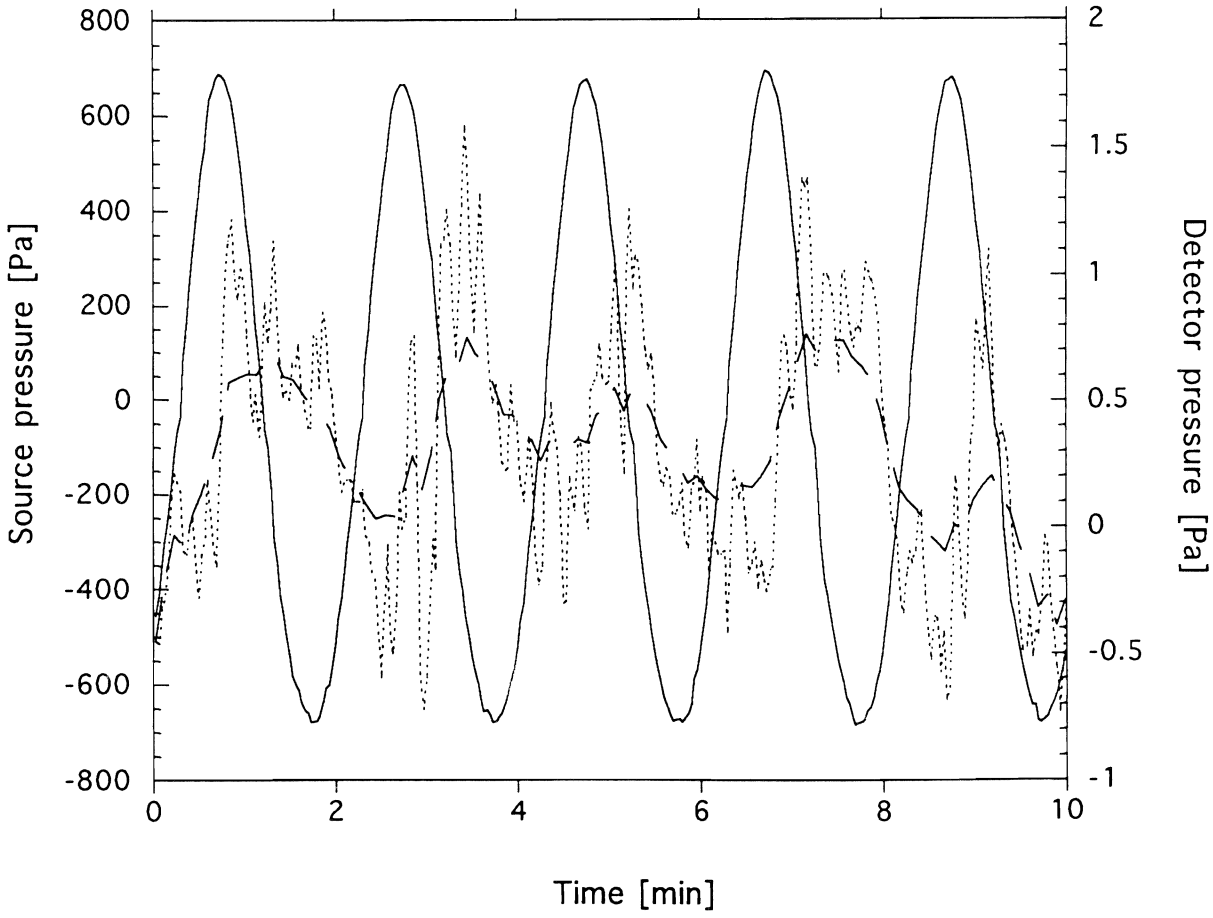


Figure 2. An example of raw pressure data acquired during a DDP measurement. The source and detector probes were 4.5 m apart, both at 1.5 m depth. The solid line is the source probe data; the dotted line is the detector probe data; and the dashed line is a smooth curve fitted to the detector probe data.

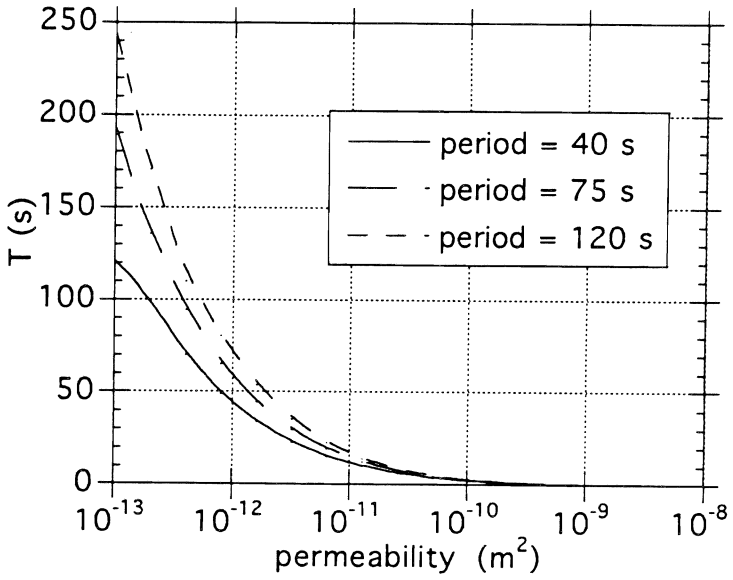


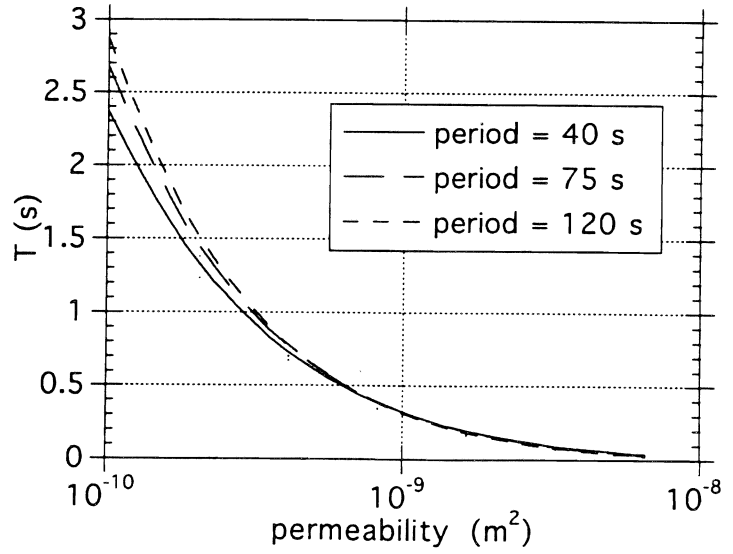


Figure 3a. (top). Time lags calculated using the model for a range of permeabilities between $10^{-13}$ and $10^{-8}$ $m^2$.

Figure 3b. (bottom). A close-up of the curves in 3a at the high end of the range of permeabilities.

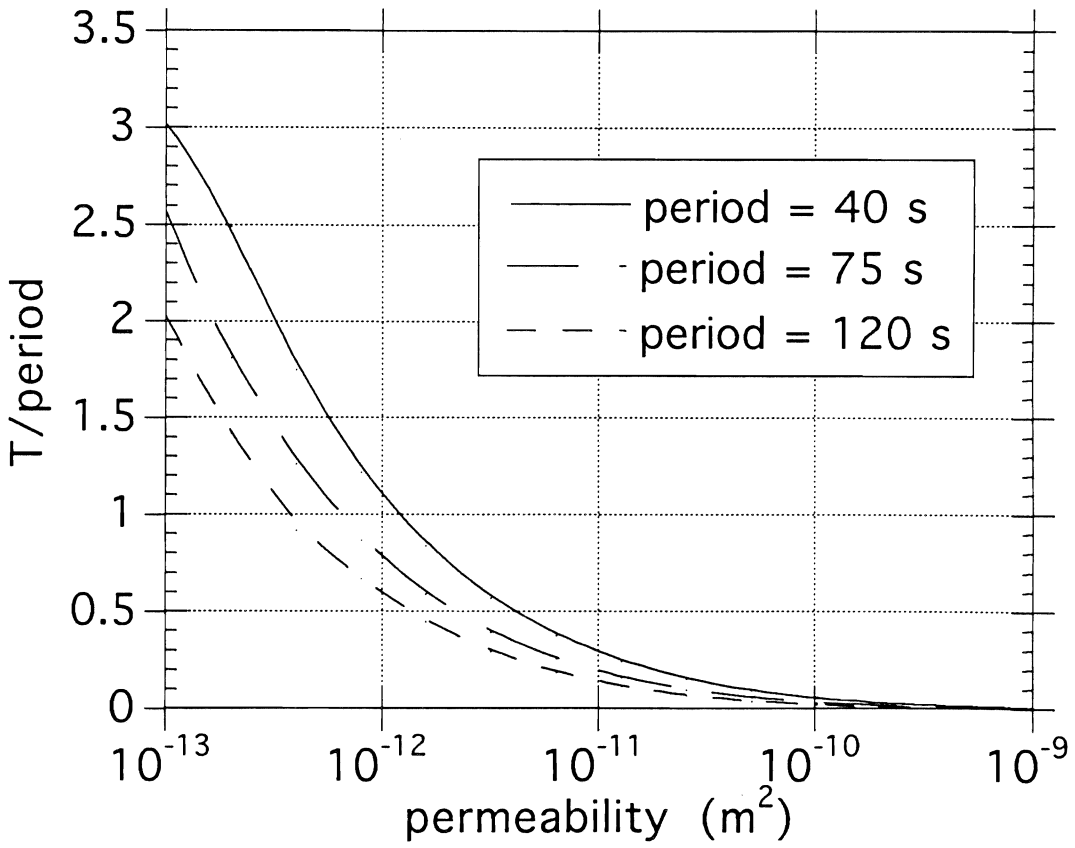


Figure 4. Model output shown is the same as in Figure 3a, but with the lag time normalized by the driving signal period.

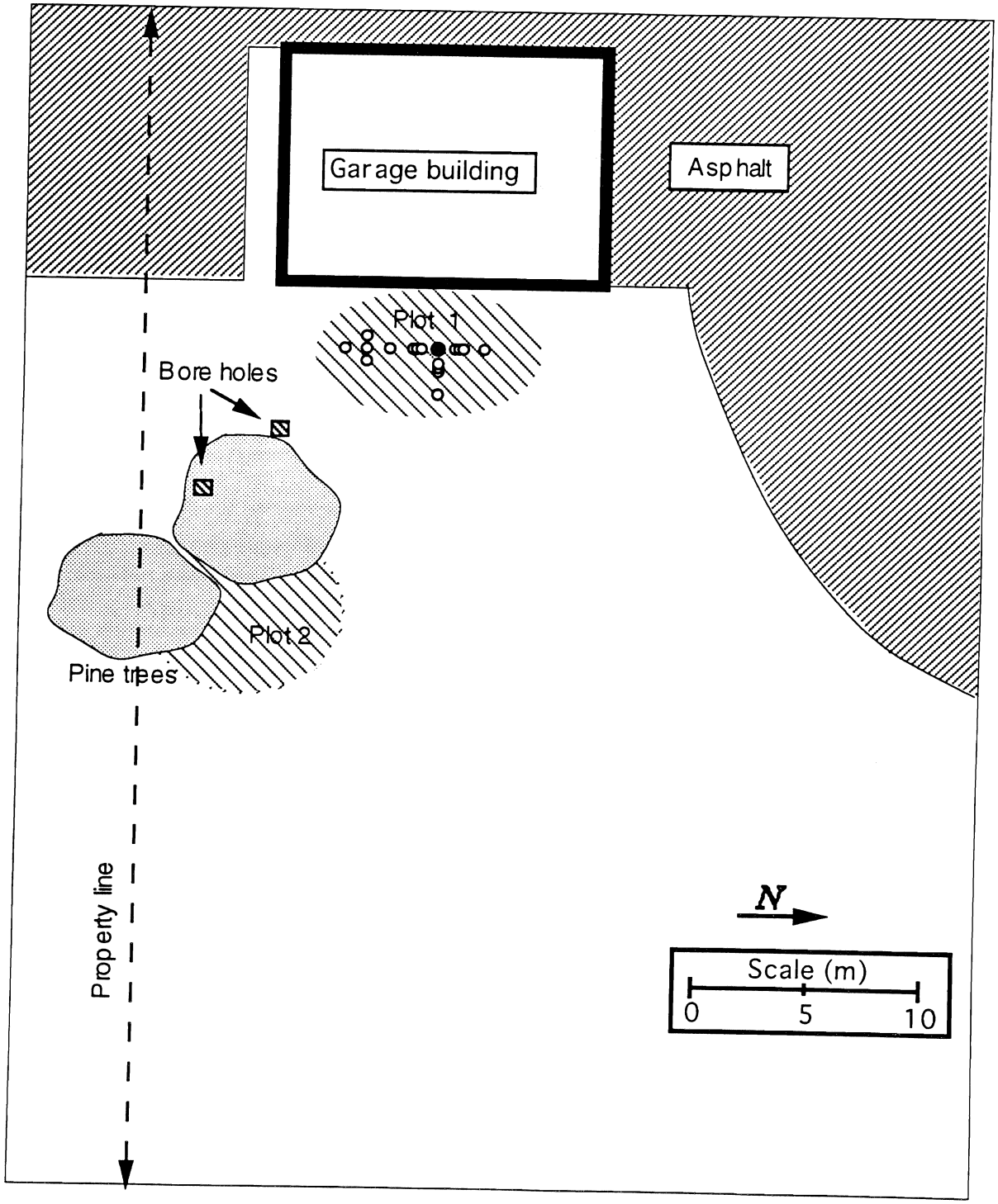


Figure 5. Map of the gasoline spill site at the Alameda Naval Air Station showing the locations of two plots used for DDP measurements and bore holes used for collecting core samples.

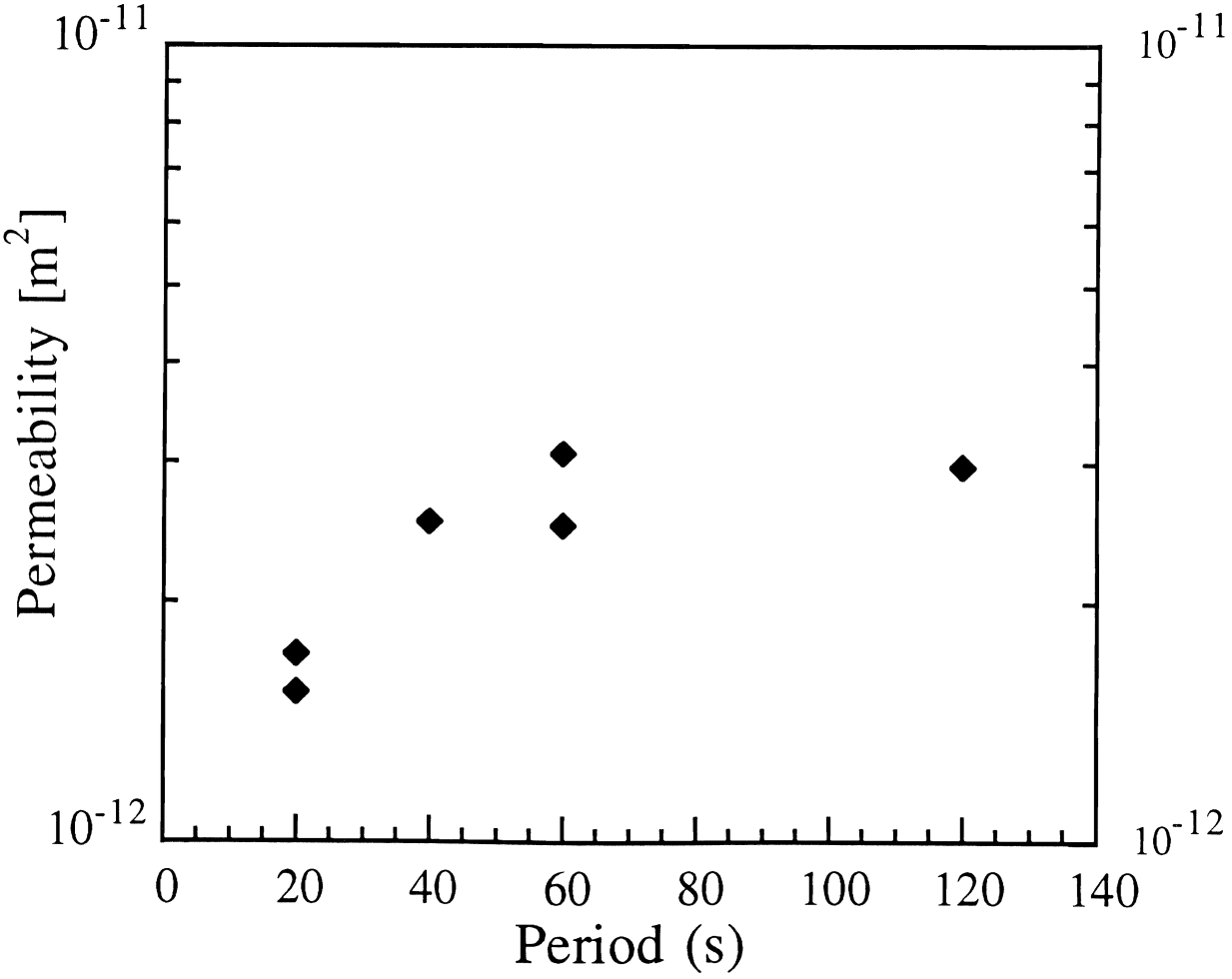


Figure 6. Results of DDP measurements made at a single probe at different source signal periods. The source and detector probes were both 1 m deep, and the detector was located 0.5 m south of the source.

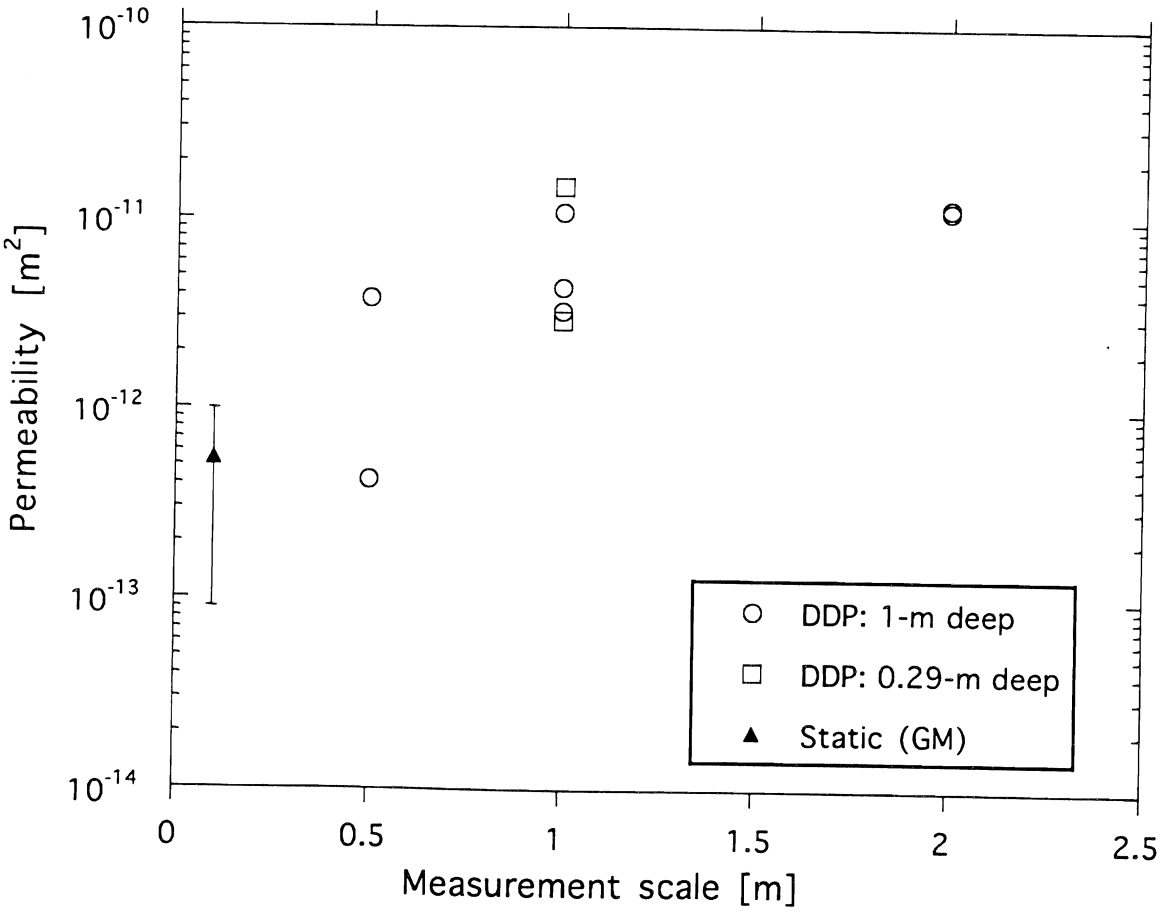


Figure 7. Scale dependence of soil air-permeability at the ANAS site. The figure plots DDP estimates of permeabilities at different length scales (open symbols), and the geometric mean permeability determined by small-scale static measurements made at each of the individual probes in plot 1. The vertical bar indicates the full range of values measured using the traditional small-scale single-probe static pressure technique.

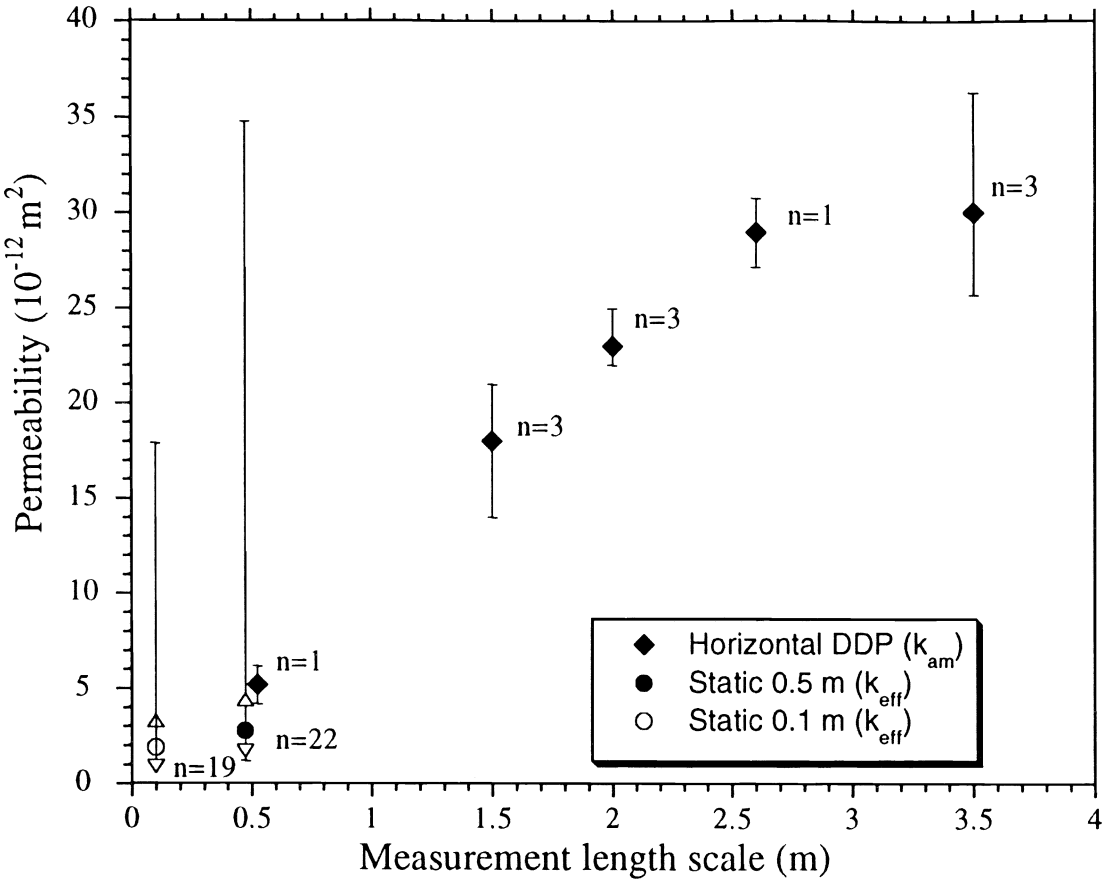


Figure 8. Scale dependence of soil air-permeability measured at the treed plot in Ben Lomond, CA. The vertical bars indicate the full range of measured values for both DDP and small-scale static permeability measurements, except where n = 1 for DDP measurements (n is the number of measurements at the same length scale made using different probes).For n=1, the bar indicates the estimated uncertainty in the measurement. The circular symbols indicate the effective permeabilities ($k_{eff}$) calculated from the 0.1 m and 0.5 m scale measurements. The effective permeability is calculated from $k_{eff} = k_g\left(1+\sigma_Y^2/6\right)$, where $\sigma_Y^2$ is the variance of log(k) and $k_g$ is the weighted geometric mean of the n measurements of k. The open triangles indicate the $k_{eff}$ multiplied by or divided by the geometric standard deviation. The closed diamonds indicate the average value of the DDP measurements.

# Objective, Organization and Function of
# The University of California
# Kearney Foundation of Soil Science

Adopted August 4, 1969
Revised June 30, 1982

## Objective

The Kearney Foundation of Soil Science shall focus its program and support research in definitive missions in the fields of soils, plant nutrition, and water science.

## Organization

A. The Kearney Foundation of Soil Science is administratively responsible to the Vice President-Agricultural and University Services (A&US) through the Director of the Agricultural Experiment Station and the Associate Director of the Agricultural Experiment Station located on the campus on which the Director of the Foundation is resident.

B. The Kearney Foundation of Soil Science is administered for the Division of Agricultural Sciences by a Director with policy guidance by an Advisory Committee and assistance from a Technical Committee.

1. The Director is appointed by the Vice President-A&US, after approval by the Dean and Associate Director of the Agricultural Experiment Station and the Chancellor of the campus on which the Director is to be resident. The Advisory Committee will propose a slate of candidates for the position of Director to the Vice President-A&US for his consideration.

2. The Advisory Committee of the Kearney Foundation is appointed by the Vice-President-A&US and is responsible to him through the Director of the Agricultural Experiment Station for guidance of the Foundation. The Chairman of the Committee is the Associate Director of the Agricultural Experiment Station at the location where the Director of the Foundation resides. The remaining members are the chairmen, or designees, of the Departments of Land, Air and Water Resources at Davis, Plant and Soil Biology at Berkeley, Soil and Environmental Sciences at Riverside, and one representative from a crop production department, one representative from Agricultural Economics and one representative from Agricultural Extension.

3. The Technical Committee of the Kearney Foundation is appointed by the Vice President-A&US. The Technical Committee shall consist of the Foundation Director as Chairman and four to seven other individuals. Individuals will be selected for the Technical Committee on the basis of their expertise on the Kearney Foundation mission subject matter with consideration for appropriate campus, cooperative extension and possibly non-university representation.

4. The Foundation Director may employ necessary administrative, technical or clerical staff to accomplish the Kearney Foundation goals, but there shall be no permanent staff for the Foundation. The Foundation Director will submit an annual report as prescribed by the University for Multi-campus Research Units.

## Functions

A. The function of the Kearney Foundation is to encourage and support research and information dissemination on a specific definitive mission approved by the Vice President-A&US upon the recommendation of the Advisory Committee for a period of five years. The mission shall be one of public concern on which useful contributions are likely to be made in a five-year period. Successive missions will be selected each five years with a new Director for each mission.

B. The Foundation Director shall (1) keep faculty and cooperative extension individuals on various campuses informed on the Foundation goals and objectives and on funding opportunity from the Foundation, (2) solicit research proposals from UC investigators and with help from the Technical Committee develop a proposal funding priority list for review by the Advisory Committee, (3) allocate funds, after review by the Advisory Committee, to accomplish the Foundation mission, (4) be responsible for administrative details including preparation of appropriate reports, (5) assist faculty members to seek funds from sources other than Kearney Foundation that will contribute to the Foundation mission, (6) encourage information dissemination on the mission subject matter to appropriate segments of society, and (7) prepare "wrap-up" document(s) which synthesize the information gained during the five year mission.

C. The Advisory Committee shall (2) advise the Foundation Director when needed, (2) recommend research policy, (3) evaluate progress on the mission research, (4) review recommended allocation of funds by Foundation Director, (5) encourage inter-campus coordination and cooperation to make optimum use of resources and facilities, (6) select a definitive five year research mission to succeed an existing mission, and (7) nominate qualified candidates for a succeeding Director of the Foundation.

D. The Technical Committee shall (2) assist the Director in defining research priorities, (2) evaluate and develop a priority rating on research proposals, and (3) provide advice as requested by the Foundation Director on matters related to technical subject matter.

## General Operational Guidelines

A. Recommended missions and Foundation Director candidates are to be submitted to the Director of the Agricultural Experiment Station and the Vice President-A&US by July 1 preceding the final year of an existing research mission. The new mission and Director-designate are to be selected as soon thereafter as possible to enable the Director-designate to plan the program for activation the following July 1.

B. The Director will manage and authorize expenditures of all funds transferred to the Kearney Foundation as of July 1 of the last year of the mission. Any funds transferred into the Kearney Foundation after that time will be used to accomplish the goals of the succeeding mission.

C. The Director normally will use the year after the five year mission period to "wrap up" the mission by holding symposia, preparing publications, etc. Funds to accomplish this task must be reserved from the budget specifically assigned tot he mission during the preceding five years. The immediate past Kearney Foundation Director will report to the Vice President-A&US through the appropriate Dean and Advisory Committee on progress and budgetary expenditures in achieving wrap up of the mission. At the appropriate time, the mission will be considered complete, the Director formally released from responsibility and any unexpended funds will revert back to the Kearney Foundation for use in subsequent missions.

D. The Director and members of the Advisory and Technical Committees are eligible to submit proposals for funding. They must, however, be excluded from discussion or action related to the particular project.

E. Normally extramural contracts or grants supporting activities consistent with the Kearney Foundation mission will be assigned directly to the Department of the scientist serving as PI rather than to the Kearney Foundation. When an outside agency makes an offer or solicits a proposal from the Foundation Director, the Director will make that information known to the Advisory Committee.

F. Kearney Foundation resources are to supplement Agricultural Experiment Station budgets and provide incentives for research redirection. Because of the temporary nature of the funds, funding of non-career employees such as post-doctoral appointments, research assistantships and part time laboratory helpers is strongly encouraged and routinely approved. Justified funding for career employees with supplemental employee benefit costs must be approved by the Advisory Committee.

## Kearney Foundation of Soil Science Advisory Committee

Dr. John M. Duniway
Chair, Department of Plant Pathology
Professor of Plant Pathology and Plant Pathologist
University of California
Davis, CA 95616
(916) 752-0324 or (916) 752-4269

Dr. Mary K. Firestone
Chair, Department of Environmental Science, Policy and Management
Professor of Soil Microbiology
University of California
Berkeley, CA 94720
(510) 642-3677

Dr. Steven Grattan
Cooperative Extension Water Relations Specialist
Department of Land, Air, & Water Resources, Hydrologic Science Section
University of California
Davis, CA 95616
(916) 752-1130

Dr. William A. Jury
Chair, Professor of Soil Physics and Soil Physicist
Department of Soil & Environmental Sciences
University of California
Riverside, CA 92521
(909) 787-5134

Dr. Keith C. Knapp
Professor of Resource Economics
Department of Soil & Environmental Sciences
University of California
Riverside, CA 92521
(909) 787-4195

Dr. Lanny J. Lund
Associate Dean, Agricultural Experiment Station
College of Natural and Agricultural Sciences
Chair, Kearney Foundation of Soil Science Advisory Committee
Professor of Soil Science and Soil Scientist
Department of Soil & Environmental Sciences
University of California
Riverside, CA 92521
(909) 787-7291 or (909) 787-3859

Dr. Randal J. Southard
Director, Soil Science & Biogeochemistry Program
Associate Professor and Associate Soil Genesis and Morphologist
Department of Land, Air & Water Resources
University of Calfiornia
Davis, CA 95616
(916) 752-1407

# Kearney Foundation of Soil Science Technical Committee

Dr. Andrew C. Chang
Chair, Kearney Foundation of Soil Science Technical Committee
Director, Kearney Foundation of Soil Science
Professor of Agricultural Engineering and Agricultural Engineer
Department of Soil & Environmental Sciences
University of California
Riverside, CA 92521
(909) 787-5325

Dr. Arthur L. Craigmill
Cooperative Extension Toxicology Specialist
Department of Environmental Toxicology
University of California
Davis, CA 95616
(916) 752-2936

Dr. Dennis D. Focht
Professor of Soil Microbiology and Soil Microbiologist
Department of Soil & Environmental Sciences
University of California
Riverside, CA 92521
(909) 787-3446

Dr. Jan W. Hopmans
Associate Professor of Water Management and Assoc. Water Management Specialist
Director, Hydrologic Science Section, Department of Land, Air & Water Resources
University of Calfornia
Davis, CA 95616
(916) 752-3060 or (916) 752-0453

Dr. John G. McColl
Professor of Forest Soils
Department of Soil Science
University of California
Berkeley, CA 94720
(510) 642-1028 or (510) 643-6088

Dr. T. Ishwar Murarka
Senior Program Manager, Land and Water Quality Studies
Electrical Power Research Institute
P. O. Box 10412
Palo Alto, CA 94303
(415) 855-2150

Dr. Albert L. Page
Professor of Soil Science and Chemist
Department of Soil & Environmental Sciences
University of California
Riverside, CA 92521
(909) 787-3654

Dr. Martinus Th. Van Genuchten
Adjunct Professor of Soil Physics
Department of Soil & Environmental Sciences
United States Salinity Laboratory
University of California
Riverside, CA 92521
(909) 369-4847

# Index of Principal Investigators

Sam Alvey
Graduate Student
Department of Soil & Environmental Sciences
University of California
Riverside, CA 92521
(909) 787-3785

Dr. Michael A. Anderson
Assistant Professor of Soil Chemistry and Assistant Soil Chemist
Department of Soil & Environmental Sciences
University of California
Riverside, CA 92521
(909) 787-3757

Dr. Paula Bosserman
Spectroscopist
Department of Soil & Environmental Sciences
University of California
Riverside, CA 92521
(909) 787-2970

Dr. S. A. Bradford
Graduate Research Associate
United States Salinity Laboratory
University of California
Riverside, CA 92521
(909) 369-4851

Dr. Maria Brennerova
Post-Doctoral Research Associate
Department of Soil & Environmental Sciences
University of California
Riverside, CA 92521
(909) 787-3785

Dr. William H. Casey
Associate Professor and Associate Aqueous Geochemist
Department of Land, Air & Water Resources, Soil Science & Biogeochemistry Section
University of California
Davis, CA 95616
(916) 752-3211

Dr. Charles E. Castro
Professor of Nematology and Chemist
Department of Nematology
University of California
Riverside, CA 92521
(909) 787-3766

Volker Clausnitzer
Graduate Student
Deptartment of Land, Air & Water Resources, Hydrologic Science Section
University of California
Davis, CA 95616
(916) 752-3060

Dr. David E. Crowley
Assistant Professor of Soil Science and Assistant Soil Chemist
Department of Soil & Environmental Sciences
University of California
Riverside, CA 92521
(909) 787-3785

Kristie A. Dunkin
Graduate Research Assistant
Department of Environmental Science, Policy and Management
University of Calfiornia
Berkeley, CA 94720
(510) 624-6847

Dr. Walter J. Farmer
Professor of Soil Science and Chemist
Department of Soil & Environmental Sciences
University of California
Riverside, CA 92521
(909) 787-3756

Dr. Mary K. Firestone
Chair, Department of Environmental Science, Policy and Management
Professor of Microbiology
University of Calfiornia
Berkeley, CA 94720
(510) 642-3677

Dr. Karina Garbesi
Post Doctoral Researcher
MS 90-3058
Lawrence Berkeley Laboratory
1 Cyclotron Road
University of California
Berkeley, CA 94720
(510) 486-5180

Paul Haby
Graduate Student
Department of Soil & Environmental Sciences
University of California
Riverside, CA 92521
(909) 787-3785

Dr. John Harte
Energy and Resources Group
University of California
Berkeley, CA 94720
(510) 642-8553

Dr. Zeina Hinedi
Post-Doctoral Research Associate
Department of Soil & Environmental Sciences
University of California
Riverside, CA 92521
(909) 787-3892

Dr. Jan W. Hopmans
Associate Professor of Water Management and Asst. Water Management Specialist
Department of Land, Air, & Water Resources, Hydrologic Science Section
University of California
Davis, CA 95616
(916) 752-3060 or (916) 752-0453

Cathy Irwin
Graduate Student
Department of Soil & Environmental Sciences
University of California
Riverside, CA 92521
(909) 787-3785

Dr. William A. Jury
Chair, Department of Soil & Environmental Sciences
Professor of Soil Physics and Soil Physicist
University of California
Riverside, CA 92521
(909) 787-5134 or (909) 787-5116

Dr. Roy B. Leipnik
Professor of Mathematics
Department of Mathematics
University of California
Santa Barbara, CA 93106
(805) 893-2738 or (805) 893-2171

Dr. F. J. Leij
Assistant Research Soil Physicist
Department of Soil & Environmental Sciences
United States Salinity Laboratory
University of California
Riverside, CA 92521
(909) 369-4851

Dr. John Letey
Associate Director, Centers for Water and Wildland Resources
Professor of Soil Physics and Soil Physicist
Department of Soil & Environmental Sciences
University of California
Riverside, CA 92521
(909) 787-5105 or (909) 787-4327

Dr. Hugo A. Loaiciga
Professor of Geography/Hydrology
Department of Geography
University of California
Santa Barbara, CA 93106
(805) 893-8053 or (805) 893-3663

Dr. Miguel A. Marino
Professor of Water Science and Ground Water Hydrologist
Department of Land, Air & Water Resources, Hydrologic Science Section
University of California
Davis, CA 95616
(916) 752-0684 or (916) 752-0453

Dr. John G. McColl
Professor of Forest Soils
Department of Environmental Science, Policy and Management
University of California
Berkeley, CA 94720
(510) 642-1028 or (510) 643-6088

Dr. Donald R. Nielsen
Assoc. Chair, Department of Land, Air & Water Resources, Hydrologic Science Section
Professor of Soil & Water Science and Water Scientist
University of California
Davis, CA 95616
(916) 752-0695 or (916) 752-0453

John Owens
Graduate Stucent
Lawrence Berkeley Laboratory
University of California
Berkeley, CA 94720
(510) 486-5180

Dr. David R. Parker
Assistant Professor of Soil Chemistry and Assistant Soil Chemist
Department of Soil & Environmental Sciences
University of California
Riverside, CA 92521
(909) 787-5126

Dr. Carlos E. Puente
Assistant Professor of Hydrologic Science and Assistant Hydrologist
Department of Land, Air, and Water Resources
University of California
Davis, CA 95616
(916) 752-0689 or (916) 752-0453

Steve Ries
Graduate Student
Department of Soil & Environmental Sciences
University of California
Riverside, CA 92521
(909) 787-3785

Dr. Peter A. Rock
Professor of Chemistry
Department of Chemistry
University of California
Davis, CA 95616
(916) 752-0940

Dr. Kate M. Scow
Assistant Professor of Soil Science and Assistant Soil Microbial Ecologist
Department of Land, Air, & Water Resources, Soils & Biogeochemistry Section
University of California
Davis, CA 95616
(916) 752-4632 or (916) 752-1406

Dr. Peter J. Shouse
Soil Scientist
United States Salinity Laboratory
University of California
Riverside, CA 92521
(909) 369-4849

Mr. John Steude
Director of Scanning Services
Scientific Measurement Systems, Inc.
(Precision Measurement and Nondestructive Inspection Systems)
2209 Donley Drive
Austin, TX 78758
(512) 837-4712

Dr. Garrison Sposito
Professor of Soil Physical Chemistry
Department of Environmental Science, Policy and Management
University of California
Berkeley, CA 94720
(510) 643-8297 or (510) 643-9171

Dr. Martinus Th. Van Genuchten
Adjunct Professor of Soil Physics
Department of Soil & Environmental Sciences
United States Salinity Laboratory
University of California
Riverside, CA 92521
(909) 369-4847